1988

X-ray diffraction characterization of the quality and thermal stability of II-VI semiconductor superlattices

Ralph David Knox
Iowa State University

INFORMATION TO USERS

The most advanced technology has been used to photograph and reproduce this manuscript from the microfilm master. UMI films the original text directly from the copy submitted. Thus, some dissertation copies are in typewriter face, while others may be from a computer printer.

In the unlikely event that the author did not send UMI a complete manuscript and there are missing pages, these will be noted. Also, if unauthorized copyrighted material had to be removed, a note will indicate the deletion.

Oversize materials (e.g., maps, drawings, charts) are reproduced by sectioning the original, beginning at the upper left-hand corner and continuing from left to right in equal sections with small overlaps. Each oversize page is available as one exposure on a standard 35 mm slide or as a 17″ × 23″ black and white photographic print for an additional charge.

Photographs included in the original manuscript have been reproduced xerographically in this copy. 35 mm slides or 6″ × 9″ black and white photographic prints are available for any photographs or illustrations appearing in this copy for an additional charge. Contact UMI directly to order.

UMI
Accessing the World's Information since 1938

300 North Zeeb Road, Ann Arbor, MI 48106-1346 USA

Order Number 8825934

X-ray diffraction characterization of the quality and thermal stability of II–VI semiconductor superlattices

Knox, Ralph David, Ph.D.

Iowa State University, 1988

U·M·I
300 N. Zeeb Rd.
Ann Arbor, MI 48106

PLEASE NOTE:

In all cases this material has been filmed in the best possible way from the available copy. Problems encountered with this document have been identified here with a check mark __✓__.

1. Glossy photographs or pages __✓__
2. Colored illustrations, paper or print _____
3. Photographs with dark background __✓__
4. Illustrations are poor copy _____
5. Pages with black marks, not original copy _____
6. Print shows through as there is text on both sides of page _____
7. Indistinct, broken or small print on several pages __✓__
8. Print exceeds margin requirements _____
9. Tightly bound copy with print lost in spine _____
10. Computer printout pages with indistinct print _____
11. Page(s) _____ lacking when material received, and not available from school or author.
12. Page(s) _____ seem to be missing in numbering only as text follows.
13. Two pages numbered _____. Text follows.
14. Curling and wrinkled pages _____
15. Dissertation contains pages with print at a slant, filmed as received __✓__
16. Other _____

_____

_____

X-ray diffraction characterization of the quality and thermal stability of II-VI semiconductor superlattices

by

Ralph David Knox

A Dissertation Submitted to the

Graduate Faculty in Partial Fulfillment of the

Requirements for the Degree of

DOCTOR OF PHILOSOPHY

Department: Physics

Major: Solid State Physics

Approved:

Signature was redacted for privacy.

In Charge of Major Work

Signature was redacted for privacy.

For the Major Department

Signature was redacted for privacy.

For the Graduate College

Iowa State University
Ames, Iowa

1988

TABLE OF CONTENTS

I. INTRODUCTION

A. Preliminary Remarks

The ability to deposit material on an atomic scale has lead to the development of superlattice (SL) structures. A SL is defined as the periodic arrangement of two layers in alternation. This somewhat generic definition places no restriction on the type of constituent materials that are involved.

Research on semiconductor SLs was instigated with the theoretical proposal by Esaki and Tsu (1970). This proposal was based on a one-dimensional periodic structure consisting of ultrathin semiconducting materials. Many interesting and verifiable effects are possible, when the electronic mean free path is larger than the modulation period.

This research investigation concerns the structural characterization of semiconductor SLs. There are many excellent review articles in the literature that describe the profound properties of SLs, Capasso (1987), for example. McWhan (1985) provides a detailed discussion of SL structure, while Esaki (1985) and Burns (1985) present a concise summary of the SL electronic properties.

The remainder of this introduction is divided into five sections. Sections I.B and I.C provide background information about semiconductor and SL properties. The potential applications of II-VI SLs are discussed in section I.D. The structural aspects of semiconductor SLs are introduced in section I.E. Finally, the purpose of this research investigation is discussed in section I.F.

This dissertation comprises two parts: background and experiment.

Chapters II and III concern x-ray diffraction from single crystals and SLs, respectively. Chapters IV, V, and VI discuss the experimental aspects of this research investigation. Specifically, chapter IV provides an overview of both the research apparatus and general experimental techniques. Chapters V and VI, which concern $Hg_{1-x}X_xTe$-CdTe and CdTe-ZnTe SLs, respectively, provide a discussion of the individual research experiments and the presentation of experimental results.

B. Semiconductor Properties

A very brief summary of semiconductor properties will provide the necessary framework for a discussion of semiconductor SL applications. Most of the semiconductor properties can be understood within the quantum mechanical formalism, and unless otherwise stated, the following discussion is based on a quantum mechanical description.

By definition, a semiconductor is a crystalline solid with predominantly covalent bonding (Welker & Kellner, 1983). A nonzero energy gap separating the filled valence and empty conduction bands distinguishes a semiconductor from a metal. Because of the finite band gap, a pure semiconductor becomes an insulator at zero temperature. However, impurities or external radiative interactions can promote electrons from the valence band to the conduction band, allowing current conduction.

Essentially all semiconductor research is focused on exploiting the unique band structure properties for electronic device applications. Energy bands, which arise from the splitting of single atom energy

states through collective interactions of all crystal atoms, define the permissible energy states that an electron can occupy within the crystal. The energy band structure is typically expressed through the energy dependence on momentum (Kittel, 1986). Current conduction occurs only when the net momentum distribution is shifted to a nonzero value.

For comparison purposes, the free electron situation will be discussed first. An electron can be described by an oscillating wavefunction $\Psi=e^{i\kappa\cdot r}$, where r is the position vector and κ is the wave vector. The wave vector is related to the wavelength of the traveling wave λ by $|\kappa|=2\pi/\lambda$. By applying the quantum mechanical momentum operator ($p=-ih\nabla/2\pi$) to Ψ, the relationship between momentum and wave vector can be represented by $p=h\kappa/2\pi$, where h is Planck's constant. The energy ($E=p\cdot p/2m_e$, m_e is the electron mass) is proportional to $\kappa\cdot\kappa$. The allowed momentum states form a quasi-continuous distribution of discrete momentum values. The extremely small spacing between adjacent quantized momentum states is inversely proportional to the confinement length of the electron along the same momentum direction. This is a consequence of applying the macroscopic boundary conditions to the quantum mechanical description (Schrodinger's equation, for example). Having an unbounded energy, the free electron is not confined to a band structure.

Electron propagation inside a crystal is quite different from the free electron situation. The wave-like property of electrons interfere with the periodic potential of the crystal lattice, modifying the simple free electron relationship between energy and momentum. A nearly free electron model, which assumes that valence electrons are weakly perturbed by the ion cores, can be used to explain many of the

predominant features that are observed for electrons traveling in a lattice.

Figure I.1a shows the modified energy-wave vector relation for an electron propagating along a direction that has a translational invariant spacing a. As in the free electrons situation, the allowed momentum values form a quasi-continuous distribution. However, because of the lattice interaction, forbidden energy gaps exist, forming bands of allowed energy states. Energy gaps occur when the electron wave vector corresponds to an integral multiple of the reciprocal lattice vector, defined as the reciprocal of the lattice unit cell length, along the propagation direction. With the scattered and transmitted electron wavefunctions having the same phase, this situation produces standing waves which can not transport momentum. Each primitive unit cell of the crystal lattice contributes one independent value of momentum to each energy band (Kittel, 1986).

The Pauli exclusion principle, which forbids fermions (electrons) from simultaneously sharing one quantum mechanical state, is responsible for the distribution of electrons within the allowed energy states of a semiconductor. All electrons are assigned, in ascending order of energy, to the allowed energy states. The Fermi energy is defined as the energy of the topmost filled level in the ground state or lowest energy state. Thus, no current can flow through a crystal that has a Fermi energy equal to the top of an energy band, unless the electron population has been redistributed so that a nonzero net momentum is possible.

When an electron is promoted to a higher energy band, a 'hole' will

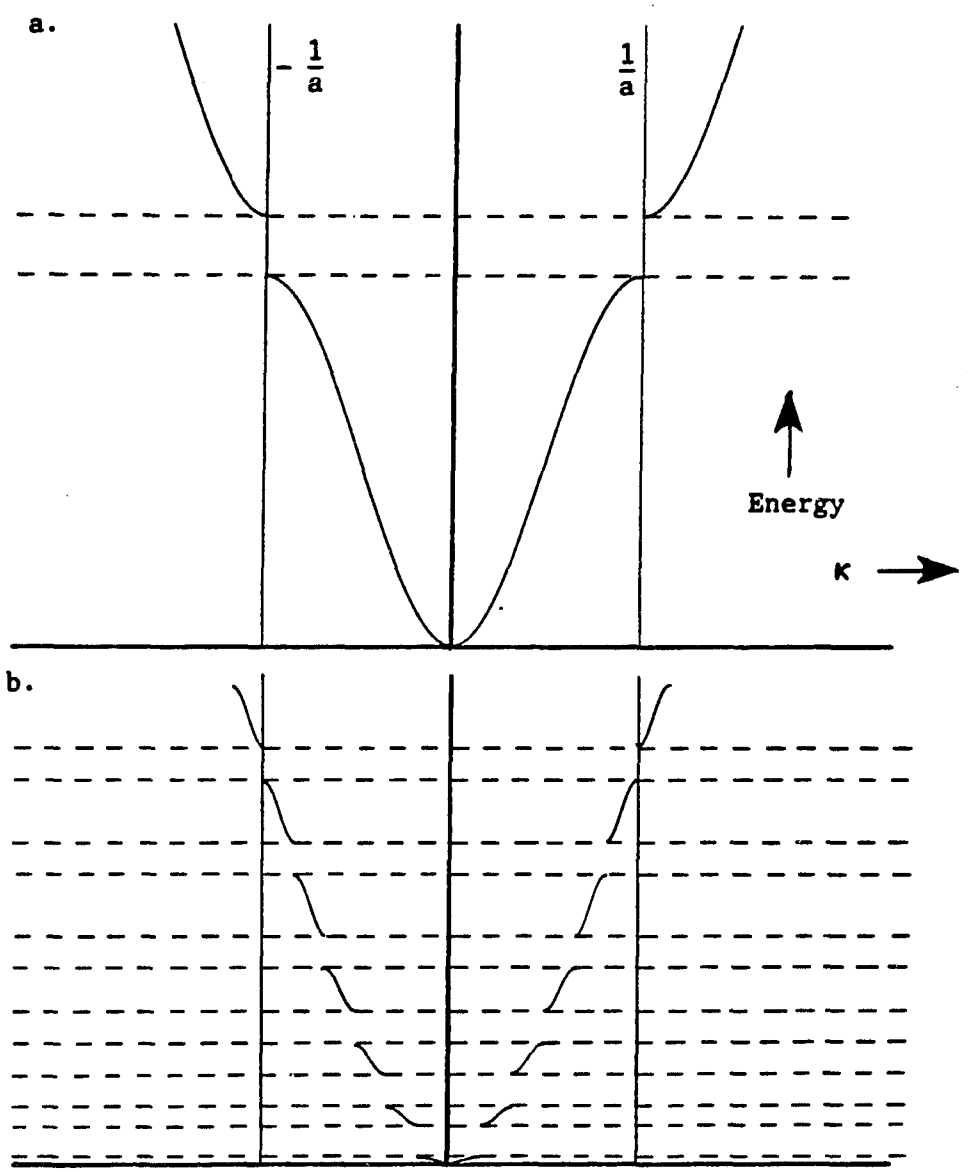

Figure I.1a Energy (E) as a function of wavevector (κ) for an electron travelling inside a bulk semiconductor. The electron is travelling along a component of the lattice that has a spatial period a. The energy within the dotted region is forbidden for the electron and defines the energy gap

Figure I.1b Energy (E) as a function of wavevector (κ) for an electron travelling inside a semiconductor SL. The electron is travelling along a component of the SL structure that has an average constituent lattice period (a) and a composition superperiod (L=6a). The additional periodicity produces additional and narrower forbidden energy regions, compared to a bulk semiconductor

be formed in the previously occupied band. An intrinsic semiconductor has an equal number of electrons and holes, and both are capable of current conduction. Additional electrons, or holes, can be incorporated into the material by substituting a fraction of bulk atoms with donor or acceptor impurity atoms. This can increase the number of current carriers. However, the impurity atoms will reduce the electron mean free path length by forming point defects in the crystal lattice. In addition to impurity doping, thermal activation and radiation absorption can also influence the semiconductor band occupation.

C. Semiconductor Superlattice Properties

A semiconductor SL is an artificially modulated structure which is produced by depositing two crystalline semiconductor materials, in alternation, along a single direction. No restrictions are placed on the relative thickness of the two semiconductor materials within each modulated period. However, the constituent layer ratio, modulation wavelength (SL period), and growth direction must be consistent throughout the deposition process. Ideally, the crystal lattice of both constituent materials should be coherently related across the each interfaces.

The physical properties of a SL can be designed by selecting the materials, constituent layer ratio, period, growth direction, and total film thickness. This is analogous to an alloy having predetermined physical properties which are different from the constituent materials. Although a SL and corresponding homogeneous alloy have many similar properties, the presence of a SL period yields electronic properties

which can not be achieved by an alloy.

The wave-like properties of the valence electrons interact with the periodic modulated structure of the SL, which is completely analogous to the electron interaction within a bulk crystal lattice. Since the SL period is typically much greater than the lattice constant of the constituent materials, the allowed energy regions, called minibands, are very narrow. Many minibands are formed within the host energy band of the constituent crystal lattice. This situation is shown in Figure I.1b.

There are three very useful properties which provide the main motivation for fabricating the SLs considered in this research investigation. First, the narrow allowed energy region of the minibands enhances the current carrier lifetime. This is a consequence of the conservation of energy. The electrons can loose energy and settle to the bottom of conduction band by various relaxation mechanisms. For bulk semiconductors having a large energy region, lattice vibrations (longitudinal optic phonons) can absorb a quanta of energy that is comparable to the band gap and provide a predominant relaxation mechanism (Burns, 1985). An electron can change energy states, provided that the final energy value is allowed within the system under consideration. The phonon relaxation mechanism which plagues bulk semiconductors is greatly restricted since the energies that a phonon can absorb are typically larger than narrow energy region of SLs. Since the final energy states of these electron-phonon interactions lie in forbidden energy regions, the interaction process is forbidden.

Second, SLs allow for the spatial separation of charge carriers from the parent donors. As discussed in section B of the introduction, an impurity material can be incorporated into a bulk semiconductor to enhance the current carrier concentration. The impurity atoms, however, are homogeneously distributed and act as scattering sites for the electrons. This undesirable effect can be avoided in a SL structure. Impurity atoms can be introduced and spatially trapped in one constituent layer while the donated carriers become trapped in the "quantum well" structure of the second material, depending on the individual properties of the constituent materials. Thus, the carrier concentration can be enhanced within one of the constituent layers without the adverse carrier scattering effects (Arch, Shur, Abrokwah & Daniels, 1987). This SL property can be exploited for ballistic electron applications.

Third, the constraint required to artificially adjust the band gap of a SL is less restrictive than the analogous alloy system. The SL band gap is related to the constituent layer ratio which can be controlled with high precision (Glass, 1987). The semiconductor alloy band gap is related to the constituent concentration ratio which is typically more difficult to control. In addition, the band gap dependence on the constituent layer ratio for a SL is generally less sensitive than the band gap dependence of the constituent concentration ratio for the corresponding alloy. Band gap tunability is an essential feature for photon detector applications.

D. II-VI Superlattice Applications

This research investigation concerns two SL systems: CdTe-ZnTe and $Hg_{1-x}X_xTe$-CdTe, X=Cd, Mn, Zn. Te is the only group VIA element, Cd, Hg, and Zn are group IIB elements, and Mn is a group 7B element of the periodic table. Optoelectronic device applications provide the primary motivation for growing the SLs discussed in this dissertation.

The HgTe-CdTe SL was originally proposed as an infrared material by Schulman and McGill (1979). Theoretically, the band gap was shown to be related to the SL layer thickness. The band gaps of the constituent materials define the possible range of SL band gap energies. HgTe is a semimetal with a direct band gap (Γ_6-Γ_8) of ~-0.3 electron volts (eV), while CdTe is a semiconductor having a direct band gap (Γ_6-Γ_8) of ~1.6 eV (Long & Schmit, 1970). Figure I.2 shows the energy band structure of CdTe and HgTe (Long and Schmit, 1970).

The original work of Schulman and McGill predicted that very thin layer SLs were required for infrared applications. Since these SLs had not been grown, the demanding constraint of very thin layers was considered a major disadvantage. However, the successful growth of HgTe-CdTe SLs by Faurie, Million, and Piaguet (1982) established that good quality HgTe-CdTe SLs could be grown.

Photon detection is easily accomplished by semiconductors that have an appropriate energy band gap. Incident radiation excites electrons from states near the top of the valence band to the low energy states of the conduction band. This produces electron-hole pairs, which change the electrical properties of the material. Depending on the detector design, either a photocurrent or enhanced conductivity is detected as

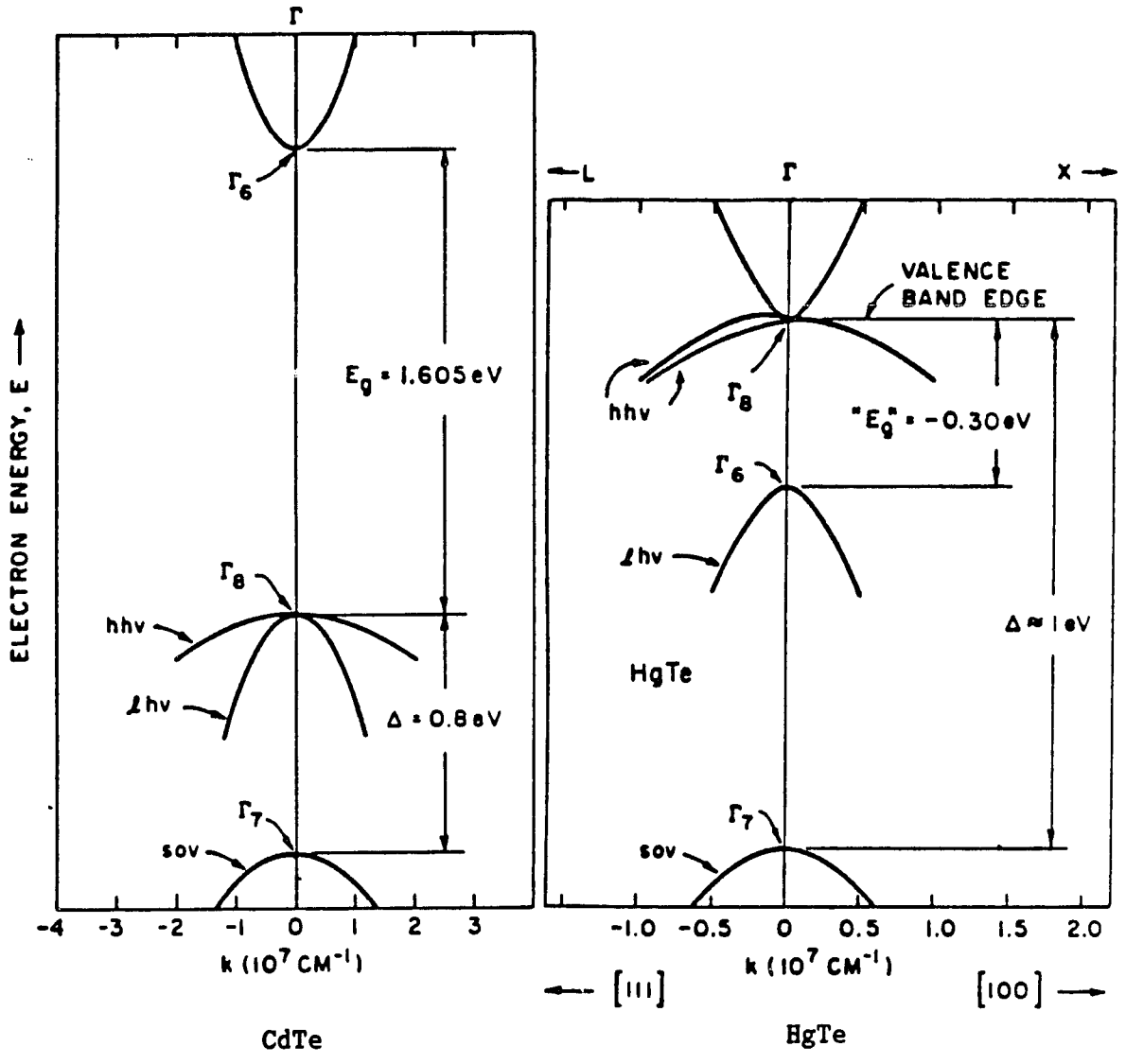

Figure I.2 Energy band structure of CdTe (left) and HgTe (right) at T~0°K in the vicinity of the Γ point (κ=0), where the valence and conduction band extrema typically occur for the zincblende structure. Γ_8 defines the valence band extremum and Γ_6 is the conduction band minimum

the electron-hole pairs are created (Kruse, McGlauchlin & McQuistan, 1962).

The $Hg_{1-x}Cd_xTe$ alloy is the material most often used to fabricate infrared detectors. By varying the x concentration, the $Hg_{1-x}Cd_xTe$ energy band gap can be varied continuously and nearly linearly between the HgTe and CdTe band gaps, with the alloy band gap crossing zero at x~0.2 at 77°K. However, large tunneling currents and the large composition dependence of the band gap present two major difficulties of using the $Hg_{1-x}Cd_xTe$ alloy as detectors.

On a theoretical basis, Smith, McGill, and Schulman (1983) have demonstrated that HgTe-CdTe SLs potentially offer three inherent advantages over the $Hg_{1-x}Cd_xTe$ alloy. First, tunneling currents in SLs are much less than in the alloy having the same band gap. Second, the fractional uncertainty in the band gap control parameter permissible in the SL is greater than that permissible in the alloy for fixed band gap tolerance requirements. This is illustrated in Figure I.3 (Smith, McGill & Schulman, 1983), where the detector wavelength dependence on composition for a SL has a smaller slope compared to the alloy. Third, p-side diffusion currents in the SL are expected to be less than in the alloy of the same band gap.

The incorporation of Cd, Mn, and Zn into HgTe-CdTe SLs in the form of $Hg_{1-x}X_xTe$-CdTe was devised in an effort to better understand the stability of these systems (Staudenmann, Knox & Faurie, 1987a). Since these SLs are grown at elevated temperatures of approximately 180°C, some interdiffusion of atoms across the interfaces might be expected, especially for layers that were deposited early during growth.

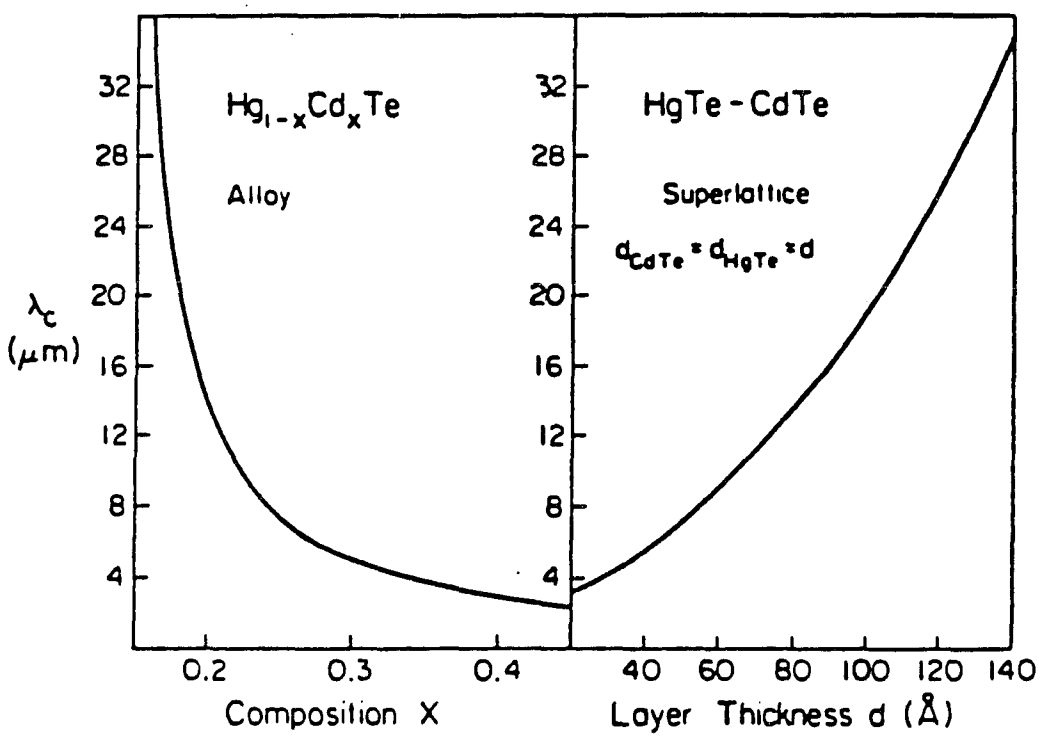

Figure I.3 Wavelength absorption edge (λ_c=hc/2πE, h=Planck's constant, c=speed of light, and E=energy band gap) as a function of composition for a $Hg_{1-x}Cd_xTe$ alloy (left) and HgTe-CdTe SL (right). The alloy composition parameter is the Cd concentration (x) and the SL composition parameter is the common layer thickness (d) of the CdTe and HgTe constituent layers. The SL period (L) is twice the individual constituent layer thickness for this example

Although there is no direct application, an investigation of these SLs is important.

CdTe-ZnTe SLs are thought to be particularly promising for optoelectronic devices that operate in the visible light spectrum (Monfroy, Sivananthan, Chu, Faurie, Knox & Staudenmann, 1986). Tunable color light emitting diodes (LEDs) and short wavelength semiconductor lasers are two motivating applications which are generating current interest (Kobayashi, Konagai & Takahashi, 1986). The possible band gap range is ~1.6eV-~2.1eV (Abrikosov, Bankina, Poretskaya, Shelimova & Skudnova, 1969), which is defined by the bulk direct band gaps of CdTe and ZnTe, respectively.

E. Composite Superlattice Structure

The SLs under investigation have been grown by either molecular beam epitaxy (MBE) or Metalorganic Chemical Vapor Deposition (MOCVD) processes. A extended summary of both the MBE and MOCVD growth processes can be found in the National Research Council's report on artificially structured materials (Brinkman, 1985). Both techniques alternately deposit the constituent materials onto a crystalline substrate material. Besides providing a mechanical support, a substrate is used to influence the growth of the SL film. The growth rate, film quality, and crystallographic orientation with respect to the growth direction are primarily affected by the substrate temperature. Although there are many contributing factors, the substrate crystal structure and surface orientation greatly influence the lattice orientation of the SL film. Both GaAs and CdTe substrates were used to grow the SLs for this

research investigation.

The structural integrity of the SL film is primarily influenced by the degree of lattice coherence across each interface. This applies with equal importance to the substrate-SL interface. Ideally, the crystallographic orientation of two materials that form an interface should be related. That is, during the formation of an interface, the second material should be deposited epitaxially on the first (Zur & McGill, 1983). This condition is extremely important and is not always present in SL systems. Without epitaxic interfaces, a consistent transition between interfaces can not be maintained. This will greatly affect the SL electrical properties, which require long range period coherence.

The difficulty in achieving epitaxy between materials that have identical crystal structures is based on the degree of lattice parameter matching across the interface. In particular, the lattice constants parallel to the interface plane should be matched as closely as possible. For this investigation, the amount of mismatch is defined as twice the lattice parameter difference divided by the lattice parameter sum (Picraux, Dawson, Osbourn & Chu, 1983). This definition eliminates the awkwardness of specifying the lattice parameter to which the mismatch is based.

Epitaxic interfaces require both involved materials to be elastically strained. The strain along any given direction is defined by the fractional change of the atomic bond length or lattice constant when compared to the bulk value (Vook, 1975). Elastic strain is one mechanism that can reduce or eliminate the misfit at an interface. If

the misfit is only reduced, the remainder is accommodated by misfit dislocations (Matthews, Mader & Light, 1970). The division of misfit accommodation between dislocations and elastic strain depend on the difference between the two bulk lattice parameters, the constituent layer thickness, the dislocation geometry, the bonding across the interface, and the elastic parameter that characterize the two materials. A misfit energy can be attributed to the interface, which is related to the interfacial bonding and the degree of misfit. As the bonding strength increases, the interface tends to be pseudomorphic in an effort to reduce the misfit energy (Woltersdorf, 1981).

GaAs, which is commonly used as a substrate for the SLs under investigation, has a significantly smaller lattice parameter than the constituent materials. The mismatch between GaAs and ZnTe, HgTe, and CdTe is 7.4%, 13.3%, and 13.6%, respectively. Because of these large mismatches, a buffer layer is usually deposited on the substrate before the SL is grown. The buffer layer should provide a compatible crystal structure having an intermediate surface lattice constant. A buffer layer is commonly deposited, even for a small or negligible substrate-SL mismatch. This provides a fresh surface for SL deposition. Thus, the SL composite system typically consists of a substrate, one or more buffer layers, and a SL film.

F. Research Motivation

The successful growth of HgTe-CdTe (Faurie, Million & Piaguet, 1982) and CdTe-ZnTe (Monfroy, Sivananthan, Chu, Faurie, Knox & Staudenmann, 1988) SLs was accomplished only a few years ago. Ultimately, these SLs

will be used commercially as optoelectronic devices. Much progress, however, is needed before these s can compete with the corresponding homogeneous alloys (McGill, Wu & Hetzler, 1986). The ability to grow good quality SLs with known and reproducible specifications is imperative for commercial success.

The structural characterization of SLs is fundamentally important. Most investigational techniques that probe the electronic properties of SLs provide indirect information. Specific electronic quantities are extracted with respect to an assumed crystal structure. It is tempting to attribute non-alloy properties to a SL structure without exploring other possibilities, such as local nonhomogeneity of the deposited film or the presence of multiple domains, for example. This tendency is quite common in the literature. A thorough investigation of SL properties must include structural analyses to complement electrical measurements.

Many structural characterization techniques can be applied to SL systems. Transmission electron microscopy (TEM), electron energy loss spectroscopy (EELS), energy dispersed x-ray spectroscopy (EDXS), and scanning electron microscopy (SEM) are commonly used to probe the SL structure. However, as with any analytical tool, there are limitations to these methods. Since the SL electrical properties depend on the long range coherence of the modulated period, large regions, defined by distances of a micron (μ) or more, must be structurally assessed. The techniques introduced above have a common limitation--each probe a very spatially localized region of the SL. In addition, these techniques

require special sample preparations and often are destructive.

X-ray diffraction is a nondestructive technique that provides structural information on the SL composite system (Segmuller & Murakami, 1985; Staudenmann, Horning & Knox, 1987). The penetrating x-ray radiation can probe the SL film, buffer layer(s), and substrate simultaneously. For example, the intensity I_0 of 0.71Å x-ray radiation will be reduced to I_0/e after traveling through a 25μ thick HgTe-CdTe SL. This is assuming equal portions of HgTe and CdTe within each period of the SL. SL films are typically less than 5μ thick.

The scattering of x-ray radiation by a crystalline solid is analogous to the electron-lattice interaction. A significant diffracted x-ray intensity requires the coherent scattering of many atoms. Deviations in the crystal lattice will reduce this coherent scattering, and can be detected. This makes x-ray diffraction an indispensable investigational tool for assessing the structural order of composite SL systems.

X-ray diffraction can also provide information on the structural profile of the interface regions. This is very important, since many of the predicted electronic properties of SLs are based on abrupt heterointerfaces. Both misfit dislocations and interdiffusion reduce the structural quality at the interfaces. Misfit dislocations can greatly reduce the long range coherence and virtually eliminate all SL properties.

SL interdiffusion can restrict the initial quality during growth and affect the long term stability after growth. During SL growth, the

constituent materials are deposited at elevated temperatures. HgTe-CdTe and CdTe-ZnTe SLs are grown at approximately 180°C and 285°C, respectively. These elevated temperature enhance the mobility of the constituent atoms, producing less abrupt interfaces. Early deposited interfaces will continue to diffuse as the final layers are formed. This can reduce the long range coherence of the SL. The interdiffusion process will continue after growth at a rate that depends on the surrounding temperature. By affecting the electronic properties (Schulman & Chang, 1985), interdiffusion will restrict SL applications at elevated temperature environments.

This research investigation addresses both the structural quality and thermal stability of HgTe-CdTe and CdTe-ZnTe SLs. X-ray diffraction is the principal investigational tool used in the analyses. The structural information provided by this research investigation is intended to aid the growth development of II-VI semiconductor SLs. The thermal stability component of this investigation is a continuation of the HgTe-CdTe SL interdiffusion research instigated by David Arch (Arch, Faurie, Staudenmann, Hibbs-Brenner & Chow, 1986) using an improved experimental procedure (Staudenmann, Horning, Knox, Reno, Sou, Faurie & Arch).

II. X-RAY DIFFRACTION BACKGROUND: THEORY

A. Mathematical Discussion of Crystal Lattices

A crystal is a periodic three dimensional arrangement of atoms. For real crystal solids, the degree of periodic perfection varies from the perfect crystalline state to the randomly ordered amorphous state. Point, line, and planar defects disrupt the periodic atomic arrangement of real crystals (Anderson, Leaver, Rawlings & Alexander, 1985). Depending on the defect structures present, the macroscopic crystal perfection is replaced by a collection of domains, which preserve the lattice periodicity on a small scale. X-ray diffraction is very sensitive to these crystal domains. A mathematical overview of perfect crystal lattices will facilitate a discussion of x-ray diffraction from crystal domains. A more detailed treatment can be found in any introductory crystallography book, such as Ladd and Palmer (1978).

A crystal can be represented by a common pattern attached to a periodic point lattice. This representation exploits the crystal symmetry. The common pattern defines a unit cell, which represents the local symmetry of the crystal lattice and the point lattice describes the translational symmetry of the crystal. Attaching the unit cell to every lattice point reconstructs the entire crystal. Mathematically, the point lattice is described by a set of three lattice vectors a, b, and c, having magnitudes a, b, and c, respectively. The lattice vectors are defined with respect to an origin, which is assumed to be any one of the equivalent lattice points. The volume of the unit cell is given by the geometrical relation $V=\mathbf{a}\cdot\mathbf{b}\times\mathbf{c}$. The position vector r, which locates

any lattice point from the origin, is described by

$$\mathbf{r} = u\mathbf{a} + v\mathbf{b} + w\mathbf{c} \ , \qquad \text{(II.1)}$$

where u, v, and w are integers that range from zero to the total number of points along the lattice vector direction N_1, N_2, and N_3, respectively.

The unit cell boundary is defined by the lattice vectors. The unit cell of a real crystal solid contains a specific distribution of atoms. For convenience, the atoms are represented as points within the unit cell. Analogous to the lattice point position vector, the unit cell position vector can be written

$$\mathbf{r}_i = u_i\mathbf{a} + v_i\mathbf{b} + w_i\mathbf{c} \ , \qquad \text{(II.2)}$$

where i is the integer atom index, ranging from zero to the total number of atoms within the unit cell, and $u_i=a_i/|\mathbf{a}|$, $v_i=b_i/|\mathbf{b}|$, and $w_i=c_i/|\mathbf{c}|$ are the fractional coordinates of atom i, defined between zero and one. Thus, a particular atom within a crystal can be referenced by $\mathbf{R}=\mathbf{r}+\mathbf{r}_i$.

Crystallographic directions are defined with respect to any one of the equivalent lattice points without a loss of symmetry. This simply states that a vector is precisely defined by its magnitude and direction, regardless of the vector position. The nomenclature of crystallographic directions is based on a line, parallel to the direction of interest, that is drawn through a unit cell. The line

originates at one of the corner lattice points and intersects the unit cell boundary at the fractional coordinates u_i, v_i, and w_i. The direction of this line is denoted by [u,v,w], where u, v, and w are the smallest set of integers that equal u_i, v_i, and w_i after multiplication by a common constant. Positive and negative directions, defined with respect to the crystallographic axes, are conveniently described by selecting an appropriate originating corner of the unit cell, as illustrated in Figure II.1 (Cullity, 1978). Negative fractional coordinates are written with a bar over them. For example, a line originating from the unit cell origin and intersecting the unit boundary at the fractional coordinates u_i=0.25, v_i=-0.125, and w_i=1 is represented by $[4,\bar{1},8]$.

The orientation of a crystallographic plane is based on the points of intersection between the crystallographic axes, which form a convenient reference frame, and the plane. Like crystallographic directions, the points of intersection are expressed in terms of the fractional coordinates u_i, v_i, and w_i. A plane is represented by (h,k,l), where $h=1/u_i$, $k=1/v_i$, and $l=1/w_i$ are the Miller indices. By convention, a plane that is parallel to an axis intersects that axis at infinity. If a plane intersects an axis at a negative value, the fractional coordinate is negative, and a bar is written over the corresponding Miller index.

For the purpose of x-ray diffraction, which is a cooperative process that involves many unit cells within a crystal, the representation of crystallographic planes is more restrictive than the above definition. The (h,k,l) plane, when reproduced in every unit cell of a crystal,

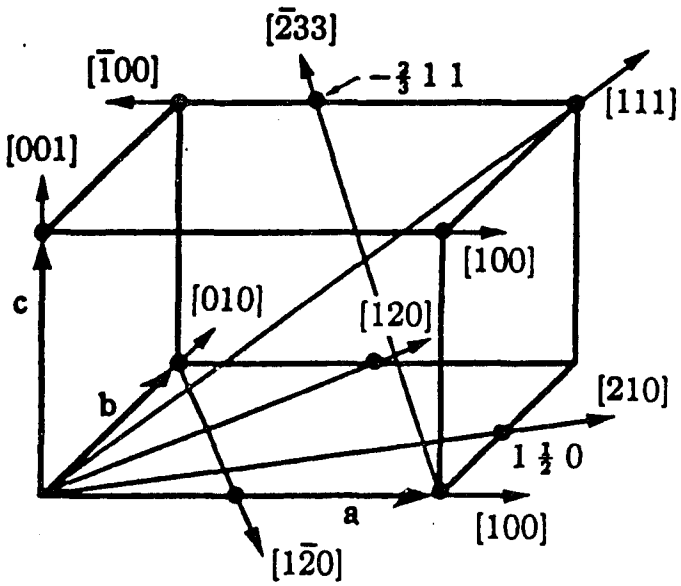

Figure II.1. Specific examples of crystallographic directions, denoted [uvw]. Different unit cell corners are used to describe directions that have negative components

should form a continuous and consistent set of planes. This necessarily defines not just one, but many parallel and equivalently spaced planes that are represented by (h,k,l). This is illustrated in Figure II.2, where the original plane, seen on edge, is represented by a solid line. All other dotted lines of Figure II.2 represent planes that must be considered equivalent to the original line so that the above restriction is satisfied. As a consequence of the consistency restriction, h, k, and l can be multiplied by a common constant, so that three integers are the result. In other words, each fractional coordinate must be a rational fraction. Following crystallographic nomenclature, all sets of planes are represented by integer Miller indices.

In addition, a unique interplanar spacing $d_{h,k,l}$ can be assigned to a set of (h,k,l) planes. This requires that two distinguishable sets of planes, which are parallel, have different interplanar spacings. In particular, the (nh,nk,nl) planes are parallel to the (h,k,l) planes and have a $d_{h,k,l}/n$ spacing. Figure II.3 illustrates several sets of (h,k,l) planes (Cullity, 1978). Notice that an individual plane can be represented by several (h,k,l) sets. For example, planes of the (2,1,0) set form every second plane in the (4,2,0) set. A special relationship exists for the cubic unit cell; the [h,k,l] direction is always perpendicular to the (h,k,l) planes.

Associated with each crystal lattice vector is a reciprocal lattice vector, which is a mathematical construction that simplifies x-ray diffraction expressions. The usefulness of the reciprocal lattice vectors will become apparent later. The reciprocal lattice vectors, a^*, b^*, and c^* are derived from the direct lattice according to

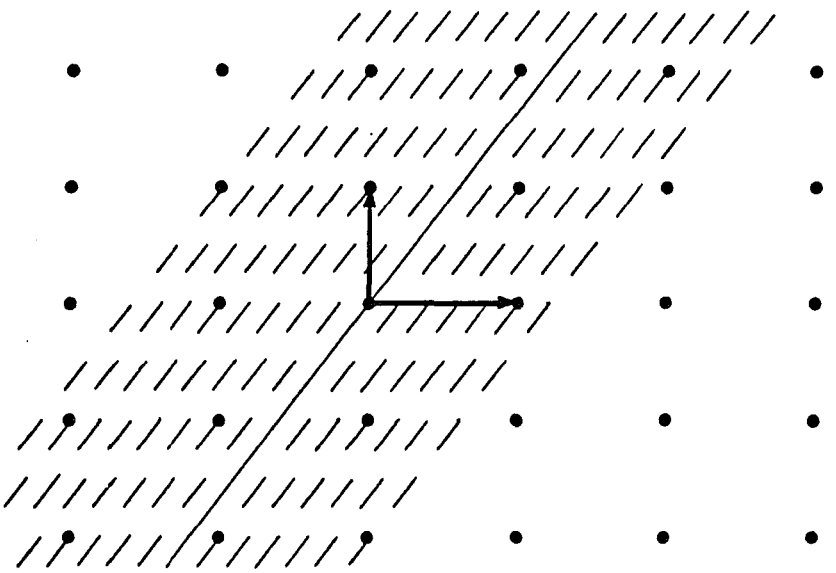

Figure II.2. Equivalent crystallographic planes seen on edge. Since the original plane (solid line) passes through a lattice point, all other lattice points must lie on equivalent planes (dashed lines) so that the crystal symmetry is preserved

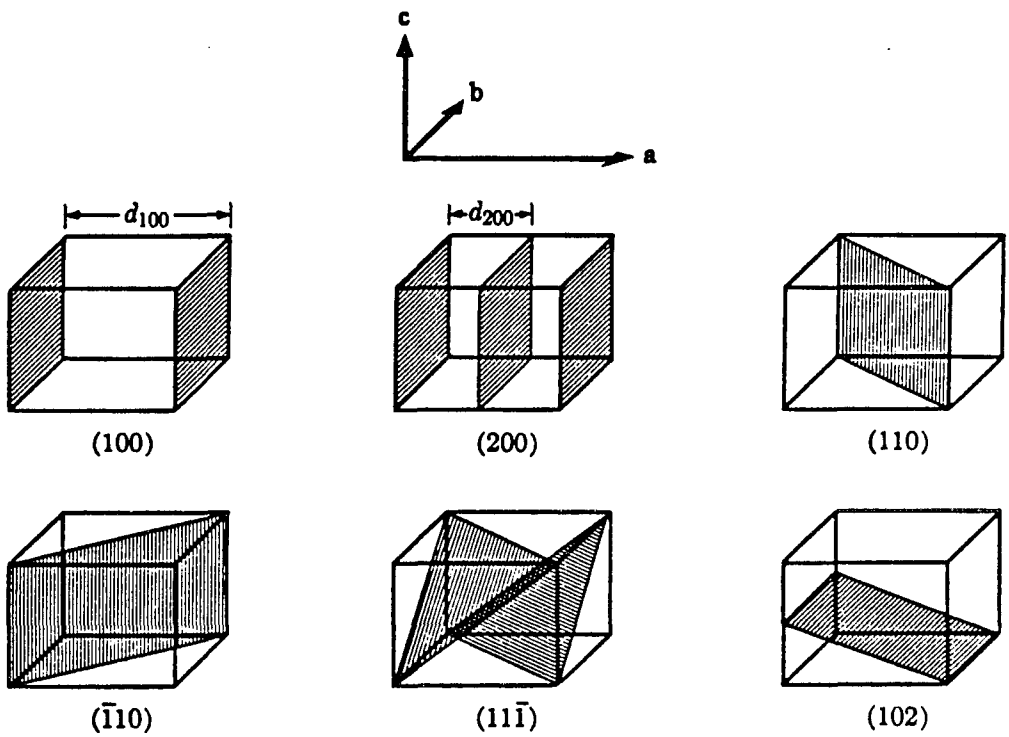

Figure II.3. Specific examples of crystallographic directions, denoted (hkl). The planes intersect the unit cell at the fractional coordinates u=1/h, v=1/k, and w=1/l. A bar over a Miller index indicates a negative fractional coordinate. Associated with each (hkl) plane is a plane spacing d_{hkl}, which is the distance from the origin to the nearest plane. Since the plane spacing depends on the Miller indices, common factors are not removed

the following definitions:

$$\mathbf{a}^*\cdot\mathbf{b} = \mathbf{a}^*\cdot\mathbf{c} = \mathbf{b}^*\cdot\mathbf{a} = \mathbf{b}^*\cdot\mathbf{c} = \mathbf{c}^*\cdot\mathbf{a} = \mathbf{c}^*\cdot\mathbf{b} = 0 \ , \qquad \text{(II.3a)}$$

$$\mathbf{a}^*\cdot\mathbf{a} = \mathbf{b}^*\cdot\mathbf{b} = \mathbf{c}^*\cdot\mathbf{c} = 1 \ . \qquad \text{(II.3b)}$$

The reciprocal lattice vectors have reciprocal length units. The right side constant of equation II.3b is arbitrary. In the crystallographic context, equating this constant to unity is most convenient. However, for solid state physics applications, a 2π constant is most convenient. The individual reciprocal lattice vectors are compactly written

$$\mathbf{a}^* = \mathbf{b}\mathbf{x}\mathbf{c}/V \ , \qquad \text{(II.4a)}$$

$$\mathbf{b}^* = \mathbf{c}\mathbf{x}\mathbf{a}/V \ , \qquad \text{(II.4b)}$$

$$\mathbf{c}^* = \mathbf{a}\mathbf{x}\mathbf{b}/V \ , \qquad \text{(II.4c)}$$

where V is the unit cell volume in real space. These vectors form a basis that describe a reciprocal space, which is a useful concept that will be utilized during the discussion of x-ray diffraction. The reciprocal and direct unit cell volumes are related by $V^*=V^{-1}$. Analogous to the real space lattice vector

$$\mathbf{r} = u\mathbf{a} + v\mathbf{b} + w\mathbf{c} \ , \qquad \text{(II.1)}$$

the reciprocal lattice vector H has the form

$$\mathbf{H} = h\mathbf{a}^* + k\mathbf{b}^* + l\mathbf{c}^* \ , \qquad \text{(II.5)}$$

where h, k, and l are integers. Unlike the real space analog, h, k, and l are not bound. An extremely important crystallographic relationship exists between the reciprocal lattice vector **H** and sets of planes (u,v,w); the direction of H(h,k,l) is normal to the (u,v,w) planes and the magnitude of H(h,k,l) is the reciprocal of the (u,v,w) interplanar spacing, when h=u, k=v, and l=w. This is written

$$|\mathbf{H}(h,k,l)| = \frac{1}{|d_{h,k,l}|} \quad . \qquad \text{(II.6)}$$

A proof of equation II.6 is presented in the second appendix of James (1982). Figure II.4 illustrates the necessary geometry to demonstrate the validity of equation II.6. An (h,k,l) plane intersects the crystal lattice vectors at fractional coordinates a/h, b/k, and c/l. These coordinates are designated A, B and C, respectively. Three obvious in-plane vectors are established in Figure II.4: AB, BC, and CA. The scalar product of these vectors with the reciprocal lattice vector **H**(h,k,l) is zero. For example, AB=(**b**/k-**a**/h), and $(h\mathbf{a}^*+k\mathbf{b}^*+l\mathbf{c}^*)\cdot(\mathbf{b}/k-\mathbf{a}/h)=\mathbf{a}^*\cdot\mathbf{a}-\mathbf{b}^*\cdot\mathbf{b}=0$. The reciprocal lattice vector must be perpendicular to the plane. Thus, the direction of **H** is directed along the plane normal **n**. The relationship between the magnitude of **H** and the plane spacing is established as follows. The plane spacing is the magnitude of vector ON, where ON intersects the plan at a right angle. The magnitude of ON is the scalar product between ON and any one of the vectors OA, OB, or OC. Representing the plane normal by $\mathbf{H}/|\mathbf{H}|$ and the vector OA by **a**/h, the plane spacing is established:

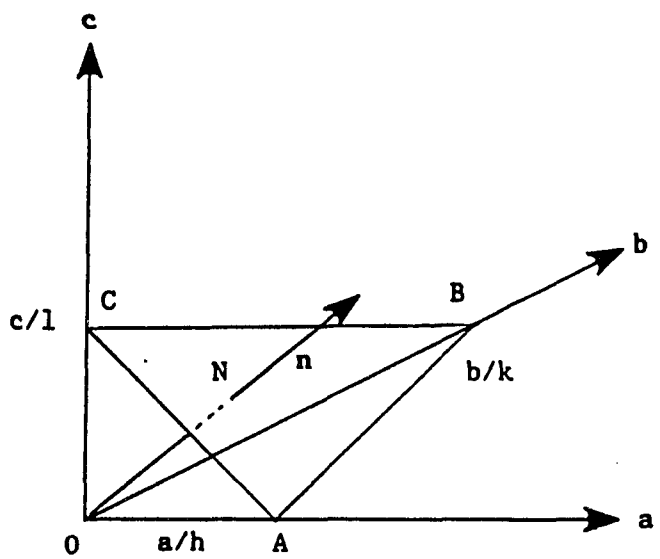

Figure II.4. The geometry required to prove equation II.6. The (h,k,l) plane intercepts the lattice vectors at a/h, b/k, and c/l, which are the points A, B, and C, respectively. The lattice origin is located at 0. The unit plane normal is **n**, which is proven to be parallel to the reciprocal lattice vector **H**(h,k,l). The line ON intersects the plane at a right angle and represents the plane spacing

$d_{h,k,l}=\mathbf{n}\cdot(a/h)=1/|\mathbf{H}|$. The above discussion establishes the validity of equation II.6. The general relationship between the reciprocal lattice vector and the corresponding crystallographic planes simplify crystal geometry considerations; sets of planes are replaced by the geometrically simplified set of reciprocal lattice points.

B. The Cubic Zincblende Unit Cell

GaAs, CdTe, HgTe, ZnTe, and all relevant binary mixtures of these materials predominantly crystallize in the zincblende structure. The zincblende crystal is composed of two interpenetrating face-centered cubic (FCC) sublattices displaced by a (1/4,1/4,1/4) translation along the body diagonal. The cubic zincblende unit cell is illustrated in Figure II.5. The 4a zincblende sites correspond to both the cube corners and the face-centered positions (dark atoms). The 4c zincblende sites define the other FCC lattice displaced along the body diagonal (light atoms). Both the 4a and 4c sites have four nearest neighbors that are located at the vertices of a tetrahedron. Representing the II-VI (III-V) compounds generically as AB, the A atoms occupy one of the FCC sublattice sites while the B atoms occupy the other sublattice. For example, the 4a sites would host A atoms and the 4c sites would host B atoms. Each cation has two (three) valence electrons outside the filled inner shells, and each anion has six (five). The crystal bonding is primarily covalent, with the valence electrons shared between adjacent atoms to form tetrahedrally-directed bonds (Parthe, E. 1964). Since the atomic charges of the A and B atoms are different, there is also an ionic contribution to the crystal bonding.

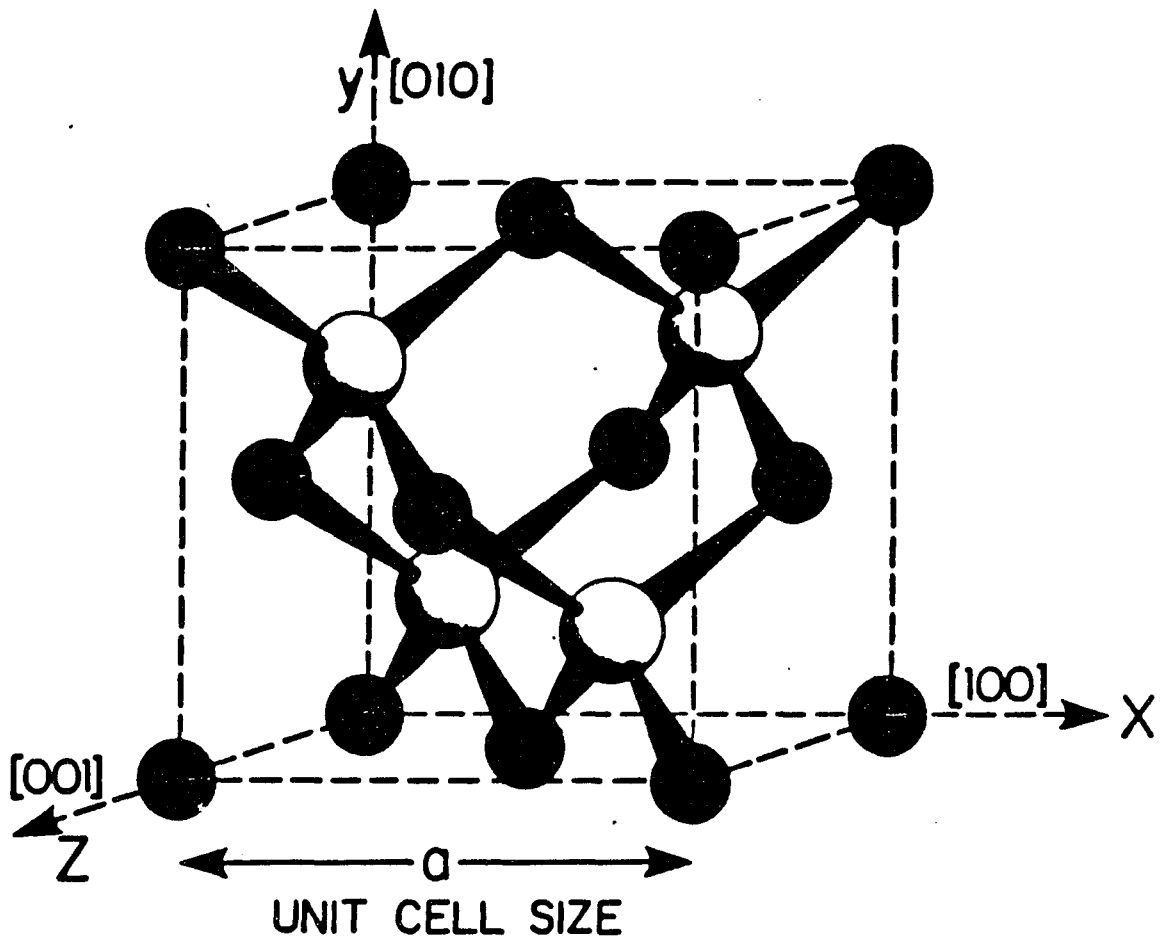

Figure II.5. The cubic zincblende unit cell (space group $F\bar{4}3m$). The dark atoms are located on the 4a sites and the light atoms are located on the 4c sites. Each of the 4a sites are tetrahedrally bounded to 4c sites. Both the 4a and 4c sites represent FCC sublattices, which are displaced by one-fourth of the body diagonal length along the body diagonal

The SLs studied in this research investigation are grown with zincblende constituent materials. SL growth can be visualized as the stacking of constituent unit cells along a defined growth direction. In particular, the SLs under investigation have growth directions along the [0,0,1] and [1,1,1] directions. SL growth along the [0,0,1] crystallographic direction refers to the stacking of cubic zincblende cells, face to face, along the constituent c axis. All atoms in the zincblende cell have one of four possible fractional coordinates along c: 0, 0.25, 0.5, 0.75. The same atom species occupy the the 0 and 0.5 fractional coordinate positions and the second atom species occupy the 0.25 and 0.75 positions. Thus, planes of atoms, containing one atom species (A or B), alternate along the [0,0,1] crystallographic direction. Each plane is separated by one-fourth of the cubic lattice constant.

SL growth along the [1,1,1] direction can be visualized as the stacking of cubic zincblende cells, cube corner to cube corner, along the body diagonal. The unit cell boundaries do not form planes parallel to the growth direction, as they do for [1,0,0] growth. This awkward stacking arrangement complicates the mathematical description of SL structure. However, the crystal lattice can be equivalently represented by a different unit cell, which allows for a simple stacking arrangement. This is accomplished by a cubic to hexagonal unit cell transformation. The details of unit cell transformations are found in the first volume of the International Tables for X-Ray crystallography (Henry & Lonsdale, 1952). Essentially, a matrix of 9 numbers describe the relationship between two sets of crystallographic axes. This matrix

maps atomic positions, Miller indices, and lattice vectors from one unit cell coordinate system to another. The inverse matrix maps these quantities from the second system back to the first. The specific matrices that relate the cubic and hexagonal unit cells are

$$T_{C\rightarrow H} = \begin{bmatrix} -4/3 & -2/3 & 1/3 \\ 2/3 & -2/3 & 1/3 \\ 2/3 & 4/3 & 1/3 \end{bmatrix} , \qquad \text{(II.7a)}$$

$$T_{H\rightarrow C} = \begin{bmatrix} -1/2 & 1/2 & 0 \\ 0 & -1/2 & 1/2 \\ 1 & 1 & 1 \end{bmatrix} . \qquad \text{(II.7b)}$$

The above transformation is illustrated in Figure II.6 (Parthe, 1964). The fractional coordinates of the hexagonal system are derived from the multiplication of the cubic coordinates, arranged in row vector form, with $T_{C\rightarrow H}$. Mathematically, this is written

$$(u_i,v_i,w_i)_{cubic} \cdot T_{C\rightarrow H} = (u_i,v_i,w_i)_{hexagonal} . \qquad \text{(II.8a)}$$

Miller indices are transformed as row vectors,

$$T_{H\rightarrow C} \cdot \begin{bmatrix} h \\ k \\ l \end{bmatrix}_{cubic} = \begin{bmatrix} h \\ k \\ l \end{bmatrix}_{hexagonal} . \qquad \text{(II.8b)}$$

Table II.1 relates each atomic position of the zincblende lattice between the cubic and hexagonal systems.

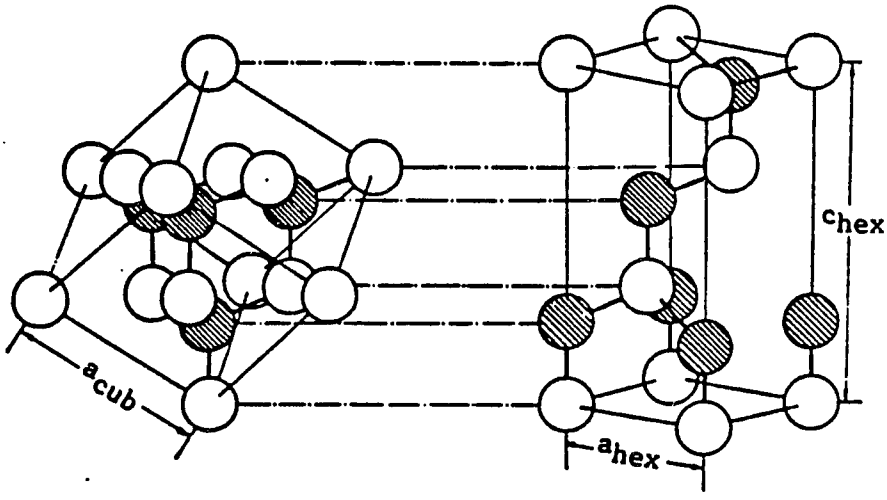

Figure II.6. An illustration of the cubic to hexagonal zincblende unit cell transformation. Both are equally capable of representing the zincblende crystal lattice. The hexagonal a_{hex} and b_{hex} crystallographic axes are not perpendicular. The c_{hex} axis is perpendicular to a_{hex} and b_{hex}, but has a larger magnitude equal to the cubic cell body diagonal

The [1,1,1] direction defines a surface normal for three atomic planes per unit cell that contain both A and B atomic species. Figure II.7 illustrates these "polar" zincblende planes (Staudenmann, Horning, Knox, Reno, Sou, Faurie & Arch, 1986), which are separated by one-third of the cubic lattice constant. The A and B atoms within a single plane are separated by 1/12 of the cubic lattice constant along the [1,1,1] direction.

Table II.1. The relationship between cubic and hexagonal fractional coordinates of the AB zincblende crystal lattice

Atom type	Cubic u_i	Cubic v_i	Cubic w_i	→	Hexagonal u_i	Hexagonal v_i	Hexagonal w_i
A	0	0	0		0	0	0
A	1/2	1/2	0		1/3	2/3	2/3
A	1/2	0	1/2		1	1	0
A	0	1/2	1/2		2/3	1/3	1/3
B	1/4	1/4	1/4		0	0	1/4
B	3/4	3/4	1/4		1/3	2/3	11/12
B	3/4	1/4	3/4		1	1	1/4
B	1/4	3/4	3/4		2/3	1/3	7/12

C. X-Ray Scattering by Electrons

An excellent treatment of the electron-electromagnetic interaction can be found in Landau and Lifshitz (1975). The scattering of x-ray radiation by a free classical electron will provide the essential features required for a discussion of x-ray diffraction. Although the electrons are bound in atoms, the free electron model is fairly accurate

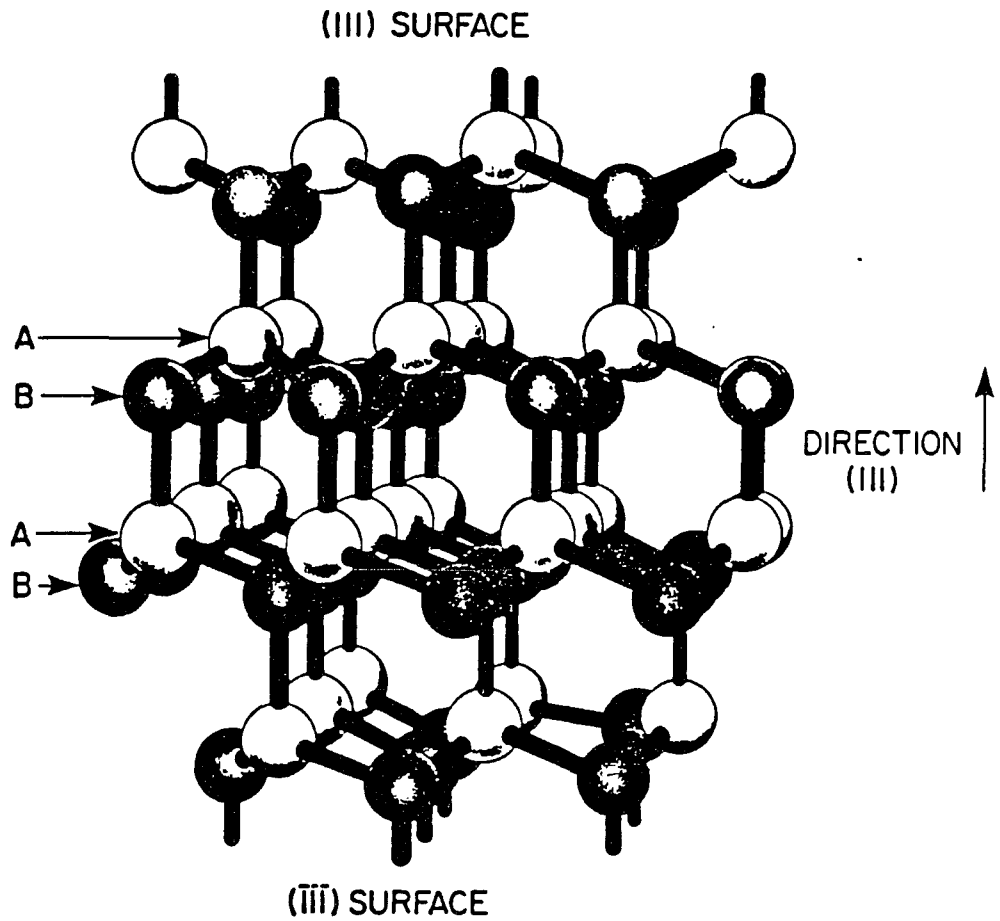

Figure II.7. A region of the zincblende lattice displayed in a perspective that emphasizes the polar atomic plane structure along the [1,1,1] crystallographic direction. The plane polarity is derived from the closely spaced A and B atoms. The A and B atoms do not lie on a single plane, but rather all A atoms and all B atoms lie on separate planes that are separated by 1/12 of the body diagonal distance

in describing the scattering process, especially for electrons in outer atomic shells. Since x-ray diffraction is a coherent scattering process, the polarization and phase relationship between the incident and scattered radiation is of principal interest.

The scattering of electromagnetic radiation by a free electric charge was first treated by J. J. Thomson (1893). Qualitatively, the electron interacts with the electric component of the incident electromagnetic field, which causes the electron to accelerate and emit electromagnetic radiation. The electron interaction with the magnetic component of the incident radiation is negligible, and can be ignored. The emitted radiation can be described by the dipole approximation, which asserts that the velocity acquired by the charge is small compared to the velocity of light. Figure II.8 illustrates the scattering geometry.

The electric component of the scattered radiation is described by

$$E_d = \frac{(a x s_d) x s_d}{c^2 R_d} \quad , \quad a = \frac{d^2 d}{dt^2} \quad , \qquad \text{(II.9)}$$

where the unit vector s_d defines the propagation direction of the scattered radiation, a is the acceleration of the electric dipole moment d, c is the speed of light, and R_d is the radial distance from the scattering point to the observation point. The induced acceleration of the electric dipole moment a is related to the incident radiation E_i by

$$a = \frac{e^2}{m} E_s \quad , \qquad \text{(II.10)}$$

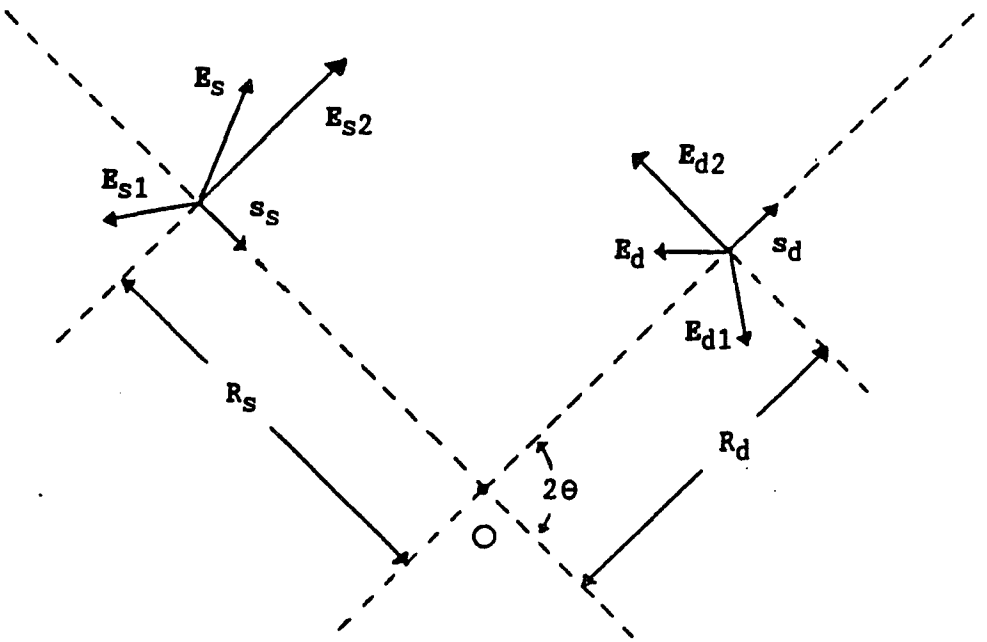

FIGURE II.8. Transverse electric field scattering from an electron located at O. The incident field E_s (source) is decomposed into two mutually perpendicular directions E_{s1} and E_{s2}, which are perpendicular to the propagation direction s_s. The scattered transverse electric field is detected along s_d and is decomposed into two mutually perpendicular components E_{d1} and E_{d2}, which are perpendicular to s_d. The unit propagation vectors s_s and s_d define the scattering plane and scattering angle 2θ. Both E_{s2} and E_{d2} are defined to lie in the scattering plane

where e and m are the electron charge and mass, respectively. This is analogous to the driven oscillator problem. Considering only coherent (elastic) scattering, the scattered and incident frequencies are assumed equivalent. Equations II.9 and II.10 combine to relate the electric field component of the incident and scattered radiation

$$E_d = \frac{e^2}{mc^2 R_d} (E_s x s_d) x s_d \quad . \tag{II.11}$$

Since the electric component of electromagnetic radiation is transverse to the propagation direction, an arbitrary incident orientation of the electric field propagating along s_s can be decomposed into two special directions of the scattering geometry--parallel and perpendicular to the scattering plane defined by s_s and s_d (see Figure II.8). Applying equation II.11, the scattered electric field from incident radiation that is perpendicular (E_{d1}) and parallel (E_{d2}) to the scattering plane can be written in the following form

$$E_{d1} = \frac{r_e}{R_d} E_{s1} \quad \text{(perpendicular)} \quad , \tag{II.12a}$$

$$E_{d2} = \frac{r_e \cos(2\theta) E_{s2}}{R_d} \quad \text{(parallel)} \quad , \tag{II.12b}$$

where $r_e = e^2/mc^2$ is the classical electron radius, 2θ is the scattering angle, and E_{s1} and E_{s2} are the incident electric field components perpendicular and parallel to the scattering plane. This decomposition is useful for describing the polarization effects of Thomson scattering. Assuming that all electrons scatter similarly, equations II.12a and

II.12b will describe the polarization of scattered radiation from atoms.

D. Kinematical Theory of X-Ray Diffraction

There are many excellent treatments of x-ray diffraction theory. James (1982) provides an extensive and thorough theoretical treatment, which has provided the underlying framework of thought for the application of x-ray diffraction. Other useful theoretical references include Zachariasen (1945), Guinier (1963), and Warren (1969). A useful experimental treatment of x-ray diffraction applications is found in Cullity (1978).

The kinematical diffraction theory is a simplified approximation of the more precise dynamical theory. The kinematical theory is based on three simplifying assumptions. First, the incident electric field amplitude is constant throughout the sample. Second, the scattering process is purely elastic, which is the Thomson scattering discussed in section II.B. Third, multiple scattering does not occur. The first and third assumptions accurately describe x-ray diffraction for very small crystals, where the amount of interactive volume is minimal. The second assumption is not very restricting. As discussed below, diffracted intensities require the coherent addition of scattered radiation. Incoherently scattered radiation contributes only slightly to the total diffracted intensity in the form of slowly varying "background" radiation. Justification of the three kinematical assumptions will be further discussed when appropriate.

Consider x-ray radiation incident on a charge distribution, which is not necessarily a crystalline solid. The distance to the x-ray source

is assumed much larger than the average spacing of atoms within the sample. This allows for the incident radiation (E_S) to be approximated by plane waves of the form

$$E_S = \frac{1}{|R_S|} E_o e^{i(k\cdot R_S - \omega t + \phi)} \quad , \qquad \text{(II.13a)}$$

$$E_S = E_S(E_{S1}+E_{S2}) \quad , \qquad \text{(II.13b)}$$

$$E_{S1}\cdot E_{S1}+E_{S2}\cdot E_{S2} = 1 \quad , \qquad \text{(II.13c)}$$

where E_S is the incident electric field amplitude, E_{S1} and E_{S2} define the polarization perpendicular and parallel, respectively, $k=(2\pi/\lambda)s_o$ is the wave vector that describes radiation of wavelength λ propagating along s_S, R_S is the position vector from source to scattering point, ω is the angular frequency, and ϕ is an arbitrary phase factor.

Figure II.9 defines the scattering arrangement based on an arbitrarily selected origin. The position vector r locates the charge distribution within the diffracting material, R_S connects the x-ray source to the material origin, and R_d is directed from the origin to the detection point. s_S and s_d are unit vectors that define the incident and scattered propagation directions. The phase of radiation scattered at r is based on the additional path length traveled, compared to radiation scattered at the origin for reference. The scattered wave is written

$$E_d = \frac{r_e}{|R_d|} E_{do} e^{ik(s_S\cdot R_S + s_S\cdot r - s_d\cdot r + s_d\cdot R_d - \omega t + \phi)} \quad , \qquad \text{(II.14)}$$

where E_{do} defines the scattered amplitude and polarization at the

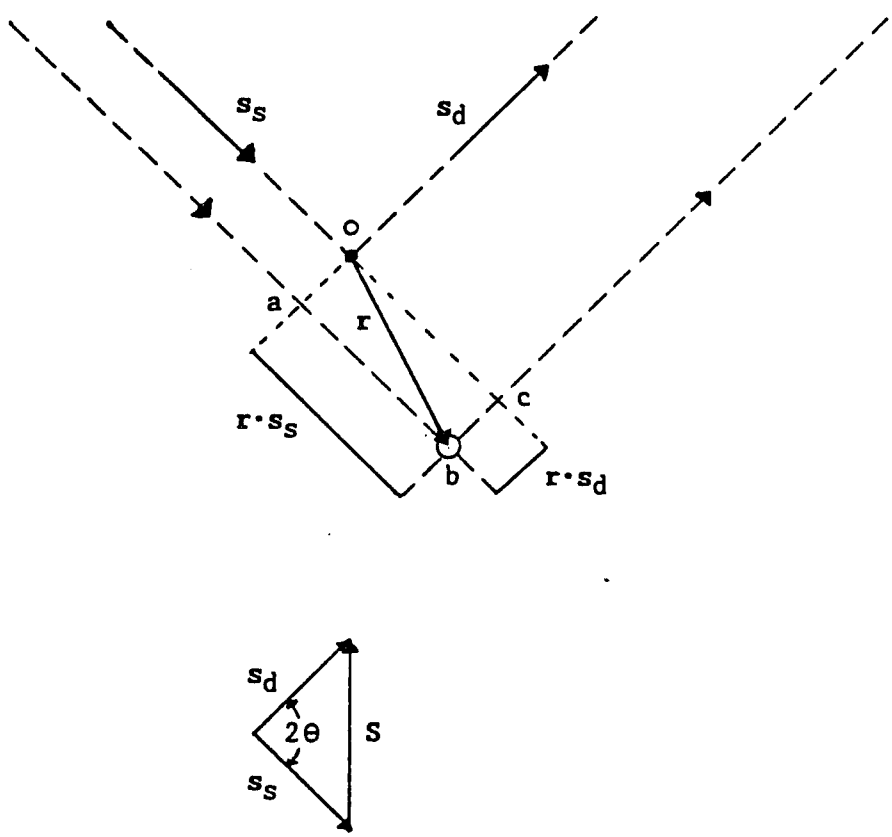

Figure II.9. The scattering geometry for incident radiation propagating along s_s and scattered radiation detected along s_d. Radiation scattered at b has a different phase compared to radiation scattered at the origin O. This phase difference is due to the extra path length $ab+bc=r \cdot s_s - r \cdot s_d$ traveled by radiation scattered at b. The bottom drawing illustrates the relationship between 2θ and the unit propagation vectors s_s and s_d

scattering point (R_d=0), $\mathbf{r}\cdot\mathbf{s}_s-\mathbf{r}\cdot\mathbf{s}_d$ is the additional path length of radiation scattered from r, compared to the origin, and $k=2\pi/\lambda$ is the wave number of the incident and scattered radiation. The resultant electric field of the scattered x-ray radiation is simply the addition of all scattered radiation. A common phase $e^{i\phi'}$, where $\phi'=k(\mathbf{s}_s\cdot\mathbf{R}_s+\mathbf{s}_d\cdot\mathbf{R}_d-\omega t+\phi)$, can be factored out of the summation of $\mathbf{E}_d$ terms. If the charge distribution is represented by a charge density $\rho(\mathbf{r})$, the summation of scattered contributions must be replaced by an integral over radiation scattered by infinitesimal charge elements $\rho(\mathbf{r})dV$. The charge density is not restricted to the description of continuous charges. For example, electrons, which are point charges, are represented by delta functions under the charge density formalism. The total electric field contribution of x-ray scattering by an arbitrary charge density distribution $\rho(\mathbf{r})$ can be written

$$\mathbf{E}_R = \frac{r_e\mathbf{E}_{do}}{|\mathbf{R}_d|}\, e^{i\phi'}\int\rho(\mathbf{r})dVe^{-ik\mathbf{r}\cdot\mathbf{S}} \quad , \qquad \text{(II.15)}$$

where $\mathbf{E}_R$ is the resultant electric field at $\mathbf{R}_d$, $\mathbf{S}=\mathbf{s}_d-\mathbf{s}_s$ is the scattering vector, and the integration is over the volume of the diffracting material.

Since materials are composed of atoms, the charge can be organized into the sum of individual atomic charge densities. Regions of extended charge that result from bonding are associated with the bonding atoms under this scheme. By specifically referencing atoms positioned at $\mathbf{r}_j$, the resultant electric field can be written

$$E_R = \frac{r_e E_{do}}{|R_d|} e^{i\phi'} \sum_j \int \rho_j(r') d^3r' e^{-ikS\cdot(r_j+r')} \quad , \qquad \text{(II.16)}$$

where the summation is over all atoms located at r_j and the integration is over the atomic charge density $\rho(r')$ located at r_j. Figure II.10 illustrates the use of R_s, R_d, r_j, and r', where r' locates the element of charge density $\rho_j(r')$ within an atom at position r_j. After separating the r_j and r' dependent terms, equation II.16 is compactly written

$$E_R = \frac{r_e E_{do}}{R_d} e^{i\phi'} \sum_j f_j e^{-ikS\cdot r_j} \quad , \qquad \text{(II.17)}$$

where the sum is over all atoms of the diffracting material and f_j is the atomic scattering factor that describes the collective scattering of radiation by the charge distribution associated with the atom at r_j. Equation II.17 is completely general within the constraints of the three assumptions discussed above. The atoms are not necessarily coherently ordered, however, as will be demonstrated below, intense diffracted radiation occurs only for periodically ordered materials.

The remainder of this discussion will concern the application of equation II.17 to periodically ordered solids. The position vector that locates all atoms within the solid is written

$$r_j(u,v,w) = (ua+vb+wc) + (u_j a+v_j b+w_j c) \quad , \qquad \text{(II.18)}$$

where $0 \leq u < N_a$, $0 \leq v < N_b$, and $0 \leq w < N_c$ are integers that index one of the $N=N_aN_bN_c$ unit cells, and u_j, v_j, and w_j are the fractional coordinates

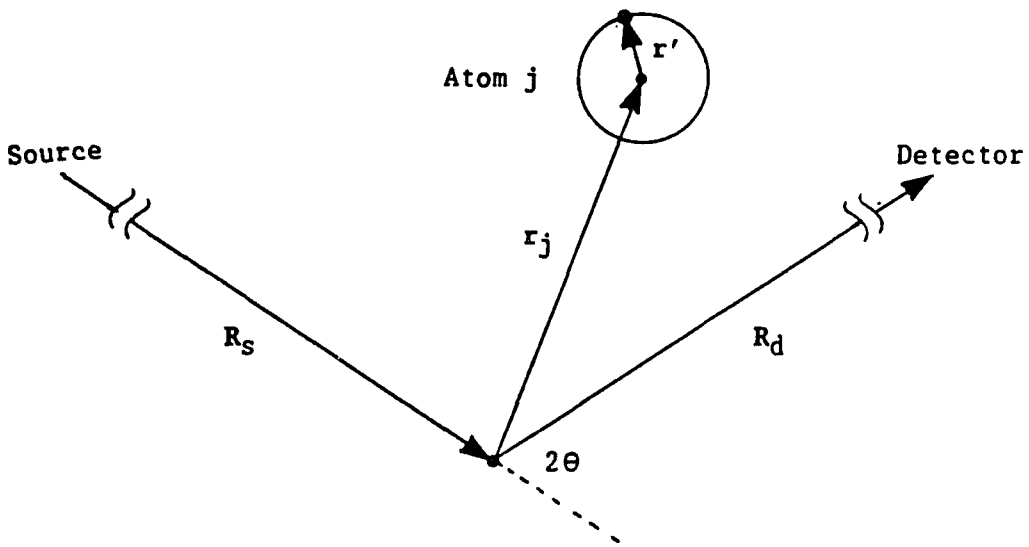

Figure II.10. The position vectors used in equation II.16. The atom position vector r_j and the local vector r' locate an element of charge. r' originates from the atom center and terminates within the local atomic charge distribution. The source and detector vectors R_s and R_d, respectively, are much larger in magnitude than the sample vectors r_j and r'

of atom j within the unit cell. Using the position vector of equation II.18, equation II.17 is written

$$E_R = \frac{r_e E_{do}}{R_d} e^{i\phi'} \sum_{u=0}^{N_a-1} \sum_{v=0}^{N_b-1} \sum_{w=0}^{N_c-1} \sum_{j}^{u} f_j e^{-ikS\cdot r_j(u,v,w)} \quad , \qquad \text{(II.19)}$$

where the single summation of equation II.17 is replaced by the summation over all unit cells and a summation over the atoms within one unit cell. Equation II.19 assumes that the atomic scattering factor for any particular atom is independent of the unit cell. For an ideal crystal of consistent periodicity, this is valid.

The first three sums involving u, v, and w can be performed separately. Each is a geometrical progression that can be represented by an exact expression. For example, the summation over u can be expressed

$$\sum_{u=0}^{N_a-1} e^{-ikS\cdot(ua)} = e^{-i\phi_a} \left[\frac{\sin(N_a \Psi_a)}{\sin(\Psi_a)} \right] \quad , \qquad \text{(II.20a)}$$

$$\phi_a = \frac{k(N_a-1)S\cdot a}{2} \quad , \qquad \text{(II.20b)}$$

$$\Psi_a = \frac{k}{2} S\cdot a \quad . \qquad \text{(II.20c)}$$

The fourth sum in equation II.19 describes the x-ray scattering within the unit cell. The result of this summation, known as the structure factor, is analogous to the atomic scattering factor. The structure factor is written

$$F(kS) = \sum_j f_j e^{-ikS\cdot(u_j a+v_j b+w_j c)} \quad , \qquad (II.21)$$

where the sum is over all atoms in the unit cell. In practice, the resultant intensity is measured, not the electric field amplitude discussed above. The intensity is simply the square of the resultant amplitude, $I=E_R^*\cdot E_R$, where E_R^* is the complex conjugate of E_R. Applying equations II.20a-c and II.21, the resultant diffracted intensity from a periodically ordered material has the form

$$I(kS) = \frac{I_o P(S,E_S)}{R_d^2}\left[\frac{\sin(N_a\Psi_a)}{\sin(\Psi_a)}\right]^2\left[\frac{\sin(N_b\Psi_b)}{\sin(\Psi_b)}\right]^2\left[\frac{\sin(N_c\Psi_c)}{\sin(\Psi_c)}\right]^2 |F(kS)|^2 \quad , \qquad (II.22)$$

where $I_o=|r_e E_{do}|^2$ is the scattering amplitude, and $P(S,E_S)$ is the polarization factor that accounts for a change in the electric field polarization of E_S after scattering. The ratio of sine-squared terms of equation II.22, known as interference functions, have principal maxima at $\sin(\Psi)=0$. Applying Hospital's rule, the principal maxima have the value N^2. Between each principal maxima are N-2 subsidiary maxima, which occur at $\sin(N\Psi)=1$. Figure II.11 illustrates the behavior of the interference function. Each principal peak width, from maximum to adjacent minimum, is π/N in Ψ. These widths become very narrow for large N.

The value of neighboring subsidiary maxima decrease away from the principal peaks. The first subsidiary maximum is ~4.5% of the principal maximum. Since the diffracted intensity of equation II.22 contains the multiplication of three interference terms, an appreciable intensity

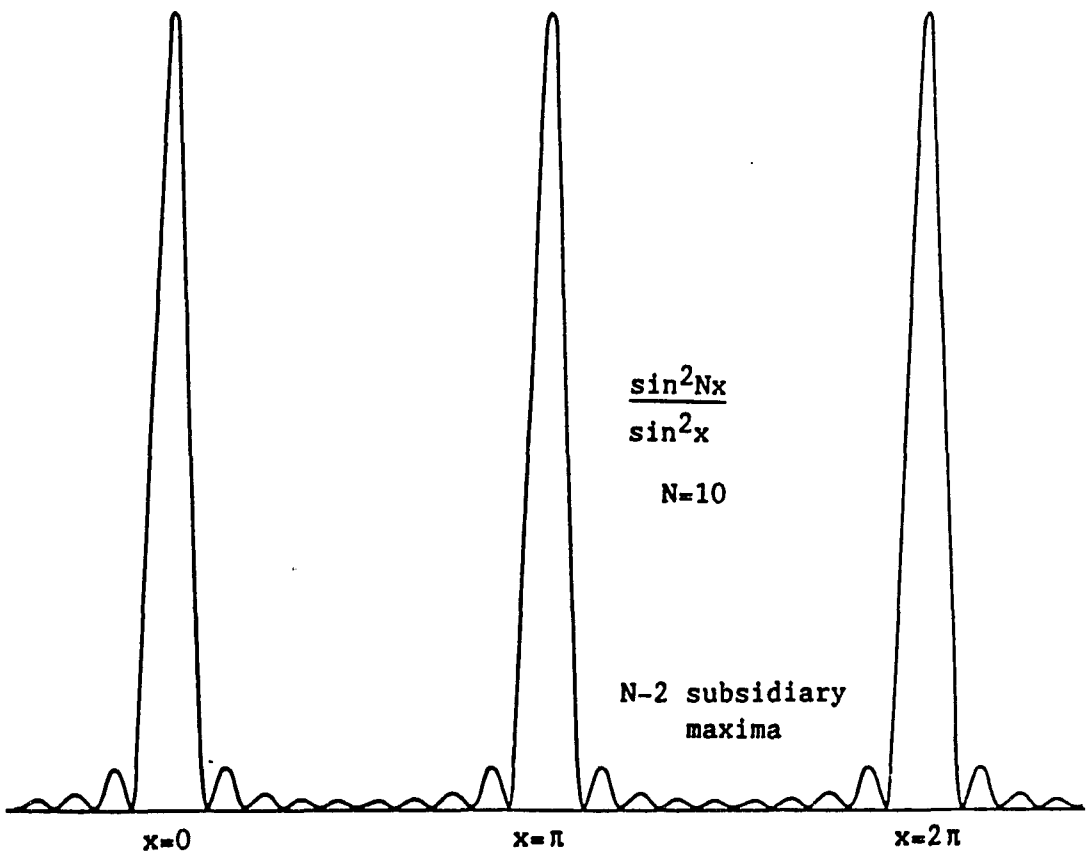

Figure II.11. A graph of the interference function for N=10. The first subsidiary maximum is ~4.5% of the principal maximum. All peak widths are inversely related to N

will be observed only when each interference term is principally maximum. This occurs when the conditions

$$\Psi_a = \frac{k}{2}\mathbf{S}\cdot\mathbf{a} = \pi h \text{ or } \mathbf{S}\cdot\mathbf{a} = h\lambda \quad , \tag{II.23a}$$

$$\Psi_b = \frac{k}{2}\mathbf{S}\cdot\mathbf{b} = \pi k \text{ or } \mathbf{S}\cdot\mathbf{b} = k\lambda \quad , \tag{II.23b}$$

$$\Psi_c = \frac{k}{2}\mathbf{S}\cdot\mathbf{c} = \pi l \text{ or } \mathbf{S}\cdot\mathbf{c} = l\lambda \quad , \tag{II.23c}$$

are satisfied for integer h, k, and l values. Equations of II.23a-c represent the Laue condition for x-ray diffraction by a periodically ordered material (James, 1982).

Comparing equations II.3b and II.5 with the Laue condition, the vector $\mathbf{S}/\lambda$ precisely represents a reciprocal lattice vector of the sample. For reference this is written

$$\frac{\mathbf{S}}{\lambda} = h\mathbf{a}^* + k\mathbf{b}^* + l\mathbf{c}^* \quad . \tag{II.24}$$

In principle, $\mathbf{S}/\lambda$ can have any value. However, an appreciable diffracted intensity will occur only when $\mathbf{S}/\lambda$ coincides with a reciprocal lattice vector associated with the crystal lattice. Thus, x-ray diffraction occurs only for discrete scattering geometries with each diffraction maximum indexed by h, k, and l.

The Laue diffraction condition has an elegant geometrical form when expressed with respect to the reciprocal lattice of a crystal. This is illustrated in Figure II.12, where s_s/λ, s_d/λ, and $\mathbf{S}/\lambda$ are drawn on a two dimensional slice of the crystal reciprocal lattice. Since x-ray

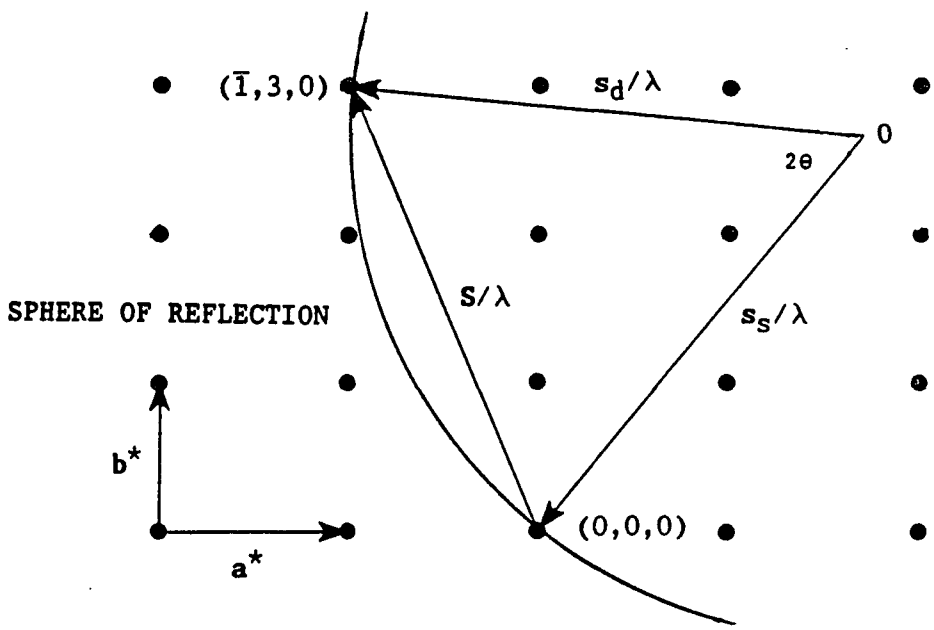

Figure II.12. The Ewald construction of x-ray diffraction from a crystal lattice. This is a two dimensional illustration of the three dimensional reciprocal space. s_s and s_d represent the incident and scattered propagation directions, and S is the scattering vector. s_s is positioned so that it terminates at an arbitrary reciprocal lattice point, defining the origin (0,0,0). An appreciable diffracted intensity is observed when S/λ, originating from (0,0,0), terminates at another reciprocal lattice point (h,k,l). For a fixed scattering geometry, only the reflections associated with reciprocal points that intersect the sphere of reflection (solid line) can be observed. $\mathbf{a}^*$ and $\mathbf{b}^*$ are the reciprocal lattice vectors of the crystal in this two dimensional illustration

diffraction occurs only when $\mathbf{S}/\lambda$ coincides with a reciprocal lattice vector, the Laue condition can be expressed in an alternate form, known as the Ewald representation (James, 1982); if the vector $\mathbf{S}/\lambda$ originates from a reciprocal lattice point, it must terminate on another reciprocal lattice point. Since the reciprocal lattice is not bound, any one of the reciprocal lattice points can be arbitrarily selected as the origin for $\mathbf{S}/\lambda$. All points that surround the selected origin define allowed scattering vectors. Although all possible $\mathbf{S}/\lambda$ are identified by the surrounding reciprocal points, not all points correspond to nonzero diffracted intensities.

Since the magnitude of a reciprocal lattice vector $|\mathbf{H}(h,k,l)|$ is the reciprocal of the (h,k,l) interplane spacing $1/d_{h,k,l}$ (equation II.6), the Laue conditions can be reduced to an angular relationship of the form

$$\left|\frac{\mathbf{S}}{\lambda}\right|_{h,k,l} = \frac{1}{d_{h,k,l}} \quad \text{or} \quad 2d_{h,k,l}\sin\theta = \lambda \ , \qquad \text{(II.25)}$$

where $|\mathbf{S}|=2\sin\theta$ and θ is one-half of the scattering angle. This is known as the Bragg condition for x-ray diffraction. Equation II.25 can be interpreted as x-ray radiation specularly reflecting from parallel crystallographic planes having a uniform spacing equal to $d_{h,k,l}$. Figure II.13 illustrates this interpretation (Cullity, 1978), where $\theta_B \equiv \theta$ is known as the Bragg angle for diffraction from the (h,k,l) planes. Diffraction at the Bragg angle assures that radiation scattered from each Bragg plane constructively combines to produce a strong intensity. Diffraction experiments have demonstrated that the Bragg planes are

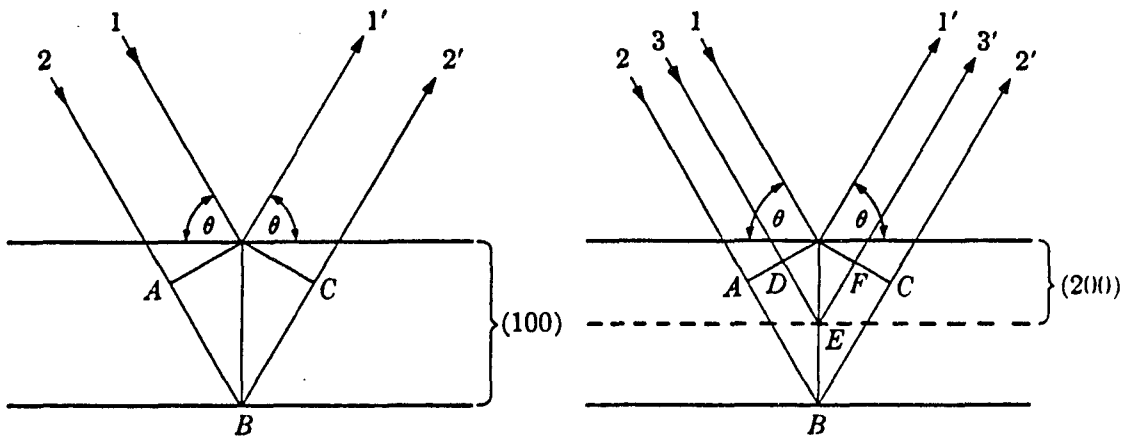

Figure II.13. Bragg reflection from crystallographic planes. Both the incident and reflected propagation directions form an angle Θ with the Bragg plane (specular reflection). Because of the crystal symmetry, the interaction between the two illustrated planes occurs for any adjacent crystal planes. A diffracted peak results when the phase of ray 1 and 2 interfere constructively. This depends on both the wavelength and the additional path traveled by ray 2 (AB+BC). Constructive interference is achieved when an integral number of wavelengths span the path length AB+BC. The right illustration represents a second order reflection. A peak is observed when an integral number of wavelengths span both AB+BC and DE+EF

parallel to planes of atoms within the crystal. The Bragg condition stresses the angular and wavelength dependence of the scattering geometry.

Before continuing, a few comments on the polarization and interference factors of equation II.22 is instructive. The polarization factor $P(S,E_S)$ represents the modification of E_{S2} (the electric field component that is parallel to the scattering plan) upon scattering from a charge distribution. The general form of $P(S,E_S)$ is written

$$P(S,E_S) = (E_{S1} + E_{S2}\cos 2\theta)^2 = E_{S1}^2 \sin^2 2\theta + \cos^2 2\theta \quad , \qquad \text{(II.26)}$$

where E_{S1} and E_{S2} are the incident electric field polarization components that are perpendicular and parallel to the scattering plane, respectively. The second expression of equation II.26 uses equation II.13c. Thus, if an incident E_{S2} component is present and contributes to the total measured intensity, a decrease in intensity is observed after scattering.

The interference functions of equation II.22 predict very narrow diffraction peaks. After correcting for radiation divergence, the diffracted intensities of some crystals are found to be appreciable over a larger range in $S(\theta)$, compared to the angular range predicted by equation II.22. This broadening of the diffracted intensity width lead C. G. Darwin (1914) to postulate the mosaic structure model for real crystals. A mosaic crystal is derived from many crystal blocks, each being a perfect crystal and slightly misoriented with respect to all other blocks. Both a small average mosaic block size and an appreciable range of block orientation, known as the crystal mosaic spread,

contribute to the diffracted peak breadth. According to equation II.22, the principal maximum breadth of the interference function increases as the crystal size decreases. Since each crystal block is assumed to diffract incoherently with the others, the interference function width directly contributes to the observed peak width. In addition to crystal size, the crystal mosaic spread also contributes to the diffracted peak width. Each block requires a particular scattering vector for diffraction, which is different from its neighbors, depending on the misalignment between the blocks. The diffracted intensity width due to mosaic spread corresponds to the range of scattering vectors required to satisfy the Laue conditions for each crystal block of the mosaic crystal.

Each block diffracts according to equation II.22 and the total observed intensity is the total contribution of all diffracting blocks over the required range of scattering vectors. Although the mosaic interpretation is oversimplified, predictions of the mosaic postulate have been correlated with experiments for crystals that are not macroscopically perfect. Mosaic crystals are also known as imperfect crystals in the literature. In practice, diffracted intensities correspond to calculated intensities that are intermediate between the dynamical and kinematical diffraction theories, depending on the degree of crystal perfection. The samples examined in this research investigation are more accurately represented by the kinematical theory.

The first and third assumptions of the kinematical theory are particularly relevant for diffraction from mosaic crystals. The first assumption, negligible x-ray radiation absorption, requires

interpretation with respect to the macroscopic crystal. Since the mosaic blocks are considered small, the absorption effects within the block are assumed negligible. On a macroscopic scale, however, a mosaic crystal will attenuate the x-ray radiation as it traverses many blocks. While macroscopic absorption must be reconciled before comparing the collective intensity from all mosaic blocks with experiment, the first assumption is locally valid and allows the use of equation II.22 to describe diffraction from each mosaic block.

The third assumption, no multiple scattering, is also consistent with the diffraction from mosaic crystals. Since each mosaic block is slightly misaligned with respect to the other blocks, only a few will satisfy the Laue condition and scatter for any precisely defined scattering vector. Once scattered, the x-ray radiation can only be rescattered if it encounters another mosaic block that is oriented identically with the previous block. The probability of this situation is assumed low and multiple scattering is considered negligible.

In addition to the crystal mosaic spread, divergence of the incident propagation direction and multiple wavelength components of the incident radiation can broaden the diffracted intensity distribution. Variations in the incident radiation direction cause different crystal regions to diffract differently, depending on the local value of the incident and scattered propagation directions. Wavelength variations of the incident radiation alter the Laue conditions, requiring each wavelength component to scatter at different angles. All intensity broadening effects can be represented within the Ewald representation of x-ray diffraction; the broadened range of S/λ that correspond to appreciable diffracted

intensities are represented by finite extensions of the reciprocal lattice points. Even if there were no broadening, the reciprocal points used in the Ewald construction have a finite extent, which is attributed to the breadth of the interference functions.

The calculated intensity I(kS) of equation II.22 is difficult to compare with experimental measurements. Intensity broadening effects and finite instrumental resolution prevent accurate intensity measurements at precisely known values of S/λ. Regardless of experimental resolution, a slight misalignment of diffraction apparatus will modify the intensity distribution for any given (h,k,l) reflection. Thus, I(kS) is an undesirable quantity to measure experimentally. The integrated intensity $J(kS_L)$, however, is a realistically measurable quantity that does not demand infinite instrumental resolution. $J(kS_L)$ is obtained by integrating I(kS) over all S/λ, centered about S_L/λ, that contribute an appreciable diffracted intensity. The details of this integration are presented in Warren (1969) and James (1982). Assuming negligible absorption, the integrated intensity

$$J(S_L/\lambda) = \int I(kS)\frac{dS}{\lambda} = \frac{I_o N^2 \lambda^3 |F(S_L/\lambda)|^2 r_e^2 P(S,E_S)\,\delta V}{R_d^2 \sin(2\theta_B)} \quad , \qquad \text{(II.27)}$$

where N is the number of crystal unit cells per unit volume, λ is the incident radiation wavelength, $F(S_L/\lambda)$ is the structure factor calculated at S_L/λ, r_e is the classical electron radius (see equations II.12a and II.12b), $P(S,E_S)$ is the polarization factor (see equation II.26), δV is the fully irradiated crystal volume, and θ_B is the Bragg angle for the S_L/λ reflection. The $1/\sin(2\theta_B)$ factor in equation II.27 is known as the Lorentz factor. Equation II.27, which represents the

power that is reflected from a small crystal, is derived using equation II.22 and does not represent diffraction from a mosaic crystal. However, equation II.27 does apply to each individual mosaic block within an imperfect crystal. The integrated intensity of a mosaic crystal $J_K(S_L/\lambda)$, based on the kinematical diffraction theory, can be derived by summing the total intensity contribution from each block. Since each mosaic block scatters incoherently with respect to other blocks, intensities, not electric field amplitudes, are added.

Table II.2. Mass absorption coefficients as a function of wavelength for all atoms that are relevant to this research investigation

Atom	Atomic number	Mass absorption coefficient μ/ρ (cm^2/gm) 1.47639 Å	1.28181 Å	1.09855 Å	0.70930 Å
Mn	25	238.9	163.9	108.0	31.9
Zn	30	48.1	258.7	170.3	52.7
Ga	31	51.7	34.7	177.9	55.6
As	33	62.3	41.9	27.1	64.5
Cd	48	193.1	131.7	86.4	25.7
Te	52	232.6	159.3	104.9	31.6
Hg	80	179.6	124.6	83.3	110.7

Absorption can be included in the mosaic crystal intensity derivation by replacing I_o with I(z), which is the attenuated intensity at a depth z in the crystal. The attenuation of x-ray radiation decays

exponentially with distance,

$$I(z) = I_i e^{-\mu z} \quad , \tag{II.28}$$

where μ is the linear absorption coefficient, z is the path length that the radiation traverses inside the absorbing medium, and I_i is the incident intensity at z=0. Since μ is proportional to the material density ρ, the quantity μ/ρ, known as the mass absorption coefficient, is a constant for a material and is independent of its physical state. The mass absorption coefficient is usually tabulated in the literature for each element and is proportional to $\lambda^3 Z^3$ at radiation energies that are not too close to absorption edges, which represent atomic energy transitions. The mass absorption coefficients have been computed by Cromer (1983). Table II.2 summarizes these values for all relevant atoms at the wavelengths used in this investigation. For absorbing materials having more than one atomic constituent, the total mass absorption coefficient $(\mu/\rho)_T$ is calculated by performing a weighted sum of the constituent atomic μ/ρ values. This is expressed

$$\left[\frac{\mu}{\rho}\right]_T = \sum_i w_i \left[\frac{\mu}{\rho}\right]_i \quad , \tag{II.29}$$

where w_i is the fractional atomic weight of atom i that has a mass absorption coefficient $(\mu/\rho)_i$ (Cullity, 1978). This expression does not depend on the structure of the material. However, the density, which must be known before calculating the linear absorption coefficient μ, does depend on the material structure. Thus, a density that represents

the entire material ρ_T must be used to extract μ_T from $(\mu/\rho)_T$:

$$\mu_T = \rho_T(\mu/\rho)_T \quad . \tag{II.30}$$

Table II.3 lists the relevant densities and cubic lattice parameters of this investigation. Although some of the binary constituent materials crystallize in the wurtzite structure, only the zincblende structure is encountered in this investigation.

Table II.3. Bulk mass densities and bulk cubic zincblende lattice parameters of all binary alloys considered in this research investigation

Compound	Mass density (gm/cm^3)	Cubic lattice parameter (Å)
GaAs	5.3174[a]	5.65325[a]
ZnTe	5.7[b]	6.09[c]
HgTe	8.42[b]	6.46[c]
CdTe	5.86[b]	6.48[d]

[a]Blakemore (1982).

[b]Hamilton (1964).

[c]Elliott (1965).

[d]Lawson, Nielsen, Putley & Young (1959).

Returning to the derivation of the mosaic integrated intensity J_K, the collective intensity from each mosaic block is obtained by adding all individual integrated intensities, with I_o of equation II.27 replaced by the attenuated intensity. This is most easily represented by an integral

$$J_K = \sum_n J[I_n] = \int J[I(z,\Theta)]dN \quad , \tag{II.31}$$

where dN represents the number of mosaic blocks in a volume dV at depth z in the imperfect crystal. The number of mosaic blocks in dV is simply the ratio $dV/\delta V$. The volume element dV represents the irradiated volume element. For this research investigation, the samples are rectangular plates having a width w_S, thickness t, and height h_S. The incident radiation cross section is typically rectangular having a width w_I and height h_I. When a rectangular beam cross section is used, the incident height is usually set equal to the sample height. Figure II.14a illustrates the sample geometry, where dV=wh(dz) is the elemental volume used in the integration of II.31. The integrated intensity is expressed in terms of the incident intensity I_o, using equation II.28, and is explicitly written

$$J_K = \int_0^t Jg(\Theta)e^{-\mu r(z,\Theta)}\frac{w(\Theta)h\ dz}{\delta V} \quad , \tag{II.32}$$

where $g(\Theta)$ represents the fraction of incident radiation that is scattered by the sample, μ is the linear absorption coefficient of the

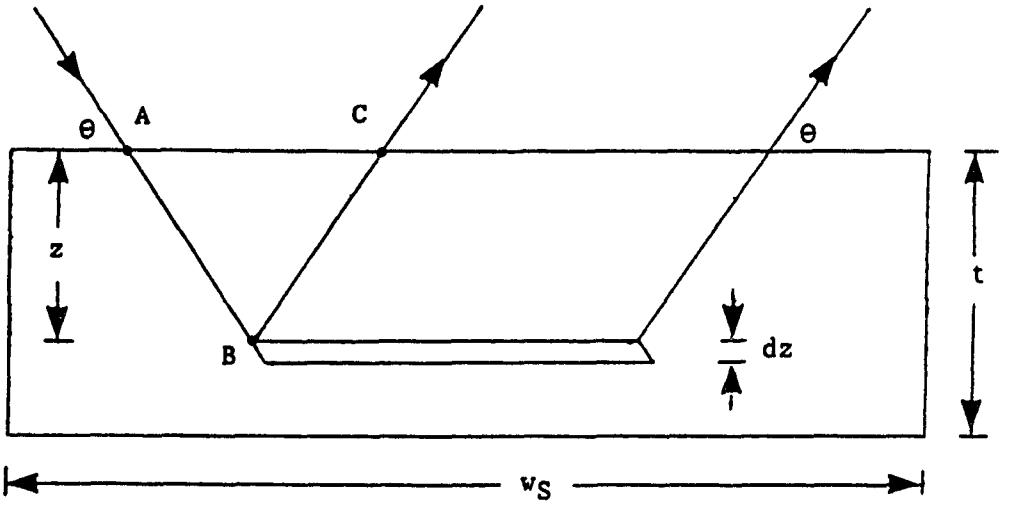

Figure II.14a. The sample geometry used to derive the integrated intensity from a mosaic crystal (equation II.34). The sample thickness is t and the sample width is w_S. The x-ray radiation must traverse a distance AB+BC inside the absorbing medium. The volume element dV has a thickness dz located at a depth z below the mosaic crystal surface

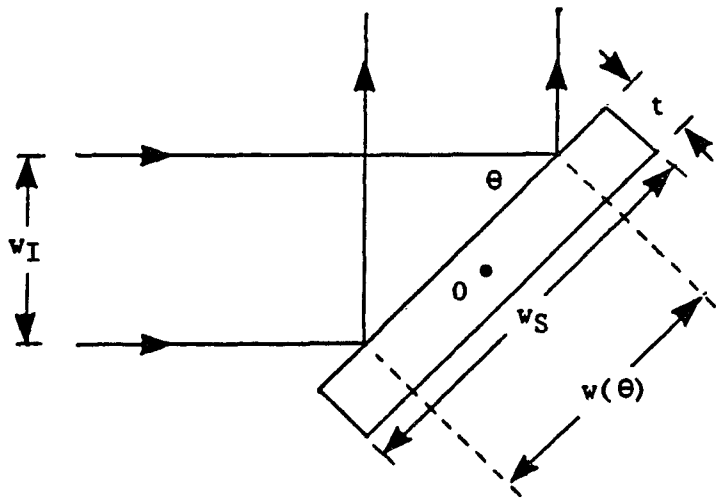

Figure II.14b. The diffraction geometry used to derive g(θ) and w(θ), (equations II.33a-II.33g). The irradiated width w(θ) and sample width w_S are equivalent for $\theta \ll \theta_g$. However, not all of the incident radiation is intercepted for angles below θ_g. The sample rotates about 0, which changes the Bragg angle θ

film, θ (the Bragg angle) is one-half of 2θ (the scattering angle), $r(z,\theta)$ is the total distance that the radiation traverses inside the sample, $w(\theta)$ is the irradiated width, h is the irradiated height, t is the film thickness, and δV is the average mosaic block volume of the film. $g(\theta)$ is the ratio of the intercepted and incident radiation cross sections, assuming that all scattered radiation is detected. The sample height h_S, irradiated height h, and incident beam height h_I are measured along the axis of rotation that defines the scattering angle 2θ. The sample width w_S, irradiated width $w(\theta)$, and incident beam width w_I are measured in the scattering plane. Both $w(\theta)$ and $g(\theta)$ depend on the sample and beam cross section geometry.

During a typical diffraction experiment, the sample rotates about the 2θ axis while the scattering plane remains stationary. This places an angular dependence on the irradiated sample width $w(\theta)$ while the irradiated sample height h remains constant. In addition, the beam height is set equal to the sample height so that $h_I=h_S=h$. This diffraction geometry is illustrated in Figure II.14b. Under these specific conditions, two special situations are encountered, depending on w_I and w_S. For $w_I \geq w_S$, the full sample width is irradiated at any Bragg angle, $w(\theta)=w_S$, and the fraction of scattered radiation $g(\theta)$ depends on the radiation area intercepted by the sample, $g(\theta)=(w_S/w_I)\sin\theta$. For $w_I \leq w_S$, the full sample width is irradiated for all angles less than θ_g, where $\theta_g=\arcsin(w_I/w_S)$. For $\theta \leq \theta_g$, $w(\theta)$ and $g(\theta)$ have a form identical to the situation defined by $w_I \geq w_S$. However, for $\theta \geq \theta_g$, the irradiated width is less than the sample width, $w(\theta)=w_I/\sin\theta$, and the entire incident radiation cross section is

scattered ($g(\theta)=1$). Summarizing,

$$w(\theta) = w_S \qquad (w_I \geq w_S) \quad , \tag{II.33a}$$

$$g(\theta) = \frac{w_S \sin\theta}{w_I} \tag{II.33b}$$

$$\theta_g = \text{arcsine}\frac{w_I}{w_S} \qquad (w_I \leq w_S) \quad , \tag{II.33c}$$

$$w(\theta) = w_S \qquad (w_I \leq w_S), \ (\theta \leq \theta_g) \quad , \tag{II.33d}$$

$$g(\theta) = \frac{w_S \sin\theta}{w_I} \tag{II.33e}$$

$$w(\theta) = \frac{w_I}{\sin\theta} \qquad (w_I \leq w_S), \ (\theta \geq \theta_g) \quad . \tag{II.33f}$$

$$g(\theta) = 1 \tag{II.33g}$$

After performing the integration, j_K is compactly written

$$J_K(S_L/\lambda) = \frac{I_o N^2 \lambda^3 |F(h,k,l)|^2 r_e^2 P(S,E_S) A(\theta_B,t,\mu) g(\theta) w(\theta) h}{R_d^2 \sin(2\theta_B)} \quad , \tag{II.34}$$

where $A(\theta_B,t,\mu)$ is the absorption factor for a flat plate film of thickness t. If the scattering vector is parallel to the surface normal of the film, $r(z,\theta)=2z/\sin\theta$, and the absorption factor is written

$$A(\theta,t,\mu) = \frac{\sin\theta}{2\mu}\left[1-e^{-2\mu t/\sin\theta}\right] \quad . \tag{II.35}$$

As the film thickness increases, $A(\theta,t)$ approaches the limiting value $(\sin\theta)/2\mu$. This equation must be modified if the scattering vector is not parallel with the film surface normal.

The structure, polarization, absorption, Lorentz, scattering fraction, and irradiated width factors of equation II.34 are of principle interest. These factors, which only affect the intensities, depend on the scattering geometry, while all other factors in equation II.34 are constants of the experiment. Figure II.15 graphically represents the scattering fraction, Lorentz, and polarization factors as a function of angle. These factors are unitless and depend on w_I and w_S. The absorption factor, irradiated width, and sample height describe the effective diffracting volume. Figure II.16 graphically represents this effective volume, denoted ΔV, compared to the total sample volume V. Figure II.17 summarizes Figures II.15 and II.16 and represents the total intensity dependence on Bragg angle. The structure factor contains the unit cell information and correlates experimental observations with the crystal structure. All other scattering dependent terms of equation II.34 describe intensity dependencies that concern only the scattering geometry and provide a normalization scheme that enables direct comparison of different diffracted intensities.

Summarizing, equations II.25 and II.34 provide the fundamental x-ray diffraction relationship between experiment and theory. Equation II.25, the Bragg condition or Bragg's law, describes the positions of the diffracted intensity maxima. For this research investigation, the diffraction geometry is situated so that the scattering vector direction is fixed while peak positions are observed as a function of angle. The

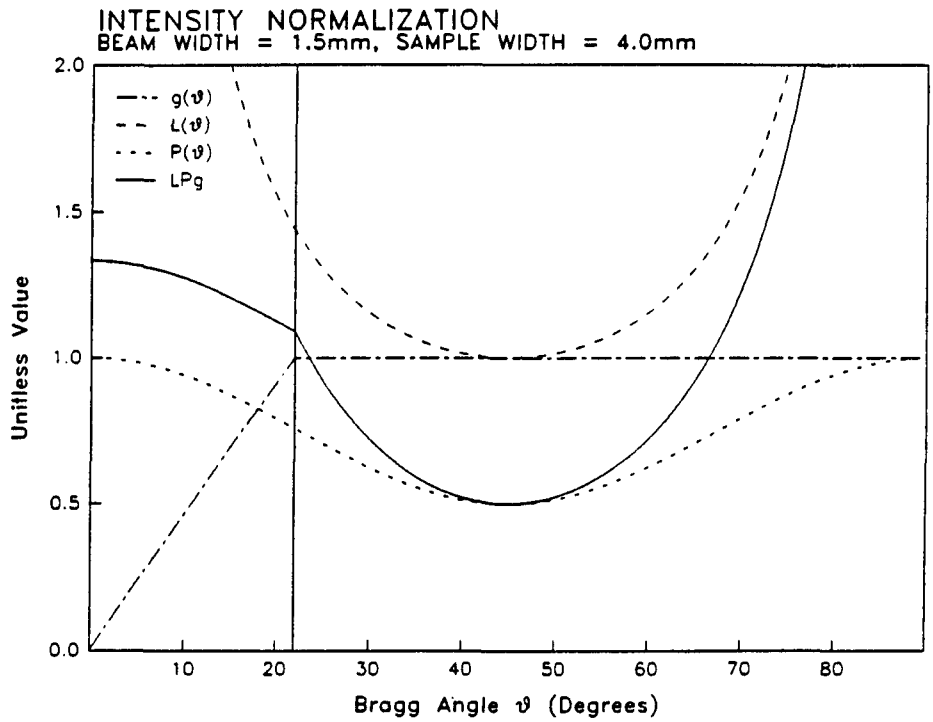

Figure II.15. The (L) Lorentz, (P) polarization (equation II.26), and (g) scattering fraction (equations II.33b,e, and g) factors for a specific situation. The incident radiation is assumed to be unpolarized. The incident beam width w_I is 1.5 mm and the sample width w_S is 4 mm. The solid curve represents the total contribution. The ratio w_I/w_S determines the critical angle θ_g (equation II.33c), which is represented by the solid vertical line

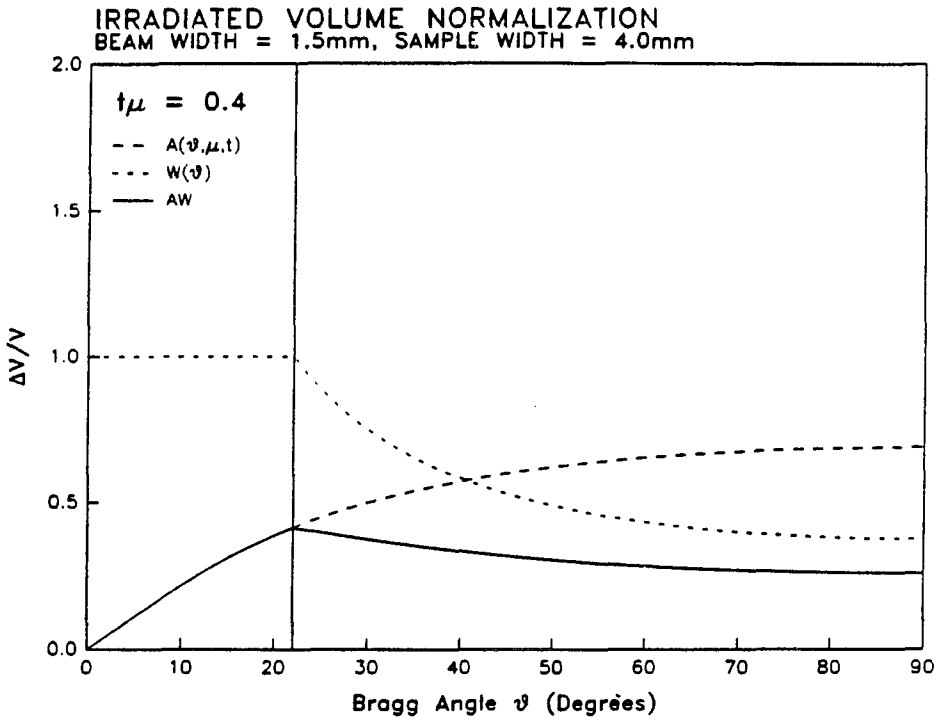

Figure II.16. The effective sample volume that contributes to the scattered intensity (solid line). $\Delta V = w(\Theta) h_S A(\Theta, t, \mu)$ and $V = w_S h_S t$. The absorption factor μ is defined so that $\mu t = 0.4$. The sample width w_S is 4 mm and the incident beam width w_I is 1.5 mm. The critical angle Θ_g (equation II.33c) is marked by the solid vertical line. $A(\Theta, t, \mu)$ (equation II.35) and $w(\Theta)$ (equations II.33a, II.33d, and II.33f) have length units and $\Delta V/V$ is unitless

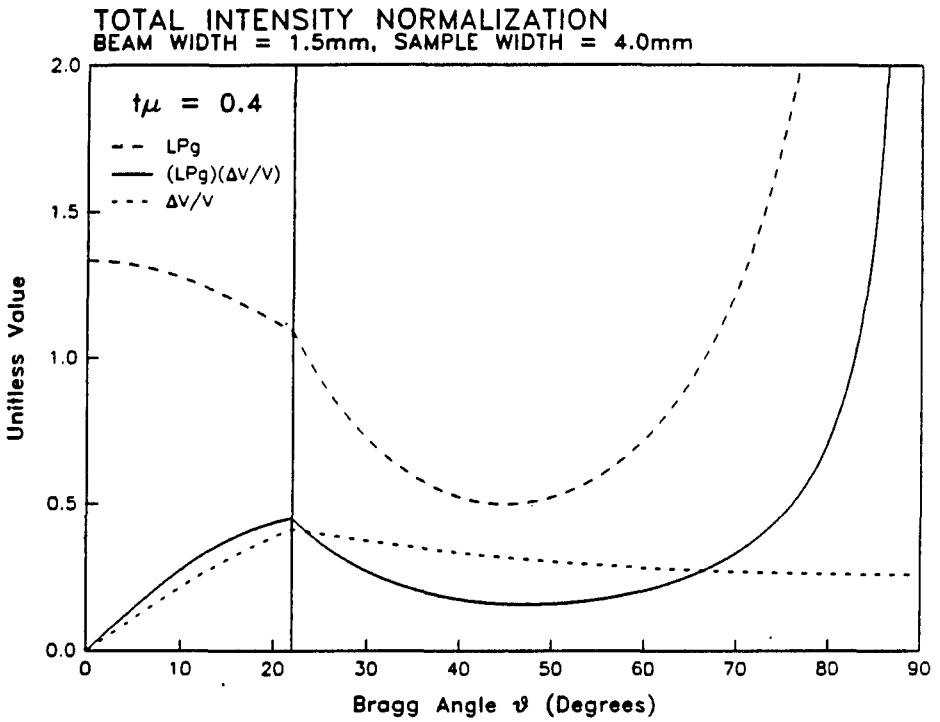

Figure II.17. The total diffracted intensity dependence on scattering angle for the specific example illustrated in Figures II.15 and II.16 (solid line). This curve determines the required intensity normalization before useful structure factor information can be extracted from the diffracted intensity

unit cell dimensions are extracted from peak positions, and peak widths are related to the number of unit cells that coherently contribute to the diffracted peak.

Information about the distribution of atoms within the unit cell is extracted from the application of equation II.34 to observed peak intensities. In particular, the structure factor F provides the important link between experiment and theory, after correcting the observed intensities for the Lorentz, polarization, absorption, scattering fraction, and irradiated width factors. F is determined by one of two common techniques; $|F|$ is derived directly from observed peaks or a model is proposed and fit to the peak intensity data. Since the intensity is proportional to $|F|^2$, the former technique requires an appropriate assignment of phase factors. This phase information, however, is present in a structure factor model. Knowledge of both the SL growth process and the bulk constituent material properties provides the framework for constructing a SL structure factor model.

E. The Atomic Scattering Factor

The atomic scattering factor was briefly introduced during the derivation of equation II.22. It represents the scattering of x-ray radiation by the atomic electron charge distribution. The atomic scattering factor f(q) is defined by

$$f(q) = \int \rho(r') e^{-q \cdot r'} d^3 r' \quad , \qquad \text{(II.36)}$$

where $\rho(r')$ is the electron charge density at location r' from the atom

center, $q=kS=2\pi(S/\lambda)$ is represented in reciprocal space and depends on the scattering vector S, and the integration is over the entire charge distribution about an atom. Equation II.36, which defines f(q) as the Fourier transform of the charge density in reciprocal space, is expressed in terms of the amplitude scattered by a single classical electron in accordance with the Thomson formula (equation II.11). The atomic scattering factor is only an approximation and asserts that the atomic electrons remain in one energy orbital during the scattering process. f(q), which depends on $\sin\theta/\lambda$, represents the interference of the spatially distributed charge density. For small scattering vectors, f(q) is expected to approach Z, the number of atomic electrons representing total constructive interference. As the scattering vector differs from zero, f(q) is expected to decrease as the atomic electrons destructively interfere with each other.

In addition to coherent scattering, electrons can be promoted to different atomic energy levels during the scattering interaction. This incoherent contribution requires that the scattered radiation have a longer wavelength in accordance with the conservation of energy. Since incoherently scattered radiation can be alternately described by fewer electrons contributing to the scattering process, f(q) can be modified to better represent the x-ray interaction with atoms. By convention, this is represented by

$$f(q,\lambda) = f(q) + \Delta f'(\lambda) + i\Delta f''(\lambda) \quad , \qquad \text{(II.37)}$$

where f(q) represents the interference effects of the spatial atomic

charge distribution and $f'(\lambda)$ and $f''(\lambda)$ represent wavelength modified scattering that is in phase and 90° out of phase, respectively, with the incident radiation. f(q) values for free atoms as a function of $\sin\theta/\lambda$ are tabulated in the forth volume of the International Tables for X-Ray Crystallography (Cromer & Waber, 1974). The analytic expression

$$f(\sin\theta/\lambda) = \sum_{i=1}^{4} a_i e^{-b_i \lambda^{-2} \sin^2\theta} + c \quad , \qquad \text{(II.38)}$$

provides an excellent fit to the atomic scattering term f(q) and eliminates the need to extrapolate between tabulated values of $\sin\theta/\lambda$. This is discussed by Cromer and Waber (1974). The a_i, b_i, and c coefficients are tabulated for each atom in the same reference. For convenience, these coefficients are reproduced in Table II.4 for all atoms relevant to this research investigation and Figures II.18a-c graphically represent the analytical expression II.38 for these atoms.

$f'(\lambda)$ and $f''(\lambda)$, which are corrective terms that account for dispersion within a material, are predominantly influenced by the inner atomic core electrons. Since the core electrons are very localized, the scattering dependencies of f′ and f′′ are small. However, for wavelengths that correspond to energies near the atomic transition values, f′ and f′′ become appreciable. Cromer (1983) has computed these dispersion terms for free atoms as a function of wavelength. For reference, $f'(\lambda)$ and $f''(\lambda)$ are reproduced in Table II.5 for all relevant atoms and wavelengths. These values are expected to differ slightly for crystalline environments, which distort the free atom charge density. If required, better accuracy can be attained by

Table II.4. Atomic scattering factor coefficients used in equation II.38 for all atoms relevant to this research investigation

Atom	a_1	b_1	a_2	b_2	a_3	b_3	a_4	b_4	c
Mn	11.2819	5.34090	7.35730	0.343200	3.01930	17.8674	2.24410	83.7543	1.08960
Zn	14.0743	3.26550	7.03180	0.233300	5.16520	10.3163	2.41000	58.7097	1.30410
Ga	15.2354	3.06690	6.70060	0.241200	4.35910	10.7805	2.96230	61.4135	1.71890
As	16.6723	2.63450	6.07010	0.264700	3.43130	12.9479	4.27790	47.7972	2.53100
Cd	19.2214	0.594600	17.6444	6.90890	4.46100	24.7008	1.60290	87.4825	5.06940
Te	19.9644	4.81742	19.0138	0.420885	6.14487	28.5284	2.52390	70.8403	4.35200
Hg	20.6809	0.545000	19.0417	8.44840	21.6575	1.57290	5.96760	38.3246	12.6089

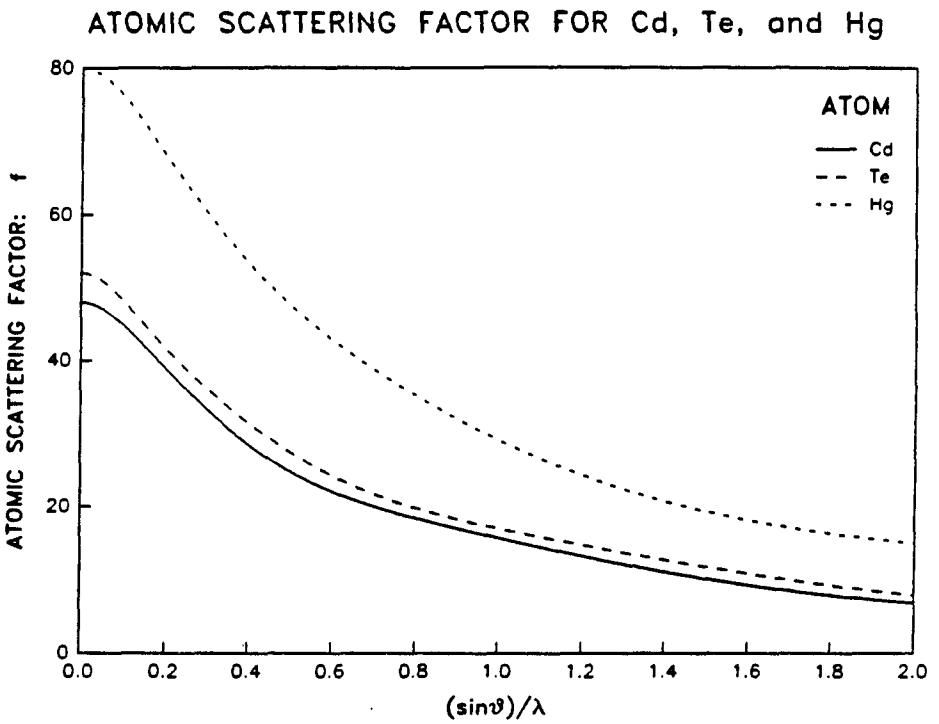

Figure II.18a. The atomic scattering factors for Cd, Te, and Hg. These curves are based on equation II.38 using the appropriate constants from Table II.4. At zero angle, the atomic scattering factor is the atomic number. At large $(\sin\theta)/\lambda$, only the core electrons contribute to the scattering factor

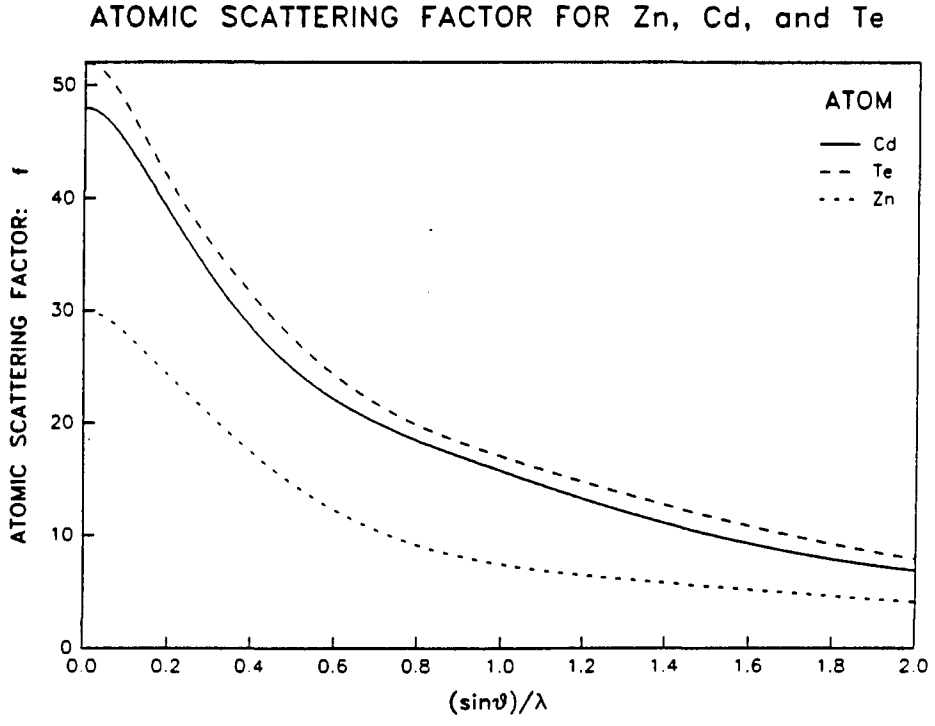

Figure II.18b. The atomic scattering factors for Cd, Te, and Zn. The Cd and Te curves (see Figure III.18a) are reproduced here for comparison with the Zn scattering factor. These curves are based on equation II.38 using the appropriate constants from Table II.4. At zero angle, the atomic scattering factor is the atomic number. At large $(\sin\theta)/\lambda$, only the core electrons contribute to the scattering factor

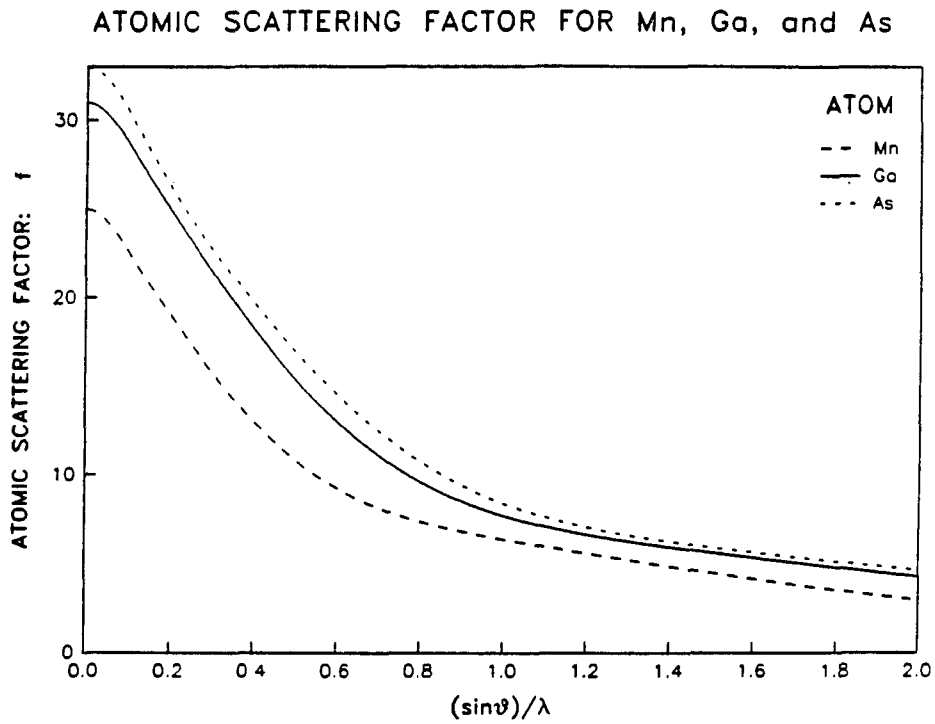

Figure II.18c. The atomic scattering factors for Mn, Ga, and As. These curves are based on equation II.38 using the appropriate constants from Table II.4. At zero angle, the atomic scattering factor is the atomic number. At large $(\sin\theta)/\lambda$, only the core electrons contribute to the scattering factor

refining these values during a fit of the structure factor.

Table II.5 Anomalous dispersion correction factors for all atoms and wavelength used in this research investigation

Atom	1.47639 Å		1.28181 Å		1.09855 Å		0.70930 Å	
	f′	f′′	f′	f′′	f′	f′′	f′	f′′
Mn	-0.37	2.62	0.04	2.07	0.23	1.59	0.28	0.73
Zn	-1.83	0.63	-6.31	3.89	-0.91	2.99	0.20	1.43
Ga	-1.50	0.72	-2.40	0.56	-1.62	3.33	0.14	1.61
As	-1.11	0.93	-1.51	0.72	-2.67	0.54	-0.05	2.01
Cd	-0.08	4.33	-0.15	3.40	-0.32	2.60	-1.03	1.20
Te	-0.33	5.92	-0.19	4.67	-0.23	3.59	-0.80	1.67
Hg	-5.18	7.19	-6.04	5.74	-8.03	4.48	-3.13	9.22

F. The Structure Factor

The structure factor is defined by equation II.21. Representing kS by **q**, the structure factor is written

$$F(\mathbf{q}) = \sum_j f_j e^{-i\mathbf{q}\cdot\mathbf{r}_j} , \qquad \text{(II.39)}$$

where $\mathbf{r}_i=(u_j\mathbf{a}+v_i\mathbf{b}+w_i\mathbf{c})$ is the atomic position within the unit cell. $F(\mathbf{q})$ represents the total scattered amplitude of the unit cell with respect to one electron scattering at the unit cell origin. Even when the Laue conditions are fulfilled, the structure factor can have zero value and prohibit a diffracted intensity. Complete destructive

interference between all like atomic species produces these forbidden reflections. Using equations II.2 and II.24, the exponent of equation II.39 becomes

$$i\mathbf{q}\cdot\mathbf{r}_j = i2\pi(hu_j+kv_j+lw_j) \quad . \tag{II.40}$$

If the Laue conditions are fulfilled, h, k, and l are integers. A general property of the structure factor is emphasized in equation II.40; the structure factor depends on the fractional coordinates, which are independent of the unit cell size. The Laue conditions provide unit cell dimension information. Knowing the fractional atomic positions of a unit cell, the allowed and forbidden reflection are determined. For example, using the zincblende coordinates (see Table II.1), the allowed reflections are

$$(h+k+l) \text{ odd} \rightarrow |F|^2 = 16(f_A^2+f_B^2) \quad , \tag{II.41a}$$

$$(h+k+l) \text{ odd multiple of } 2 \rightarrow |F|^2 = 16(f_A-f_B)^2 \quad , \tag{II.41b}$$

$$(h+k+l) \text{ even multiple of } 2 \rightarrow |F|^2 = 16(f_A+f_B)^2 \quad . \tag{II.41c}$$

No diffracted intensity is observed when a set of h, k, and l integers contains both even and odd values. All other reflections are allowed. Notice that the intensity is weak for the condition stated in equation II.41b. Equation II.41c represent the strongest reflections from a zincblende crystal lattice.

Small random variations of the atomic positions can be included into the structure factor, if there are no long range correlation effects

that occur over distances longer than the unit cell boundary. These variations can be "frozen" into the crystal lattice or can have a time dependence. Thermal motion of the atoms is an example of the latter, which was first considered by Debye (1913). Debye considered materials having only one atom type. Laue (1918) extended this work to include mixed crystal, which have more than one atom type. Including random variations, the structure factor is written

$$F(\mathbf{q}) = \sum_j f_j e^{-i\mathbf{q}\cdot(\mathbf{r}_j+\Delta\mathbf{r}_j)} \quad , \qquad \text{(II.42)}$$

where $\Delta\mathbf{r}_j$ is the small displacement from the average center of atom j. Since the intensity is proportional to the structure factor multiplied by its complex conjugate, the quantity of interest is

$$|F(\mathbf{q})|^2 = \sum_{j,k} f_j f_k e^{-i\mathbf{q}\cdot(\mathbf{r}_j-\mathbf{r}_k)} e^{-\mathbf{q}\cdot(\Delta\mathbf{r}_j-\Delta\mathbf{r}_k)} \quad , \qquad \text{(II.43)}$$

where both j and k index each atom within the unit cell. However, $\Delta\mathbf{r}_j$ and $\Delta\mathbf{r}_k$ are not explicitly known. The observed effect of these random fluctuations depends on an average of equation II.43 over all possible displacements

$$\langle|F(\mathbf{q})|\rangle^2 = \sum_{j,k} f_j f_k e^{-i\mathbf{q}\cdot(\mathbf{r}_j-\mathbf{r}_k)} \langle e^{-\mathbf{q}\cdot(\Delta\mathbf{r}_j-\Delta\mathbf{r}_k)}\rangle \quad , \qquad \text{(II.44)}$$

where the averaging only affects the random displacement vectors. Equation II.44 can be simplified, if the random fluctuation magnitudes are small. This is accomplished by the approximation

$$\langle e^{-i\alpha} \rangle \simeq e^{\langle -\alpha^2/2 \rangle} \quad , \tag{II.45}$$

which is valid for small α. Using equation II.45, the averaged exponential term of equation II.44 is written

$$\langle e^{-iq\cdot(\Delta r_j - \Delta r_k)} \rangle = e^{-M_j} e^{-M_k} e^{\langle (q\cdot\Delta r_j)(q\cdot\Delta r_k) \rangle} \quad , \tag{II.46a}$$

$$M_j = \frac{\langle q\cdot\Delta r_j \rangle^2}{2} \quad . \tag{II.46b}$$

The factor e^{-M} is known as the Debye factor. The third exponential term, which represents the cross terms, depends on the correlation effects between Δr_j and Δr_k. For purely random fluctuations, no correlation exists and the third exponential term of equation II.46a is unity. If Δr_j and Δr_k are uncorrelated, equation II.44 can be expressed as $|F|^2 = F_R^* F_R$, using a modified definition of the structure factor

$$F_R(q) = \sum_j f_j e^{-M_j} e^{-iq\cdot r_j} \quad . \tag{II.47}$$

According to equation II.47, random fluctuations decrease the scattered amplitude of the atoms. In the context of thermal vibrations, e^{-M} is known as the Debye temperature factor or the Debye-Waller factor. Since the amplitude of atomic thermal motions increase with temperature, equation II.39 states that the diffraction intensities will decrease with increasing temperature. By explicitly writing q,

$$M_j = \frac{8\pi^2 (\sin\theta)^2 \langle \Delta r_{js} \rangle^2}{\lambda^2} \quad , \tag{II.48}$$

where $\langle \Delta r_{js} \rangle$ is the average fluctuation amplitude along the scattering vector. Equation II.48 emphasizes the angular dependence of the Debye-Waller factor. Thus, if random thermal motions are present, the diffracted intensity will decrease with not only temperature, but also angle. Since the Debye-Waller factor correction concerns the structure factor, and not the Laue conditions, the diffracted peak breadth is unaffected by random fluctuations. This is not necessarily true, however, for correlated effects that extend beyond a single unit cell description.

G. Peak Broadening

The diffracted peak breadth, which represents the range of S/λ vectors that correspond to an appreciable diffracted intensity, is affected by many factors. For a small perfect crystal, the interference functions of equation II.22 determine the intensity distribution, which broadened with a decrease in crystal size. For mosaic crystals, the peak breadth is attributed to both the small mosaic block size and the mosaic spread. A nonuniform strain distribution, which modifies the crystal lattice parameters across a sample, contributes to the peak breadth by locally varying the Laue diffraction conditions across the sample. Instrumental resolution and a divergent radiation source broaden the diffracted peak distribution, regardless of the crystal sample. Each broadening effect has a specific dependence on S/λ, which can be exploited when analyzing diffraction data.

Ideally, the entire diffracted intensity distribution should be compared with theory to extract structural information. This tedious

procedure, however, is impractical to perform on a routine basis. Analysis of a suitably defined peak breadth provides a reasonable compromise. By convention, the peak breadth is defined as the range of S/λ vectors that correspond to a diffracted intensity that is greater than one-half of the maximum. This is known as the full width at half maximum (FWHM) of the intensity distribution.

The dependence of peak breadth on crystal size is easily evaluated within the Ewald construction of x-ray diffraction. The interference function of equation II.22 defines an intensity distribution around each reciprocal lattice point; as the S/λ vector approaches S_L/λ, the diffracted intensity increases and is maximum at S_L/λ. This is illustrated in Figure II.19a, where the boundary around each lattice point represents zero intensity. Since equation II.22 contains three interference functions, one for each crystallographic direction, the peak breadth depends on the particular path of the changing S/λ vector through reciprocal space. A general reciprocal space path can be decomposed into components that describe either a change in direction at constant magnitude or a change in magnitude along a fixed direction. These two special directions are illustrated in Figures II.19b and II.19c and have a different S/λ dependence.

The FWHM of the intensity distribution must be related to a change in S/λ, which will be denoted $\Delta = \Delta S/\lambda$. This is accomplished by considering the interference function dependence on Δ. According to equation II.22, the interference function depends on $N_i Y_i$ and Y_i along a specified crystallographic axis. Without a loss of generality, the direction of Δ is assumed to lie along one of the crystallographic axes

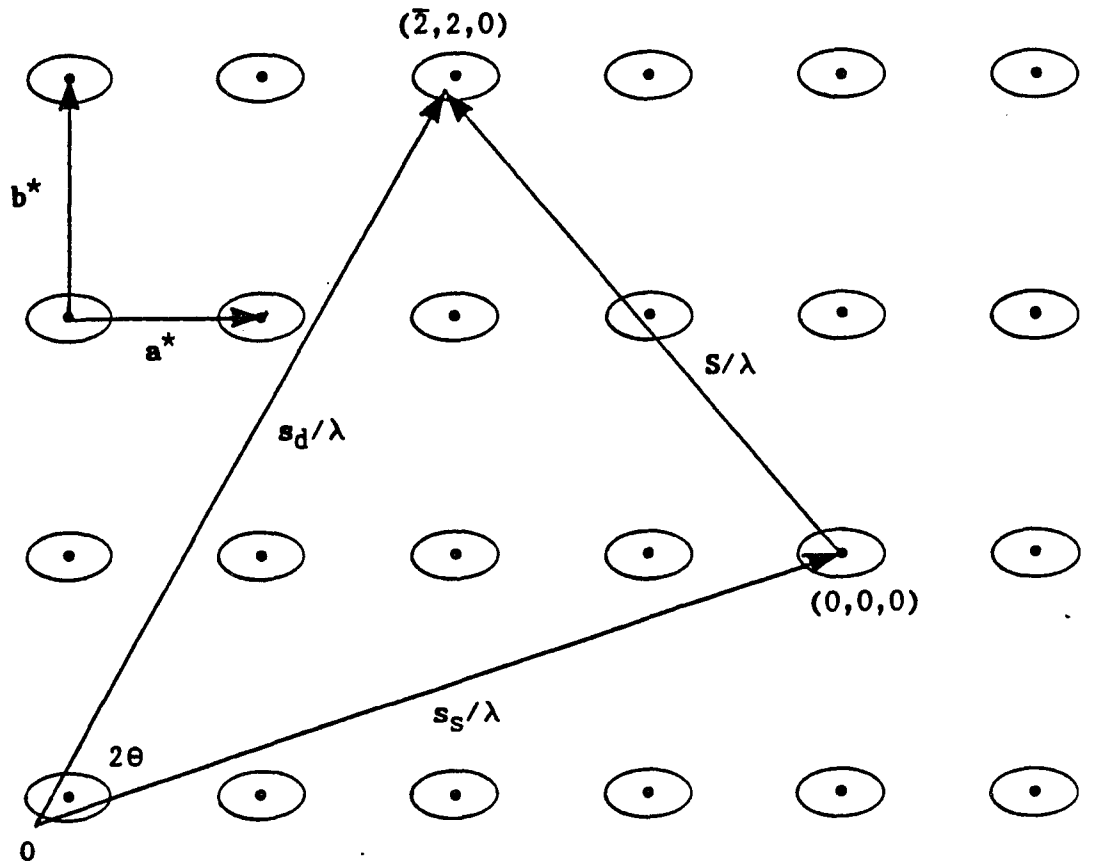

Figure II.19a. A two dimensional representation of the Ewald construction emphasizing a significant diffracted peak breadth. The boundaries around each reciprocal lattice point represent the first zero intensity minimum. An appreciable diffracted intensity occurs when S/λ terminates inside the reciprocal lattice boundary. The intensity increases as S/λ terminates closer to the reciprocal point center. Since the illustrated S/λ does not terminate at the reciprocal point center, only a fraction of the maximum intensity is diffracted

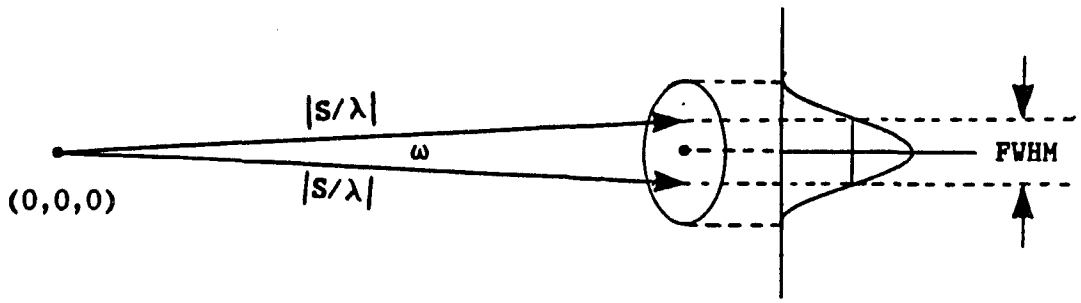

Figure II.19b. The peak breadth observed when S/λ changes direction at constant magnitude. The right end of the drawing shows the relationship between the observed peak profile and the reciprocal lattice boundary. The FWHM corresponds to the diffracted peak profile as illustrated

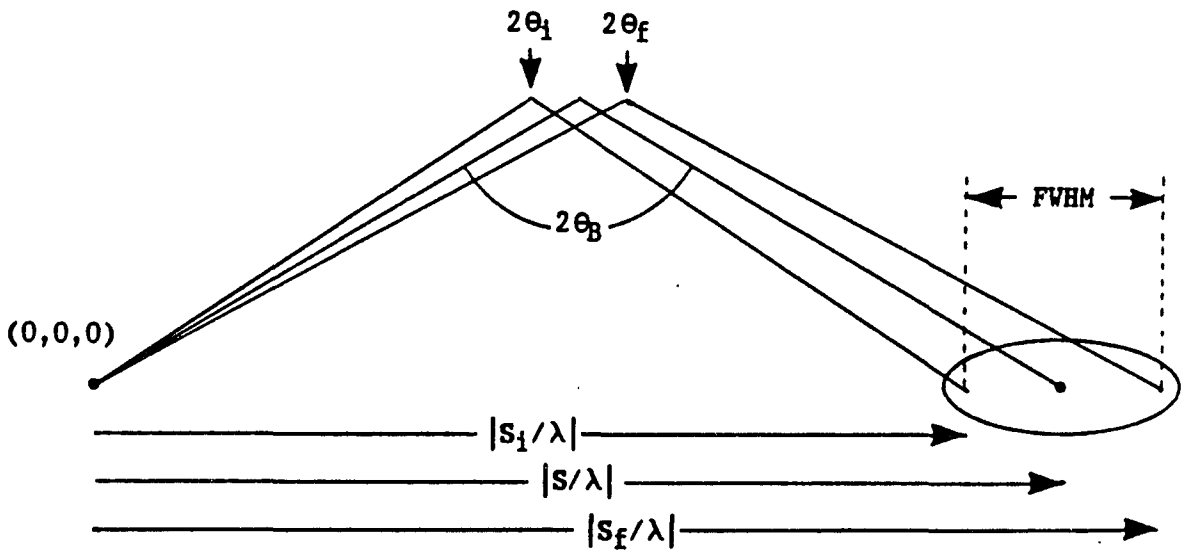

Figure II.19c. The peak breadth observed when S/λ changes in magnitude at constant direction. θ_B is the Bragg angle at which the maximum intensity is observed. θ_i and θ_f are the Bragg angles that correspond to the half maximum diffracted intensity

having N_i unit cells of length a_i. Since the principal maximum of the interference function is N_i^2, the FWHM condition is expressed

$$\frac{\sin^2 N_i \Delta\Psi_i}{\sin^2 \Delta\Psi_i} = \frac{N^2}{2} \quad , \tag{II.49a}$$

$$\Delta\Psi_i = \pi|\Delta S/\lambda|a_i \quad . \tag{II.49b}$$

The magnitude of $\Delta\Psi_i$ can be approximated by the first zero minimum of the interference function. This occurs at $\Delta\Psi_i=\pi/N_i$, which is quite small for moderate values of N_i. Since the half maximum value is even smaller, $\sin\Delta\Psi_i$ can be approximated by $\Delta\Psi_i$. Using this approximation, equation II.49a is written

$$2\sin^2 N_i \Delta\Psi_i = (N_i \Delta\Psi_i)^2 \quad . \tag{II.50}$$

The numerical solution of equation II.50 is $N_i \Delta\Psi_i=0.444\pi$, which relates the change in S/λ required to change the interference function from maximum to one-half the maximum value. The FWHM is twice this change. Using the solution of equation II.50,

$$|\Delta| = \frac{0.888}{L} \quad , \tag{II.51}$$

where $L=N_i a_i$ is the crystal length along the directional change of S/λ. If Δ does not lie along a crystallographic axis, L must be replaced by $L\cos\alpha$, where α is the angle between Δ and the crystallographic axis represented by L.

In practice, the crystal sample and detector position are rotated during a diffraction experiment. Since the reciprocal lattice has a fixed relationship with the crystal lattice, a sample rotation moves the reciprocal lattice points of Figure II.19a as the scattering vector remains fixed. A change in the detector position s_d changes S/λ as the reciprocal lattice points remain fixed. A peak profile is represented by the diffracted intensity as a function of angle for these rotations. Thus, expressing the peak breadth in terms of an angular movement is useful.

Figure II.19b represents a crystal rotation about the origin. The magnitude $|S/\lambda|$ remains constant while the scattering vector direction changes by a rotation of ω about the origin. According to Figure II.19b,

$$\sin(\omega/2) = \frac{|\Delta/2|}{|S/\lambda|} \quad . \tag{II.52}$$

Since the peak breadth $|\Delta|$ is assumed small, $\sin(\omega/2)$ can be approximated by $\omega/2$. If ω is to represent the peak breadth, $|\Delta|$ of equation II.52 must be replaced by equation II.51. The peak breadth becomes

$$\omega_{FWHM} = \frac{0.444\lambda}{L\sin\theta_B} \quad , \tag{II.53}$$

where $2\sin\theta_B = |S|_B$ is the scattering vector magnitude for a particular Bragg reflection and ω_{FWHM} is the angular width (in radians) at constant $|S/\lambda|$ that corresponds to the FWHM of the intensity distribution.

Figure II.19c illustrates a different scanning geometry that involves a change in the scattering angle 2Θ for a fixed scattering vector direction. The FWHM is expressed in terms of Θ for this situation. According to Figure II.19c,

$$|\Delta| = \frac{[2\sin(\Theta_f/2)-2\sin(\Theta_i/2)]}{2} = \sin\Theta_f - \sin\Theta_i \quad , \qquad (II.54)$$

where $|S_i/\lambda|2\sin\Theta_i$, $|S_f/\lambda|=2\sin\Theta_f$, and $2\Theta_i$ and $2\Theta_f$ are the initial and final scattering angles, respectively. Using a trigonometric identity, the right side of equation II.54 becomes

$$\sin\Theta_f - \sin\Theta_i = 2\cos\frac{(\Theta_f-\Theta_i)}{2}\sin\frac{(\Theta_f-\Theta_i)}{2} = 2\cos\Theta_B\sin\delta\Theta \quad , \qquad (II.55)$$

where Θ_B is the Bragg angle at maximum intensity and $\delta\Theta$ is the change in Bragg angle that must be associated with the FWHM of the intensity distribution. Again, $\delta\Theta$ is small so that $\sin\delta\Theta\simeq\delta\Theta$ is a reasonable approximation. The FWHM of the intensity distribution is determined by substituting equation equation II.51 for $|\Delta|$ in equation II.54. Then, using the identity of equation II.55, the peak breadth becomes

$$\delta\Theta_{FWHM} = \frac{0.444\lambda}{L\cos\Theta_B} \quad , \qquad (II.56)$$

where $\delta\Theta_{FWHM}$ is the angular range (in radians) that corresponds to the FWHM of the intensity distribution, and Θ_B is the Bragg angle at maximum intensity. Equation II.56 is known as the Scherrer equation for particle size broadening (Scherrer, 1918).

Equations II.53 and II.56 can be applied to both small perfect crystals and mosaic crystals. For small perfect crystals, L represent the macroscopic physical dimension along the appropriate crystallographic axis. For a mosaic crystal, L represents the average length of the diffracting mosaic blocks. The peak breadth formulas must be applied with caution, however. A mosaic spread will also contribute to the peak breadth for mosaic crystals, and a divergent incident radiation source will artificially broaden the diffracted intensity distribution, independent of the sample type.

Instrumental broadening prevents the direct application of equations II.53 and II.56 to experimental data. Warren (1969) discusses this problem and summarizes several procedures that identify and separate instrumental and crystal broadening effects. Most correction techniques require Fourier decomposition of isolated diffraction peaks, which is impractical for SL diffraction spectra. However, a general discussion of instrumental broadening is useful and provides a simplified procedure that can be applied to SLs.

Although many factors contribute to instrumental broadening, only the characterization of the total broadening contribution is necessary. Instrumental broadening is characterized by observing the diffracted spectrum from a standard crystal of known quality. According to equation II.22, the theoretical peak profiles from a nearly perfect crystal are too narrow to be resolved by experimental apparatus. The observed peak profiles, however, are resolved and represent the total broadening contribution of the apparatus. In principle, by observing a reference peak profile under the exact diffraction conditions of the

sample, the instrumental broadening contribution can be removed from the sample profile.

The total diffracted peak profile that contains both instrumental and sample broadening is investigated with the aid of Figure II.20 (Warren, 1969). Ideally, curve f(y), which represents only sample broadening, is desired. If no sample broadening were present, f(y) would be sharply concentrated at y=0. The sample profile must be extracted from the experimentally observed profiles h(x) and g(z), which represent the total diffracted peak profile and the instrumental broadening from a reference sample, respectively. The relationship between h(x), f(y), and g(z) is derived by considering an element of area g(z)dz. If no sample broadening were present, this area element would directly contribute to an element h(x)dx, and the h(x) and g(z) profiles would be identical. However, sample broadening redistributes g(z)dz into a broadened profile that extends over an appreciable region of z, as depicted under g(z) in Figure II.20. Since f(y) describes the redistribution of g(z)dz,

$$g(z)dz = C\int f(y)dy = CA_f \quad , \tag{II.57}$$

where C is simply a scale factor and A_f is the area under f(y). Each redistribution of g(z)dz for all z values contributes to h(x). According to Figure II.20 and equation II.57,

$$dh(x) = Cf(y) \quad , \tag{II.58}$$

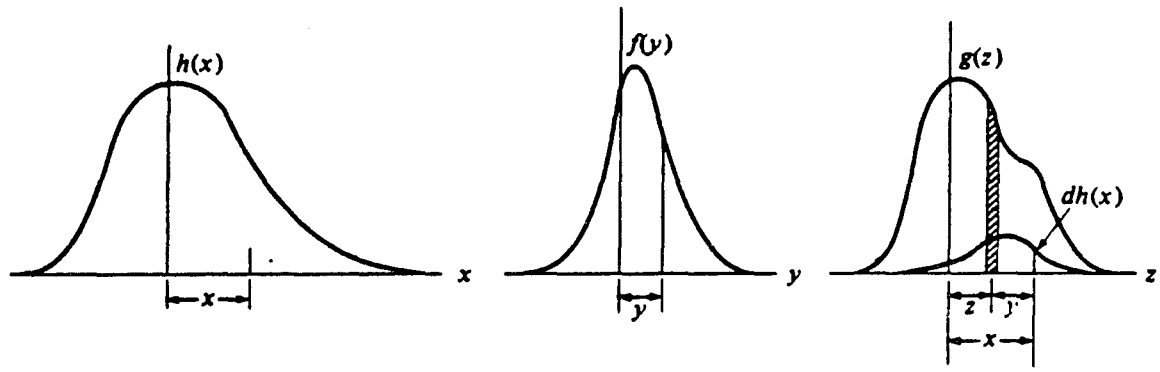

Figure II.20. · A representation of instrumental broadening. h(x) represents the measured diffracted peak, which includes both sample and instrumental broadening. f(y) represents broadening effects from the crystal alone and g(z) represents instrumental broadening alone. g(z) is obtained from a reference reflection. Only h(x) and g(z) are directly measurable. The peak breadth of profile f(y) must be extracted from h(x) using g(z)

where dh(x) is the elemental contribution to h(x) from the redistributed area g(z)dz. For each possible area element g(z)dz, an elemental contribution dh(x) contributes to h(x). Integrating equation II.58 and using equation II.57,

$$h(x) = \frac{1}{A_f}\int g(z)f(x-z)dz \quad , \qquad \text{(II.59)}$$

where x=z+y as illustrated in Figure II.20.

Equation II.59 is the basis for all instrumental broadening correction schemes. The direct application of II.59 is not convenient, since the desired diffraction profile f(y) is part of the integrand. However, by assuming a particular profile form for f(y), equation II.59 can be integrated, allowing the isolation of f(y). In particular, both the Gaussian and Lorentzian distributions fit actual x-ray diffraction profiles with moderate success. Assuming that f(y) and g(z) can be described by Gaussian (Warren, 1941) or Lorentzian (Jones, 1939) profiles, the following peak breadth relationships are obtained:

$$\text{Gaussian:} \quad x(y) = Ae^{-a^2y^2} \rightarrow B^2(h) = B^2(g) + B^2(f) \quad , \qquad \text{(II.60a)}$$

$$\text{Lorentzian:} \quad x(y) = \frac{A}{(1+a^2y^2)} \rightarrow B(h) = B(g) + B(f) \quad , \qquad \text{(II.60b)}$$

where B(h), B(g), and B(f) are the total diffracted peak breadth, the instrumental broadening breadth of the reference reflection, and the true sample breadth, respectively, and are measured using radian units. Equations II.60a and II.60b provide a crude method of peak breadth

correction. Some of the SLs of this research investigation are grown on high quality GaAs substrates, which provide convenient reference reflections that can be measured concurrently with the SL peaks.

III. X-RAY DIFFRACTION FROM A SUPERLATTICE

A. Ideal Superlattice Diffraction Conditions: Bragg's Law

The diffraction background of Chapter II is directly applicable to SL structures of arbitrary crystalline quality. The SLs of this research investigation involve two crystalline constituent materials which are periodically layered along one direction, known as the growth direction $\mathbf{n}_g$. The wavelength of the SL modulation along $\mathbf{n}_g$ is known as the SL period L. Both constituents crystallize in the zincblende structure and are oriented identically along $\mathbf{n}_g$. That is, if the growth direction is represented by $[h_1,k_1,l_1]$ and $[h_2,k_2,l_2]$ in constituents one and two, respectively, then $h_1=h_2$, $k_1=k_2$, and $l_1=l_2$. In particular, only the [0,0,1] and the [1,1,1] growth directions are encountered in this investigation. Although both constituents crystallize in the cubic zincblende structure, the constituent bulk lattice parameters are different, producing lattice misfit at the interfaces. The quality and structural coherence of each interface depends on the type of misfit accommodation. For the following SL discussion, complete structural coherence is assumed at each interface. This requires that the in-plane lattice parameters (perpendicular to $\mathbf{n}_g$) be equivalent in magnitude and direction, $\mathbf{a}_1=\mathbf{a}_2$ and $\mathbf{b}_1=\mathbf{b}_2$. Deviations from this ideal situation are discussed when appropriate.

Because of the special relationship between the constituent and SL unit cells, the SL vectors are easily described in terms of the constituent lattices. For mathematical convenience, $\mathbf{n}_g$ is chosen to coincide with the c axes of the constituent materials. This describes

general [0,0,1] SL growth. Using the cubic to hexagonal unit cell transformation outlined in equations II.7a and II.7b, [1,1,1] SL growth is described by [0,0,1] growth within the hexagonal unit cell representation. Thus, there is no loss of generality in defining $\mathbf{n}_g$ along [0,0,1], assuming the appropriate choice of unit cell. The SL unit cell vectors $\mathbf{a}'$, $\mathbf{b}'$, and $\mathbf{c}'$ are conveniently described in terms of the constituent cell parameters by the following relationships

$$\mathbf{a}' = a\hat{\mathbf{a}} = \mathbf{a} \quad , \tag{III.1a}$$

$$\mathbf{b}' = b\hat{\mathbf{b}} = \mathbf{b} \quad , \tag{III.1b}$$

$$\mathbf{c}' = L\hat{\mathbf{c}} \quad , \tag{III.1c}$$

where L is the SL period, $\mathbf{a}'$, $\mathbf{b}'$, and $\mathbf{c}'$ are the SL lattice vectors, $\mathbf{a}$ and $\mathbf{b}$ are the in-plane constituent lattice parameters, and $\hat{\mathbf{a}}$, $\hat{\mathbf{b}}$, and $\hat{\mathbf{c}}$ are the constituent unit lattice vectors. Since the constituent lattice parameters along $\mathbf{n}_g$ are not necessarily equal, $c_1 \neq c_2$, an average constituent lattice parameter $\langle c \rangle$ is defined by

$$\langle c \rangle = \frac{n_1 c_1 + n_2 c_2}{n_1 + n_2} = \frac{L}{n_1 + n_2} \quad , \tag{III.2a}$$

$$L = N\langle c \rangle \quad , \quad N = n_1 + n_2 \quad , \tag{III.2b}$$

where n_1 and n_2 are the number of unit cells per period of each constituent and L is the length of the SL unit cell (SL period). The SL reciprocal lattice vectors are obtained by applying equations II.4a-c to equations III.1a-c. Using equations III.2a and III.2b to express L in terms of $\langle c \rangle$,

$$\mathbf{a'}^* = \mathbf{a}^* \quad , \tag{III.3a}$$

$$\mathbf{b'}^* = \mathbf{b}^* \quad , \tag{III.3b}$$

$$\mathbf{c'}^* = \frac{\langle c \rangle n_g}{N} \quad , \quad \frac{\langle c \rangle}{N} \quad , \tag{III.3c}$$

where $\mathbf{a'}^*$, $\mathbf{b'}^*$, and $\mathbf{c'}^*$ are the SL reciprocal lattice vectors, and $\mathbf{a}^*$ and $\mathbf{b}^*$ are the constituent in-plane reciprocal lattice vectors. The introduction of the SL period increases the number of reciprocal lattice points along <c>. According to the Ewald construction, more reciprocal lattice points can intersect the Ewald sphere along n_g^*, creating additional reflections. Since both **a** and **b** are perpendicular to n_g, the reciprocal lattice direction n_g^* is parallel to n_g (see equation II.4c). This special condition, which is relevant to all SL considered in this investigation, corresponds to the monoclinic crystal system.

Bragg's law for a SL is derived directly from equation II.25, where $d_{h,k,l}$ relates the lattice plane spacing to the Miller indices of a monoclinic unit cell. The relationship between the crystallographic plane spacing and the Miller indices for any crystal system can be found in most introductory diffraction texts such as Cullity (1978). Using primed Miller indices to represent crystallographic planes of the SL unit cell,

$$\frac{1}{d^2_{h',k',l'}} = \frac{1}{\sin^2\gamma}\left[\frac{h'^2}{a'^2} + \frac{k'^2}{b'^2} + \frac{l'^2\sin^2\gamma}{c'^2} - \frac{2h'k'\cos\gamma}{a'b'}\right] \quad , \tag{III.4}$$

where a', b', c' are the SL lattice vectors and γ is the angle between **a'** and **b'**. Equations II.25 and III.4 combined represent Bragg's law for

SL having a monoclinic unit cell.

The SL period is measured by observing the scattering angle Θ for the (0,0,l′) reflections. Because of the deposition process, the SL film is perpendicular to $\mathbf{n}_g$. (0,0,l′) reflections are the most accessible experimentally and are always measured to obtain period information. Setting h and k equal to zero in equation III.4,

$$d_{l'} = \frac{c'}{l'} = \frac{L}{l'} \quad , \tag{III.5}$$

where $d_{l'}$ represents the (0,0,l′) crystallographic spacing. Combining equations II.25 and III.5,

$$\sin\Theta = \frac{\lambda l'}{2L} \quad . \tag{III.6}$$

This is Bragg's law for (0,0,l′) reflections.

Once the l′ indices are known, the SL period is derived by measuring $\sin\Theta$ as a function of l′. The zero order reflection, l′=0, is observed at Θ=0. Since l′ is an integer, all subsequent diffraction peaks are indexed by a nonzero integers with adjacent peaks representing an l′ increment of one. If all SL peaks are observed, the l′ indices are assigned by inspection, with the first peak at a nonzero scattering angle assigned l′=1. However, because of the structure factor, the intensities of many SL peaks may be too weak to observed experimentally. This prevents an unambiguous assignment of l′ indices. The SL period can be measured without knowing the proper l′ assignment, provided that pairs of adjacent peaks are observed. Since adjacent peaks correspond

to an l' increment of one, the period is extracted from peak pairs using equation III.6.

By introducing the average constituent lattice parameter $\langle c \rangle$ into equation III.6, an equivalent representation of Bragg's law can be derived. Replacing L by $N\langle c \rangle$,

$$\sin\theta = \frac{\lambda l'}{2N\langle c \rangle} \quad . \tag{III.7}$$

Since l' is an arbitrary integer, the following substitution can be applied with no loss of generality,

$$l' = Nl+m \quad , \quad -N<m<N \quad , \tag{III.8}$$

where m and l must be integers. Substituting equation III.8 into equation III.7,

$$\sin\theta = \frac{\lambda}{2}\left[\frac{l}{\langle c \rangle} + \frac{m}{L}\right] \quad . \tag{III.9}$$

Comparing equation III.9 to the form of equation III.6, l has a simple interpretation; l is the Miller index that corresponds to an average lattice unit cell of length $\langle c \rangle$ along n_g. The introduction of the SL period generates additional diffraction peaks that are indexed by nonzero m values. The integer index m is known as the satellite index and defines two SL peak categories: central peaks ($m=0$) and satellite peaks ($m\neq0$). This terminology is common in the literature. The

satellite index associates a particular satellite to a central peak. Thus, each SL peak has two (l,m) indices, (l,m) and (l+1,m-N), depending on the central peak that is associated with the satellite. Additional index redundancy is prevented by restricting m to integers between ±N.

The (l,m) index scheme is useful when the bulk constituent lattice parameters are known, provided that there are no crystal lattice phase transformations induced during the SL film deposition. According to equation III.8, adjacent central peaks are separated by N-1 satellites. This reduces the number of central peak candidates that must be considered during the assignment of (l,m) indices. Knowing an approximate average lattice parameter <c> usually provides sufficient information to assign (l,m) indices by inspection. The l′ index assignment immediately follows using equation III.8. The use of l′ or (l,m) is arbitrary. However, mathematically, one scheme may be more natural to use than the other. The above discussion does not require h and k to be zero; general reflections are represented by either the (h′,k′,l′) or (h,k,l,m) notation.

Figure III.1 illustrates a two dimensional slice of SL reciprocal space. Both the l′ and (l,m) index schemes are indicated. The filled circles represent central peaks and the open circles are satellites. If the SL periodicity were removed, only central peaks would be present. In the context of atomic diffusion, Figure III.1 represents a good quality SL, which has suffered negligible atomic migration across the interfaces. If the SL was heated for a time sufficient to completely diffuse all constituent material interfaces, then only the central peaks (filled circles) would remain. This provides a method for analyzing SL

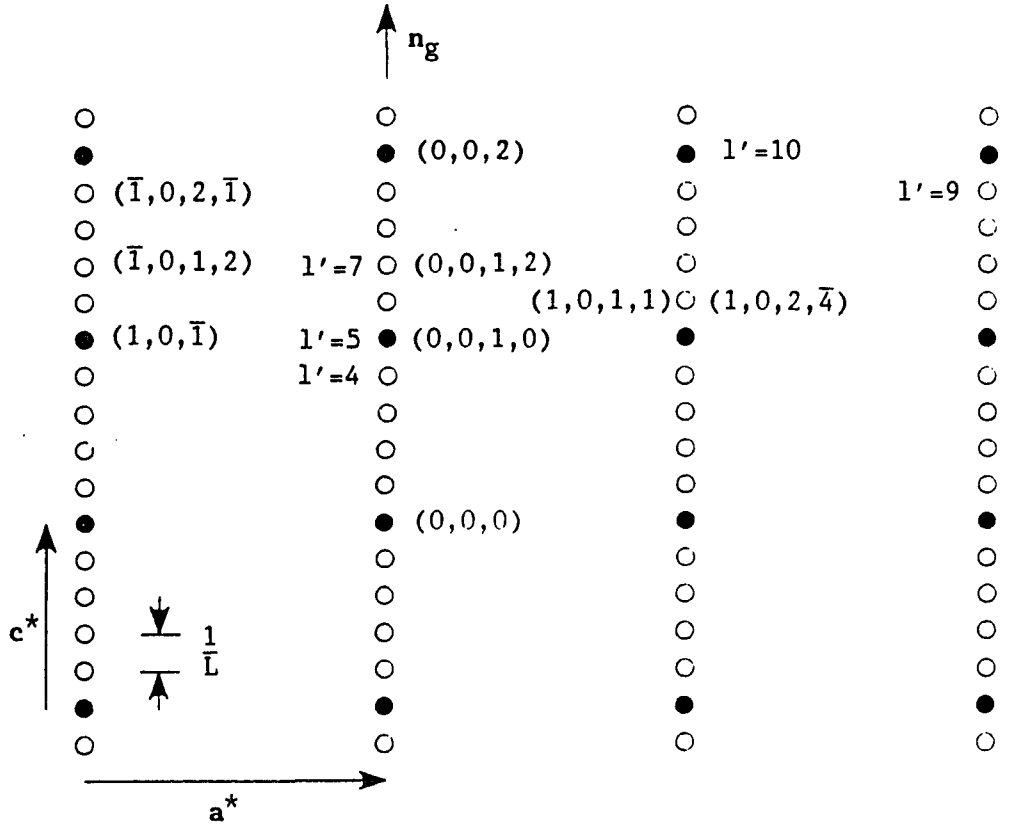

Figure III.1. A two dimensional section of a SL reciprocal space. The growth direction $\mathbf{n}_g$ is directed along the **c** crystallographic axis, which is parallel to the reciprocal lattice vector **c***. The reciprocal lattice vector **a*** is perpendicular to **c*** for this example and **b*** is directed into the page. The filled and open circles correspond to the central and satellite reflections, respectively. Three index schemes are shown: (h,k,l), (h,k,l,m), and l′. The l′ varies along the growth direction only. Notice that the (1,0,1,1) satellite peak is equivalently indexed as (1,0,2,-4). There are five constituent unit cells per SL period for this example

diffusion, which is discussed in Chapter V.

B. The Superlattice Structure Factor: Step Model

Once the distribution of atoms within the unit cell is known, the structure factor is computed using equation II.47. For simplicity, the structure factor of an ideal SL is derived. This is known as the step model in the literature, which assumes abrupt and coherent constituent interfaces (McWhan, Gurvitch, Rowell & Walker, 1983). The step model has been applied to experimental observations with much success (Vandenberg, Hamm, Macrander, Panish & Temkin, 1986; Vandenberg, Bean, Hamm & Hull, 1988) and demonstrates the essential structure factor features present in any crystalline SL.

Figure III.2 illustrates the step model and introduces the essential terminology. The subscripts 1 and 2 distinguish between the two constituent materials. The SL unit cell consists of N constituent cells stacked along the growth direction $\mathbf{n}_g$. There are $n_1+n_2=N$ constituent unit cells per period. $\mathbf{n}_g$ is directed along [0,0,1] in both materials so that equations III.2a and III.2b are valid.

The position vector $\mathbf{r}_j$ of equation II.47 can be decomposed into two vectors; the first vector, which is parallel to $\mathbf{n}_g$, locates a particular constituent unit cell origin with respect to the SL unit cell origin and the second vector $\mathbf{r'}_i$ locates an individual atom with respect to the constituent lattice origin. This is illustrated in Figure III.2. The individual constituent unit cell vectors are defined according to equation II.2,

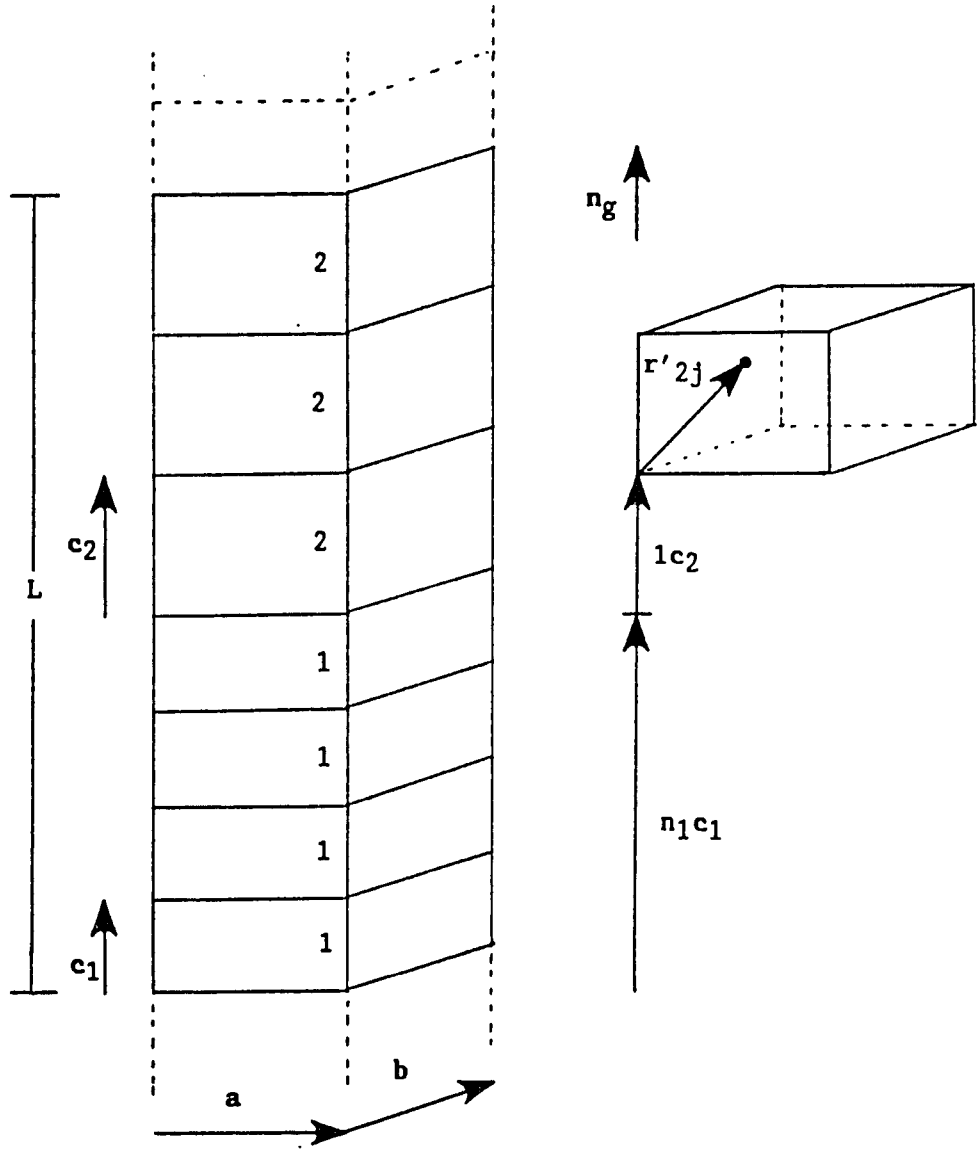

Figure III.2. A schematic representation of the step model. The left illustration depicts the stacking of constituent cells having lattice vectors c_1 and c_2. The in plane unit cell lattice vectors **a** and **b** are common between constituents. The right illustration shows the decomposition of the SL position vector into a component along the growth direction n_g and a constituent cell position vector r'_{2j}

$$r'_{1j} = u_{1j}\mathbf{a} + v_{1j}\mathbf{b} + w_{1j}c_1 \quad , \quad 1 \leq j \leq t_1 \quad , \qquad \text{(III.10a)}$$

$$r'_{2j} = u_{2j}\mathbf{a} + v_{2j}\mathbf{b} + w_{2j}c_1 \quad , \quad 1 \leq j \leq t_2 \quad , \qquad \text{(III.10b)}$$

where u, v and w are the fractional coordinates of the atomic positions within the constituent material, **a**, **b**, and **c** are the constituent lattice vectors, and t_1 and t_2 are the number of atoms within each constituent unit cell. By decomposing r_j, the structure factor expression, equation II.47, can be segregated into terms involving only one constituent,

$$F(\mathbf{q}) = \sum_{j=0}^{T_N} f_j e^{-M_j} e^{-i\mathbf{q}\cdot r_j} \quad , \qquad \text{(III.11a)}$$

$$= \left[\sum_{s=0}^{n_1-1} e^{-i\mathbf{q}\cdot c_1 s}\right]\left[\sum_{t=1}^{t_1} f_{1,t} e^{-M_{1,t}} e^{-i\mathbf{q}\cdot r'_{1t}}\right]$$

$$+ e^{-i\mathbf{q}\cdot c_1 n_1}\left[\sum_{s=0}^{n_2-1} e^{-i\mathbf{q}\cdot c_2 s}\right]\left[\sum_{t=1}^{t_2} f_{2,t} e^{-M_{2,t}} e^{-i\mathbf{q}\cdot r'_{2t}}\right] \quad , \qquad \text{(III.11b)}$$

where $T_N = n_1 t_1 + n_2 t_2$ is the total number of atoms in the SL unit cell, c_1 and c_2 are the constituent lattice parameters along the growth direction, $f_{1,t}$ and $f_{2,t}$ are the atomic scattering factors of the atoms within constituent one and two, respectively, and $M_{1,t}$ and $M_{2,t}$ are the associated Debye-Waller factors of atom t in constituents one and two. The first line of equation III.11b represents the structure factor summation over the first constituent material. The second line concludes the structure factor summation over the second constituent material. The additional exponential factor in the second line of

equation III.11b accounts for the vector component common to all position vectors terminating inside the second constituent lattice. The summations over t represent the structure factors of the individual constituent unit cells. Representing these individual structure factors as $F_1(\mathbf{q})$ and $F_2(\mathbf{q})$, equation III.11b is written,

$$F(\mathbf{q}) = \left[\sum_{s=0}^{n_1-1} e^{-i\mathbf{q}\cdot\mathbf{c}_1 s}\right] F_1(\mathbf{q}) + e^{-i\mathbf{q}\cdot\mathbf{c}_1 n_1}\left[\sum_{s=0}^{n_2-1} e^{-i\mathbf{q}\cdot\mathbf{c}_2 s}\right] F_2(\mathbf{q}) \quad . \quad \text{(III.12)}$$

The summations of equation III.12 are geometric progressions that can be alternatively expressed using equation II.20a, repeated below with the current notation:

$$J(\mathbf{q}\cdot\mathbf{c}_j, n_j) = \sum_{s=0}^{n_j-1} e^{-i\mathbf{q}\cdot\mathbf{c}_j s} = e^{-i\phi_j}\left[\frac{\sin(n_j \Psi_j)}{\sin(\Psi_j)}\right] \quad , \quad \text{(III.13a)}$$

$$\phi_j = \frac{(n_j-1)\mathbf{q}\cdot\mathbf{c}_j}{2} \quad , \quad \text{(III.13b)}$$

$$\Psi_j = \frac{1}{2}\mathbf{q}\cdot\mathbf{c}_j \quad . \quad \text{(III.13c)}$$

Finally, representing the summations of equation III.12b by $J(\mathbf{q}\cdot\mathbf{c}_j, n_j)$ and expressing $\mathbf{c}_1$ and $\mathbf{c}_2$ in terms of $\mathbf{n}_g$, the step model structure factor is compactly written,

$$F(\mathbf{q}) = J(\mathbf{q}\cdot\mathbf{n}_g c_1, n_1)F_1(\mathbf{q}) + e^{-i\mathbf{q}\cdot\mathbf{n}_g c_1 n_1} J(\mathbf{q}\cdot\mathbf{n}_g c_2, n_2)F_2(\mathbf{q}) \quad . \quad \text{(III.14)}$$

Equation III.14 is easily adaptable to a computer algorithm and can be fit to measured intensities. The two terms of equation III.14 result from the two distinct constituent regions of the SL unit cell that are

separated by an interface perpendicular to $\mathbf{n}_g$. This provides a general prescription to determine the structure factor for a unit cell that is separated into an arbitrary number of regions having interfaces perpendicular to $\mathbf{n}_g$. For example, a strained layer SL, which is composed of two constituent lattices having significantly different lattice parameters along $\mathbf{n}_g$, might have a third buffer region that slightly relaxes the lattice parameter mismatch between the two constituents. The structure factor for this situation would have three terms, the third term having a form similar to the second term of equation III.14. Although the step model assumptions are ideal, experimental comparisons to this model provides some measure of the SL quality.

The continuous structure factor distribution is not experimentally observable. Only the scattering vectors that satisfy the Bragg condition allow the SL unit cells to constructively interfere and diffract an appreciable intensity. As discussed in section II.D, this follows by considering the total scattered amplitude from all unit cells. Ignoring the common phase factors and the inverse radial distance dependence of the scattered radiation, the total scattered amplitude is proportional to $A(\mathbf{q})$, where

$$A(\mathbf{q}) = \sum_{j=0}^{N_T} e^{-i\mathbf{q}\cdot(L\mathbf{n}_g)j} F(\mathbf{q}) = J_{SL}(\mathbf{q}\cdot\mathbf{n}_g L, N_T)\ F(\mathbf{q}) \quad , \qquad \text{(III.15)}$$

N_T is the total number of coherently diffracting unit cells, and $F(\mathbf{q})$ is the SL structure factor. $J_{SL}(\mathbf{q}\cdot\mathbf{n}_g L, N_T)$ determines the SL peak position and is principally maximum when

$$\mathbf{q}\cdot(L\mathbf{n}_g) = 2\pi l' \quad , \quad |J_{SL}(2\pi l', N_T)| = N_T \quad . \qquad \text{(III.16)}$$

This is precisely Bragg's law, which was derived from lattice vector considerations in section III.A (see equation III.6). Using equations III.8 and III.2b, the Bragg law requirement becomes,

$$\mathbf{q}\cdot\mathbf{n}_g = 2\pi\left[l + \frac{m}{N}\right]\frac{1}{\langle c\rangle} \quad , \qquad \text{(III.18)}$$

where l is the Miller index along the the growth direction, m is the satellite index, and <c> is the average constituent lattice parameter along $\mathbf{n}_g$. Equation III.18 associates all allowed $\mathbf{q}\cdot\mathbf{n}_g$ values to an (l,m) peak index. The diffraction spectrum of a step SL is completely determined by equations III.14 and III.18.

Several general aspects of the step model are understood by reviewing the behavior of each term in equation III.14. The constituent structure factor $F_j(\mathbf{q})$ was discussed in section II.F. Figures III.3 and III.4 show $|F(\mathbf{q})|$ for the zincblende unit cell having a scattering vector directed along the [0,0,1] and [1,1,1] crystallographic directions, respectively. The general form of $F_j(\mathbf{q})$ depends on the direction of $\mathbf{q}$. Interference from the (0,0,1) and (1,1,1) atomic planes are responsible for the [0,0,1] and [1,1,1] structure factor behavior. The decrease in atomic scattering efficiency for increasing $|\mathbf{q}|$ is responsible for the decreasing trend of the structure factor amplitude. The structure factor extrema are summarized by equations II.41a-c, which depend both on the atoms that occupy the A and B zincblende sites and on the the scattering vector. The relevant extrema of $|F(\mathbf{q})|$ have four

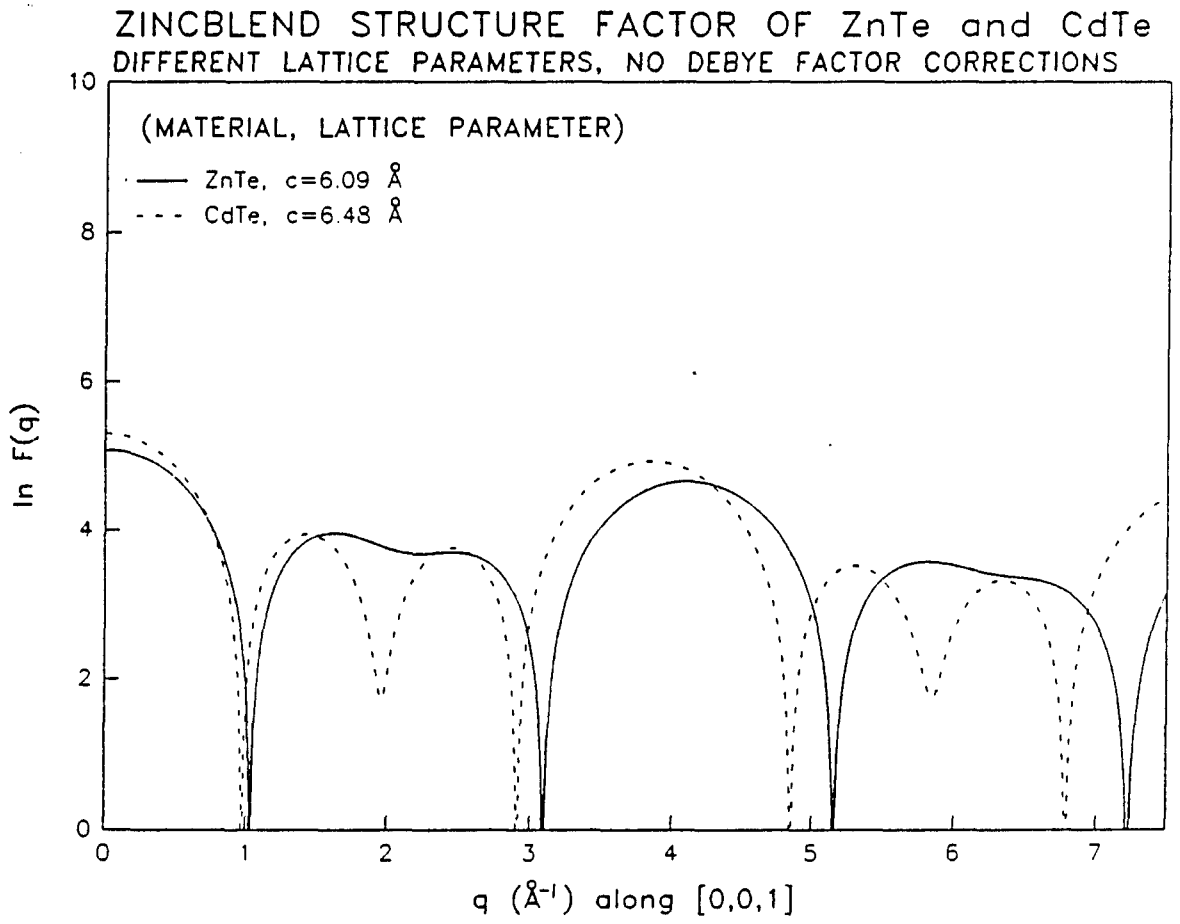

Figure III.3. The zincblende constituent cell structure factor evaluated along the [0,0,1] crystallographic direction for ZnTe and CdTe. The $\log_e$ of the structure factor modulus (equation II.39) is plotted as a function of $q=(4\pi\sin\theta)/\lambda$, where θ is the one-half of the scattering angle and λ is the radiation wavelength. The Debye-Waller thermal factors are set to zero. The bulk crystal cubic cell sizes are used in the calculation, 6.09 Å for ZnTe and 6.48 Å for CdTe. Equation II.38 is used to compute individual atomic scattering factors. Anomalous dispersion at 1.47639 Å is included in the calculation

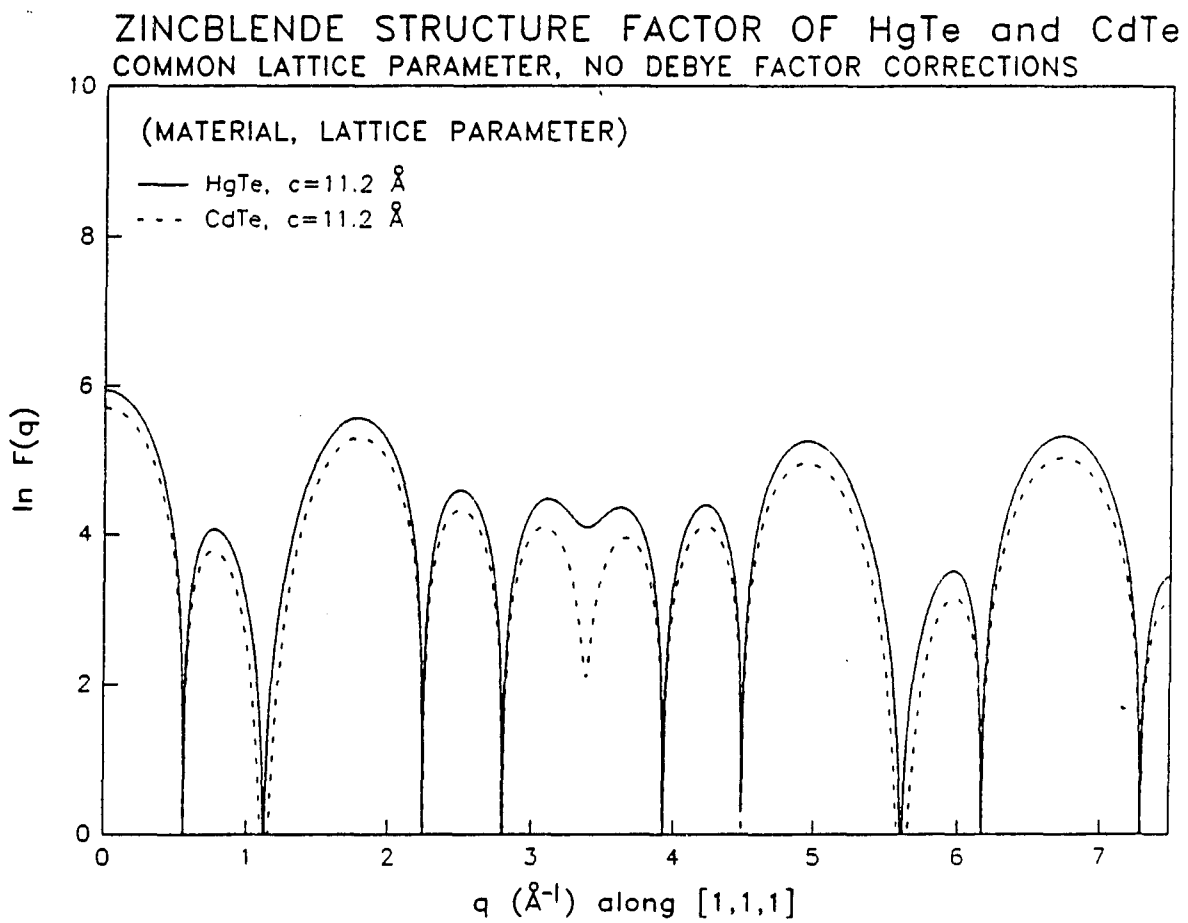

Figure III.4. The zincblende constituent cell structure factor evaluated along the [1,1,1] crystallographic direction for HgTe and CdTe. The $\log_e$ of the structure factor modulus (equation II.39) is plotted as a function of $q=(4\pi\sin\theta)/\lambda$, where θ is the one-half of the scattering angle and λ is the radiation wavelength. The Debye-Waller thermal factors are set to zero. A common 11.2 Å cell length along the c hexagonal axis is used for both materials (11.2 Å is the body diagonal length of a cube having a side length of 6.466 Å). Equation II.38 is used to compute individual atomic scattering factors. Anomalous dispersion at 1.28181 Å is included in the calculation

characteristic forms: $(f_A+f_B)^2$, $(f_A^2+f_B^2)$, $(f_A-f_B)^2$, and 0. These forms are responsible for the relative differences between HgTe, CdTe, and ZnTe that are observed in Figures III.3 and III.4. The unit cell dimensions determine the extremum positions. Referring to the atomic plane view associated with the [0,0,1] and [1,1,1] zincblende directions, a smaller plane separation requires larger scattering angles to accomplish the same resultant phase difference from planes spaced further apart. Since **q** is proportional to sinΘ, the extrema positions of large unit cells are located at smaller **q** values, compared to small cells. This is observed in Figure III.3; the smaller lattice parameter of ZnTe expands all structure factor features, compared to the larger lattice parameter of CdTe.

In addition to the constituent structure factors, equation III.14 depends on the geometrical progression factors $J(\mathbf{q}\cdot\mathbf{n}_g c_1, n_1)$ and $J(\mathbf{q}\cdot\mathbf{n}_g c_2, n_2)$, which are periodic functions of **q**. The principal maximum positions are determined by

$$\mathbf{q}\cdot\mathbf{n}_g = \frac{2\pi l}{c_j} \quad , \quad |J(2\pi l, n_j)| = n_j \quad , \qquad \text{(III.19)}$$

where l is the Miller index that corresponds to the unit cell length c_j along $\mathbf{n}_g$. The principal peak width depend on the total length of the diffracting constituent region and is related to the **q** difference between principal maxima and adjacent minimum,

$$\Delta\mathbf{q}\cdot\mathbf{n}_g = \frac{\pi}{n_j c_j} \quad , \qquad \text{(III.20)}$$

where $n_j c_j$ is the total length of the diffracting region along $\mathbf{n}_g$. Figure III.5 shows the form of $|J(\mathbf{q}\cdot\mathbf{n}_j, n_j)|$ for two specific examples.

The constituent structure factor terms of equation III.14 modulate the interference between $J(\mathbf{q}\cdot\mathbf{n}_g c_1, n_1)$ and $J(\mathbf{q}\cdot\mathbf{n}_g c_2, n_2)$. This modulation forms constituent diffraction regions in the total structure factor. These regions are characteristic of all crystalline SLs and do not depend on the validity of the step model. Figures III.6 and III.7 show the square of equation III.14 for the two specific examples introduced above. The constituent diffraction regions are easily identified for these examples. Since both constituent materials have the same constituent unit cell orientation, an (h,k,l) index can be assigned to each region, see Figures III.6 and III.7, provided that the individual lattice parameters along $\mathbf{n}_g$ are not too different.

Only the peak intensity is observed experimentally, which is proportional to $|A(\mathbf{q})|^2$ (see equation III.15). The behavior of $J(\mathbf{q}\cdot\mathbf{n}_g L, N_T)$, which defines the Bragg relationship, is similar to $J(\mathbf{q}\cdot\mathbf{n}_g c_1, n_1)$ and $J(\mathbf{q}\cdot\mathbf{n}_g c_2, n_2)$. However, since N_T is typically much greater than n_1 and n_2, the principal maxima associated with $J(\mathbf{q}\cdot\mathbf{n}_g L, N_T)$ are very narrow. Thus, an appreciable diffracted intensity occurs only for the $\mathbf{q}\cdot\mathbf{n}_g$ defined by equation III.18, and the corresponding intensity is proportional to $|N_T F(\mathbf{q}\cdot\mathbf{n}_g)|^2$. Figures III.8 and III.9 show the SL peak intensities of the diffraction spectrum for the specific examples represented by Figures III.6 and III.7, respectively.

According to equation III.19, the principal maxima of both constituents are coincident for lattice-matched SLs, which have equivalent constituent lattice parameters along $\mathbf{n}_g$. Within any

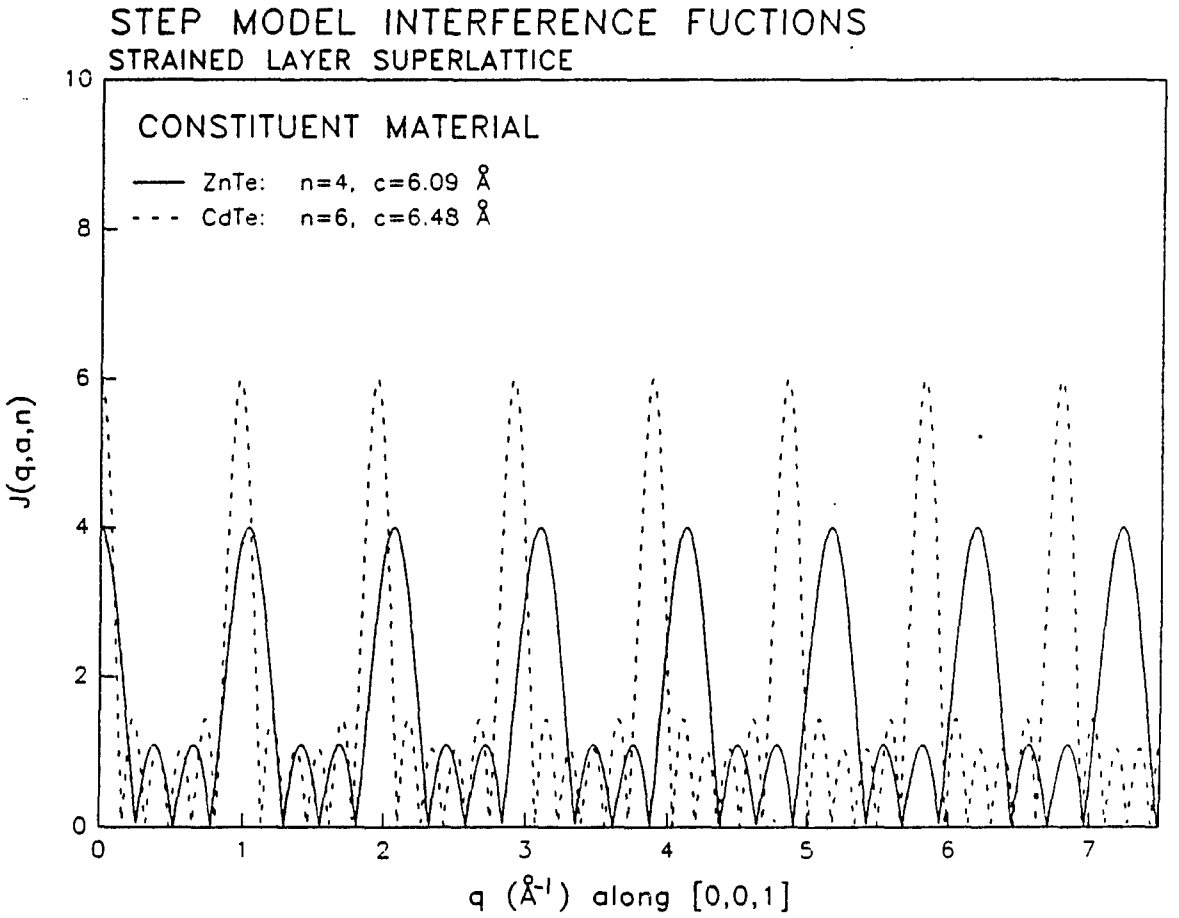

Figure III.5. The step model interference function computed for two specific cases: a summation over four constituent cells having a 6.09 Å length along the scattering vector direction and a summation over six cells of length 6.48 Å. These two examples correspond to bulk ZnTe and CdTe zincblende cubic cells, respectively. The modulus of the interference function along the [0,0,1] crystallographic direction is plotted as a function of $q=(4\pi\sin\theta)/\lambda$, where θ is one-half of the scattering angle and λ=1.47639 Å is the radiation wavelength. Notice that there are N-2 subsidiary maxima, where N is the number of cells summed. The principal maxima of each example are coincident only at zero q

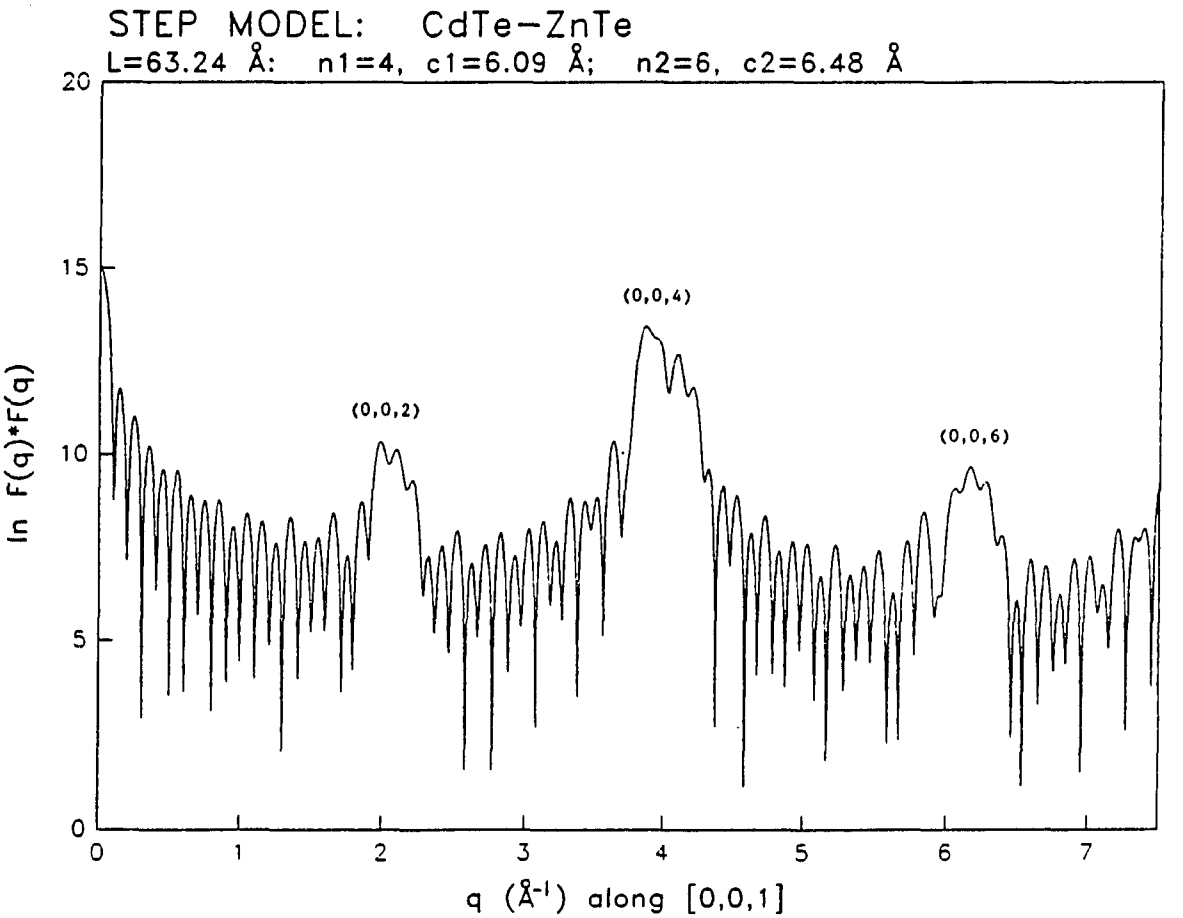

Figure III.6. The [0,0,1] crystallographic component of the step model structure factor for a specific example having four CdTe zincblende cells and six ZnTe cells. The constituent cell structure factors for this example are shown in Figure III.3. The bulk constituent cell sizes are used in the calculation. The $\log_e$ of the structure factor modulus squared is plotted as a function of $q=(4\pi\sin\theta)/\lambda$, where θ is one-half of the scattering angle and $\lambda=1.47639$ Å is the radiation wavelength. The constituent diffraction regions are labeled according to the (h,k,l) reflecting planes. The measured intensity is proportional to $|F(q)|^2$

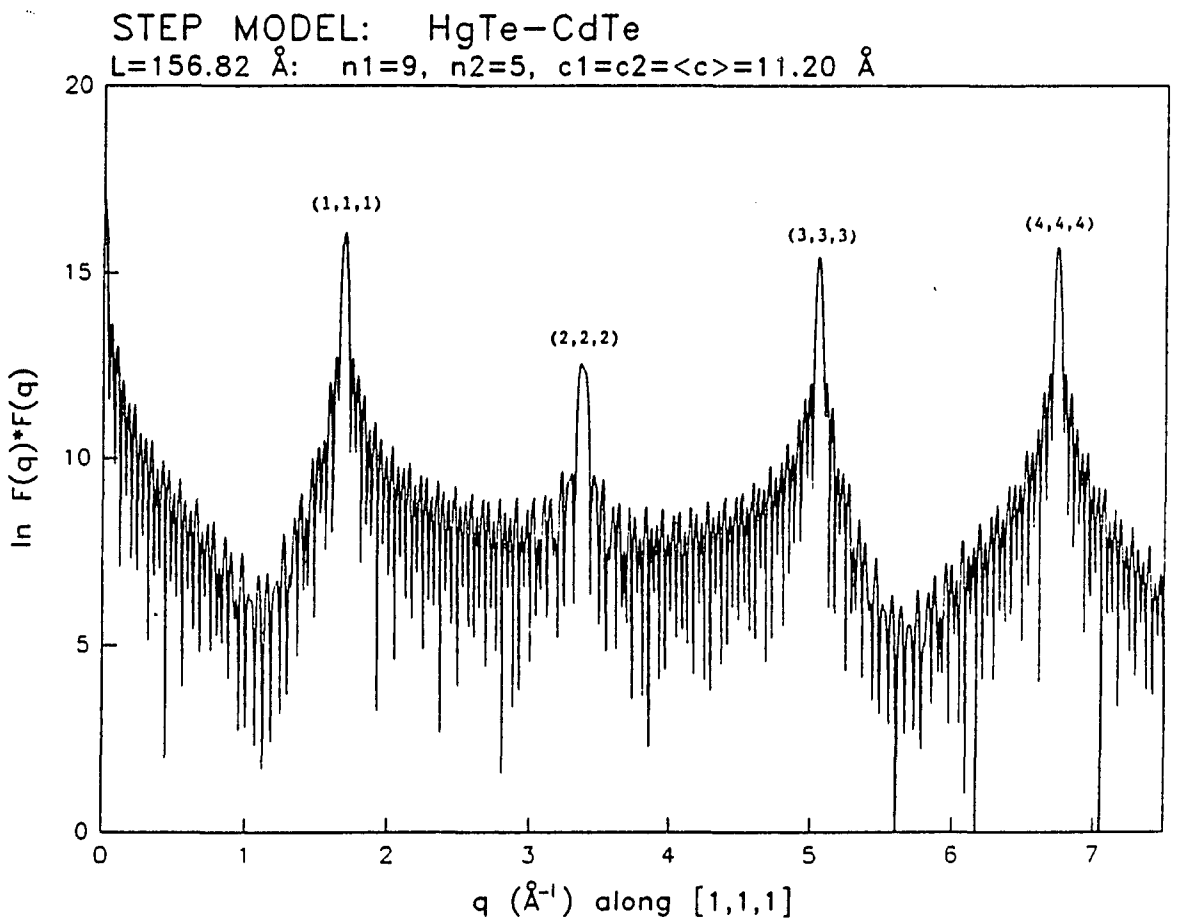

Figure III.7. The [1,1,1] crystallographic component of the step model structure factor for a specific example having nine HgTe zincblende cells and five CdTe cells. The constituent cell structure factors for this example are shown in Figure III.4. A common $|c_{hex}|$ length of 11.2 Å is used for both constituent materials. The $\log_e$ of the structure factor modulus squared is plotted as a function of $q=(4\pi\sin\theta)/\lambda$, where θ is one-half of the scattering angle and $\lambda=1.28181$ Å is the radiation wavelength. The constituent diffraction regions are labeled according to the (h,k,l) reflecting planes. The measured intensity is proportional to $|F(q)|^2$

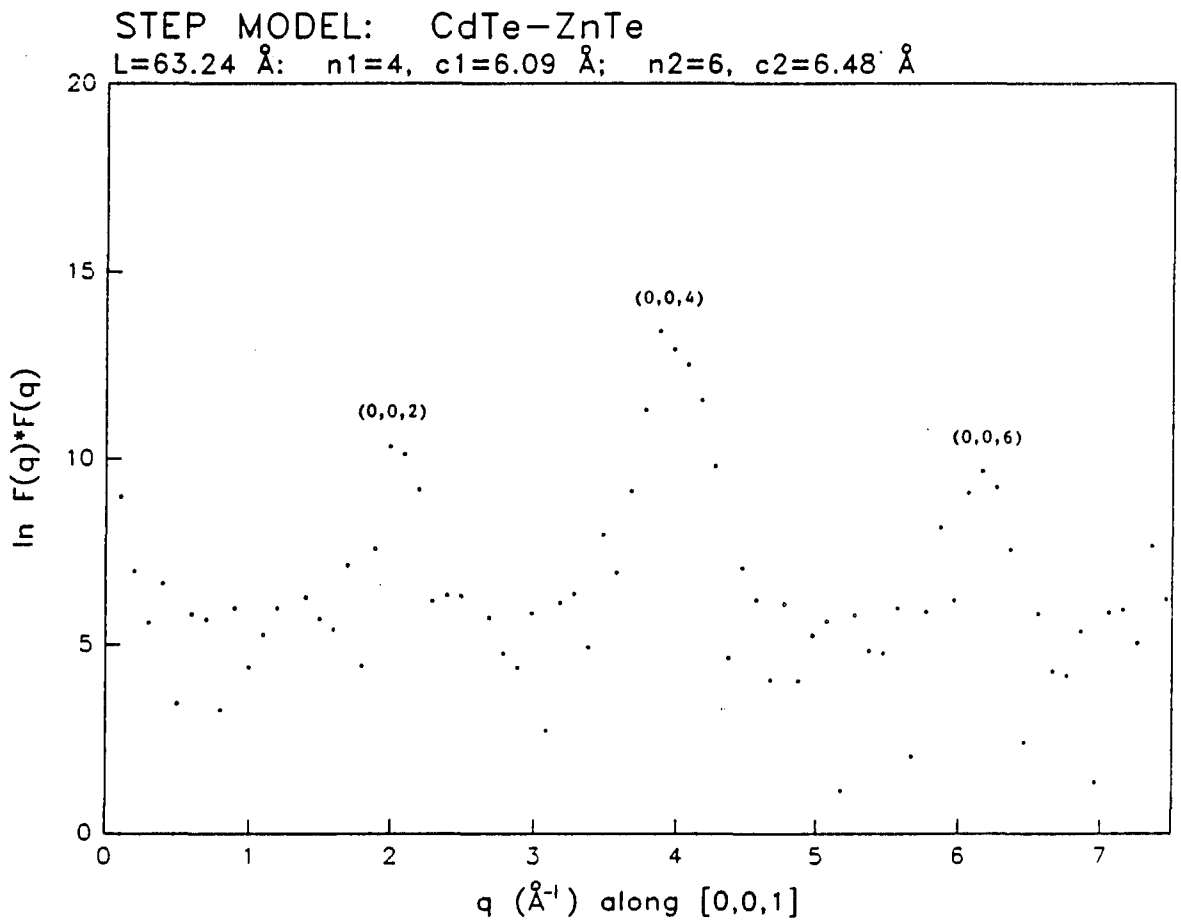

Figure III.8. The step model example of Figure III.6 evaluated at the allowed Bragg scattering vectors, based on an L=63.24 Å SL period. Each dot represents the calculated peak intensity. The constituent diffraction regions are indexed (h,k,l)

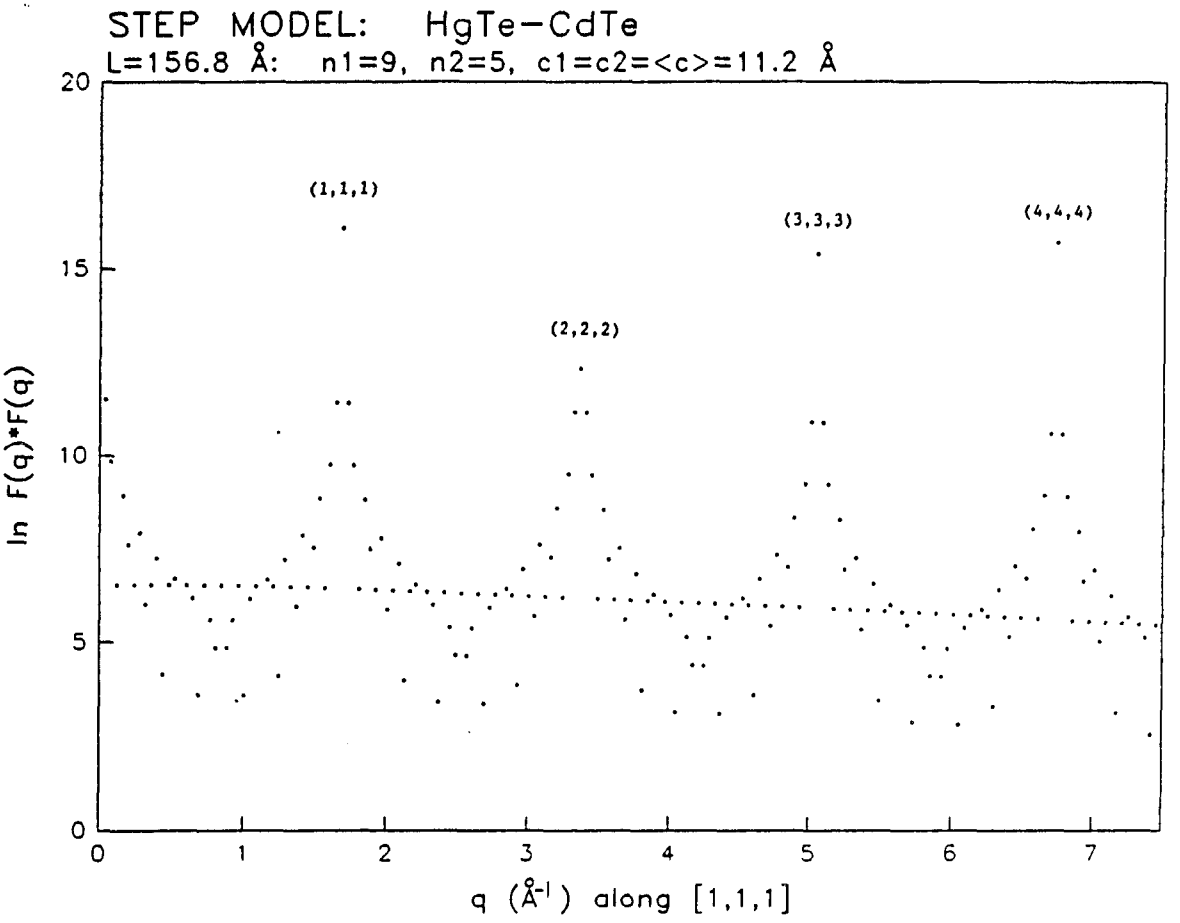

Figure III.9. The step model example of Figure III.7 evaluated at the allowed Bragg scattering vectors, based on an L=156.8 Å SL period. Each dot represents the calculated peak intensity. The constituent diffraction regions are indexed (h,k,l). The larger period, compared to Figure III.8, generates more allowed Bragg reflections per volume in reciprocal space

constituent diffraction region, SL peaks having allowed $\mathbf{q}\cdot\mathbf{n}_g$ values closest to the those defined by equation III.19 are the most intense. Comparing equations III.18 and III.19, these peaks are precisely the central peaks (m=0). Since both $J(\mathbf{q}\cdot\mathbf{n}_g c_1, n_1)$ and $J(\mathbf{q}\cdot\mathbf{n}_g c_2, n_2)$ are symmetrical about any principal maximum (see Figure III.5), their combined interference is symmetrically related about each central peak. In addition, the distribution of intensity among the satellites is essentially preserved in all constituent diffraction regions. This is observed in Figure III.9.

Except for the broad asymmetry resulting from the constituent structure factor terms, only the lattice parameter difference $\Delta c = c_1 - c_2$ affects the satellite symmetry about the central peaks. The number of constituent cells affect the peak amplitude and width of $J_j(\mathbf{q}\cdot\mathbf{n}_g, n_j)$ without altering the symmetry about each principal maximum. As Δc deviates from zero, the central peak intensities decrease. This is best understood with the aid of Figure III.5. According to equation III.19, the principal maxima of both constituent materials are no longer coincident for equal nonzero l. The position difference between the constituent maxima increase linearly with $\mathbf{q}$ and is enhanced by larger $|\Delta c|$. This destroys the symmetry of the satellite intensity distribution about all central peaks that diffract at nonzero $\mathbf{q}$. A loss of symmetry is observed in Figure III.8, compared to the symmetrical distribution of Figure III.9. However, independent of Δc, all SL peak intensities are symmetrically related about the zero order reflection (l=0,m=0). This follows from equation III.19; the l=0 principal maximum of both constituent materials are coincident at zero $\mathbf{q}\cdot\mathbf{n}_g$. Finally, the

satellite intensity distribution within each constituent diffraction region is not preserved for nonzero Δc, which is a consequence of the increasing separation between constituent principal maxima for increasing $\mathbf{q}\cdot\mathbf{n}_g$. This is illustrated in Figures III.8 and III.9. The relative form of the (1,1,1) series of reflections is preserved. The (0,0,1) series of reflections, however, vary in form between constituent regions.

The diffracted intensity dependence on Δc is easily understood with the aid of a simple one dimensional model, illustrated in Figures III.10a and III.10b. This model replaces constituent unit cells with scattering points. Specular scattering from all points is assumed and the amplitude of the scattered radiation depends on $F_j(\mathbf{q})$. The spacing between scattering points represents the constituent lattice parameters along $\mathbf{n}_g$. The small and large filled circles represent the two constituent materials. For reference, the open circles represent the scattering positions of the average lattice spacing $\langle c \rangle$ (see equation III.2a). Diffraction from the one-dimensional lattice depends on the phase difference of radiation scattered at each point. The phase is define to be zero for radiation scattered at the arbitrarily selected origin O. The phase of any point depends both on the radiation wavelength and on the additional path length $A_iB_iC_i=2z\sin\Theta$ that the radiation traverses from scattering a distance z from the origin. The scattered phase, $\phi=2\pi(2z\sin\Theta)/\lambda$, is related to $\mathbf{q}\cdot\mathbf{n}_g$ by $\phi=\mathbf{q}\cdot\mathbf{n}_g z$.

Bragg's law stipulates that the phase difference between any two points separated by the period L must differ by an integral number of 2π radians. This must be satisfied for all central and satellite peaks.

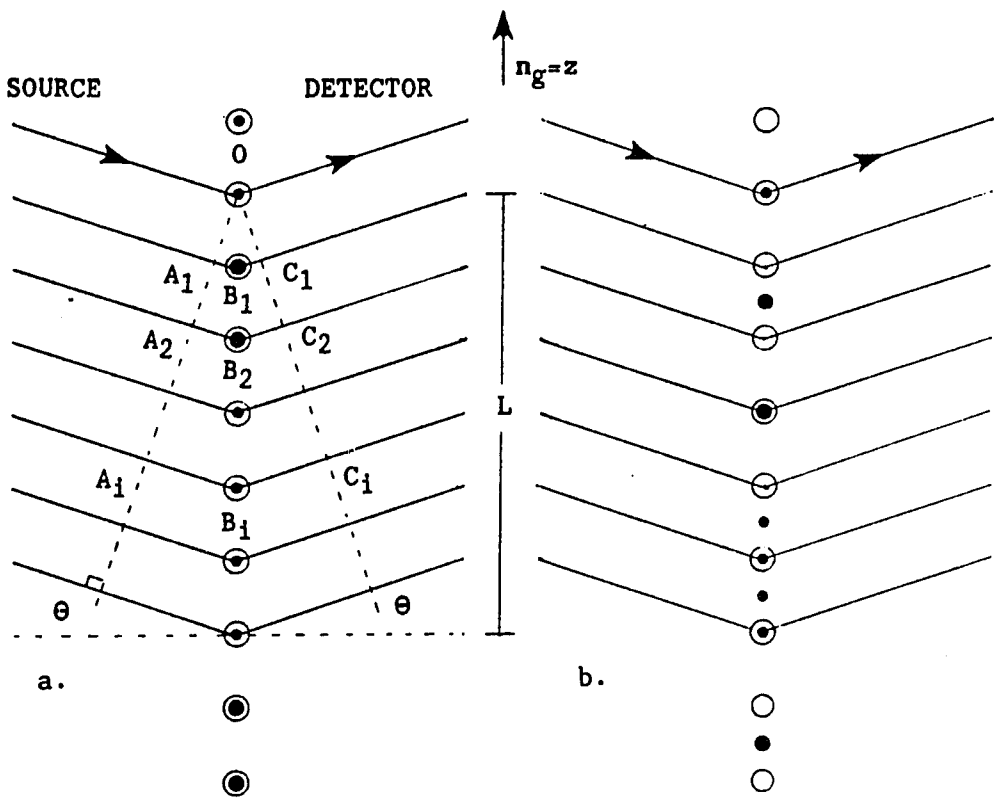

Figure III.10. A one-dimensional analog to diffraction from a series of crystallographic planes perpendicular to n_g. The large and small filled circles represent the two constituent cells of each material. The open circles represent the average constituent cell spacing (equation III.2a). L is the SL period along the growth direction n_g. Parallel plane waves arrive from the source and scatter from the one-dimensional chain. The phase difference, with respect to the arbitrarily selected origin 0, of each scattered ray depends on the additional path length $A_iB_iC_i$. The left illustration (a) corresponds to a lattice-matched SL. The right illustration (b) represents a strained-layer SL, where the lattice spacing changes along the growth direction

According to equation III.9, central peak diffraction requires that the phase at every average lattice point (open circles) is an integer number of 2π radians. However, scattering occurs at the physical scattering centers (filled circles). For a lattice-matched SL, depicted in Figure III.10a, all scattering centers are coincident with the average lattice positions. Since both constituent materials are constructively diffracting, the central peaks are expected to be the most intense within any constituent diffraction region.

Figure III.10b illustrates a strained layer system. The average scattering point positions (open circles) are no longer coincident with the physical scattering points (filled circles). The central peak requirement is unaffected by the strained layer system, however, since there are no physical scattering points located at the average lattice positions, complete constructive interference from both constituents is impossible. A different scattering angle is required to achieve complete constructive interference with each constituent region. This reduces the central peak intensity, compared to a lattice-matched system having the same average lattice spacing. The lattice mismatch destroys constructive scattering from both constituents and disrupts the symmetry of the satellite intensity distribution about the central peaks.

The successful application of the step model to real SL films depends on three fundamental assumptions. First, the interfaces between constituent regions must be abrupt. In general, the molecular beam deposition techniques satisfy this requirement. However, atomic diffusion can destroy the abrupt interface quality. This degrades the square-well composition profile required by the step model. A more

general approach to this problem, which is applicable to arbitrary composition profiles, is discussed in the next section.

Second, the reproducibility of the SL period during film deposition is assumed precise. This assumption is founded in equation III.15. Realistically, slight changes in the growth conditions during the film deposition can introduce deviations in the modulated period. These deviations, which can affect three-dimensional integrity of the SL, prevent the application of equation III.15. By assuming a specific form of the period deviations, certain characteristics of the diffraction spectrum can be predicted and compared with experiment. For example, one-dimensional fluctuations along n_g described by a Gaussian distribution reduce the intensity of high order SL peaks. This intensity reduction has a form similar to the Debye-Waller factor (McWhan, 1985; Clemens & Gay, 1986). Cumulative deviations affect both the peak intensity and breadth as a function of scattering angle (Sevenhans, Gijs & Bruynseraede, 1986). Lateral interface roughness also affects the peak intensities and breadths (Chrzan & Dutta, 1985). Comparisons between the step model theory and experiment provide some insight into these effects.

Third, the growth direction is assumed parallel to both c_1 and c_2. This is a fairly safe assumption since the growth temperature is high enough to allow freshly deposited atoms to migrate uniformly across growth domains or islands. However, physical placement of the constituent effusion cells can promote an inhomogeneous film thickness across the sample surface and produce nonparallel growth. X-ray diffraction can detect nonparallel growth by comparing satellite and

central peak positions. This phenomena is discussed in section III.D.

C. Diffraction from Arbitrary One Dimensional Periodic Structures

The investigation of SL stability, interdiffusion in particular, requires a general structure factor model which relates the diffracted intensity distribution to the chemical composition profile. A particular model is developed by considering the anticipated structural changes associated with the atomic migration. Since the SLs of this research investigation are composed of stable zincblende constituents having the same crystallographic orientation and, at most, a 6.2% maximum lattice parameter mismatch, no spontaneous phase transformations are anticipated. Ideally, the constituent atoms are expected to occupy the zincblende (diamond) lattice sites. However, both the lattice spacing and site occupation within the SL unit cell vary according to the composition modulation.

The SL structure factor establishes the relationship between the x-ray diffraction spectrum and the chemical composition profile. Equation II.47 provides the general structure factor definition, which must be adapted to the SL system,

$$F_S(\mathbf{q}) = \sum_{j=0}^{T_N-1} f_j'(\mathbf{q}) e^{-i\mathbf{q}\cdot\mathbf{r}_j} \quad , \qquad \text{(III.21a)}$$

$$f_j'(\mathbf{q}) = f_j(\mathbf{q}) e^{-M_j} \quad , \qquad \text{(III.21b)}$$

where $\mathbf{r}_j$ is the SL position vector, T_N is the total number of atoms that compose the SL unit cell, and $f_j'(\mathbf{q})$ compactly represents both the

atomic scattering factor and associated Debye-Waller factor. The SL growth direction n_g is assumed coincident with the [0,0,1] crystallographic axis, which is common to both constituent lattices. This is not a restrictive assumption since [1,1,1] cubic SL growth can be expressed as [0,0,1] hexagonal growth (see section III.A). The chemical composition profile is investigated by aligning the diffraction scattering vector with the growth direction. Restricting the scattering vector to the [0,0,1] crystallographic direction, equation III.21a becomes,

$$F_S(q) = \sum_{j=0}^{T_N-1} f_j'(q)e^{-iqc_j} \quad , \qquad \text{(III.22)}$$

where q is the magnitude of $q=qn_g$, and c_j is the position of the j^{th} atom along the [0,0,1] crystallographic axis. If no phase changes occur, the tetrahedral bonding arrangement of the zincblende lattice is maintained throughout the SL, with the atom occupation and bond length varying periodically along n_g. Although these variations prevent the reference to constituent zincblende cells, the general zincblende characteristics can be incorporated into equation III.22.

Two FCC sublattices compose the zincblende lattice and segregate the atomic species by column on the periodic chart (see section II.B). This is a consequence of the tetrahedral bonding exhibited by the constituent atoms. The chemical composition of a SL must be derived from the two constituent materials, A_1B_1 and A_2B_2, where A and B represent columns on the periodic chart. Only A_i atoms occupy the A FCC sublattice and the B_i atoms occupy the B sublattice (see Table II.1). Along the [0,0,1]

axis, site occupation alternates between A and B type atoms. The structure between like atom types repeats, establishing a two atom basis that can be incorporated into equation III.22. Representing the repeat length as r_j for the j^{th} A-B atom basis, equation III.22 is written,

$$F_S(q) = \sum_{j=0}^{N_p-1} F'(A_j,B_j,\Delta_j,q)e^{-iqr_j} \quad , \qquad \text{(III.23a)}$$

$$F'(A_j,B_j,\Delta_j,q) = n_A f'(A_j,q) + e^{-iq\Delta_j w} n_B f'(B_j,q) \quad , \qquad \text{(III.23b)}$$

where $f'(A_j,q)$ and $f'(B_j,q)$ represent the atomic scattering factors and associated Debye-Waller factors of the A and B type atoms located at a distance r_j from the SL unit cell origin along [0,0,1], w is the fractional coordinate of the second atom, $\Delta_j=r_{j+1}-r_j$ is the basis length, n_A and n_B are the number of atoms located at r_j, and N_p is the number of two atom bases composing the SL unit cell. $F'(A_j,B_j,\Delta_j,q)$ represents the structure factor for the two atom basis, which is analogous to the constituent structure factor expression defined by equation II.47. If the SL is grown by stacking cubic zincblende unit cells, Δ_j represents one-half of the constituent cell length along the $[0,0,1]_{cub}$ axis, w is one-half, atoms of the same type are located at each r_j, and $n_A=n_B=2$. If the SL is grown by stacking hexagonal zincblende cells, Δ_j is one-third of the cell length along the $[0,0,1]_{hex}$ axis, w is one-fourth, one atom is located at each Δ_j, and $n_A=n_B=1$. These two special cases, which represent all SLs of this research investigation, are illustrated in Figure III.11. Since the scattering vector is parallel to the growth direction, the lateral atom

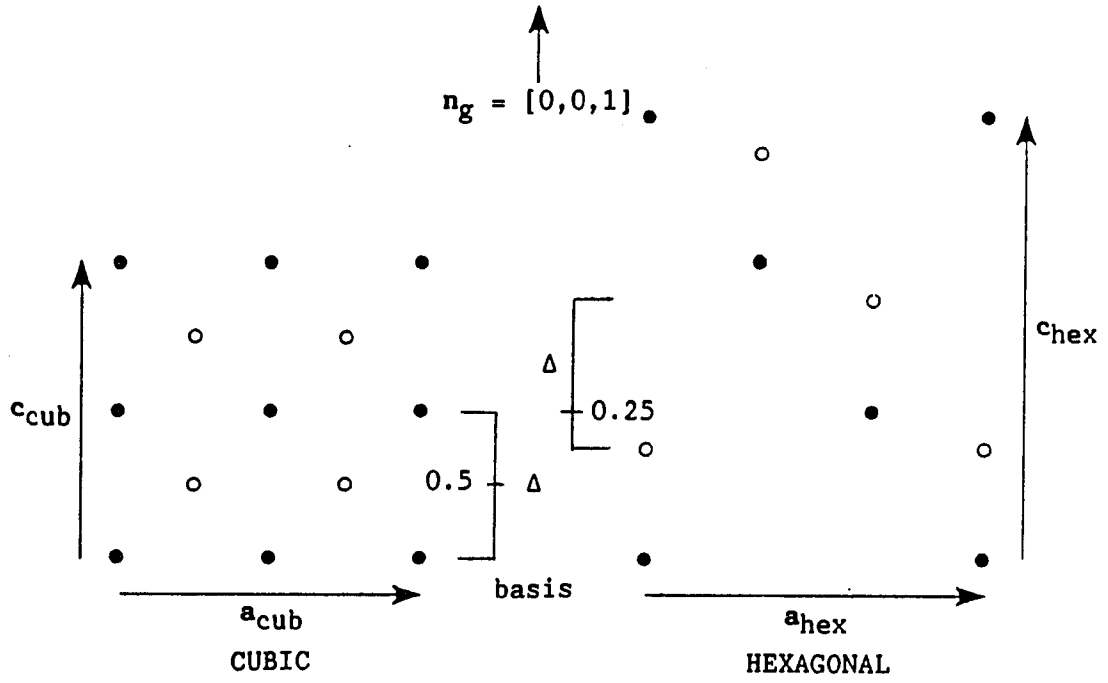

Figure III.11. Side view of the cubic (left) and hexagonal (right) zincblende unit cell. The filled and open circles distinguish the A and B atomic species. The growth direction (n_g) is parallel to the c crystallographic axis. For scattering vectors parallel to n_g, only the atom positions along the c crystallographic axis affect the phase of scattered radiation. Ignoring atom positions along the a and b axes, the zincblende structure repeats twice within the cubic cell and three times within the hexagonal cell. Thus, for n_g along c, the constituent cells are reduced to a smaller one-dimensional basis, designated Δ, which is one-half of |c| in the cubic cell and one-third of |c| in the hexagonal cell. Both subdivisions contain both atom species, one located at the basis origin, and the other located at one-half the basis length in the cubic cell and one-fourth the basis length in the hexagonal cell

distribution (the horizontal axis in Figure III.11) does not affect the structure factor--only the atom spacing and site occupation along the growth direction is relevant to following discussion, allowing the use of a two atom basis. Both the basis structure factor and basis length both depend on the composition along the growth direction within the SL unit cell and can be explicitly related to the concentration of constituent elements.

The chemical composition is mathematically described by a concentration function. This function specifies the concentration of one constituent material relative to the other and depends only on the component $r_j \cdot n_g = r_j$. The composition function $C_k(r_j)$ defines the probability that the atom pair located at r_j is associated with the k^{th} constituent material (k=1,2). Assuming that neither vacancy nor interstitial defects occur, the presence of one constituent atom at a particular position precludes the existence of the other constituent atom at that same location,

$$C_2(r_j) = 1 - C_1(r_j) \quad . \tag{III.24a}$$

In addition, the concentration functions must preserve the SL period L,

$$0 \leq C_k(r_j) = C_k(r_j+L) \leq 1 \quad . \tag{III.24b}$$

Ideally, $C_k(r_j)$ is either one or zero, with the same position in other SL unit cells having the same concentration value. However, SL interdiffusion disrupts this simple scenario. Atomic migration is

governed by a tunneling probability, which introduces variations in site occupation among SL unit cells. These variations are incorporated into the concentration functions by defining $C_k(r_j)$ as the statistical occupation probability over many SL unit cells. This definition is consistent with the x-ray diffraction analysis, which characterizes the collective diffraction of many SL unit cells inside the irradiated volume.

Relating concentration dependent parameters of equation III.23a to their average value aids the interpretation of the SL structure factor. The average basis length $\langle\Delta\rangle$, averaged over the SL period L, provides a consistent incremental reference for the summation of equation III.23a. Expressed in terms of $\langle\Delta\rangle$, the distance from the SL unit cell origin to the j^{th} atom pair is written,

$$r_j = j\langle\Delta\rangle + \delta_j \quad , \tag{III.25}$$

where δ_j represents the deviation from the average basis position $j\langle\Delta\rangle$. Using equation III.25, the j^{th} basis length is expressed in terms of δ_i,

$$\Delta_j = r_{j+1} - r_j = \langle\Delta\rangle + [\delta_{j+1} - \delta_j] \quad . \tag{III.26}$$

The dimensionless ratio $[\delta_{max}-\delta_{min}]/\langle\Delta\rangle$ is related to the size mismatch of the constituent cells. The mismatch between bulk values represents the upper limit to this ratio, which is 0.063 for CdTe-ZnTe SLs and 0.003 for HgTe-CdTe. The amplitude of basis length variations depends on the amount of lattice relaxation.

Position deviations from the average basis sites are expected to be linearly related to concentration deviations from the average chemical concentration for a small constituent cell mismatch. This relationship is based on Vegard's law (Cullity, 1978). Relating the basis position r_j to the chemical concentration evaluated at $j\langle\Delta\rangle$, equation III.25 becomes,

$$r_j = j\langle\Delta\rangle + \gamma_k\Gamma_k(j\langle\Delta\rangle) \quad , \tag{III.27a}$$

$$\Gamma(r_j) = C_k(r_j) - \langle C_k\rangle \quad , \tag{III.27b}$$

where γ_k relates the basis position response to the chemical composition, and the average chemical concentration $\langle C_k\rangle$ represents an average over one SL period L. If the average chemical composition occupies the j^{th} basis, $\Gamma_k(j\langle\Delta\rangle)$ is zero and r_j is the average basis position $j\langle\Delta\rangle$. The k subscript on both γ and Γ emphasize the equivalence of basing δ on either constituent concentration. However, the basis position length r_j must not depend on the constituent concentration reference,

$$\gamma_1\Gamma_1(r_j) = \gamma_2\Gamma_2(r_j) \quad . \tag{III.28}$$

According to equation III.27a, the basis length Δ_j also depends on $\Gamma_k(r_j)$,

$$\Delta_j = \langle\Delta\rangle + \gamma_k\{\Gamma_k[(j+1)\langle\Delta\rangle] - \Gamma_k[j\langle\Delta\rangle]\} \quad . \tag{III.29}$$

Analogous to equation III.27a, the atomic scattering functions $f'(A_j,q)$ and $f'(B_j,q)$ of equation III.23b are related to $\Gamma_k(r_j)$.

$$f'(A_j,q) = \langle f'_A(q)\rangle + \alpha_k\Gamma_k(j\langle\Delta\rangle) \quad , \tag{III.30a}$$

$$f'(B_j,q) = \langle f'_B(q)\rangle + \beta_k\Gamma_k(j\langle\Delta\rangle) \quad , \tag{III.30b}$$

where α_k and β_k relate the statistical atom occupation to the chemical concentration of constituent k. Equation III.28 must apply equally to both α_k and β_k,

$$\alpha_1\Gamma_1(r_j) = \alpha_2\Gamma_2(r_j) \quad , \tag{III.31a}$$

$$\beta_1\Gamma_1(r_j) = \beta_2\Gamma_2(r_j) \quad . \tag{III.31b}$$

Since the concentration of both constituent materials are related by equation III.23, the constituent subscript k will not be written unless reference to a specific constituent is required.

The SL structure factor, equation III.23a, can be explicitly related to $\Gamma(r_j)$. Equations III.27a, III.29, III.30a, and III.30b relate the basis position r_j, the basis length Δ_j, and atomic scattering functions $f'(A_j,q)$ and $f'(B_j,q)$ to deviations from the average chemical concentration $\Gamma(r_j)$. Since the basis positions are expected to deviate only slightly from their average positions ($\delta<0.06$), the exponential terms involving $\gamma\Gamma(r_j)$ can be approximated by a linear expression,

$$e^{-iq[a+\gamma\Gamma(r_j)]} \simeq e^{-iqa}[1-iq\gamma\Gamma(r_j)] \quad , \qquad \text{(III.32)}$$

where a is constant larger than $\gamma\Gamma(r_j)$. Applying this approximation and retaining terms to first order in $\gamma\Gamma(r_j)$, the one-dimensional SL structure factor is written,

$$\begin{aligned} F_S(q) \simeq & \langle F' \rangle \sum_{j=0}^{N_p-1} [1-iq\gamma\Gamma(j\langle\Delta\rangle)]e^{-iqj\langle\Delta\rangle} + \\ & \langle F' \rangle \delta F' \sum_{j=0}^{N_p-1} \Gamma(j\langle\Delta\rangle)e^{-iqj\langle\Delta\rangle} + \\ & \langle F' \rangle(-iqw\gamma)e^{-iqw\langle\Delta\rangle} \sum_{j=0}^{N_p-1} \{\Gamma[(j+1)\langle\Delta\rangle]-\Gamma[j\langle\Delta\rangle]\}e^{-iqj\langle\Delta\rangle} \quad , \qquad \text{(III.33a)} \end{aligned}$$

$$\langle F' \rangle = n_A\langle f'_A(q)\rangle + n_B\langle f'_B(q)\rangle e^{-iqw\langle\Delta\rangle} \quad , \qquad \text{(III.33b)}$$

$$\delta F' = n_A\alpha + n_B\beta e^{-iqw\langle\Delta\rangle} \quad , \qquad \text{(III.33c)}$$

where $\langle F' \rangle$ represents diffraction from a basis of average composition and $\delta F'\Gamma(r_j)$ multiplied by $\langle F' \rangle$ represents the scattering amplitude difference between a basis containing the average chemical composition and the actual basis located at r_j.

The three terms of equation III.33a are grouped according to their physical significance. The first term represents pure modulation of the basis position throughout a unit cell of average composition. For no modulation of basis position, γ is zero, reducing this term to $N_p\langle F'(q)\rangle$. The second term represents a pure modulation of chemical composition with a uniform average basis spacing. This term is zero for no variation in chemical composition, since α and β would be zero. The third term represents the modulation of basis length (not position)

throughout the SL unit cell. There are N_B-1 such terms, where N_B is the number of atoms within the basis (N_B=2 for this discussion). An atom located at the origin has a zero fractional coordinate and is unaffected by variations in basis length.

The physical interpretation of equation III.33a is simplified by expanding the concentration deviation function $\Gamma(r_j)$ in a Fourier series. Although the concentration function is discrete, it can be represented by a continuous function $\Gamma(z)$ which is evaluated only at the average basis origin positions. Using the complex series expansion,

$$\Gamma(z) = \frac{1}{2}\sum_{s=-\infty}^{+\infty}\phi_s e^{ik_s z} \quad , \quad k_s=\frac{2\pi s}{L} \quad , \tag{III.34a}$$

$$\phi_s = \frac{2}{L}\int_{-L/2}^{+L/2}\Gamma(z)e^{-ik_s z}dz \quad , \tag{III.34b}$$

where L is the SL period, k_s is the harmonic wavenumber, and ϕ_s are the Fourier expansion coefficients. Each term of equation III.33a contains a geometrical progression involving $\Gamma(r_j)$. Replacing $\Gamma(r_j)$ by its Fourier expansion, each geometrical progression has the form,

$$\sum_{j=0}^{N_p-1}\Gamma(j<\Delta>)e^{-iqj<\Delta>} = \sum_{j=0}^{N_p-1}\sum_{s=-\infty}^{+\infty}\phi_s e^{ij<\Delta>(k_s-q)} \quad , \tag{III.35a}$$

which is principally maximum when

$$\frac{\langle\Delta\rangle}{2}\left[\frac{2\pi s}{L} - q\right] = \pi l \quad , \; l = 0, \pm 1, \pm 2, \ldots \quad . \qquad \text{(III.35b)}$$

In Section II.F, q was defined to be kS, where $k=2\pi/\lambda$ and S is the scattering vector. The scattering vector magnitude $S=2\pi\sin\theta$ (see Figure II.12), where θ is the Bragg angle. Thus, the reciprocal scattering vector is equivalently written

$$q = \frac{2\pi\sin\theta}{\lambda} \quad . \qquad \text{(III.36)}$$

Substituting equation III.36 for q in equation III.35b,

$$\sin\theta = \frac{\lambda}{2}\left[\frac{s}{L} - \frac{l}{\langle\Delta\rangle}\right] \quad . \qquad \text{(III.37)}$$

This is precisely the Bragg relation for a SL (see equation III.9), which stipulates the angle of appreciable diffracted intensities. The integer l corresponds to the constituent Miller index along the growth axis and s corresponds to the satellite index. Although equations III.9 and III.36b are identical in both form and interpretation, the assumptions preceding them are quite different. Equation III.9 assumes that the period is derived from an integral number of unit cells N having length $\langle\Delta\rangle$: $L=N\langle\Delta\rangle$. This is known as the commensurate requirement. Equation III.36b assumes no relationship between the SL period and the constituent cell spacing along L. Apparently, equation III.36b is completely general and applies to both commensurate and incommensurate SLs. A physical interpretation of incommensurate SLs is discussed in section IV.D.

Restricting the remainder of this discussion to principal maxima defined by equation III.35b, the summation of equation III.35a has a very simple form. Performing the j summation first and applying equations III.13a-c, equation III.35a is equivalently written,

$$\sum_{j=0}^{N_p-1} \sum_{s=-\infty}^{+\infty} \phi_s e^{ij<\Delta>(k_s-q)} = N_p \phi_s \quad . \qquad \text{(III.38)}$$

Substituting the result of equation III.38 into the structure factor equation and replacing s with m,

$$F_S(l,0) = N_p<F'>$$

$$F_S(l,m) \simeq N_p<F'>\phi_m\{[-i2\pi\gamma(\frac{l}{<\Delta>}+\frac{m}{L})] + \delta F' + \sum_{j=0}^{N_B-1}[i2\pi\gamma w_j(\frac{l}{<\Delta>}+\frac{m}{L})][e^{2\pi i(1-w_j)m/N_p} - e^{-2\pi i w_j m/N_p}]\} \quad , \qquad \text{(III.39)}$$

where l is the constituent basis index, m is the satellite index, and the third term is expressed as a summation of basis atoms (N_B=2 for [0,0,1] SL growth). According to equation III.39, the SL structure factor is simply the average constituent structure factor for central peak reflections (m=0), and is proportional to the m^{th} Fourier expansion coefficient for m^{th} order satellite peaks.

Equation III.39 allows structural information of the chemical composition to be extracted from the diffracted intensity profile. The accuracy of the measured composition profile is limited by the number of observed satellite peaks and by the assignment of phase information.

The former constraint is a natural consequence of a finite sum approximating an infinite series--since an infinite number of satellite reflections are not observed, only a finite number of Fourier coefficients are known. The latter constraint concerns the loss of phase information when comparing the squared modulus of the structure factor to the diffracted intensity distribution--satellite intensities are related to the square of the structure factor (see equation II.22).

The intensity ratio of same-order satellite pairs among constituent diffraction regions is governed by γ, which is related to the modulation amplitude of atom positions throughout the SL unit cell. If γ is zero, the SL structure factor depends only on the basis structure factor and on ϕ_m. Thus, a quick comparison of the various observed constituent diffraction regions can provide a qualitative assessment of the variations in constituent cell size. For example, the diffracted spectrum of Figure III.8 indicates a nonzero modulation of constituent cell size, since the ratio of same-order satellite pairs changes among the constituent diffraction regions. The constituent diffraction regions of Figure III.9, however, are nearly identical in appearance, suggesting that the constituent cell size is nearly uniform throughout the SL unit cell.

The average constituent basis, having an average chemical composition within an average size basis, governs the central peak (m=0) intensity. According to equation III.27b, the average of $\Gamma(r_j)$, which is represented by ϕ_0, is zero. Thus, the SL structure factor reduces to $N_p\langle F'(q)\rangle$ for central peaks and does not depend on the spatial form of the composition profile. The central peaks, unlike the satellites, are

unaffected by changes in the composition distribution, provided that the SL system is isolated from its surroundings. This property is exploited in SL diffusion analyses.

D. Terraced Superlattices

The orientation of the impinging molecular beams with respect to the surface can affect the uniformity of SL growth. Typically, the effusion cells, which produce the molecular beam responsible for film growth, are located away from the surface normal position. This situation may promote a SL growth direction that is not coincident with a principal constituent cell axis. Nonparallel SL growth can be identified by x-ray diffraction, which is sensitive to both the constituent lattice and modulated period.

A terraced SL model was proposed by Neumann, Zabel, and Morkoc (1983) to explain diffraction from a SL having a modulation wave vector which is not coincident with the a reciprocal lattice vector of the average constituent lattice. Figure III.12a illustrates a two dimensional representation of SL terracing, and Figure III.12b illustrates the two dimensional representation of the corresponding reciprocal lattice. The central peak position are unaffected by the modulation wave vector. In reciprocal space, the satellite peaks lie along a line, passing through the central peak position, that is parallel to the growth direction. This is understood by considering a simplified representation of the diffracted amplitude. Assuming that constituent cells of uniform size and varying composition compose the terraced SL, the diffracted amplitude is proportional to,

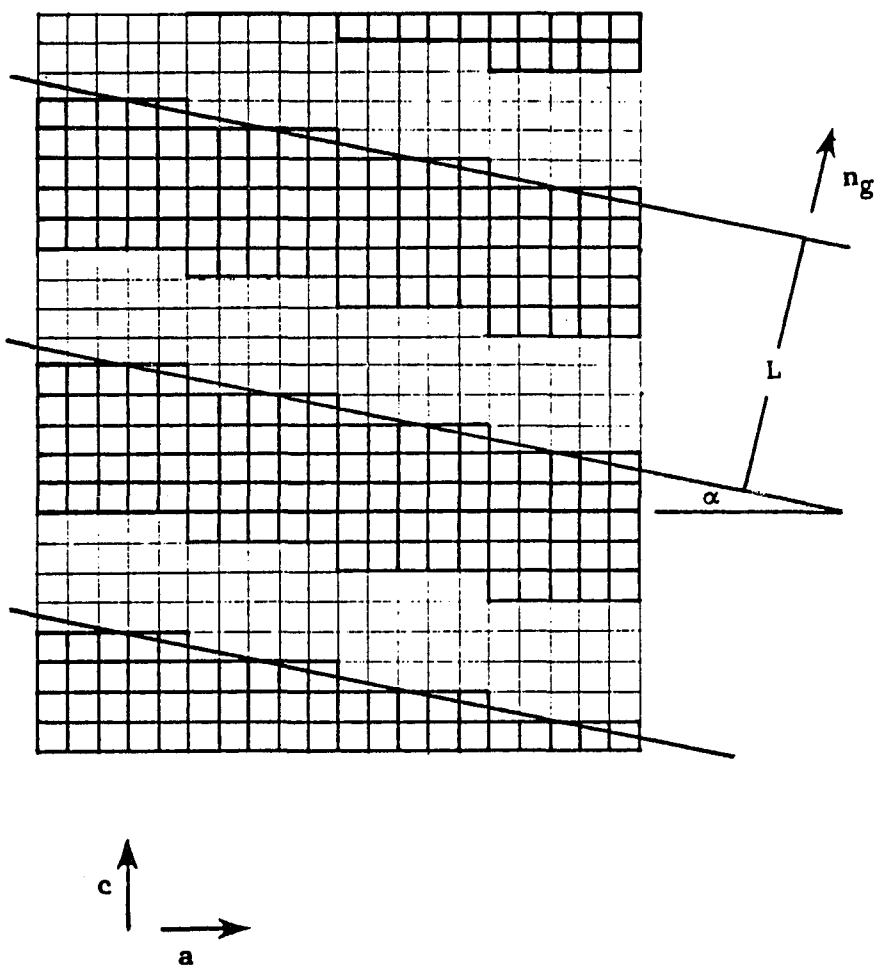

Figure III.12a. A portion of a terraced SL. The constituent cells are represented by open squares and are stacked along the c axis, the dark and light squares distinguishing the two constituent materials. The chemical composition varies along the growth direction (n_g), which forms an angle α with the c axis. The SL period L must be measured along the growth direction. The constituent cell size determines the resolution of the composition profile

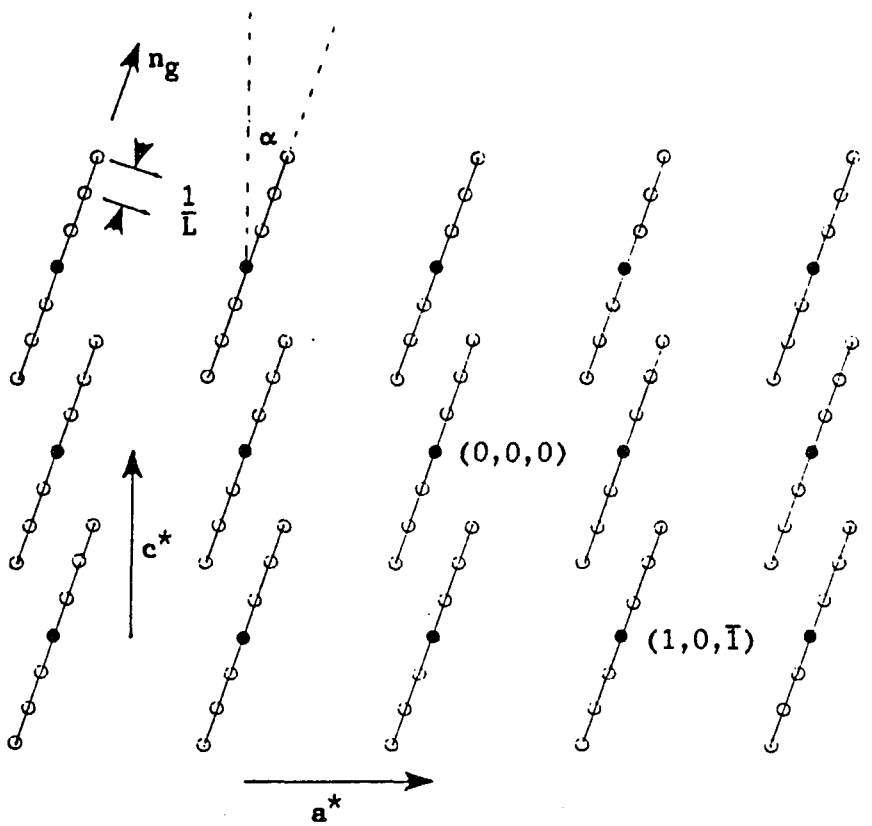

Figure III.12b. A two-dimensional section of reciprocal space for a terraced SL. The filled circles represent central peaks and lie along the c^* axis. The open circles are satellite reflections and lie on a line that forms an angle α with the c^* axis. This figure can be compared to the non-terraced SL illustrated in Figure III.1. Only three satellites are shown about the central peaks for clarity

$$A(q) = \sum_{n_a=0}^{N_a-1} \sum_{n_b=0}^{N_b-1} \sum_{n_c=0}^{N_c-1} F(r_{a,b,c}) e^{-iq \cdot r_{a,b,c}} \quad , \qquad \text{(III.40a)}$$

$$r_{a,b,c} = n_a a + n_b b + n_c c \quad , \qquad \text{(III.40b)}$$

where F is the constituent cell structure factor associated with the chemical composition at $r_{a,b,c}$, n_a, n_b, and n_c are the number of constituent cells along the constituent lattice vectors a, b, c, respectively. Equation III.40a is a generalization of equation III.23a, excluding the variations in cell position.

The constituent cell structure factor varies periodically along the growth direction n_g with period L. Following the procedure outlined in the last section, the constituent cell structure factor is represented by a Fourier expansion (see equation III.34a),

$$F(r) = \frac{1}{2} \sum_{s=-\infty}^{+\infty} F_s e^{i\tau \cdot rs} \quad , \qquad \text{(III.41a)}$$

$$\tau = \left[\frac{2\pi}{L}\right] n_g \quad , \qquad \text{(III.41b)}$$

where F_s are the Fourier expansion coefficients of the constituent cell structure factor. The scalar product $\tau \cdot r$ assures that the composition modulation has a period L along n_g.

The diffracted amplitude is calculated by inserting the Fourier expansion into equation III.40a. Each summation along a constituent cell lattice vector represents a geometrical progression of the form

$$J_a = \sum_{n_a=0}^{N_a-1} e^{n_a \mathbf{a}\cdot(\tau s - q)} \quad . \tag{III.42}$$

This is principally maximum for all $\mathbf{q}$ that satisfy

$$\mathbf{a}\cdot(\tau s - q) = 2\pi j_a = \mathbf{a}\cdot[2\pi(j_a\mathbf{a}^* + j_b\mathbf{b}^* + j_c\mathbf{c}^*)] = 2\pi\mathbf{a}\cdot\mathbf{r}^* \ , \tag{III.43}$$

where j_a, j_b, and j_c are integers and $\mathbf{a}^*$, $\mathbf{b}^*$, and $\mathbf{c}^*$ are reciprocal lattice vectors (see equation II.3b). The constituent reciprocal lattice vector $\mathbf{r}^*$ defines all central peak reflections. According to equation III.43 and the similar expressions describing maxima along $\mathbf{b}$ and $\mathbf{c}$, the reciprocal space scattering vectors of all SL peak reflections are determined by

$$\mathbf{q} = \tau s - 2\pi\mathbf{r}^* \ , \tag{III.44}$$

where s is associated with the satellite index m. Figure III.12b is based on this expression. All satellite reflections have scattering vectors directed along $\mathbf{n}_g$. Thus, SL terracing is identified by comparing the scattering vectors of central and satellite reflections; these vectors are not parallel in terraced samples.

IV. EXPERIMENTAL OVERVIEW

A. X-Ray Apparatus

The x-ray apparatus is divided into five general categories: X-ray generator, monochromator, diffractometer, detector, and signal processor. Figure IV.1 illustrates the diffraction equipment involved from x-ray generation to diffracted intensity detection. The rotating anode generator produces the large x-ray power required for this experimental arrangement. The monochromator selects a narrow range of wavelengths from the incoming superposition of continuous and excited emission radiation. The monochromator also collimates the radiation. The monochromatic and collimated radiation is incident on the sample under investigation, which is placed on a diffractometer for sample orientation with respect to the incident x-ray beam. The diffractometer also positions the x-ray detector, establishing the scattering vector. The detector electronics and computer, not illustrated in Figure IV.1, control the equipment, process the detected signal, and collect the diffraction data for analysis.

X-rays are produced by an Elliot GX21 rotating anode generator, which can maintain a maximum power of 10 kW. A typical power partition is 50 kV at 200 mA. The vacuum surrounding the target anode is approximately 10^{-6} torr. A selection of two anodes provides the four radiation wavelengths used in this research investigation; the α_1 KL_{III} characteristic line of molybdenum yields the 0.7093 Å wavelength and the α_1 $L_{III}M_V$, β_1 $L_{II}M_{IV}$, and γ_1 $L_{II}N_{IV}$ lines of tungsten yield the 1.47639 Å, 1.28181 Å and 1.09855 Å wavelengths, respectively.

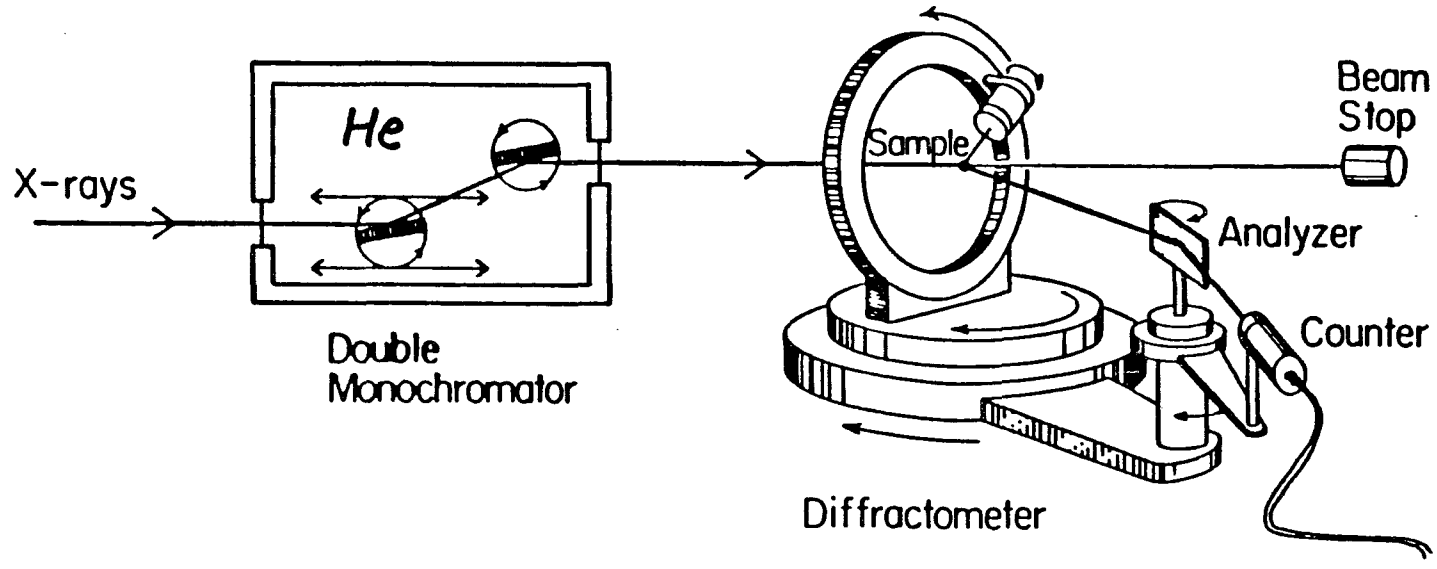

Figure IV.1. A schematic of the diffraction apparatus. The rotating anode x-ray generator, not shown, produces x-ray radiation that enters the double graphite crystal monochromator. The monochromatic and collimated x-ray beam exits the monochromator and intercepts the sample, which is mounted on the diffractometer. The diffracted radiation is detected by the counter. Although the 2θ arm can accommodate an analyzer crystal, it is not used

The unpolarized x-ray radiation passes through a beryllium window into the double graphite crystal monochromator (Staudenmann, Sandholm, Chapman & Liedl, 1984). A slight helium over pressure is circulated inside the monochromator to reduce the x-ray attenuation and to flush out corrosive ozone generated by the radiation interaction with oxygen molecules. Both monochromator crystals are ZYB grade highly oriented pyrolytic graphite. The first crystal is actually a collection of five graphite crystals arranged on a flexible support. These crystals pass incident radiation that satisfies the Bragg reflection from (0,0,2) graphite crystallographic planes. Other crystallographic planes may be used. By curving the flexible support, a large flux of generated radiation is captured and focused on the second monochromator crystal. Diffraction from the (0,0,2) planes of the second crystal, set at the Bragg angle of the first crystal bank, both enhance the energy resolution of the exit radiation and direct the radiation through the exit beryllium window. By adjusting the Bragg angles of both monochromator crystals, any narrow energy region of the generated x-ray spectrum is selected without changing the orientation of the exit beam.

Bragg reflections from both monochromator crystals polarize the generated x-ray radiation, establishing a polarization dependence on wavelength. Staudenmann, Chapman, Murphy, Horning, and Liedl (1985) measured the beam polarization of the double graphite crystal monochromator. These measurements are an extension of work performed by Murphy, Chapman, Staudenmann, and Liedl (1985) and are based on the Borrmann effect (1941, 1950). Diffracting from the (0,0,2) graphite planes, the polarization of the double crystal monochromator is found to

behave as a single perfect crystal in the dynamical theory (James, 1982). The measured beam polarization perpendicular to the scattering plane for the four relevant wavelengths are summarized in Table IV.1.

Table IV.1. X-ray wavelengths and perpendicular electric field polarization component E_{s1} (see equation II.26) used in this research investigation

Atomic Transition	Wavelength[a] (Å)	E_{s1}[b]
α_1 $L_{III}M_V$	1.47639 ± 0.00002	0.74 ± 0.09
β_1 $L_{II}M_{IV}$	1.281809 ± 0.000009	0.73 ± 0.05
γ_1 $L_{II}N_{IV}$	1.09855 ± 0.00003	0.73 ± 0.10
α_1 KL_{III}	0.709300 ± 0.000009	0.72 ± 0.07

[a]Bearden (1967).

[b]Staudenmann, Chapman, Murphy, Horning & Liedl (1985).

In addition to wavelength selection, the monochromator collimates the generated radiation. The spatial beam divergence is reduced by placing three adjustable width slits along the beam path inside the monochromator. Measured from the radiation entrance point, a horizontal slit is placed at 122 cm and both a horizontal and vertical slit are placed at 147 cm. Further collimation is achieved by placing an adjustable slit or circular collimator at the monochromator exit,

located at 180 cm, and at the detector entrance, located at ~290 cm.

The samples are placed on a goniometer head, which is mounted on a Huber four-circle diffractometer having a full Eulerian cradle. The goniometer head allows three dimensional translation, which is required to position the sample in the x-ray beam. The diffractometer provides complete angular movement once the sample is translated to the common intersection of all diffractometer rotation axes. Figure IV.2 illustrates the angular motion of the diffractometer. The incident radiation direction (s_s) from the monochromator exit and the detector position determine both the horizontal scattering plane and angle. The ω and 2θ circles, see Figure IV.1, are parallel to the scattering plane and have a common rotation axis. The detector is mounted on an arm that is attached to the 2θ circle, defining the reflected radiation direction (s_d). The detector intercepts the incident beam at zero 2θ. The ω, ϕ, and χ circles orient the sample with respect to the scattering vector. The ω and ϕ rotation axes are coincident at zero χ.

All diffractometer motors are independently controlled by a computer. The motion of both the ω and 2θ motors can be coupled together so that the 2θ movement is twice the ω angular motion. This is known as an ω-2θ motion with $\omega=2\theta/2$ representing the Bragg angle. The ω and 2θ stepping motors have an angular resolution of 8000 steps per degree. The ϕ and χ stepping motors have a 400 step per degree resolution. The computer control has a display resolution of one-thousandth of a degree.

Radiation diffracted from the sample is detected and processed by a model 7513-10195 EG&G Ortec Si(Li) x-ray detector. This detector

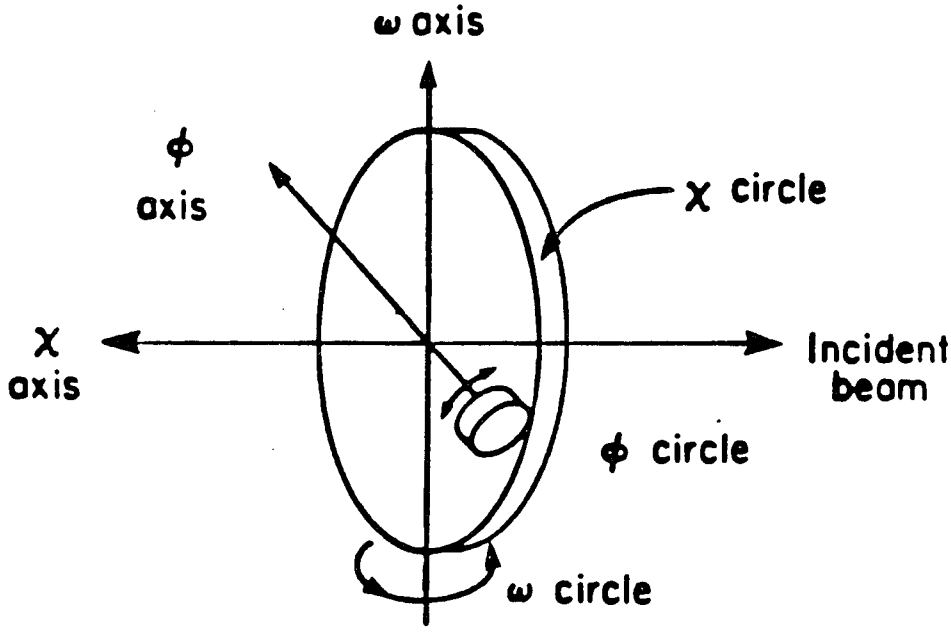

Figure IV.2. An illustration of the diffractometer circle axes. Note that the ϕ and ω axes are coincident at two orientations of the χ circle

provides ~193 eV energy resolution. Either an adjustable slit or fixed circular collimator can be mounted on the detector to provide additional beam collimation before detection. Individual x-ray photons liberate free charge carriers in the Si(Li) detector, which are collected and processed by the detector electronics. The amount of collected charge is proportional to the x-ray photon energy. The detector electronics convert collected charge to a voltage (Elad, 1970), which is shaped into a square pulse. The pulse peak height is proportional to the incident photon energy and the detected x-ray intensity is proportional to the number of pulses (photons) per unit time.

Additional energy resolution is obtained by only counting pulses having peak heights within a defined voltage range. Single channel analyzers (SCAs) are used to discriminate pulse peak heights (Walter, 1970). A primary SCA is used to discriminate the first order wavelength of the monochromator. By detecting the uninterrupted exit beam of the monochromator, the energy window of the primary SCA is set so that further narrowing of the window rejects valid x-ray photons. This enhances the energy resolution established by the double crystal monochromator. Two other SCAs are available to discriminate higher x-ray energy harmonics associated with higher order Bragg reflections of the monochromator crystals. The individual x-ray photons which have energies allowed by the primary SCA are counted for a fixed amount of time.

A second detector, not illustrated in Figure IV.1, monitors the x-ray intensity near the monochromator exit, providing a relative intensity reference of the x-ray beam incident on the sample. A thin

plastic sheet, which is placed just after the horizontal and vertical slit combination inside the monochromator, scatters a small portion of the monochromatic x-rays into a cylindrically symmetric cone about the x-ray beam. A scintillation detector positioned to one side of the beam monitors the scattered radiation, which is proportional to the exit x-ray flux. This reference monitor is used to subtract trends in the exit x-ray intensity from the recorded diffraction profile. All diffraction data are normalized to the monitor reference according to the relationship,

$$C_n = C_d\left[\frac{C_r}{C_m}\right] \quad , \qquad \text{(IV.1)}$$

where C_n is the normalized count value, C_d and C_m are the number of x-ray photons counted by the detector and monitor, respectively, during the same time interval, and C_r is a reference number which is usually set to the average monitor count recorded during the diffraction scan.

The diffractometer orients the sample so that the Laue diffraction conditions are satisfied. Recall that an appreciable diffracted intensity occurs when $\mathbf{S}/\lambda$, $\mathbf{S}=\mathbf{s}_d-\mathbf{s}_s$, terminates on a reciprocal lattice point of the sample (see section II.D). Since the incident beam $\mathbf{s}_s$ is fixed, the diffraction condition is achieved by altering the sample orientation, detector position ($\mathbf{s}_d$), or incident wavelength. Since the reciprocal lattice is rigidly attached to the crystal lattice (equations II.3a and II.3b), rotation of the sample using the diffractometer changes the reciprocal lattice orientation with respect to $\mathbf{S}/\lambda$. The magnitude and direction of $\mathbf{S}/\lambda$ is altered by either rotating 2θ, which

moves the detector position (s_d), or changing the radiation wavelength, which is fixed during a diffraction scan.

Before a diffraction scan is performed along a specific reciprocal lattice trajectory, the sample must be oriented so that the trajectory direction vector lies in the horizontal scattering plane. Knowing the approximate value of the unit cell dimensions, 2θ is set to an angular position that corresponds to Bragg reflection. The ω, χ, and ω-2θ circles, in this order, are then moved to find and optimize the diffracted radiation intensity. This places the [h,k,l] direction of the optimized (h,k,l) reflection in the scattering plane, bisecting the incident and scattered beam directions. Once the sample is optimized, reflections along a common [h,k,l] direction are found by performing an ω-2θ motion to the proper Bragg angle, leaving ϕ and χ fixed at their optimized angular values.

Both ω-2θ and ω scans are routinely performed on the SL samples. Figures IV.3a and IV.3b illustrate the ω-2θ and ω trajectories in reciprocal space. The ω-2θ scan (ω=$2\theta/2$) traverses a radial path from the reciprocal space origin. Since diffraction depends on the orientation of S/λ (equation II.24), where $|S|=2\sin\theta$, an ω-2θ scan is sensitive to the wavelength distribution of the incident radiation. For example, a longer wavelength will diffract at a smaller Bragg angle for the same (h,k,l) reflection. Thus, ω-2θ scans probe not only the crystal structure but also the wavelength distribution of the incident radiation. This can complicate the structural interpretation of these scans. For fixed scattering vectors, the reciprocal space trajectory of an ω scan is restricted to spherical surfaces centered on the reciprocal

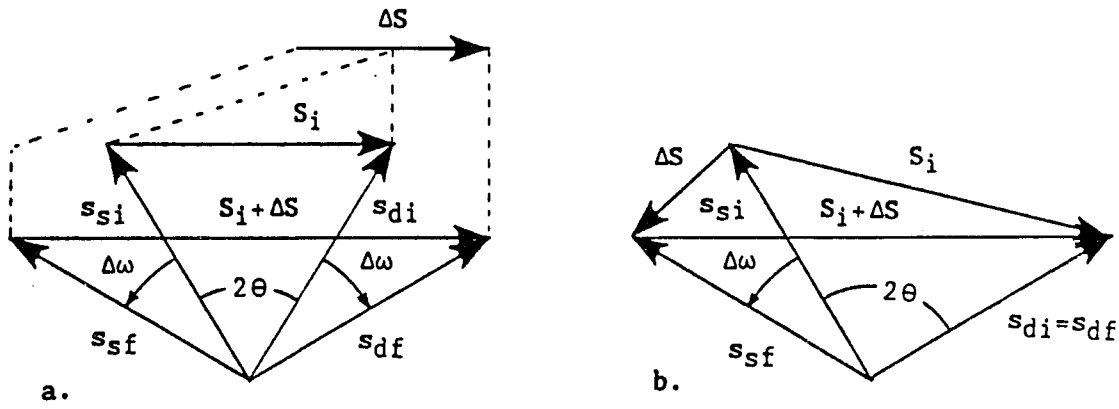

Figure IV.3a. The scattering vector movement ΔS during an ω-2θ scan. Moving the sample by Δω and the 2θ arm by 2Δθ, the scattering vector direction remains constant while its magnitude increases

Figure IV.3b. The scattering vector movement ΔS during an ω scan. Moving only the sample by Δω with respect to the fixed incident beam direction s_s, both the scattering vector direction and magnitude change. ΔS is perpendicular to S for infinitesimal ω rotations (Δω)

lattice origin. For small ω deviations, ω and ω-2Θ scans traverse perpendicular reciprocal space paths. Since the scattering vector magnitude $|S|$ remains constant, an ω scan is unaffected by the wavelength resolution of the incident beam.

B. Reduction of Diffraction Scan Information

Nearly all structural information of the composite SL system is obtained by analyzing the x-ray diffraction scans. Ideally, the entire recorded diffraction spectrum is compared or fitted to a model that includes all relevant effects. This approach, however, is not practical and usually requires specific sample dependent assumptions, which obscures general conclusions. A successful and tractable method is based on reducing the diffraction spectrum to specific parameters which are attributed to each SL peak. Structural interpretations are extracted from the summary of diffraction peak attributes. By quantitatively representing all SLs with commonly defined parameters, sample independent characteristics, which are most useful, are more easily identified. This reduction scheme is employed in this research investigation.

Each (h,k,l) diffraction peak is characterized by its angular position, envelope width, and maximum or integrated diffracted intensity. Two extensive computer programs, PEAK and PERIOD, have been developed and refined to aid both the reduction and analysis of diffraction data. Diffraction scan information is reduced using program PEAK. Angular correction factors, lattice parameter determination, and peak index assignment are computed using program PERIOD. Most of the

structural interpretations are based on the results of these programs.

All diffraction scans are characterized by a diffractometer angle, detector count value, and monitor count value. X-ray photons incident on both the Si(Li) and monitor reference detectors are counted during a time interval that is set before the scan begins. Count times ranging from one to several hundred seconds per data point are common. Begin, end, and increment angles define the angular range and resolution of the scan. The computer samples the diffraction spectrum at equal angular intervals, counting x-ray photons for the specified time interval. This scan information is stored for future analysis.

Program PEAK is a FORTRAN program which processes the collected scan information with the aid of user interaction. All count numbers are normalized to the monitor reference before reducing the data. Each peak is processed individually. A data window, which defines the angular limits of the peak, is selected by the user. The peak centroid, maximum height, width at half maximum, and integrated count value are extracted from the data window. Since adjacent SL peaks typically overlap, the window is selected to have approximately equal count values at the limits. This reduces the influence of the window limits on the centroid calculation.

All count values are normalized to the average monitor reference value of the scan, in accordance to equation IV.1. This normalization becomes important for scans that require many hours to complete the specified angular range. During long scans, the incident x-ray flux of the rotating anode generator may vary, establishing variations in the diffracted data which are not attributed to the sample. The monitor

reference is not an absolute standard, however, and comparisons between scans at different generator powers or different wavelengths are not meaningful.

The angular positions of both the maximum count and the calculated count centroid are record. The maximum peak height position is the angular value associated with the maximum count value inside the user specified data window. This value depends on the sampling of the scan and may not coincide with the actual peak maximum. For this reason, the peak centroid, which is a weighted average over all data in the window, is calculated. Depending on more than one data point, the centroid position provides a more reliable angular position. Various weighting schemes were compared and evaluated by inspection before selecting a weighting standard. The second moment was judged as most reliably yielding the peak center. The first moment is too sensitive to the window limits and higher weighting schemes simply reiterate the maximum peak height position. The centroid for any specified region (window) of diffraction data is defined by the following relation,

$$\theta_c = \frac{\sum_{j=L}^{U} \theta_j C_j^2}{\sum_{j=L}^{U} C_j^2} , \qquad \text{(IV.2)}$$

where θ_j and C_j are the angles and count values of the diffraction scan within the data window defined by the lower and upper angular limits $\theta_L < \theta_U$. The weighted standard deviation (Bevington, 1969) is chosen to represent the centroid uncertainty,

$$\sigma_c = \left[\frac{\sum_{j=L}^{U} (\theta_j - \theta_c)^2 C_j^4}{(U-L) \sum_{j=L}^{U} C_j^4} \right]^{\frac{1}{2}} . \qquad \text{(IV.3)}$$

Equation IV.3 provides a realistic uncertainty for all peak distributions encountered in this research investigation.

Three count values are obtained from scan data inside the user defined window: maximum, interpolated, and integrated. The maximum count value is the largest count number within the window limits. Typically, the corresponding angle is not coincident with the true peak centroid position, although, the scan can be programmed to count at that position. Thus, the maximum count value may not represent accurately the peak height. An interpolated peak height, based on the centroid position, is calculated to alleviate the problems associated with the discrete sampling of the diffraction scan. The Lagrange interpolation method, which is easily adapted to a computer algorithm (Ketter & Prawel, 1969), is used to calculate the interpolated peak height. Since the interpolation method involves more than one data point, an effective smoothing of the statistical x-ray data is established, providing a more reliable peak height value. An integration over all appreciable count values associated with the diffraction peak most accurately represents the diffracted intensity. However, overlap between adjacent peaks prevents the application of a consistent and physically reasonable integration method that does not rely on curve fitting techniques. For this reason, an integration over the data window is performed. A standard integration reference having a 0.005° angle increment and a one

second count time was adopted. The integrated count value is affected by adjacent peak overlap and is used as a comparative reference; only comparisons between peaks having the same window width are meaningful. Since the peak intensity and integrated intensity are theoretically related by equations II.22 and II.34, peak height values can represent diffracted intensities.

Finally, the full width at half maximum (FWHM) of each peak, based on the Lagrange interpolated peak height, is evaluated. Count values on each side of the centroid position are searched and compared to one-half of the interpolated peak height. Two methods are employed to calculate the half maximum angle, if count values below the half maximum are found within the data window. The first method is based on two data points near the half maximum angle, one below the half maximum value and the other above. An average of both points, weighted by the count value, establishes the half maximum position. The difference between the half maxima on each side of the diffraction peak represents the FWHM. If only one value is found within the window, the FWHM is approximated as twice that value. The second method computes each half maximum value using an inverse Lagrange interpolation method (Ketter & Prawel, 1969). Three points, which are nearest the estimated half maximum position, are used in this calculation.

General scan information is first listed in the PEAK result file, followed by peak information that is segregated by central peak regions. The (h,k,l,m) index and window limits are assigned by the user. All information to the right of the centroid window columns are based on the information within the limits. The diffraction depth is calculated

using equation II.56 and the FWHM.

A fitted integrated intensity, which is outside the scope of program PEAK, is possible by performing a nonlinear least squares fit of the diffraction data using the Pearson type VII distribution (Elderton & Johnson, 1969). This distribution, which has four parameters, can be varied continuously from the Cauchy to the Gaussian distributions. The Pearson type VII distribution has the following form,

$$y(x) = y_o\left[1+\frac{(x-x_o)^2}{ma^2}\right]^{-m} \quad , \tag{IV.4}$$

where y_o is the peak height, x_o is the peak position, and m and a are parameters which affect the distribution profile. The peak height and integrated intensity are related,

$$y_o = \frac{I}{\sqrt{\pi}a}\,\frac{\Gamma(m)}{\Gamma(m-0.5)} \quad , \tag{IV.5a}$$

$$I = \int_{-\infty}^{+\infty} y(x)dx \quad , \tag{IV.5b}$$

where I is the total integrated intensity and Γ is the Gamma factorial function (Davis, 1972). The full width at the 1/p maximum, $w(y_o/p)$, is related to m and a,

$$w^2(y_o/p) = 2am(p^{\frac{1}{m}}-1) \quad . \tag{IV.6}$$

The Cauchy and modified Lorentzian distributions are obtained by setting

m to one and two, respectively. The Gaussian distribution is obtained in the limit as m approaches infinity.

The application of the Pearson type VII distribution to symmetric x-ray diffraction peaks was demonstrated by M. M. Hall, Jr. (1977). SL diffraction data are reasonably approximated by superposing multiple Pearson type VII distributions with a quadratic function, which compensates for the background intensity present between SL peaks. However, the nonlinear fitting procedure is quite difficult to apply to the entire SL spectrum. The most successful application of the Pearson type VII distribution involves the fitting of central peak profiles, which are typically a superposition of substrate, buffer layer, and SL central peaks. A superposition of Pearson type VII distributions can fit to the recorded central peak, provided that the superposed peaks have sufficiently different profile characteristics.

Figure IV.4 beautifully illustrates a Pearson VII fit to a diffraction scan from a $Hg_xZn_{1-x}Te$ film deposited on a GaAs substrate. The film growth direction is [1,1,1], which is parallel to the [0,0,1] GaAs normal. Three independent Pearson VII peaks were fit to the diffraction scan using the nonlinear least squares fitting routine outlined by Bevington (1969). Each independent Pearson VII peak is actually a superposition of two peaks having identical a and m parameters. This compensates for the α_2 $L_{III}M_{IM}$ characteristic line of tungsten, λ=1.48743 Å, which passes through the monochromator along with the optimized α_1 $L_{III}M_{IV}$ line. The intensities of the secondary peaks are one-tenth of the principal peak. This scale factor, which is an adjustable fitting parameter, applies to all three peaks. The secondary

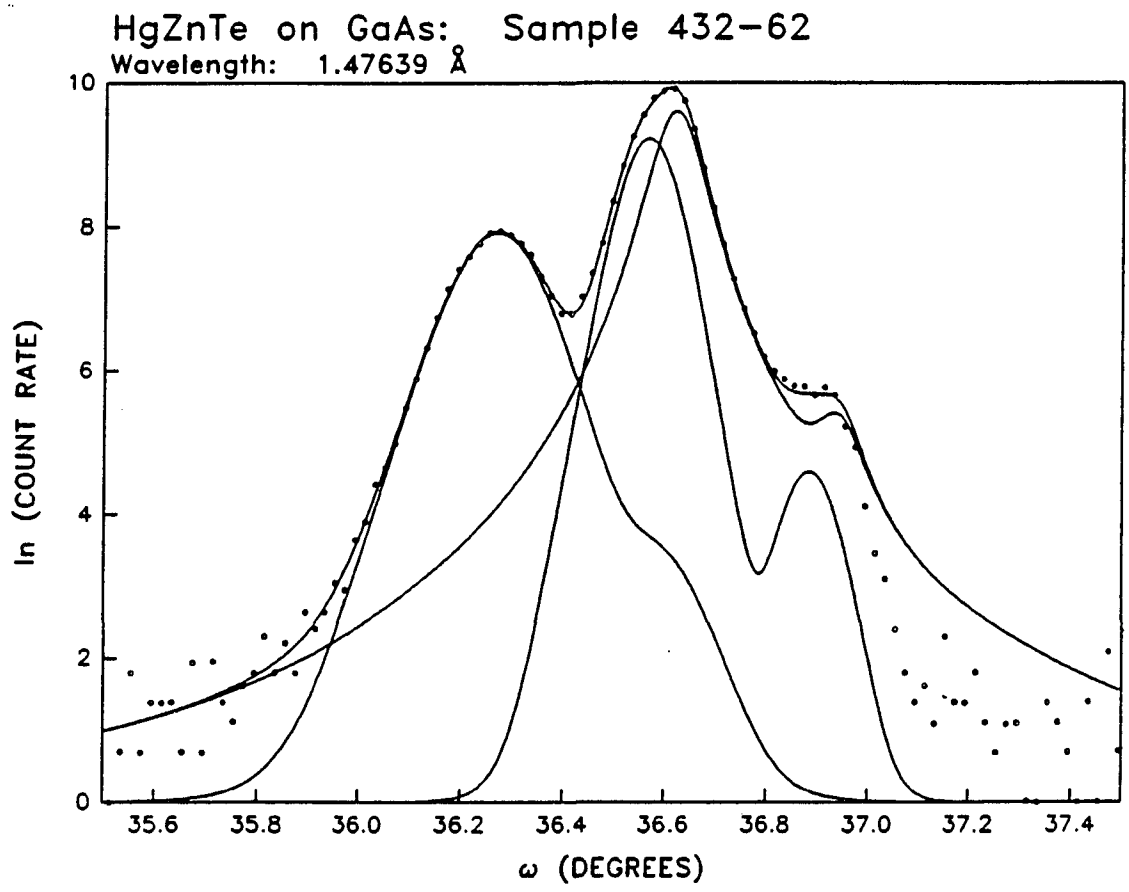

Figure IV.4. A nonlinear least squares fit (solid line) to the (3,3,3) diffraction spectra (dots) of a HgZnTe film on GaAs using 1.47639 Å radiation. The fit consists of three Pearson VII peak pairs. The primary peak of each pair is required to fit the HgZnTe structure and the secondary peak accounts for contaminating 1.48743 Å wavelength radiation that passes through the monochromator

peak positions are rigidly defined by the α_2 wavelength component. The quality of a fit is represented by both the χ^2 value and R-factor (Bevington, 1969),

$$\chi^2 \equiv \sum_i \sigma_i^{-2}[y_i - y(x_i)]^2 \quad , \tag{IV.7a}$$

$$R \equiv \left[\frac{\chi^2}{\sum_i \sigma_i^{-2} y_i}\right]^{\frac{1}{2}} \quad , \tag{IV.7b}$$

where σ_i is the uncertainty of the i^{th} data point y_i and $y(x_i)$ is the fitted function evaluated at x_i. If the fitting function is a good

Table IV.2 Fitting parameters for the Pearson VII fit illustrated in Figure IV.4

Peak	$I\alpha_1$[a] (Counts)	θ_0[a] (°)	m[a]	a[a]	FWHM[b] (°)
1	2752 (28)	36.2695 (9)	5 (1)	0.098 (2)	0.146
2	10126 (154)	36.5658 (9)	6 (1)	0.0625 (8)	0.092
3	14833 (198)	36.6201 (4)	1.55 (4)	0.0478 (5)	0.084

[a]The numbers in parentheses represent the estimated uncertainty (Bevington, 1969) in the last digits.

[b]Width at one-half maximum w(1/2) from equation IV.6.

approximation to the data (x_i,y_i), χ^2 should by approximately unity. Since x-ray generation is a random event, the square root of the recorded count value represents the count uncertainty (Bevington, 1969). Table IV.2 summarizes the Pearson VII parameters of all three peak pairs. The unweighted and weighted χ^2 values of this fit are 536.2 and 0.402, respectively. The unweighted and weighted R-factors are 0.00679 and 0.00681, respectively.

C. Angular Correction of Experimental Data

Misalignment of the diffractometer and improper centering of both the incident x-ray beam and sample with respect to the diffractometer center introduce angular deviations that must be corrected before structural information of the sample is extracted. Diffractometer alignment involves the zero definition of both ω and 2θ in addition to aligning the detector collimator so that it is coincident with radial trajectories from the diffractometer center. Both the x-ray beam and sample must be centered with respect to the diffractometer so that the same sample location diffracts at arbitrary angular settings.

Diffractometer alignment does not depend on the sample and must be performed only after each change of the monochromator wavelength, which slightly modifies the position of the exit x-ray beam. Since ω and 2θ are independently controlled, the absolute zero angle of each must be accurately defined. The incident x-ray beam defines 2θ. With no sample mounted, the incident beam travels through the diffractometer center into the detector. By performing a scan over the incident beam, the 2θ zero is defined as the centroid position of the scan. The detector

alignment is established by pivoting the detector mount using the $2\theta_a$ stepping motor. The detector position is set to the centroid angle of the $2\theta_a$ scan. The accuracy of this method is limited by the divergence of the x-ray beam and the size of both the incident and detector collimators. The ω zero must be defined indirectly. An excellent quality crystal, germanium for this research investigation, is used to set the zero of the ω circle. Once mounted, the strong (2,2,0) reflection is optimized using the established 2θ zero. The ω zero is defined to be one-half of the 2θ centroid value of the optimized reflection. During the optimization procedure, two ω scans must be performed, one with χ set near 0° and the second with χ near 180°. This separates the rotational sense of the ϕ and ω circles, which have coincident rotational axes at both χ settings.

Centering of the sample on the diffractometer is performed each time a sample is mounted. The sample surface is initially placed flush with the incident beam. The ω and 2θ circles are driven to the angular values of a known reflection and ϕ, χ, and ω-2θ are optimized in this order. Then, the sample is translated on the goniometer head to further optimize the diffracted intensity. This procedure is repeated until further translation of the sample fails to increase the diffracted intensity. The sample is centered on the diffractometer at the completion of this procedure.

Although both the diffractometer alignment and sample centering procedures are found to work well and consistently, small deviations from the optimal diffraction arrangement typically persist. These deviations, which contribute to the systematic error of the diffraction

apparatus, affect observed peak positions and reduce the precision of extracted structural information. Although diffraction peaks are recorded and corresponding centroid positions calculated, lattice parameter information is the desired quantity of interest. The precision of unit cell dimension measurements depends not on θ but on $\sin\theta$, which is a derived quantity. The lattice parameter uncertainty, $\Delta d/d$, is approximated by differentiating the Bragg relation (equation II.25),

$$\frac{\Delta d}{d} = \frac{\Delta\lambda}{\lambda} - (\cot\theta)\Delta\theta \quad , \qquad \text{(IV.8)}$$

where d is the crystallographic spacing corresponding to the diffracted intensity scattered at 2θ. Since the wavelength uncertainty of the characteristic emission lines are better than 3×10^{-5} Å, $\Delta\lambda/\lambda$ is neglected. According to equation IV.8, optimal lattice parameter precision is obtained from reflections having scattering angles near 180° (θ=90°). The nearest reflection depends on the crystallographic spacing, radiation wavelength, and largest 2θ allowed before the detector obstructs the x-ray beam.

Plotting d as a function of θ, the most precise lattice parameter value, according to equation IV.8, is obtained by extrapolating d to 90°. Unfortunately, this curve is not linear. Two related extrapolation schemes are commonly employed. The first method involves fitting d as a function of θ using a nonlinear fitting routine and extracting the lattice parameter by evaluating the fitted function at θ=90°. The second method is based on some function of θ that is

linearly related to d. Plotting the d dependence on the θ function, the lattice parameter is extracted by linearly extrapolating d to 90°. Bevington (1969) discusses both linear and nonlinear fitting techniques. The particular θ function used depends on the sources of misalignment. When using a diffractometer, the displacement of the sample center from the diffractometer axis is usually the largest single source of error (Cullity, 1978). This affects the measured lattice plane spacing,

$$\frac{\Delta d}{d} = \frac{-D\cos^2\theta}{R\sin\theta} \quad , \qquad \text{(IV.9)}$$

where D is the sample displacement parallel to the reflecting-plane normal, and R is the diffractometer radius. Nelson and Riley (1945) rigorously considered the various sources of error, including sample absorption, and obtained the following relation,

$$\frac{\Delta d}{d} = K\left[\frac{\cos^2\theta}{\sin\theta} + \frac{\cos^2\theta}{\theta}\right] \quad , \qquad \text{(IV.10)}$$

where K is a constant of proportionality and θ is measured in radians. Known as the Nelson-Riley function, equation IV.10 yields reasonably accurate lattice parameters for small θ values. Application of these techniques to SL data has been successful, however, the calculated uncertainties were found to be unreasonably small.

An alternative correction method that does not depend on extrapolation techniques, has been successfully applied to SL diffraction data. This method is based on the approximation that true angular values differ from measured angles by a constant offset θ_o.

Only pairs of reflections, (h,k,l) and (h',k',l'), that have a common Miller index multiplier are used to extract θ_0: h'=nh, k'=nk, and l'=nl. Such pairs of reflections are derived from the same set of crystallographic planes. For example, diffraction from (2,2,0) planes is equivalently described by second order reflections, 4π phase difference between adjacent planes, from (1,1,0) planes (see Figure II.13). The crystallographic plane spacing of these pairs of reflections are related,

$$d(nh,nk,nl) = nd(h,k,l) \quad . \tag{IV.11}$$

Expressing d(h,k,l) in terms of the Bragg relationship and explicitly writing the offset θ_0,

$$\frac{\lambda}{2\sin(\theta_{h,k,l}-\theta_0)} = \frac{n\lambda}{2\sin(\theta_{nh,nk,nl}-\theta_0)} \quad , \tag{IV.12}$$

where $\theta_{h,k,l}$ is the centroid angle corresponding to the (h,k,l) reflection, λ is the common x-ray wavelength, and θ_0 is the extracted offset angle. Instead of measuring two related reflections, one reflection can be measured at two wavelength harmonics. Using a trigonometric identity and solving for θ_0,

$$\theta_0 = \text{Arctan}\left[\frac{\sin\theta_{nh,nk,nl} - n\sin\theta_{h,k,l}}{\cos\theta_{nh,nk,nl} - n\cos\theta_{h,k,l}}\right] \quad . \tag{IV.13}$$

Applying equation IV.13 to all relevant reflection pairs, a set of θ_0

values are extracted from the diffraction scan. An average of all θ_0 angles, $\langle\theta_0\rangle$, is then calculated for the entire diffraction scan. The variance of this average represent a reasonable uncertainty $\Delta\langle\theta_0\rangle$. This method is further enhanced by performing a weighted average based on the estimated centroid uncertainties (equation IV.3). The corrected values $(\theta_m-\theta_0)$ represent the true centroid positions.

Comparisons between the offset and linear extrapolation methods were performed for several samples. Figures IV.5a and IV.5b illustrate a comparison between the methods for CdTe-ZnTe SL data recorded at two wavelengths. The diffractometer was aligned after each wavelength optimization and the sample was centered after each mounting on the diffractometer. Figures IV.5a and IV.5b reveal an excellent agreement for the central peak positions. The satellite peaks are not included in the offset determination. A horizontal line (dashed) can be drawn through the corrected central peak positions, which confirms the validity of the offset method. Further support of the offset method is established by noting that the calculated period at each wavelength is consistent within the calculated uncertainty: 40.956 ± 0.015 Å and 40.9376 ± 0.0023 Å. Although the extrapolation procedures are firmly founded in the literature, the offset method is considered to be a valid alternative for angular data correction. In addition, the latter method predicts more reasonable uncertainties and is more conveniently incorporated into a computer algorithm.

D. Accurate Superlattice Period Determination

Once a diffraction scan has been reduced to peak positions,

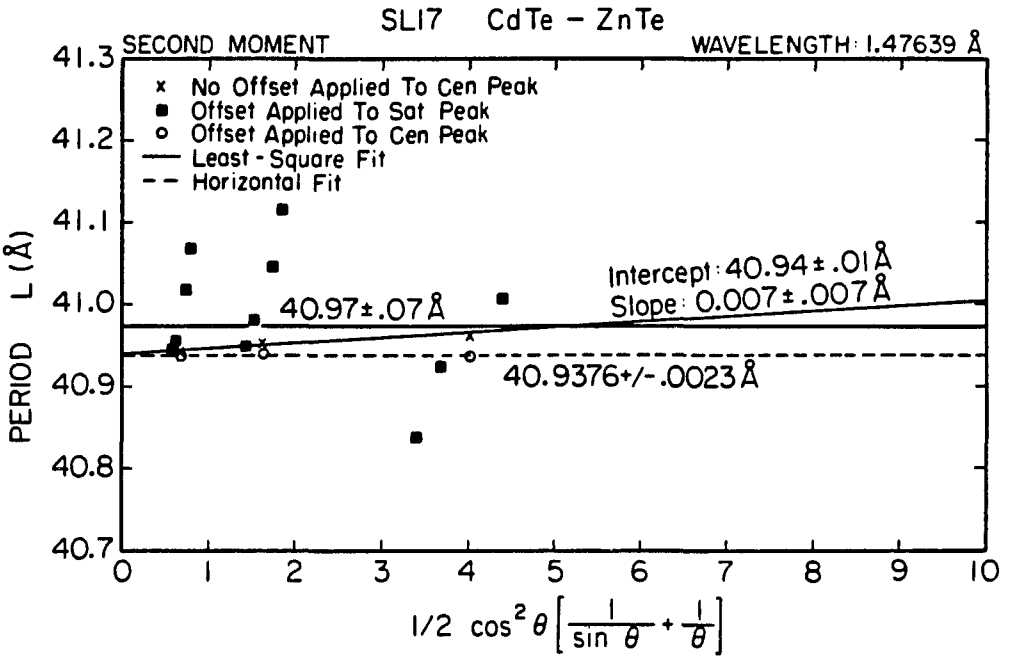

Figure IV.5a. A comparison between the Nelson-Riley (equation IV.10) and the constant angle offset θ_0 (equation IV.13) correction methods applied to SL-17 diffraction data using 1.47639 Å radiation. The period derived from each SL peak is plotted as a function of the Nelson-Riley function. X markers represent uncorrected central peak positions, and circles represent central peak positions that have been corrected for a θ_0 offset. The SL period is extracted by extrapolating a fit of the individual periods (X markers) to $2\theta=180°$. This extrapolation intersects the horizontal extrapolation of corrected data. The filled squares represent periods extracted from the satellite peaks and are not involved in this comparison

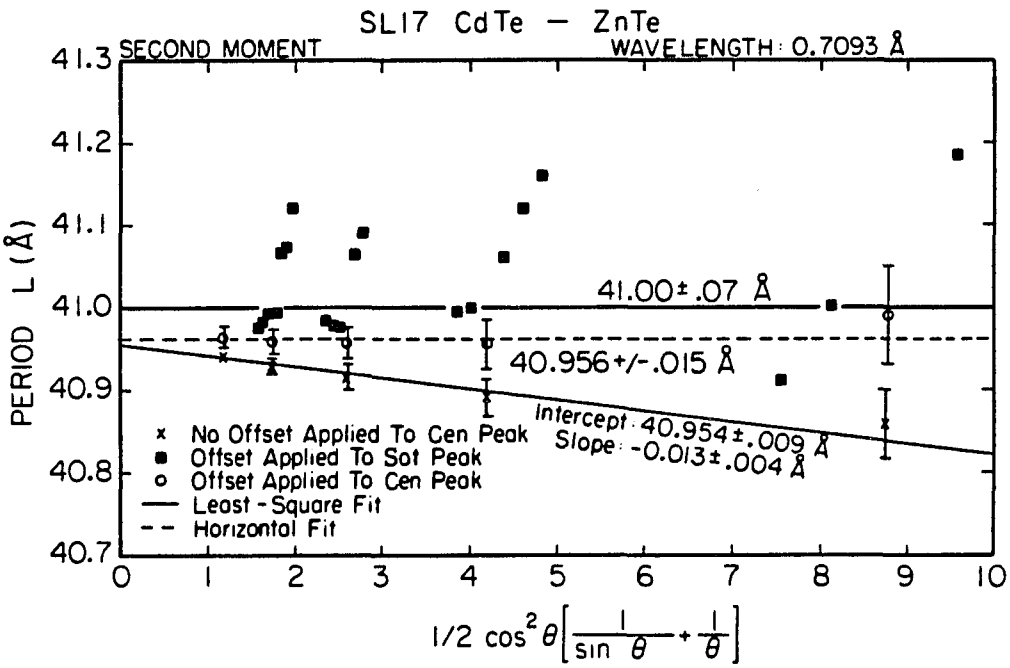

Figure IV.5b. A comparison between the Nelson-Riley (equation IV.10) and the constant angle offset θ_0 (equation IV.13) correction methods applied to SL-17 diffraction data using 0.7093 Å radiation. The period derived from each SL peak is plotted as a function of the Nelson-Riley function. X markers represent uncorrected central peak positions, and circles represent central peak positions that have been corrected for a θ_0 offset. The SL period is extracted by extrapolating a fit of the individual periods (X markers) to $2\theta=180°$. This extrapolation intersects the horizontal extrapolation of corrected data. The filled squares represent periods extracted from the satellite peaks and are not involved in this comparison

the SL period can be calculated. Two period calculations are employed in this research investigation. The first method assumes that the SL is commensurate, which is outlined in section III.A. This procedure is incorporated into an extensive FORTRAN program, PERIOD, which directly reads the data summary sheet from program PEAK, calculates and applies the angular offset θ_o, calculates the SL period, and determines the best l′ SL indices. Program PERIOD is used to calculate all commensurate SL periods of this research investigation. The second period calculation method is based on the incommensurate SL assumption, which asserts that the SL period need not be an integral number of average constituent cells (de Wolf, 1984; Watanabe & Terasaki, 1984). Both methods are discussed below.

1. Commensurate calculation: program PERIOD

The accurate SL period calculation is based on the one dimensional Bragg equation derived in section III.A,

$$\sin\theta = \frac{\lambda l'}{2L} \quad , \qquad \text{(IV.14)}$$

where θ is the Bragg angle, l′ is the one dimensional SL index, and L is the SL period. An ω-2θ scan having its scattering vector parallel with the SL growth direction provides the necessary experimental data; the angular centroid positions of all detected SL peaks represent the Bragg angles of equation IV.14. If the l′ indices are known, a SL period is extracted from each peak using equation IV.14. The best representative SL period would be the average of all individual periods and the

associated uncertainty is represented by the average variance. Unfortunately, all peaks within the angular limits of the diffraction apparatus are not observable, preventing the unambiguous assignment of l′ indices by inspection. However, knowing the approximate average constituent cell length along the growth direction, (h,k,l,m) indices can be assigned by inspection. An expression equivalent to equation IV.14, based on the (h,k,l,m) indices, provides an alternate procedure to extract the SL period from each satellite centroid position.

Every SL spectrum has a series of central peaks which correspond to the average composition of the constituent materials. For SLs that have closely matched constituent lattice parameters, the central peaks are the most intense (see section III.B, and Figure III.10). The central peaks are indexed by applying equation IV.14 to the average lattice parameter along the growth direction <c>,

$$2\langle c\rangle \sin\theta = l\lambda \quad , \qquad \text{(IV.15)}$$

where l is the Miller index associated with the average constituent cell length along the SL growth direction. Unless the constituent lattice parameters are very closely matched, <c> is not initially known. However, since <c> is usually much smaller than the modulated period, only a small subset of SL peaks are indexed as central peaks by l. This greatly reduces the number of peaks that must be considered. Assuming that the constituent materials maintain their bulk unit cell symmetry, the central peaks are easily identified and indexed by demanding that <c> have an intermediate value between the two bulk constituent lengths

c_{b1} and c_{b2}: $c_{b1} \leq \langle c \rangle \leq c_{b2}$. Both equations IV.14 and IV.15 jointly index all central peaks, establishing a relationship between l and l′,

$$\frac{\lambda l'}{2L} = \sin\theta = \frac{\lambda l}{2\langle c \rangle} \quad \text{or} \quad l' = \frac{lL}{\langle c \rangle} \quad . \tag{IV.16}$$

Equation IV.16 is valid only for central peaks having index l. Since adjacent SL peaks have an l′ increment of one, a general expression for l′ can be expressed,

$$l' = \frac{lL}{\langle c \rangle} + m \quad , \tag{IV.17}$$

where m is the satellite index (see equation III.8). Equation IV.17 is valid for all SL peaks, provided that the average lattice parameter is commensurate with the SL period. The indices l, l′, and m must be a positive or negative integer. Combining equations IV.14 and IV.17, the SL period is related to the Miller index l and the satellite index m,

$$L(\theta) = \frac{m\langle c \rangle}{\frac{2\langle c \rangle \sin\theta}{\lambda} - l} \quad . \tag{IV.18}$$

Once $\langle c \rangle$ is calculated from the central peaks, this equation is used to extract a SL period from each satellite peak.

Equation IV.18 provides the foundation of program PERIOD. The (h,k,l,m) indices, which must be known before using program PERIOD, are assigned during the user interaction with program PEAK. First, the θ_0 offset angle is extracted from only the central peaks using equation

IV.13. SL terracing, multiple domains, or growth defects prevent the successful application of equation IV.13 to satellite peaks. The data are corrected for the offset angle and the estimated offset angle uncertainty is retained for error propagation in the period calculation. A constituent unit cell length $c(\theta)$ is extracted from each corrected central peak using equation IV.15. The average cell length $\langle c \rangle$ is obtained by performing a weighted average over all $c(\theta)$,

$$\langle c \rangle = \frac{\sum_{j=1}^{N_C} c(\theta_j) \left| \cot\theta_j \Delta\theta_j \right|}{\sum_{j=1}^{N_C} \left| \cot\theta_j \Delta\theta_j \right|} , \qquad \text{(IV.19a)}$$

$$c(\theta_j) = \frac{l_j \lambda}{2\sin\theta_j} , \qquad \text{(IV.19b)}$$

where N_C is the number of central peaks, θ_j are the corrected centroid positions of central peaks having index l_j, λ is the radiation wavelength, and $\Delta\theta_j$ are the estimated angular uncertainties based on both the centroid uncertainty of equation IV.3 and the offset uncertainty $\Delta\theta_o$. The estimated uncertainty of $\langle c \rangle$ is analogous to equation IV.3. Once $\langle c \rangle$ is determined, the SL period is derived from the individual $L(\theta)$ of equation IV.18. Only the corrected satellite peak centroids are used in the weighted average,

$$L = \frac{\sum_{j=1}^{N_S} L(\theta_j) \left|\cot\theta_j \Delta\theta_j\right|}{\sum_{j=1}^{N_S} \left|\cot\theta_j \Delta\theta_j\right|} , \qquad \text{(IV.20)}$$

where N_S is the number of satellite peaks, L is the average SL period based on the periods $L(\theta_j)$ extracted from each satellite peak.

The period calculation, based on equation IV.20, provides consistent period information with a high degree of accuracy. Table IV.3 summarizes six calculated periods of the same SL sample from six independent ω-2θ scans. Before each scan, the monochromator and diffractometer were aligned, and the sample mounted and optimized. Three different wavelengths were used under a variety of collimator arrangements, count times, and scan resolutions. All extracted periods are consistent within the estimated uncertainty. The listed uncertainty is approximated by the variance of all satellite periods $L(\theta)$ of equation IV.18 using the calculated period L of equation IV.20 as the average. For comparison, the unweighted average and standard deviation of the six tabulated periods is 40.98 ± 0.02 Å. Table IV.3 also confirms the validity of the offset angle correction procedure; without correcting the angular positions, the calculated periods would not agree within the estimated uncertainties.

2. Incommensurate calculation: least-squares fit

A physical interpretation of incommensurate SLs growth is instructive before discussing the mathematical details of the x-ray

Table IV.3 Repeated period measurements of SL-17 (CdTe-ZnTe SL)

Scan date	X-ray wavelength (Å)	Collimator:[a] incident (mm)	detector (mm)	Step[b] size (°)	Count[c] time (sec.)	Peaks[d] detected	<c>[e] (Å)	L[f] (Å)	θ_o[f] (°)
26-OCT-85	1.47639	1.4 D	2.5 D	0.10	100	3/24	6.300±.003	41.0±.4	-0.05±.02
30-JUN-86	0.70930	1x5 S	1.2x8 S	0.01	5	5/20	6.300±.001	40.99±.07	+0.016±.007
27-JUL-86	1.47639	1x5 S	1.1x8 S	0.02	60	3/11	6.298±.001	40.97±.07	-0.009±.004
02-AUG-86	1.47639	1.4 D	2.5 D	0.10	100	3/15	6.297±.002	41.0±.1	-0.011±.002
06-MAR-87	1.28181	1x5 S	1.1x8 S	0.02	60	3/14	6.293±.002	41.0±.1	-0.009±.008
04-APR-87	1.47639	1x5 S	1.2x8 S	0.02	60	3/14	6.296±.002	40.97±.09	0.00±.02

[a]D = round diameter; S = slit width: (horizontal)x(vertical).

[b]ω circle resolution of the ω-2θ diffraction scan.

[c]The time that the detector measures the x-ray intensity at each angle.

[d]Number of peaks used in the calculation: central/satellite.

[e]The largest of either the variance or estimated uncertainty is listed as the uncertainty.

[f]The variance is listed as the uncertainty.

analysis. Because of the large irradiated volume (approximately 0.05 mm^3), x-ray diffraction information is based on an average over many unit cells of the crystal lattice. This averaging effect can lead to a SL modulation wavelength that is not commensurate with the periodic constituent lattice. For example, consider the atomic layer growth using molecular beam epitaxy. Neutral atoms leave the effusion cells within the growth chamber vacuum and strike the substrate target. When striking the target, atoms of the molecular beam either stick or are reflected. For a particular atomic species, the fraction of impinging atoms that stick to the target and are incorporated into the film defines the sticking coefficient (Chang & Ludeke, 1975). Deviations of the sticking coefficient across the film surface introduces inhomogeneous film growth, which can lead to incommensurate SL growth.

Figure IV.6 illustrates the gross features of SL growth when the sticking coefficient of the constituent atoms is less than unity. For simplicity, atoms are identified by the constituent material. One constituent material (e.g., HgTe) is represented by solid circles, and open circles represent the other constituent (e.g., CdTe). Within the small cross section illustrated, the impinging atoms stick to the surface and diffuse to the regular lattice sites of the atomic planes illustrated in Figure IV.6. However, since the sticking coefficient is less than unity, each constituent material fills all allowed atomic sites, except one. As the next constituent layer is formed, one atom must fill the vacancy left from the previous layer, and in addition, another vacancy is formed. By ascribing a continuous composition function to the discrete atomic plane structure, the boundary between

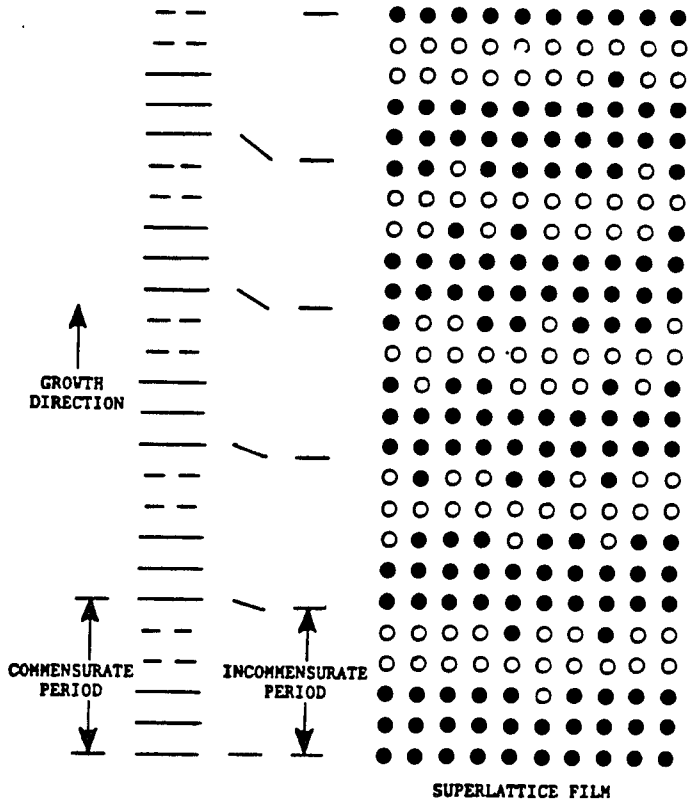

Figure IV.6. SL growth when the sticking coefficient of both constituents is less than one. The filled and open circles represent the two constituent materials. After completion of one constituent region, one atomic site remains empty. This vacancy is filled by the next constituent layer, which also forms one vacancy. Thus, after completion of one period, two vacancies remain in the top layer. These vacancies propagate throughout the SL film, which introduces a slightly shorter SL period that is incommensurate with the constituent lattice. The two columns to the left of the depicted SL mark regions that have identical composition concentrations. The far left column represents ideal commensurate growth, and the right column represents the actual SL film illustrated to the far right

adjacent SL unit cells is defined by the positions that have the same composition value. These boundaries are identified in Figure IV.6. During the growth, the distance between adjacent SL unit cells is consistent, but this distance is incommensurate with the constituent atomic planes.

Since the sticking coefficient depends on temperature, in addition to other growth conditions, a temperature gradient present within the heated substrate can produce inhomogeneous SL growth. Temperature gradients less than 5° are typically observed (Monfroy, 1987). This can severely affect HgTe-CdTe growth, for example, where a difference of 8° about the growth temperature (180 C) changes the Hg sticking coefficient by an order of magnitude (Sivananthan, Chu & Faurie, 1987).

Of course, the above discussion is one example of incommensurate SL growth. Other factors, such as the geometrical relationship between the effusion cells and substrate introduce an inhomogeneous molecular beam flux across the substrate, resulting in another form of incommensurate growth. Unfortunately, x-ray diffraction alone can not isolate the specific factors associated with incommensurate growth. Supplemental information from other microanalytical techniques, which probe a much smaller volume of the film, is required to understand the actual dynamics of SL growth. X-ray diffraction, however, can easily identify the presence of incommensurate growth.

The use of a consistent l′ index assignment that describes the positions of all SL peaks, regardless of the constituent diffraction region, must be abandoned under the incommensurate formalism. This is most easily understood by considering the relationship between the l′

index and the (h,k,l,m) index for commensurate SLs,

$$l' = \frac{lL}{\langle c \rangle} + m \quad . \tag{IV.21}$$

Since l′ must be an integer, the difference of any two l′ indices must also be an integer. By establishing a general relationship between the period L and the constituent cell spacing along the period direction c,

$$L = \alpha c \quad , \tag{IV.22a}$$

the difference between to different l′ indices has the form,

$$l'_2 - l'_1 = \Delta l' = \alpha \Delta l + \Delta m \quad , \tag{IV.22b}$$

where Δl is the difference of the constituent Miller indices along the period direction and Δm is the difference of satellite indices. Notice that, in general, $\Delta l'$ is not an integer for arbitrary α values. This is not consistent with the l′ index scheme. However, within any constituent diffraction region, where l has a common value, the l′ index scheme is consistent. The consequence of this observation is that program PERIOD, which is based on the l′ index scheme, can only be applied to individual constituent diffraction regions. A second period calculation method is required for incommensurate SLs.

According to section III.C, the general Bragg relationship is applicable to incommensurate SLs, which includes commensurate structures as a special case,

$$\sin\theta = \frac{\lambda}{2}\left[\frac{m}{L} - \frac{l}{c}\right] \quad . \qquad \text{(IV.23)}$$

This expression relates the Bragg angle of any SL peak to its (l,m) index, where l is the Miller index along the growth direction and m is the satellite index. Since the relationship between L and c is unknown, both parameters are derived from the experimental data. This is accomplished by performing a least-squares fit to the data, which is outlined by Bevington (1969). First, a weighted χ^2 value must be defined as a function of both L and c. According to equation IV.23,

$$\chi^2 \equiv \sum_{i=1}^{N}\left[(\sin\theta)_i - Al_i - Bm_i\right]^2\sigma_i^{-2} \quad , \qquad \text{(IV.24a)}$$

$$A = \frac{\lambda}{2c} \quad , \qquad \text{(IV.24b)}$$

$$B = \frac{\lambda}{2L} \quad , \qquad \text{(IV.24c)}$$

where N is the number of peaks that equation IV.23 must fit, $(\sin\theta)_i$ is the sine of the i^{th} peak centroid, σ_i is the uncertainty of $(\sin\theta)_i$, l_i and m_i are the Miller and satellite indices of the i^{th} peak, respectively, and the coefficients A and B are parameters that minimize χ^2. The fitting parameters A and B are determined by setting the derivative of χ^2 with respect to these parameters equal to zero,

$$\frac{\partial\chi^2}{\partial A} = 0 \quad , \qquad \text{(IV.25a)}$$

$$\frac{\partial\chi^2}{\partial B} = 0 \quad . \qquad \text{(IV.25b)}$$

The simultaneous solution of both equations IV.25a and IV.25b has a simple closed form. The values A and B derived from this solution minimize χ^2 and, using equations lV.24b and IV.24c, determine a period L and constituent lattice parameter c that best fit the experimental data. The simultaneous solution of equations IV.25a and IV.25b has been adapted to a FORTRAN program ALFIT. This routine reads the PEAK result files directly and computes both L and c. The application of both program PERIOD and ALFIT to experimental data is presented in sections V.B and VI.B.

E. Precession Photography of the Reciprocal Lattice

As emphasized throughout this research investigation, the reciprocal lattice concept provides a natural framework to discuss x-ray diffraction from crystals. The elegant use of the reciprocal lattice in the Ewald construction of x-ray diffraction might appear abstract. However, a reciprocal lattice image of any crystalline sample can be experimentally obtained and provides an abundance of crystallographic information. Precession photography is one technique that records an undistorted two dimensional slice of the reciprocal lattice on photographic film. Since film is used as the recording medium, precession camera information is primarily qualitative. This in no way, however, limits the usefulness of this experimental technique.

M. J. Buerger (1944) devised the precession method as an alternative to oscillating crystal methods, which preserve the crystal symmetry on the photographic film. Unlike the oscillating crystal methods, precession photography provides an undistorted view of reciprocal

lattice levels; an n^{th} level corresponds to any reciprocal lattice plane which has the Miller index n common to all reciprocal lattice points on the plane. Once the precession method was incorporated into the commercially available precession camera, the usefulness and diversity of the precession method became well established (Buerger, 1964).

Figure IV.7a illustrates the essential precession camera geometry used to record the zero reciprocal lattice level (Buerger, 1964). The incident x-ray beam, which is fixed, passes through the sphere of reflection center, a reciprocal lattice point (the origin for zero level planes), and the photographic film center. Monochromatic radiation of wavelength λ is used so that the sphere of reflection radius is constant at λ^{-1}. A significant diffracted intensity results when a reciprocal lattice point intersects the sphere of reflection (see section II.D). A line drawn from the sphere of reflection center to the intersection point defines the diffracted intensity direction. Higher order reciprocal levels are recorded using essentially the same geometry.

The sample precesses about the incident x-ray beam at a nonzero precession angel μ, causing many reciprocal lattice points to intersect the sphere of reflection. The precession angle affects the area of reciprocal space that is recorded--the larger the precession angle, the larger the reciprocal level area that is photographed. The reciprocal level intersects the sphere of reflection in a circular locus, and the precession motion maintains a constant locus radius for all sample orientations. This property is exploited so that only one of the many levels that intersect the sphere of reflection are photographed during the precession motion. This is accomplished using a layer-line screen,

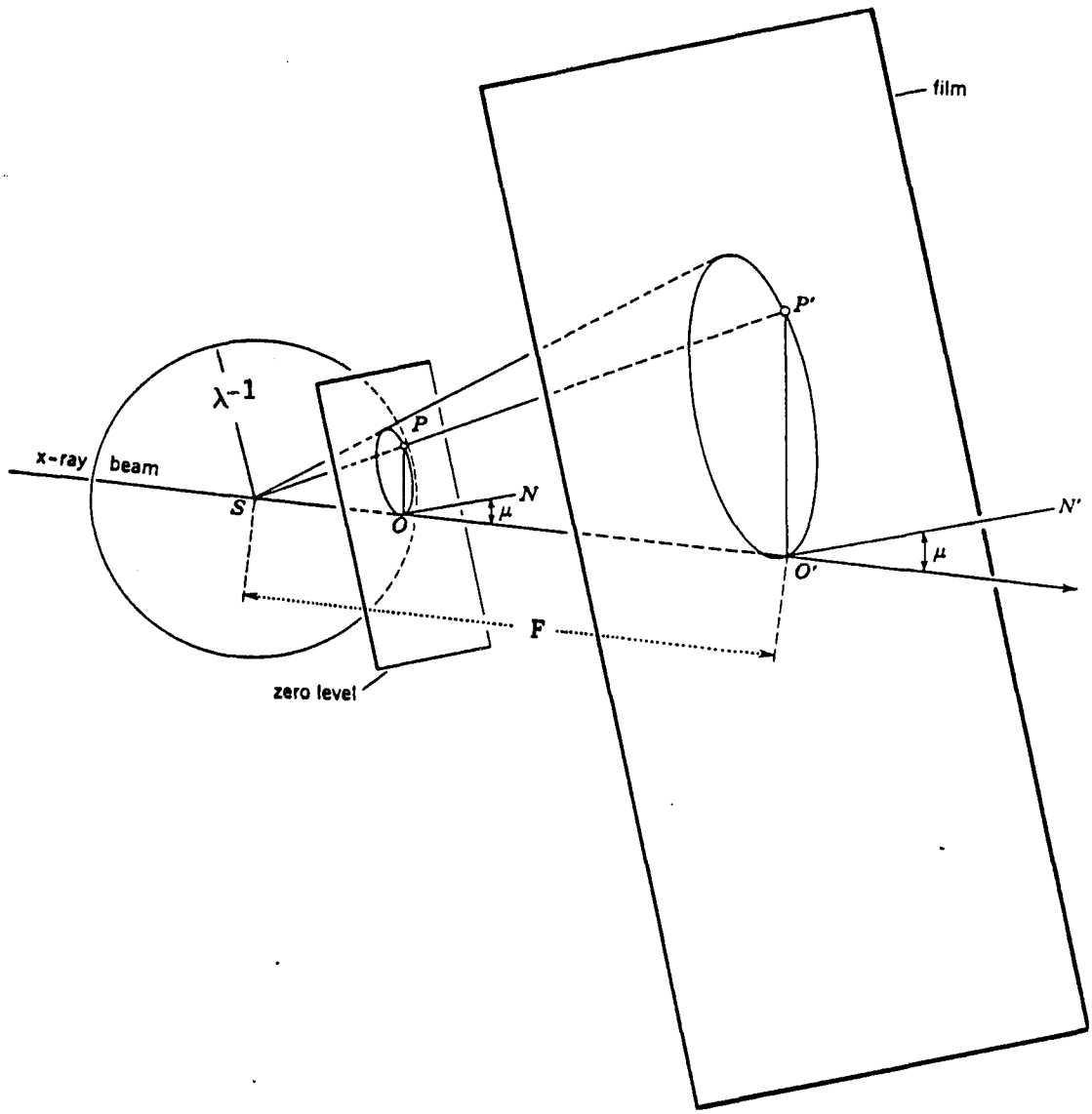

Figure IV.7a. The precession camera geometry. A reciprocal lattice point P located on the zero level intersects the sphere of reflection (radius λ^{-1}) resulting in a diffracted intensity that intersects the photographic film at P′. The reciprocal lattice level and film precess about the OO′ axis with precession angle μ

which is an x-ray absorbing sheet having a thin annulus removed. The screen, see Figure IV.7b, is positioned parallel to the reciprocal lattice level and moves with the precession motion of the reciprocal plane at a fixed distance, allowing diffraction from only one level to intersect the photographic film.

Like the layer-line screen, the film moves with the precession motion of the reciprocal level and maintains a fixed distance between sample and film centers. The recorded diffraction maxima form a magnified and undistorted image of the reciprocal lattice level. This is understood with the aid of two similar triangles shown in Figures IV.7a and IV.7b: ΔSOP and $\Delta SO'P'$. A reciprocal lattice point of the zero level intersects the sphere of reflection at point P and is responsible for the diffracted intensity that intersects the film at point P'. Provided that the film and reciprocal level are parallel,

$$O'P' = M(OP) \quad , \tag{IV.26a}$$

$$SO' = M(SO) \quad , \tag{IV.26b}$$

where the constant of proportionality M is related to the effective magnification of the recorded image. The distance OP represents the reciprocal lattice magnitude $|H(h,k,l)|$ associated with the reciprocal lattice point at P. The distance O'P' represents the distance from the film center to the recorded diffraction spot d_f. The sphere of reflection radius SO is λ^{-1}. The irradiated sample volume which diffracts radiation is located at S and the sample to film distance F is measured along SO'. Since OP and O'P' are parallel, reciprocal lattice

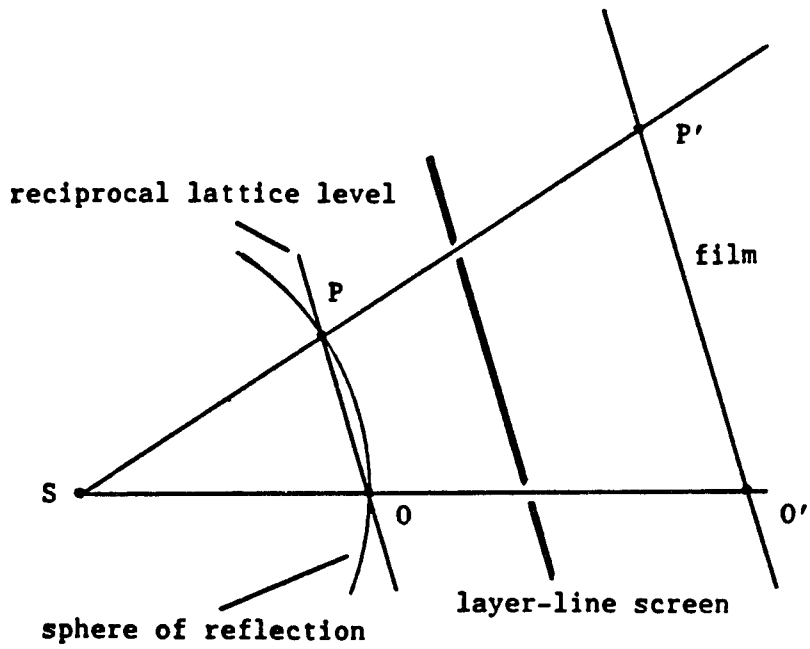

Figure IV.7b. Placement of the layer-line screen, which permits reflections from only one reciprocal lattice level to intercept the photographic film

directions within the photographed level are preserved on the film. Since $M=F\lambda$, according to equations IV.26a and IV.26b, a the linear relationship between $\mathbf{H}$ and $\mathbf{d}_f$ is expressed in terms of the apparatus parameters,

$$\mathbf{d}_f(h,k,l) = (F\lambda)\mathbf{H}(h,k,l) \quad , \qquad \text{(IV.27)}$$

where $\mathbf{d}_f(h,k,l)$ is the vector that points from the film center to the diffraction spot associated with $\mathbf{H}(h,k,l)$. Knowing the film to sample distance F and the radiation wavelength λ, distances and directions on the photographic film are converted to reciprocal lattice vectors of the crystal specimen. Since $|\mathbf{H}(h,k,l)|$ is the reciprocal of the interplanar spacing $d_{h,k,l}$ (see equation II.6), distances on the photographic film are related to unit cell distances. The above discussion is independent of the Miller index notation. For example, the (h,k,l,m) SL notation is equally valid.

Precession photographs reveal information on all SL components (substrate, buffer layer(s), and SL constituents), provided that the x-ray wavelength penetrates the substrate. The composite reciprocal lattice image is a superposition of all component reciprocal lattices, each sharing a common origin. Thus, any zero reciprocal level, which contains the reciprocal lattice origin, will reveal contributions from all SL components. Once the sample is properly oriented, a zero level precession photograph provides immediate information on both the crystallographic orientation and crystalline quality of each SL component. Using equation IV.27, the reciprocal lattice of each

component is identified, if the precession camera resolution can distinguish the differences in unit cell size. Epitaxial relationships between components are immediately assessed by inspection; parallel reciprocal lattice vectors indicate epitaxy.

Crystalline quality is directly related to the shape or distribution of diffraction maxima. Diffraction spots from good quality single crystals are sharp and localized. Diffraction from polycrystalline sample are characterized by circular streaking, the streak length being directly proportional to the degree of preferred orientation. Diffraction from amorphous materials, which lack long range periodic order, reveal diffuse rings on the precession photograph. These rings are related to average local spacings of neighboring atoms.

All precession photographs presented in this research investigation were recorded using a Huber 200 Precession Goniometer. Only zero level reciprocal planes are photographed. The crystal to film distance F is 60 mm. A molybdenum x-ray tube provides the incident radiation. A zirconium filter is placed between the tube and incident collimator to attenuate the K_β and other Mo characteristic lines. This establishes the Mo K_α emission line as the principal radiation source, which has a wavelength of 0.7093 Å. A 15 mm radius layer-line screen is situated 26 mm from the sample. The precession angle μ is 30°.

Typically, small samples having dimensions on the order of 0.1 millimeters are preferred for precession photography. This reduces absorption effects. However, composite multilayer films having lateral dimensions on the order of centimeters are applicable to precession photography (Bettini & Brandt, 1979). The precession camera procedure

used in this research investigation and its application to composite multilayer systems is described by Horning and Staudenmann (1986, 1987). Application of this procedure to additional systems is presented by Staudenmann, Horning, and Knox (1987). To compensate for the large sample size, a well collimated incident beam irradiates a small volume on the sample edge. This situation is very similar to a small sample that is completely bathed in the incident beam. Figures IV.8a and IV.8b illustrate the sample position on the precession camera spindle when the precession angle is zero (Horning & Staudenmann, 1986). Once the sample is properly oriented (Buerger, 1964), the film surface is centered and parallel to the incident beam at $\mu=0°$. The spindle axis is actually ~1 mm from the sample edge so that material intercepts the entire incident beam at arbitrary values of μ.

All samples of this research investigation are pieces of a larger crystal wafer. Samples are cut by cleaving the wafer along predominant crystallographic directions. This reduces the amount of crystal damage and provides cleaved faces which can be exploited during sample alignment on the precession camera using the autocollimator. Since the surface normal is parallel to the growth direction, the alignment procedure is relatively simple. Typically, only one alignment photograph is needed to position one of the in-plane crystallographic directions perpendicular to the x-ray beam. The orientation procedure is more difficult when no cleaved surfaces are present. A thorough treatment of sample orientation is presented by Elizabeth A. Wood (1963).

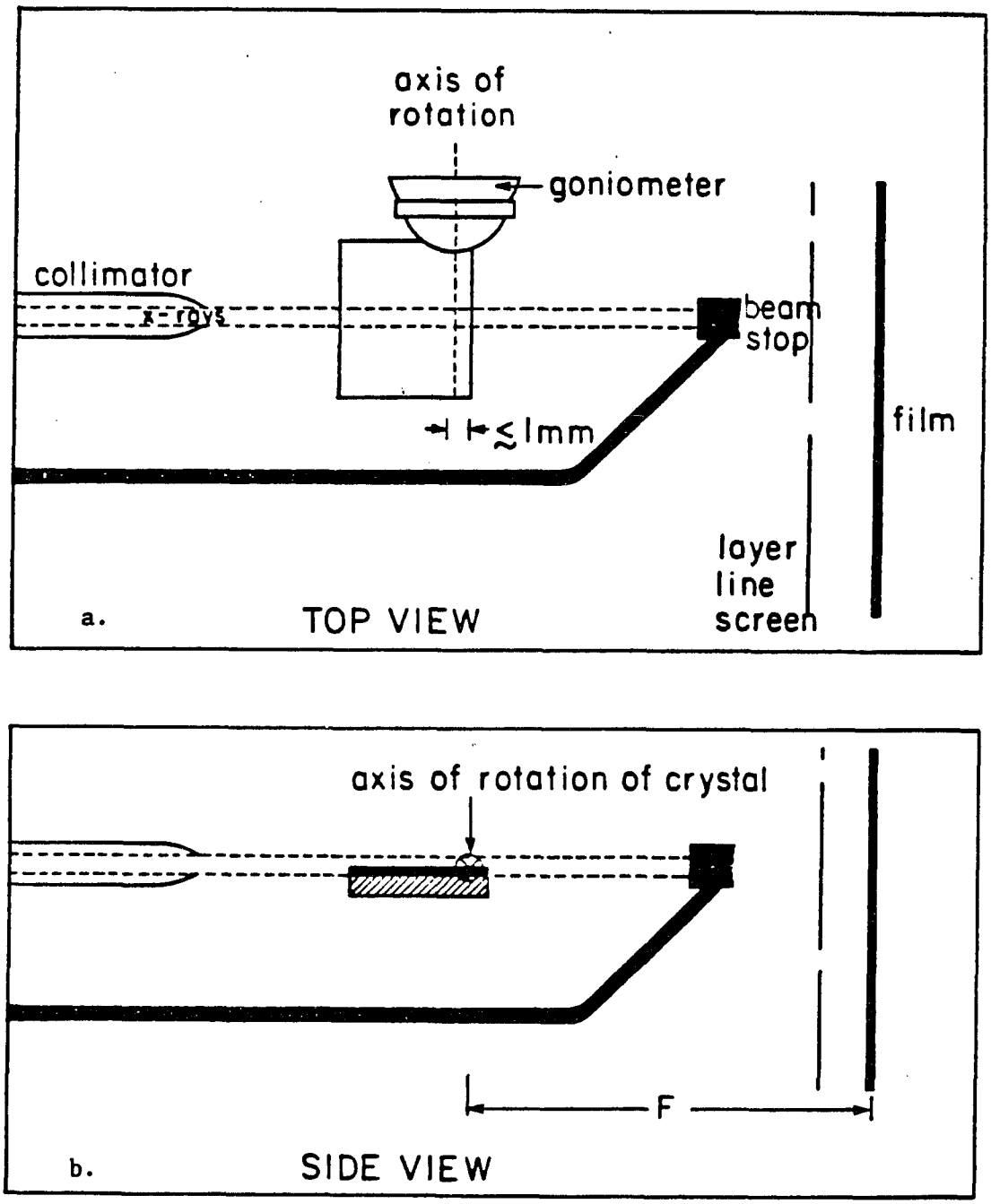

Figure IV.8. Figure (a) represents the top view and Figure (b) represents the side view of the sample placement on the precession camera spindle. The precession angle is set to 0° in both figures

Before placing a SL sample on the diffractometer, precession photographs are recorded to assess both the crystallographic orientation and overall quality of the composite SL system. This information aids the diffractometer optimization procedure. Precession photographs of SL samples are presented in the final two experimental chapters. A structural interpretation of each photograph is discussed and correlated to other results. These examples demonstrate the wealth of structural information that precession photography provides.

V. EXPERIMENTAL RESULTS: $Hg_{1-x}X_xTe$-CdTe

A. Experiment Overview

This chapter contains a summary of all experimental investigations related to HgTe-CdTe, $Hg_{1-x}Mn_xTe$-CdTe, $Hg_{1-x}Zn_xTe$-CdTe, and $Hg_{1-x}Cd_xTe$-CdTe SLs. The experimental results are divided into four sections: precession photography, diffractometer data, interdiffusion, and growth interdiffusion. In section V.B, precession photography is discussed. The information necessary for the structural interpretation of precession films is discussed first, followed by specific examples.

Section V.C concerns diffractometer results. This section is separated into four subsections, where each subsection concerns one specific SL system. The SL period, average constituent cell length along the growth direction, and Scherrer lengths are extracted and discussed for each sample. An evaluation of inhomogeneous SL growth based on these SL attributes is presented.

Section V.D concerns SL interdiffusion as a function of sample temperature. First, SL interdiffusion is defined. This introduction is followed by a mathematical description of interdiffusion. Several simplifying assumptions are introduced, and the consequences of these assumptions are discussed. Next, the experimental procedure is outlined, and the application of this procedure to SL samples are discussed. Finally, several general conclusions derived from the individual interdiffusion experiments are discussed.

The final section of this chapter concerns SL interdiffusion that occurs during growth. Two samples, which were specifically grown for

this investigation are discussed, and the information extracted from these samples is presented.

B. Precession Photography

1. Introduction

Precession photographs of $Hg_{1-x}X_xTe$-CdTe SLs do not reveal satellite structure, unlike the CdTe-ZnTe system. There are two primary reasons for this general observation. First, the SL periods of the $Hg_{1-x}X_xTe$-CdTe samples under investigation are typically larger than 70 Å. These large periods produce very closely spaced SL peaks for the 0.7093 Å wavelength of the precession apparatus. Consequently, the satellite peak spacing is below the limit of resolution for the precession geometry. Second, the $Hg_{1-x}X_xTe$-CdTe system is relatively free of strain. The bulk constituent cell lengths are approximately 0.3% different. Thus, the satellite peaks closest to the central peak are the most intense. However, compared to the central peaks, even the intensity of the first order satellites is much less. For example, the intense constituent diffraction regions such as the cubic (1,1,1) and (3,3,3) have first order satellite intensities which are several orders of magnitude less than the central peaks. Precession photographs of the $Hg_{1-x}X_xTe$-CdTe SLs reveal only the central peak SL reflections in addition to the substrate and buffer layer reflections.

Although the satellite peaks are not visible, precession photographs of the $Hg_{1-x}X_xTe$-CdTe system do provide valuable information on the composite SL system. The shape of the diffraction spots is related to the crystalline quality. Nearly perfect crystals will produce very

localized spots, while polycrystalline samples produce concentric diffraction rings that are centered on the precession film origin. Radial streaks that originate at each diffraction spot are associated with the less intense continuum radiation. The crystallographic relationship between the substrate and SL film is immediately identified by inspection of the precession photographs. Hence, the epitaxial quality of the composite SL system can be evaluated.

Table V.1 Sample review and precession camera summary

Sample	Substrate	Film	Orientation[a]			
			Substrate		Film	
			$\parallel$	$\perp$	$\parallel$	$\perp$
SL-24	GaAs	HgTe-CdTe	[1,1,0]	[0,0,1]	[$\bar{1}$,1,0]	[1,1,1]
					[1,$\bar{1}$,0]	
SL-63	GaAs	$Hg_{.9}Mn_{.1}Te$-CdTe	[$\bar{1}$,1,0]	[0,0,1]	[$\bar{1}$,$\bar{1}$,2]	[1,1,1]
					[1,1,$\bar{2}$]	
CT-1	GaAs	CdTe	[1,1,0]	[0,0,1]	[$\bar{1}$,1,0]	[1,1,1]
					[1,$\bar{1}$,0]	
			[$\bar{1}$,1,0]	[0,0,1]	[$\bar{1}$,$\bar{1}$,2]	[1,1,1]
					[1,1,$\bar{2}$]	

[a]With respect to the deposition surface.

Table V.1 summarizes the relevant attributes of the samples discussed in this section. All samples were provided by Jean-Pierre Faurie at the University of Illinois at Chicago, and were grown using the molecular beam epitaxy deposition process. The precession camera geometry is outlined in section VI.E. The incident radiation is derived from a molybdenum x-ray target. The 0.7093 Å Mo K_α emission line is isolated by passing the incident radiation through a zirconium filter, which reduces the K_β radiation component. Only zero-level precession photographs are recorded. The precession angle is 30° and the sample to film distance (F) is 60 mm.

Diffraction spots are indexed using equation IV.27. Inserting the values of F and λ, this equation becomes,

$$\mathbf{d}_f(h,k,l) = (42.558 \text{ mm Å})\mathbf{H}(h,k,l) \quad , \tag{V.1}$$

where $\mathbf{d}_f(h,k,l)$ is the position vector from film center to the (h,k,l) reflection measured in mm and $|\mathbf{H}(h,k,l)|$ is the reciprocal interplane spacing of the (h,k,l) reflection measured in $Å^{-1}$. Since both the GaAs and CdTe substrates are cubic materials, H(h,k,l) is simply related to the cubic cell dimension a by the following relation,

$$H^2(h,k,l) = \frac{[h^2+k^2+l^2]}{a^2} \quad , \tag{V.2}$$

where h,k, and l are the Miller indices. Combining equations V.1 and V.2,

$$(h^2+k^2+l^2) = \left[\frac{d_f a}{42.558}\right]^2 \quad . \qquad (V.3)$$

The procedure of assigning Miller indices to diffraction spots begins by computing $(h^2+k^2+l^2)$ for all spots. This implies knowledge of a, which is either 5.653 Å for GaAs or approximately 6.47 Å for HgTe and CdTe. Since the precession photographs represent an undistorted view of reciprocal space, [h,k,l] directions are easily identified, establishing a complete and consistent index assignment. Table V.2 lists the allowed reflections of the FCC (zincblende) structure for reflections having a maximum $(h^2+k^2+l^2)$ value of 80. In addition to the allowed reflections, Table V.2 lists the relative intensity of each reflection. The intensities are represented by three values: weak, medium, and strong. This assignment is based on equations II.41a-c. Reflections having both even and odd indices are forbidden in the zincblende system.

The use of equation V.3 to index a precession photograph is best demonstrated by example. Figure V.1 is a precession photograph of a HgTe-CdTe SL (SL-24) that was deposited on a GaAs substrate. The vertical direction of Figure V.1 represents reflections from crystallographic planes that are nearly perpendicular to the film surface. Since the precession photograph represents an undistorted view of reciprocal space, the horizontal direction corresponds to diffraction from planes having normals nearly parallel to the film surface. Miller indices are assigned to each diffraction spot (reciprocal lattice point) by computing the corresponding $(h^2+k^2+l^2)$ value and comparing it to the allowed zincblende values listed in Table V.2. Since GaAs and HgTe-CdTe

Table V.2 Allowed cubic zincblende reflections and corresponding intensities

$(h^2+k^2+l^2)$	(h,k,l)	Intensity[a]
3	(1,1,1)	M
4	(2,0,0)	W
8	(2,2,0)	S
11	(3,1,1)	M
12	(2,2,2)	W
16	(4,0,0)	S
19	(3,3,1)	M
20	(4,2,0)	W
24	(4,2,2)	S
27	(5,1,1) (3,3,3)	M
32	(4,4,0)	S
35	(5,3,1)	M
36	(6,0,0) (4,4,2)	W
40	(6,2,0)	S
43	(5,3,3)	M
44	(6,2,2)	W
48	(4,4,4)	S
51	(7,1,1) (5,5,1)	M
52	(6,4,0)	W

[a]Based on equations II.41a-c: $W \sim (f_a - f_b)^2$. $M \sim (f_a^2 + f_b^2)$, $S \sim (f_a + f_b)^2$.

Table V.2 continued

$(h^2+k^2+l^2)$	(h,k,l)	Intensity[a]
56	(6,4,2)	S
59	(7,3,1) (5,5,3)	M
64	(8,0,0)	S
67	(7,3,3)	M
68	(8,2,0) (6,4,4)	W
72	(8,2,2) (6,6,0)	S
75	(7,5,1) (5,5,5)	M
76	(6,6,2)	W
80	(8,4,0)	S

reflections are indistinguishable, an $(h^2+k^2+l^2)$ must be calculated using both cubic cell lengths. For reference, Figure V.2 represents a reproduction of Figure V.1 which labels the diffraction spots under consideration, and Table V.3 summarizes the application of equation V.3 to the labeled spots. An $(h^2+k^2+l^2)$ value need not be calculated for every spot; only a few indices are required to obtain two reciprocal basis vectors which can reconstruct all other spots. For completeness, Table V.3 lists all calculated $(h^2+k^2+l^2)$ values.

According to the vertical reflections (a-f) of Table V.3, the vertical photograph direction represents the [0,0,1] and [1,1,1] reciprocal lattice directions (from center to top) of the GaAs substrate and HgTe-CdTe constituent lattices, respectively. The horizontal photograph direction represents the [1,1,0] and $[\bar{1},1,0]$ reciprocal

Figure V.1. Precession photograph of a HgTe-CdTe SL (SL-24) deposited on a GaAs substrate. Reciprocal lattice points along both the [1,1,1] SL growth direction and the [0,0,1] GaAs surface normal are observed along the film vertical. The circled dot represents the approximate film center. Molybdenum K_α radiation, which passes through a zirconium filter, is incident on the sample (see section IV.E for precession geometry details). The attenuated molybdenum continuum radiation causes the observed radial streaking of the diffraction maxima

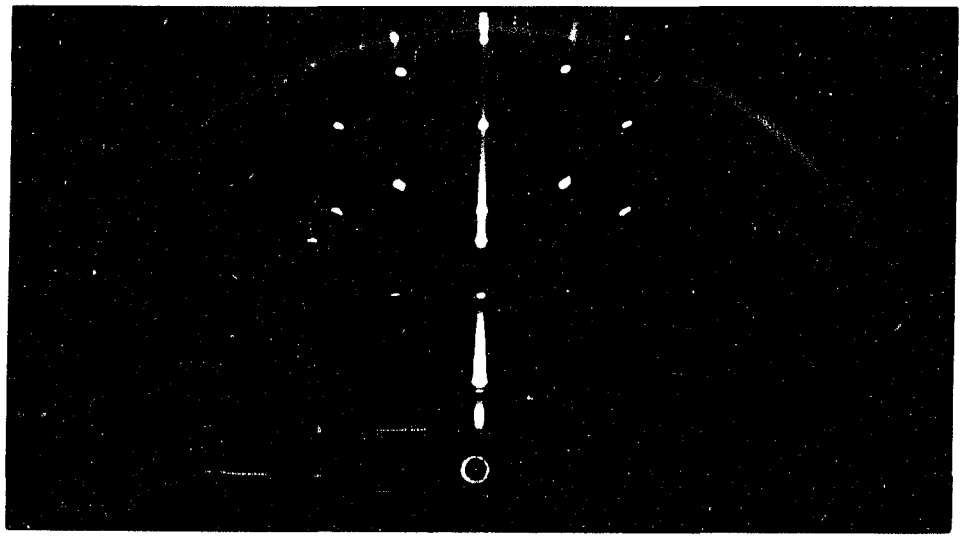

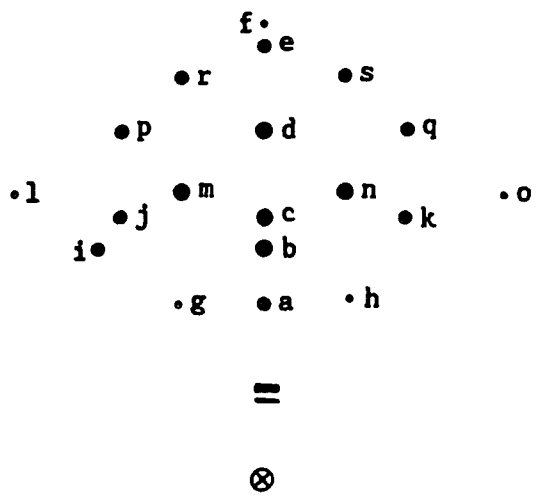

Figure V.2. A schematic of Figure V.1 (approximately to scale). The circled X marker represents the approximate precession film center. The spot labels are referenced in Table V.3

Table V.3 Radial distances, calculated $(h^2+k^2+l^2)$ values, and correct Miller index assignment for all diffraction spots labeled in Figure V.2

Spot label	Radial distance (mm)	$(h^2+k^2+l^2)$ GaAs	HgTe/CdTe	Reflection
a	22.8	9.2	12.0	(2,2,2) CdTe
b	30.0	15.9	20.8	(0,0,4) GaAs
c	34.2	20.6	27.0	(3,3,3) CdTe
d	45.3	36.2	47.4	(0,0,6) GaAs
e	57.0	57.3	75.1	(5,5,5) CdTe
f	60.3	64.2	84.0	(0,0,8) GaAs
g	25.0	11.0	14.4	$(\bar{1},\bar{1},3)$ GaAs
h	25.0	11.0	14.4	(1,1,3) GaAs
i	37.0	24.2	31.6	$(\bar{2},\bar{2},4)$ GaAs
j	38.8	26.6	34.8	(5,1,3) CdTe
k	39.0	26.8	35.2	(1,5,3) CdTe
l	49.5	43.2	56.6	$(\bar{3},\bar{3},5)$ GaAs
m	39.0	26.8	35.2	$(\bar{1},\bar{1},5)$ GaAs
n	39.2	27.1	35.5	(1,1,5) GaAs
o	49.4	43.1	56.4	(3,3,5) GaAs
p	39.4	27.4	35.9	(6,2,4) CdTe
q	39.7	27.8	36.4	(2,6,4) CdTe
r	53.6	50.7	66.4	$(\bar{1},\bar{1},7)$ GaAs
s	53.8	51.1	66.9	(1,1,7) GaAs

lattice directions (from center to right) of the substrate and SL, respectively. The SL film has been deposited epitaxially on the substrate since the reciprocal lattice of each component are related; the GaAs [0,0,1] vector is parallel to the SL [1,1,1] vector and the GaAs [1,1,0] vector lies along the SL [$\bar{1}$,1,0] direction. Figure V.1 represents the superposition of both the GaAs and HgTe-CdTe reciprocal lattices. This is illustrated by Figures V.3 and V.4, which represent isolated GaAs and HgTe-CdTe reciprocal lattice orientations present in Figure V.2. When properly scaled, the superposition of Figures V.3 and V.4 reconstructs all reciprocal lattice points observed in Figure V.2. In addition, all spots of Figure V.2, which are typical of all SLs studied in this research investigation, are localized and well defined. This suggests that the macroscopic coherence of all SL components are quite good. The enormous cell size mismatch, 5.653 Å for GaAs and approximately 6.47 Å for the HgTe-CdTe constituents, has not disrupted the majority of the SL film. Misfit dislocations are very probably present at the substrate-SL interface, however, this disrupted region is not large enough to be detected on the precession photograph.

2. Twinning

Since an investigation of the SL film is of principal interest, all samples are oriented such that the precession photographs contain the reciprocal lattice direction associated with the growth normal. This is easily accomplished using an autocollimator, which is an accessory of the precession camera used for sample alignment. Using the autocollimator, the optically reflecting film surface is positioned

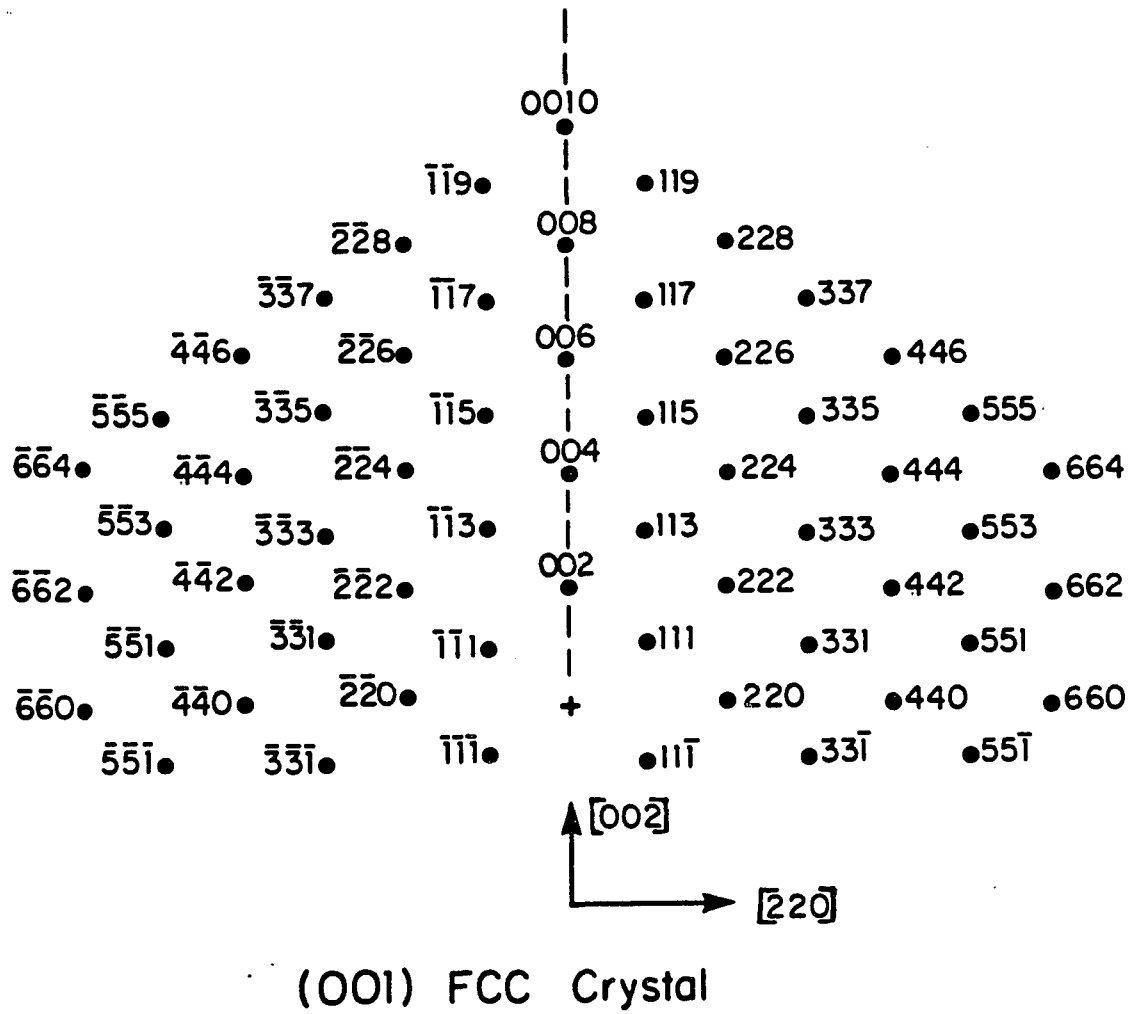

Figure V.3. An illustration of an indexed precession film that corresponds to a face-centered cubic lattice having a [0,0,1] surface normal. This plane represents the GaAs reflections of the precession film shown in Figure V.1. Notice that the reciprocal points are symmetrically distributed across the vertical [0,0,1] axis

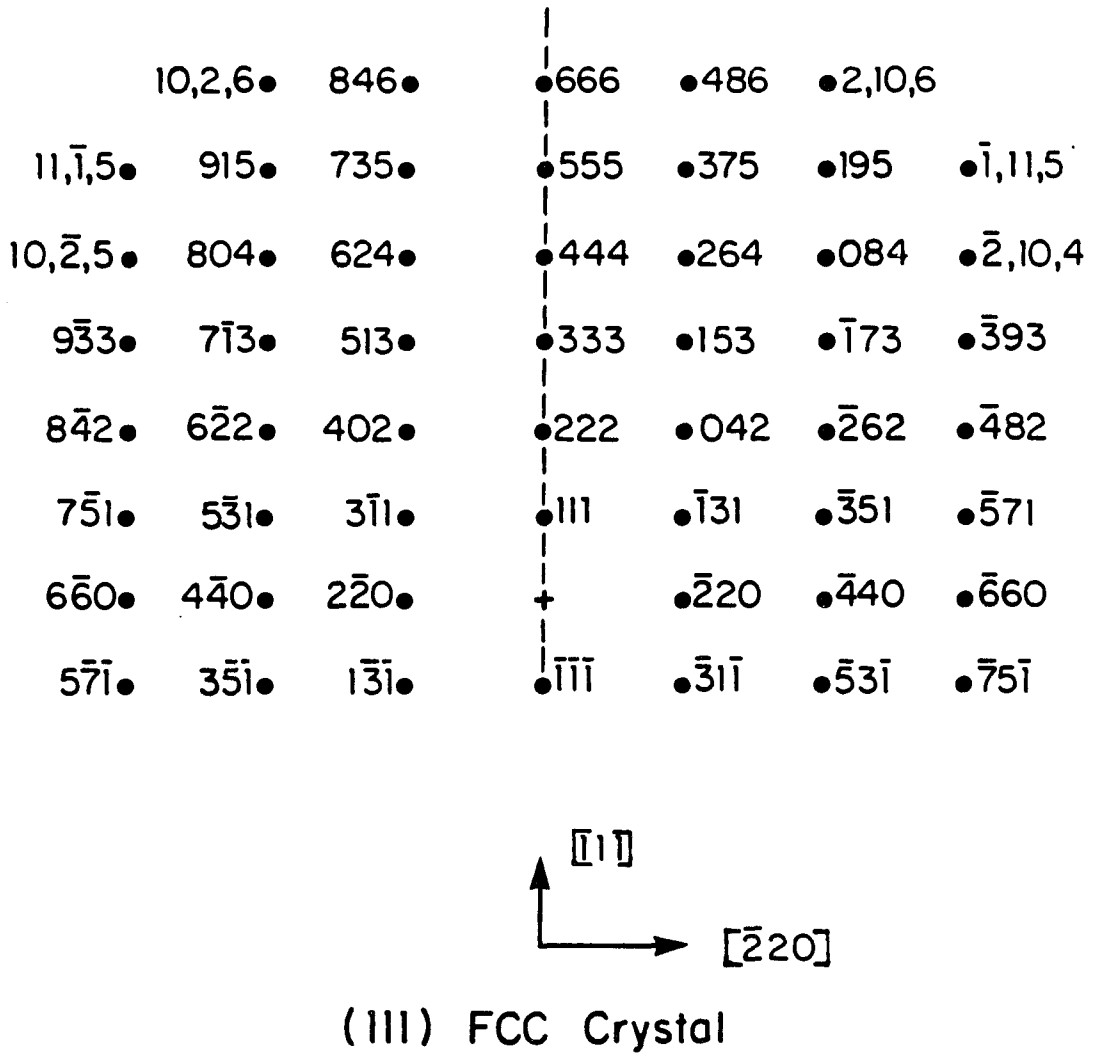

Figure V.4. An illustration of an indexed precession film that corresponds to a face-centered cubic lattice having a [1,1,1] surface normal. This plane represents the CdTe and HgTe reflections of the precession film shown in Figure V.1. Notice that the reciprocal points are symmetrically distributed across the vertical [1,1,1] axis

perpendicular to both the x-ray beam and precession camera spindle. This places the reciprocal lattice vector associated with the growth direction coincident with the precession film vertical. Once the growth direction is aligned, the sample is rotated about the growth direction axis until a predominant reciprocal lattice vector is situated parallel to the spindle and perpendicular to the x-ray beam. This reciprocal lattice vector is associated with the film horizontal.

Figure V.5a illustrates the geometrical relationship of the precession camera (spindle axis and x-ray beam), reciprocal lattice, and recorded reciprocal level for the HgTe-CdTe SL film discussed above. Figure V.4 is the recorded reciprocal level depicted in Figure V.5a. By performing a 90° rotation about the [1,1,1] axis (growth normal), a different reciprocal level is recorded by the precession camera. This geometry is illustrated in Figure V.5b and the recorded reciprocal level is illustrated in Figure V.6. The $[\bar{1},1,0]$ axis of Figure V.4 is replaced by the $[\bar{1},\bar{1},2]$ axis to form Figure V.6. Notice that the two-fold symmetry of Figure V.4 is not present in Figure V.6. A similar 90° rotation about the [0,0,1] GaAs axis replaces the [1,1,0] direction of Figure V.3 with the $[\bar{1},1,0]$ direction. Since these crystallographic directions are symmetrically identical, the observed reciprocal lattice level for the GaAs lattice appears to be unaffected by this 90° rotation.

Figure V.7 shows a precession photograph of a $Hg_{.9}Mn_{.1}Te$-CdTe SL (SL-63) that was grown on a GaAs substrate. The sample orientation is described by Figure V.5b. Like SL-24, the constituent lattice parameter of $Hg_{.9}Mn_{.1}Te$ and CdTe are approximately 6.47 Å so that one cubic cell

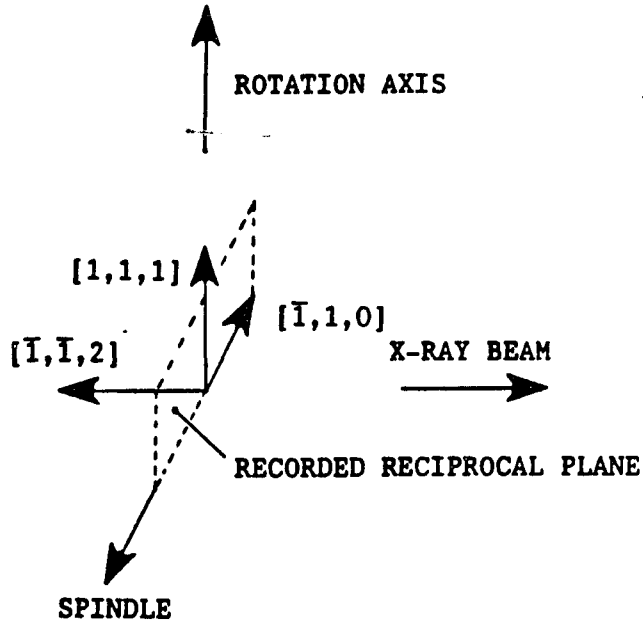

Figure V.5a. Spatial relationship of the precession camera film and the reciprocal space vectors of the mounted sample. The precession camera geometry is defined by the x-ray beam direction and spindle axis. The dotted region represents the orientation of the recorded reciprocal space plane with respect to the reciprocal lattice vectors of the sample. Twinning can not be observed with this particular sample orientation

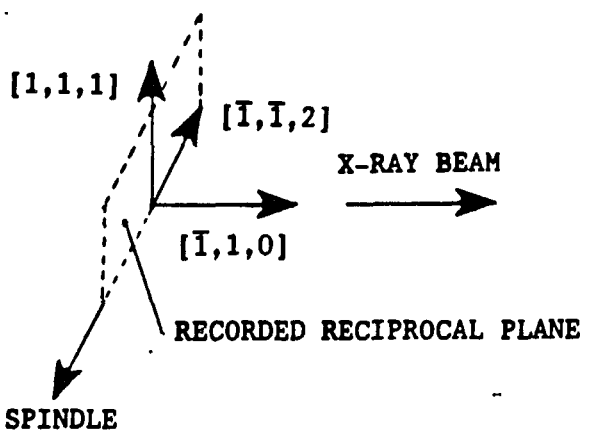

Figure V.5b. Spatial relationship of the precession camera film and the reciprocal lattice vectors of the mounted sample. The precession camera geometry is defined by the x-ray beam direction and spindle axis. The dotted region represents the orientation of the recorded reciprocal space plane with respect to the reciprocal lattice vectors of the sample. The sample orientation is derived by rotating the sample of Figure V.5a by 90° about the labeled rotation axis, which coincides with the [1,1,1] growth direction for a zero precession angle (μ=0). This rotation aligns different crystallographic axes with respect to the precession film. Twinning can be observed with this sample orientation

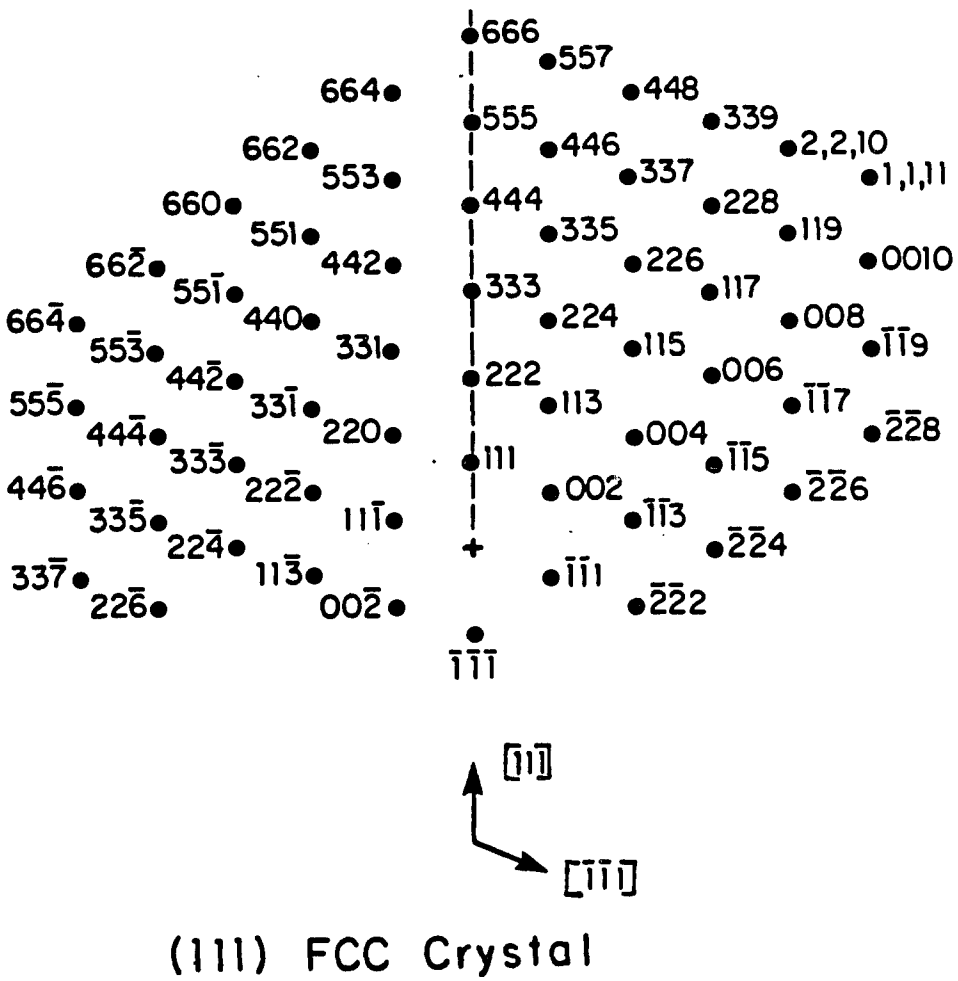

Figure V.6. An illustration of an indexed precession film that corresponds to a face-centered cubic lattice having a [1,1,1] surface normal. This reciprocal plane is derived by performing a 90° rotation about the [1,1,1] vertical axis of Figure V.4. Unlike Figure V.4, the reciprocal points are not symmetrically distributed across the dotted vertical axis

Figure V.7. Precession photograph of a $Hg_{.9}Mn_{.1}Te$-CdTe SL (SL-63) deposited on a GaAs substrate. Reciprocal lattice points along both the [1,1,1] SL growth direction and the [0,0,1] GaAs surface normal are observed along the film vertical. Twinning is observed in this figure. The circled dot represents the approximate film center. Molybdenum K_α radiation, which passes through a zirconium filter, is incident on the sample (see section IV.E for precession geometry details). The attenuated molybdenum continuum radiation causes the observed radial streaking of the diffraction maxima

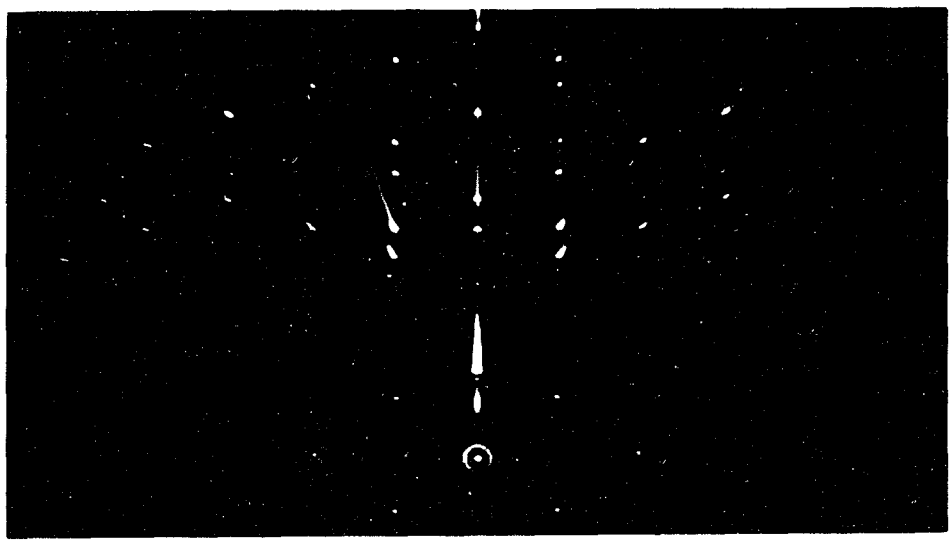

size describes the precession photograph features of the SL film. Clearly, there is two-fold symmetry present in this photograph. This unexpected observation is apparently the result of three diffraction contributions--the GaAs substrate and two orientations of the SL film. The GaAs substrate is oriented such that the [0,0,1] axis lies along the film vertical and the $[\bar{1},1,0]$ axis lies along the horizontal. This particular reciprocal level, which is illustrated in Figure V.3, is symmetric across the [0,0,1] axis. After removing the GaAs reflections from consideration, the remaining reciprocal level does not resemble Figure V.6. However, all SL reflections are consistent with a superposition of both Figure V.6 and its mirror image with respect to the [1,1,1] axis. Thus, two orientations of the SL film coexist on the substrate. Examining the symmetry present in Figures V.4 and V.6, the two SL orientations are related by a 180° rotation about the [1,1,1] crystallographic axis. The mirror related reciprocal levels are a manifestation of this rotational symmetry.

Twinning can account for the presence of two orientations that coexist in the SL film (Kelly & Groves, 1970). The 180° rotational relationship of the two orientations describes a common stacking disorder that occurs during the epitaxial deposition of zincblende materials along the [1,1,1] growth direction (Stowell, 1975). The relative abundance of the two orientations is estimated by the spot intensities of each orientation. Since the spot intensities of Figure V.7 are approximately equivalent, each orientation is equally abundant. Thus, the twinning of the SL film is extensive.

SL-24 reveals the same two fold symmetry when oriented according to

Figure V.5b. Diffraction from both crystallographic orientations are present in Figure V.1. The symmetry associated with the sample orientation of Figure V.5a requires that peaks from each crystallographic orientation diffract onto the same film positions. Thus, only the geometry illustrated in Figure V.5b is sensitive to twinning effects.

SL-63 is not an isolated example of a twinned SL. In fact, twinning was observed for every $Hg_{1-x}X_xTe$-CdTe (X=Mn, Cd, or Zn) SL that was placed on the precession camera. This includes SL films, grown by either molecular beam epitaxy or metalorganic chemical vapor deposition, that have been deposited on GaAs, CdTe, and $Cd_xZn_{1-x}Te$ substrates. Diffraction from substrates that have [1,1,1] surface normals is isolated by probing the back side of the substrate. No twinning was observed in these substrates.

Twinning is apparently not a manifestation of SL growth. Figures V.8a and V.8b are precession photographs of a CdTe film deposited on a GaAs substrate using the molecular beam epitaxy technique. Figure V.8a corresponds to the sample orientation outlined in Figure V.5a and V.8b corresponds to V.5b. Twinning is clearly revealed in Figure V.8b. This is an important observation, since a CdTe buffer layer is deposited before the SL deposition. Twinned domains which are present in the buffer layer probably propagate into the SL film.

C. Diffractometer Results

This section contains a summary of diffractometer information. The first part of this section concerns HgTe-CdTe SLs and includes an

Figure V.8a. Precession photograph of a CdTe film deposited on a GaAs substrate. Reciprocal lattice points along both the [1,1,1] CdTe growth normal and the [0,0,1] GaAs surface normal are observed along the film vertical. The sample orientation is defined by Figure V.5a. Twinning can not be observed for this orientation. The circled dot represents the approximate film center. Molybdenum K_α radiation, which passes through a zirconium filter, is used (see section IV.E for precession geometry details). The attenuated molybdenum continuum radiation causes the observed radial streaking of the diffraction maxima

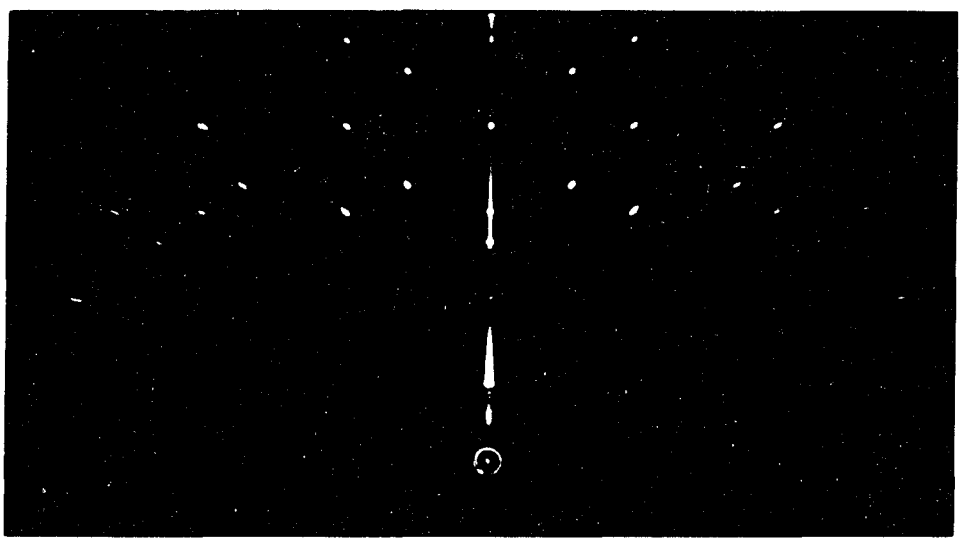

Figure V.8b. Precession photograph of a CdTe film deposited on a GaAs substrate. Reciprocal lattice points along both the [1,1,1] CdTe growth normal and the [0,0,1] GaAs surface normal are observed along the film vertical. The sample orientation is defined by Figure V.5b. Twinning is observed for this orientation. The circled dot represents the approximate film center. Molybdenum K_α radiation, which passes through a zirconium filter, is used (see section IV.E for precession geometry details). The attenuated molybdenum continuum radiation causes the observed radial streaking of the diffraction maxima

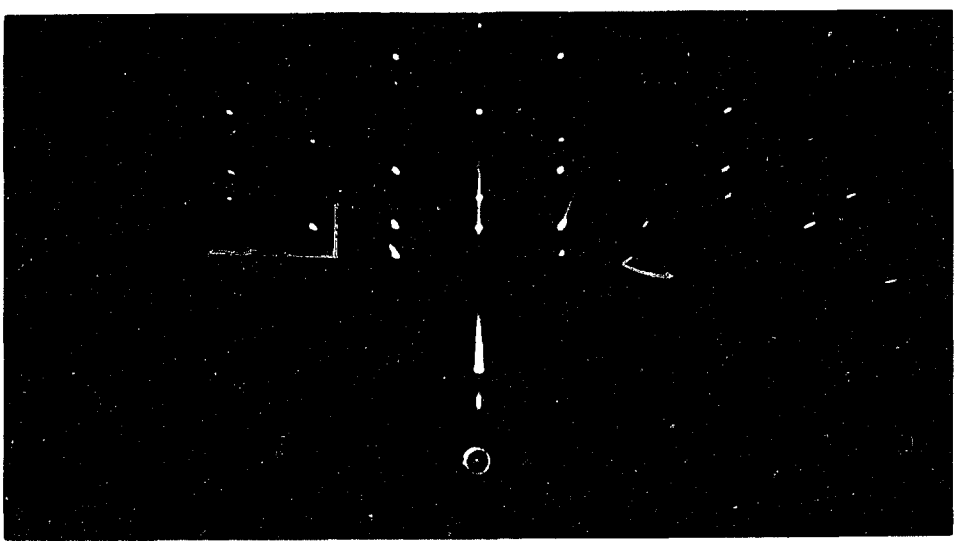

investigation on inhomogeneous SL growth. The surface size of most SL samples are approximately 3mm by 5mm. However, six of the thirteen HgTe-CdTe samples are quite large, having more than 150 mm^2 of surface area. These samples, SL-1P through SL-6P, were large enough to scan up to three different areas of the film surface, providing information on inhomogeneous SL growth. Six of the other seven SL samples were characterized before being heated at elevated temperatures during the interdiffusion investigation. The preliminary diffractometer data of these sample are discussed in the first subsection. The remainder of this section concerns the alloyed SL systems: $Hg_{1-x}Mn_xTe$-CdTe, $Hg_{1-x}Zn_xTe$-CdTe, and $Hg_{1-x}Cd_xTe$-CdTe. Diffraction results from two HgTe-CdTe SLs, SL-93 and SL-95, are not discussed in this section. These two samples were grown specifically for a growth interdiffusion investigation and the diffraction results are presented in section V.E.

1. HgTe-CdTe

Thirteen HgTe-CdTe SLs are characterized by performing ω-2Θ scans along the growth direction. Both the SL period and average constituent cell size are calculated, diffraction structure are identified, and peak breadths are assessed. The inhomogeneous SL growth investigation is discussed first, followed by the characterization of the other seven samples. The growth history of all thirteen samples is summarized in Table V.4. Samples SL-1P through SL-6P were purchased from Jean-Pierre Faurie at the University of Illinois at Chicago and provided by Elizabeth A. Patten at the Hughes Santa Barbara Research Center. ML-21B was provided by Owen K. T. Wu at the Hughes Research Laboratory.

Table V.4 Available growth history of HgTe-CdTe SLs

Sample	Substrate		Buffer layer				Superlattice	
	growth normal	type	growth normal	type	thickness (μ)	growth normal	constituent layer ratio (HgTe/CdTe Å)	thickness (μ)
SL-1P	[1,1,1]	$Cd_{.96}Zn_{.04}Te$	[1,1,1]	CdTe	0.01	[1,1,1]	69/31	1.66
SL-2P	[1,1,1]	$Cd_{.96}Zn_{.04}Te$	[1,1,1]	CdTe	0.01	[1,1,1]	85/45	2.22
SL-3P	[1,1,1]	$Cd_{.96}Zn_{.04}Te$	[1,1,1]	CdTe	0.01	[1,1,1]	70/35	1.79
SL-4P	[1,1,1]	$Cd_{.96}Zn_{.04}Te$	[1,1,1]	CdTe	0.01	[1,1,1]	61/25	1.47
SL-5P	[0,0,1]	GaAs	[1,1,1]	CdTe	3.05	[1,1,1]	45/26	1.28
SL-6P	[0,0,1]	GaAs	[1,1,1]	CdTe	1.31	[1,1,1]	37/62	1.89
ML-21B	[0,0,1]	CdTe	[0,0,1]	CdTe	1.00	[0,0,1]	50/55	1.58
SL-13	[0,0,1]	GaAs	[1,1,1]	CdTe	2.50	[1,1,1]	97/60	3.93
SL-25	[0,0,1]	GaAs	[1,1,1]	CdTe	2.20	[1,1,1]	58/35	1.40
SL-48	[1,1,1]	CdTe	[1,1,1]	CdTe	0.02	[1,1,1]	42/52	1.60
SL-49	[1,1,1]	CdTe	[1,1,1]	CdTe	0.02	[1,1,1]	35/62	1.38
SL-52	[0,0,1]	GaAs	[1,1,1]	CdTe	1.30	[1,1,1]	36/61	1.84
SL-54	[0,0,1]	GaAs	[1,1,1]	CdTe	3.10	[1,1,1]	44/25	1.24

Samples SL-13 through SL-54 were provided by Jean-Pierre Faurie at the University of Illinois at Chicago. All samples were grown by molecular beam epitaxy (Faurie, Million & Piaguet, 1982) at 185 C. A CdTe buffer layer was deposited before SL deposition.

During the inhomogeneous growth investigation, a 0.5 mm by 4 mm slit collimator was placed at the monochromator exit and a 1 mm by 8 mm collimator was placed before the detector. Maximum scan resolution was obtained by aligning the smaller dimension of each collimator parallel to the scattering plane. The 2 mm^2 beam cross sectional is a compromise between two competing factors: minimizing the diffracting volume, and maximizing the detected intensity. By minimizing the diffracting volume, more regions of the sample can be probed and local inhomogeneous effects within the diffracted volume are minimized. However, the diffracting volume must be large enough so that the count time at each diffraction angle of the scan is reasonable (under 100 seconds per point). The 2 mm^2 beam cross section allowed for only one region of SL-3P to be probed. In addition, only one diffraction scan containing more than one constituent diffraction region was recorded for SL-5P, preventing the calculation of the θ_0 offset required for period comparisons among different diffraction scans. Thus, the investigation of inhomogeneous growth is restricted to a survey of four samples. Figure V.9 illustrates the regions that were probed on each sample.

In general, the SL periods are found to be incommensurate with the average constituent unit cell. A summary of the least-squares fit to the diffraction data is listed in Table V.5. All fits are based on peak information from three constituent diffraction regions: (1,1,1),

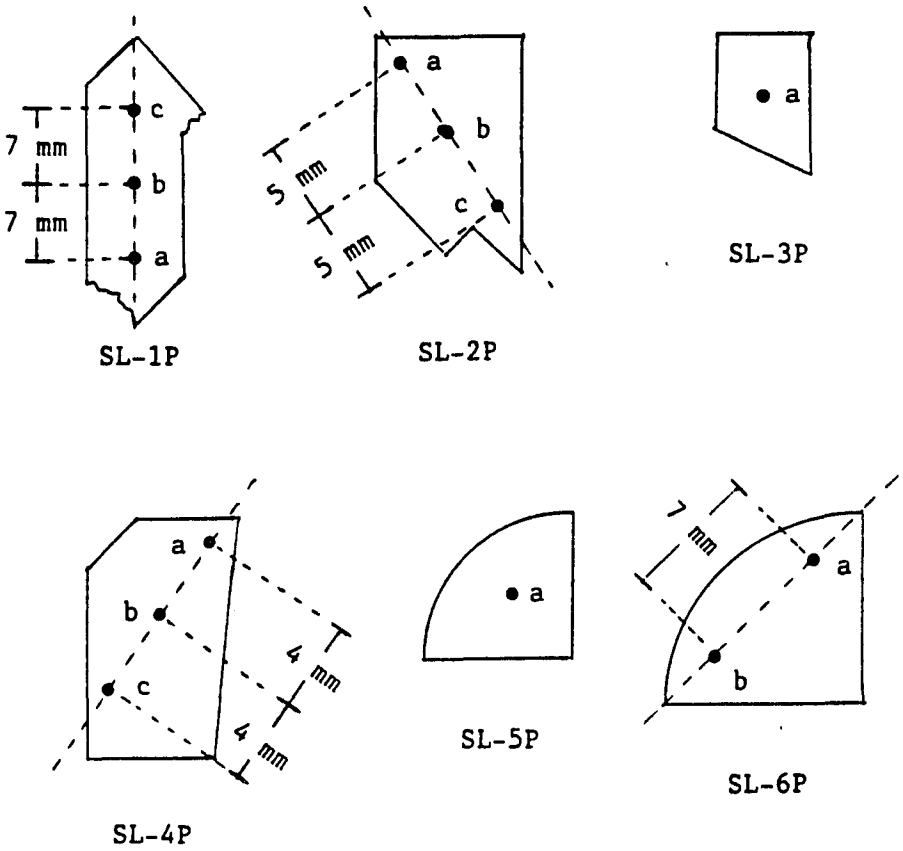

Figure V.9. Sample regions that were probed during the inhomogeneous growth investigation. The dotted line represents the orientation of the collimator slit height, which is perpendicular to the scattering plan. These sample outlines are not to scale. The labeled regions are referenced in Table V.5

Table V.5 Least-squares fit summary of both the period and average constituent cell size along the growth direction

Sample	Location[a]	Period L (Å)	Avg. const. cell length[b] <c> (Å)	Const. cells per period[c]	weighted χ^2[d]	No. of peaks included in fit (central)	(satellite)
SL-1P	a	100.8 ± 0.4	11.205 ± 0.001	8.99 ± 0.04	4.50	3	15
	b	106.3 ± 0.6	11.209 ± 0.002	9.48 ± 0.05	4.06	3	16
	c	106.1 ± 0.7	11.208 ± 0.002	9.47 ± 0.06	7.84	3	15
SL-2P	a	120. ± 1.	11.227 ± 0.002	10.66 ± 0.09	6.36	3	17
	b	109.5 ± 0.4	11.230 ± 0.001	9.75 ± 0.03	13.57	3	17
	c	106.6 ± 0.4	11.213 ± 0.001	9.51 ± 0.03	14.53	3	15
SL-3P	a	105.1 ± 0.9	11.209 ± 0.003	9.37 ± 0.08	1.53	3	16
SL-4P	a	82.9 ± 0.3	11.206 ± 0.002	7.40 ± 0.03	5.71	3	20
	b	84.6 ± 0.2	11.200 ± 0.001	7.56 ± 0.02	7.03	3	18
	c	81.4 ± 0.3	11.196 ± 0.001	7.27 ± 0.02	6.18	3	14
SL-5P	a	89.9 ± 0.4	11.219 ± 0.002	8.02 ± 0.04	7.01	3	15
SL-6P	a	78.6 ± 0.5	11.228 ± 0.003	7.00 ± 0.04	13.49	3	13
	b	94.4 ± 0.5	11.225 ± 0.001	8.41 ± 0.04	2.94	3	12

[a]Sample region probed (see Figure V.9).

[b]Average constituent cell length along the growth direction (hexagonal unit cell parameter).

[c]The SL period divided by the average constituent cell length.

[d]Defined by equation IV.24a.

(2,2,2), and (3,3,3). According to the number of average constituent cell lengths per period (see Table V.5), only two of the thirteen sample locations that were probed have commensurate periods. Observations of incommensurate SLs are not uncommon. For example, incommensurate SLs have been observed in the $Ga_{1-x}Al_xAs$-GaAs system (Kervarec, Baudet, Caulet, Auvray, Emery & Regreny, 1984).

All four samples exhibit inhomogeneous growth, with observed period variations as large as 16% over a 9 mm distance. These variations are quite dramatic and have severe consequences for device applications. Unfortunately, the film structure that is responsible for the observed inhomogeneous growth can not be identified. Specific knowledge of the growth environment, which is unknown for these samples, is required to extract additional structural information from the diffraction analysis. For example, a nonzero temperature gradient within the heated substrate can affect the concentration uniformity of the atomic species across the SL film (Sivananthan, Chu, Reno & Faurie, 1986; Reno, Sporken, Kim, Hsu & Faurie, 1987). In addition, the geometrical relationship between the surface and impinging molecular beams changes across the surface. In an effort to reduce inhomogeneous growth, film growers are rotating the substrate during film deposition (Monfroy, 1987). Diffraction information from rotated samples could gauge the effectiveness of this method.

The average constituent cell length, denoted <c>, remains fairly constant among the probed regions. All variations are smaller than 0.15% of the average lattice spacing. The is reasonable, since the difference of bulk cell sizes for HgTe (a_{hex}=11.189 Å) and CdTe

(a_{hex}=11.224 Å) is approximately 0.3%. Measured values of <c> should vary between 11.189 Å and 11.224 Å, depending on the relative concentration of the HgTe and CdTe. However, no correlation between <c> and the predicted HgTe/CdTe ratio (see Table V.4) is apparent. This discrepancy could be related to the precision of measuring <c> for any one diffraction scan.

Additional inhomogeneous growth information can be extracted from SL-4P, which actually contains two SL domains having different periods. A diffraction scan of SL-4P (position a) is shown in Figure V.10. The well defined SL peaks correspond to the principal period listed in Table V.5. The lower intensity peaks which are superposed on the principal satellite structure are satellites associated with a second period. The central peaks of both periods are coincident, indicating that both domains have a common average constituent composition. For comparison, Figure V.11 shows a diffraction scan of SL-3P, which has a single well defined period. No superposition of satellite peaks is present.

The multiple SL structure of SL-4P is consistent with the observation of multiple surface structure during growth. The growth of SL-4P was monitored using reflection high energy electron diffraction (RHEED), which provides structural information on the evolving surface during film deposition (Cohen, Pukite, Van Hove & Lent, 1986). Superstructures were observed in both the HgTe and CdTe layers throughout the SL deposition (Patten, 1986). Isolated peak positions of the second period are found only in the (3,3,3) constituent diffraction region. To be meaningful, a least-squares fit to both domains for each sample location must involve only the (3,3,3) region. A least-squares

Figure V.10. ω-2Θ scans over the (1,1,1), (2,2,2), and (3,3,3) constituent diffraction regions of SL-4P at sample location a (see Figure V.9) using a 1.47639 Å radiation wavelength. The natural logarithm of the diffracted intensity is plotted as a function of the Bragg angle Θ. The dots represent measured data, and the line represents a 3 point smooth over the measured data

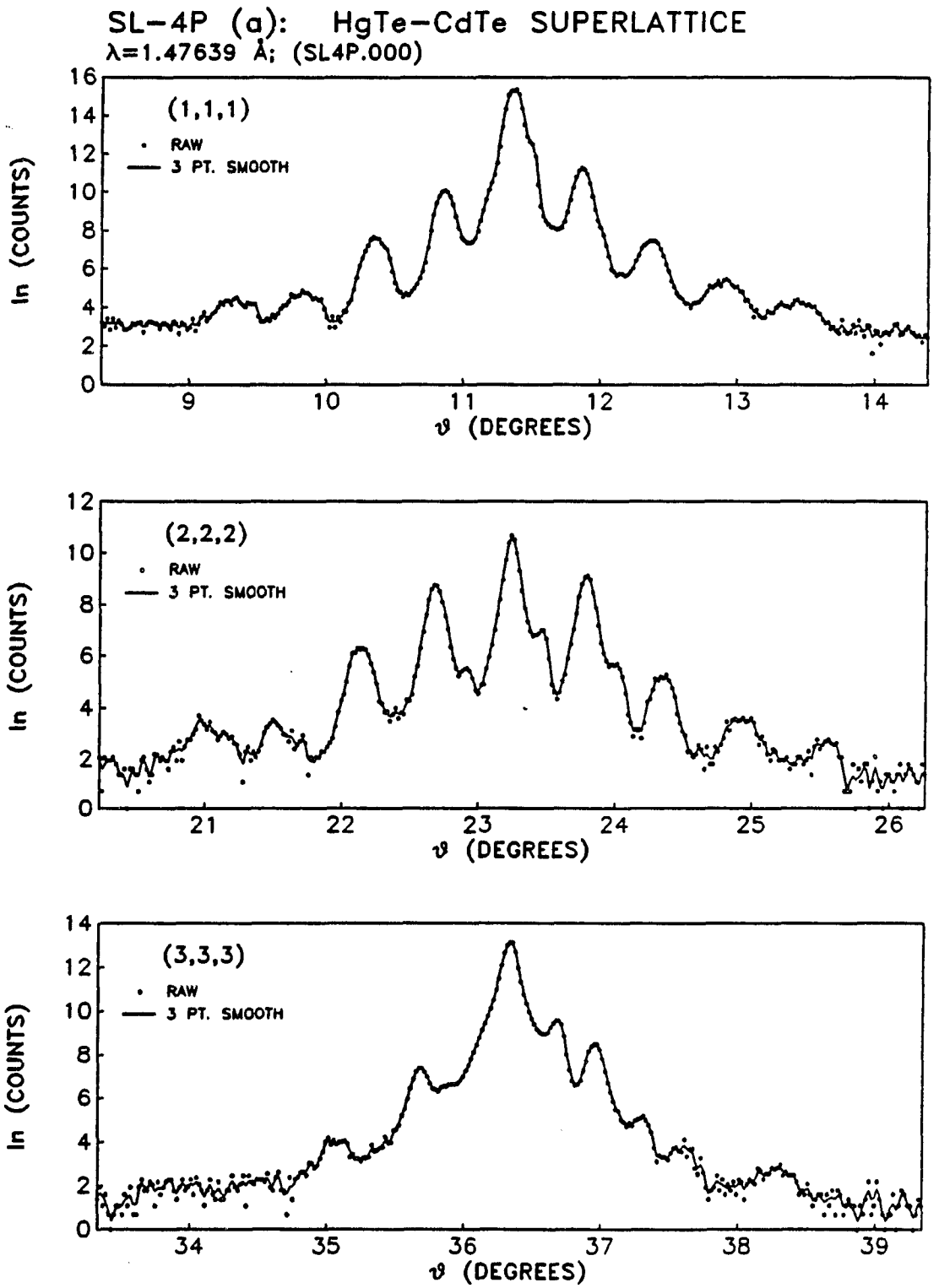
SL-4P (a): HgTe-CdTe SUPERLATTICE
λ=1.47639 Å; (SL4P.000)
(1,1,1)
RAW
3 PT. SMOOTH
ln (COUNTS)
ϑ (DEGREES)
(2,2,2)
RAW
3 PT. SMOOTH
ln (COUNTS)
ϑ (DEGREES)
(3,3,3)
RAW
3 PT. SMOOTH
ln (COUNTS)
ϑ (DEGREES)

Figure V.11. ω-2Θ scans over the (1,1,1), (2,2,2), and (3,3,3) constituent diffraction regions of SL-3P using a 1.47639 Å radiation wavelength. The natural logarithm of the diffracted intensity is plotted as a function of the Bragg angle Θ. The dots represent the measured data, and the line represents a 3 point smooth over the measured data

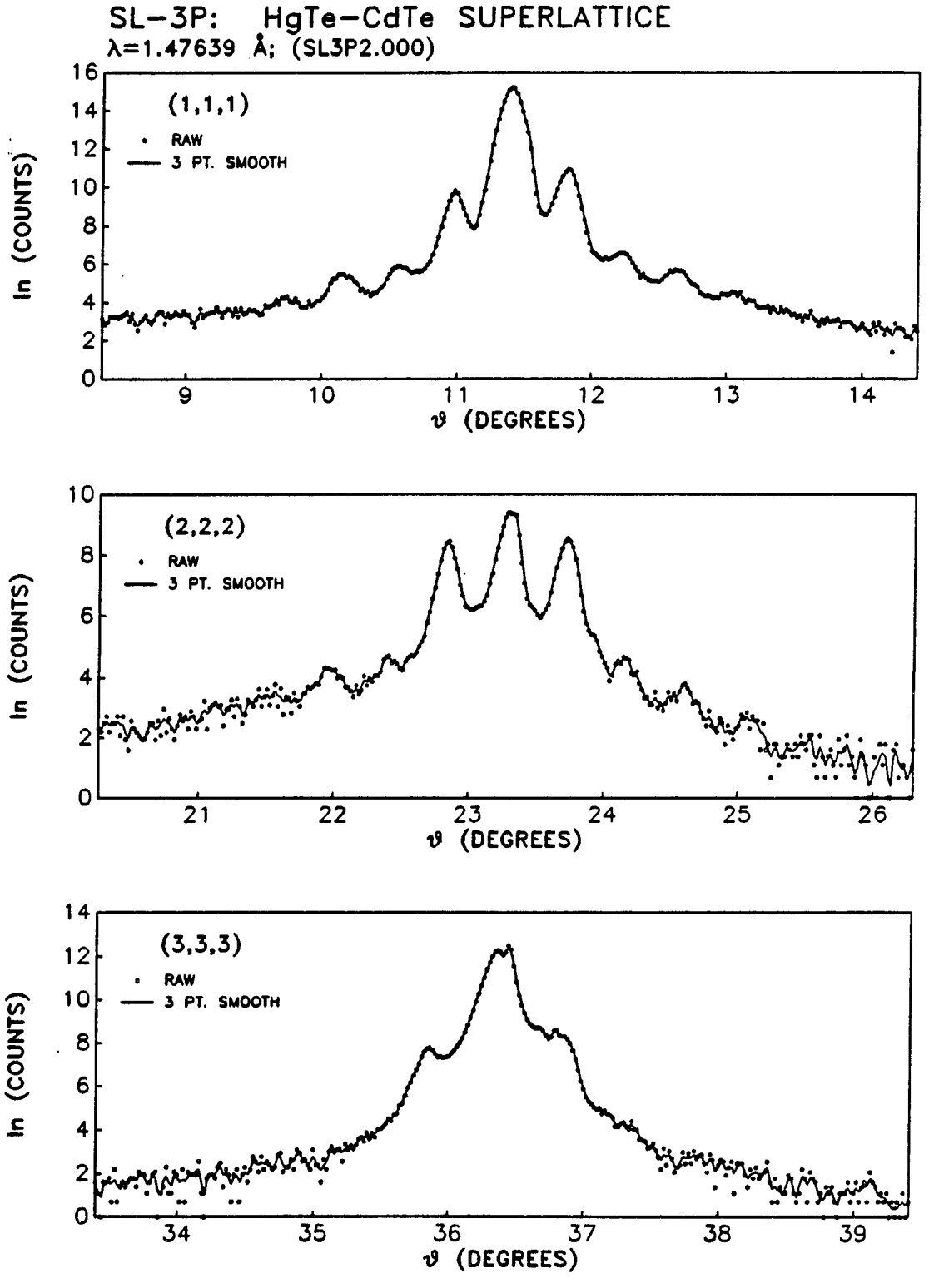
SL-3P: HgTe-CdTe SUPERLATTICE
λ=1.47639 Å; (SL3P2.000)
(1,1,1)
RAW
3 PT. SMOOTH
ln (COUNTS)
ϑ (DEGREES)
(2,2,2)
RAW
3 PT. SMOOTH
ln (COUNTS)
ϑ (DEGREES)
(3,3,3)
RAW
3 PT. SMOOTH
ln (COUNTS)
ϑ (DEGREES)

fit of the (3,3,3) region for each period was performed and the results are listed in Table V.6. The data were corrected for a θ_0 offset that was derived from all three central peaks before fitting the peak positions. The first entry of Table V.6 at each location of SL-4P represents the principal period and the following line represents the second observed period. Differences of the calculated principal period between Tables V.5 and V.6 are a consequence of restricting the least-squares fit to the (3,3,3) region. Multiple periods were observed in two other HgTe-CdTe SL films (Knox, Staudenmann, Monfroy, Faurie & Wu, 1987). Unfortunately, only the (2,2,2) constituent diffraction region of these two samples was scanned, preventing a thorough comparison between the observed periods.

Both periods of SL-4P vary identically, within the estimated uncertainty, between sample locations a and b. The calculated periods of each SL domain increase by approximately 3.1 Å. Apparently the factors contributing to inhomogeneous growth affected both SL domains similarly. However, a similar comparison involving location c reveal no correlation between the two observed domains.

According to the least-squares results, the calculated <c> of the principal SL domain has a slightly larger value compared to the secondary domain. Both values suggest that each domain contains more HgTe than CdTe, but the principal domain contains less HgTe than the other. This discrepancy could be related to the formation of a multiple domain structure.

The HgTe-CdTe SLs under investigation provide information on the effectiveness of the CdTe buffer layer. In addition to establishing a

Table V.6 Least-squares fit summary of both the period and average constituent cell size along the growth direction of multiple period SLs

Sample	Location[a] & Orientation	Period L (Å)	Avg. const. cell length[b] <c> (Å)	Const. cells per period[c]	weighted χ^2[d]	No. of peaks included in fit (central)	(satellite)
SL-4P	a [1,1,1]	81.9 ± 0.9	11.204 ± 0.003	7.31 ± 0.08	1.77	1	5
	[1,1,1]	109.9 ± 0.9	11.194 ± 0.003	9.82 ± 0.08	6.25	1	6
	b [1,1,1]	85.0 ± 0.6	11.200 ± 0.001	7.59 ± 0.06	1.71	1	4
	[1,1,1]	113.1 ± 0.5	11.186 ± 0.001	10.11 ± 0.04	7.31	1	6
	c [1,1,1]	81.5 ± 0.5	11.197 ± 0.001	7.28 ± 0.04	1.94	1	4
	[1,1,1]	113.5 ± 0.5	11.187 ± 0.001	10.15 ± 0.05	13.83	1	6
ML-21B	[1,1,1]	114. ± 3.	12.199 ± 0.004	9.3 ± 0.3	1.53	2	2
	[0,0,1]	105.0 ± 0.8	6.483 ± 0.001	16.2 ± 0.1	11.78	3	10

[a]Sample region probed (see Figure V.9) and crystallographic direction of SL growth.

[b]Average constituent cell length along the growth direction.

[c]The SL period divided by the average constituent cell length.

[d]Defined by equation IV.24a.

fresh deposited surface, which is nearly free of contamination, the buffer layer provides a surface structure that is closely matched with the SL. This is extremely important for [1,1,1] SL growth on GaAs substrates, which have a [0,0,1] surface normal and cubic lattice parameter that is approximately 13% smaller than HgTe and CdTe. For this reason, thick buffer layers are necessary to accommodate the large differences between the substrate and SL film. The thickness of CdTe buffer layers that are deposited on GaAs must be on the order of microns, see Table V.4, so that the misfit at the GaAs-CdTe boundary is spatially separated from the SL growth. In contrast, only a thin CdTe layer, on the order of 100 Å, is deposited on $Cd_{.96}Zn_{.04}Te$ and CdTe substrates. Since very little lattice accommodation is required, the purpose of this thin CdTe layer is to provide a fresh surface for SL deposition. Ideally, the buffer layer should inhibit any substrate influence on the SL film.

The existence of SL growth has been verified for film deposition on GaAs. The thick CdTe buffer layers that are deposited on GaAs substrates effectively mask the poorly matched GaAs lattice and provide a surface that is conducive to SL growth. The confinement of lattice misfit to the GaAs-CdTe interface has been confirmed using high resolution transmission electron microscopy (Wroge, Leopold, Ballingall, Peterman, Morris, Broerman, Ponce & Anderson, 1986). They conclude that the lattice misfit strain is relieved by a two-dimensional dislocation array confined to one atomic layer at the interface.

Deposition on either $Cd_{.96}Zn_{.04}Te$ or CdTe can introduce defects into the SL film. Since the lattice parameters of the substrate and CdTe

buffer layer are nearly identical, the buffer layer can propagate substrate defects. Sample ML-21B is a good example of this. The poor quality CdTe substrate of ML-21B affected both the CdTe buffer layer and SL film. Although the CdTe buffer layer is one micron thick, individual domains having two predominant crystallographic orientations propagated through the deposited CdTe buffer layer and induced two crystallographic growth directions within the SL film. Figure V.12 shows the diffraction spectrum of ML-21B between 13 and 16 degrees in theta. The sample was oriented so that the surface normal lies in the scattering plan, and 1.47639 Å radiation was used. The two large peaks represent [0,0,1] and [1,1,1] HgTe-CdTe central peaks. Satellites are present about both central peaks. The better satellite contrast about the (0,0,2) constituent diffraction region reflects the much larger size of the [0,0,1] domains in the CdTe substrate (Wu, 1987). A summary of the least-squares fit of each orientation of ML-21B is presented in Table V.6. Since both the (1,1,1) and (2,2,2) central peaks were too weak to optimize, the least-squares fit of the [1,1,1] orientation is based on the optimized [0,0,1] reflections. The observation of multiple domain structure in commercial [0,0,1] CdTe substrates was common during this research investigation.

Applying the Scherrer equation (II.56) to the observed SL peak breadths, the number of diffracting SL unit cells are found to be much less than expected. Table V.7 lists the calculated Scherrer lengths for all HgTe-CdTe SLs. Since substrate or buffer layer peaks are superimposed on the central peaks, the Scherrer equation is applied separately to the satellite and central peaks. The scan resolution

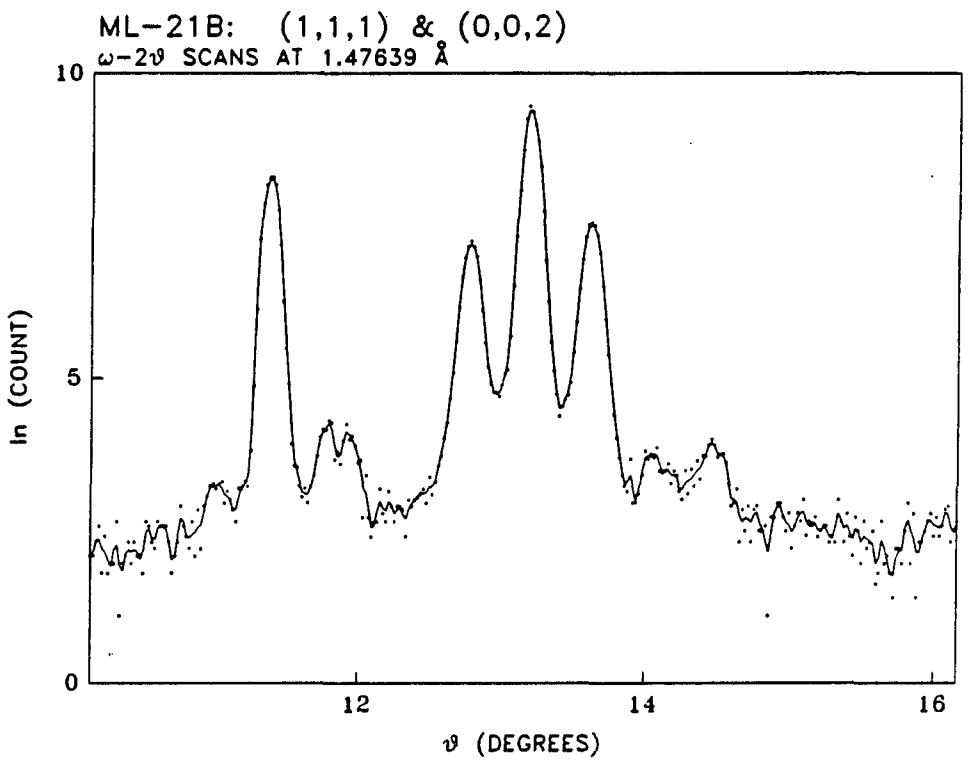

Figure V.12. ω-2θ scans over the (1,1,1) and (0,0,2) constituent diffraction regions of ML-21B using a 1.47639 Å radiation wavelength. The natural logarithm of the diffracted intensity is plotted as a function of the Bragg angle θ. The dots represent the measured data, and the line represents a 3 point smooth over the measured data. The (1,1,1) central peak is located at 11.407°. The (0,0,2) central peak is located at 13.193°. Low intensity first order satellite peaks are adjacent to the (1,1,1) peak and well defined first order satellites are adjacent to the (0,0,2) peak. This SL film was deposited on a CdTe substrate, which contains both [1,1,1] and [0,0,1] oriented domains

within the scattering plane is defined by a 0.9 mm slit width at the monochromator exit and a 1.0 mm width at the detector. The slit width perpendicular to the scattering plane is set to the height of the SL sample.

The Scherrer length extracted from satellite reflections is expected to represent the average coherence length of the SL film, and should be comparable to the SL film thickness. According to the SL film lengths listed in Table V.4, the Scherrer lengths should be larger than ten-thousand angstroms for all samples. However, lengths smaller than one-thousand angstroms are calculated from the diffraction scans. This suggests that the macroscopic crystalline perfection of the SL films are not comparable to single crystal growth (Halliwell & Lyons, 1984).

Finally, the precision of controlling the SL growth rate can be determined by comparing expected and measured SL periods. Tables V.8a and V.8b list the period information of all HgTe-CdTe SLs that were not included in Tables V.5 and V.6. Table V.8a lists information based on the commensurate period assumption, and Table V.8b pertains to the incommensurate assumption. Although there are small differences in the periods derived from each method, the average difference between the expected and calculated periods is relatively unaffected by the choice of method. Excluding the large difference of SL-25, which reflects the poor quality of the diffraction scan data, the average difference between expected and calculated period is 1 ± 1 Å for the commensurate calculations and 0.2 ± 0.7 Å for the incommensurate calculations. These values are well below the size of either the HgTe or CdTe unit cell. However, performing an identical comparison with the other seven HgTe-

Table V.7 Calculated Scherrer lengths of HgTe-CdTe SLs

Sample	Location[a]	Scherrer length[b] satellite peaks (Å)	central peaks (Å)
SL-1P	a	860. ± 302. (15)	1006. ± 186. (3)
	b	784. ± 300. (13)	1016. ± 232. (3)
	c	594. ± 190. (15)	876. ± 72. (3)
SL-2P	a	496. ± 150. (17)	718. ± 48. (3)
	b	544. ± 188. (17)	736. ± 52. (3)
	c	614. ± 264. (15)	692. ± 86. (3)
SL-3P	a	472. ± 216. (16)	678. ± 30. (3)
SL-4P	a	518. ± 212. (20)	972. ± 216. (3)
	b	512. ± 224. (18)	1112. ± 116. (3)
	c	580. ± 228. (14)	1220. ± 172. (3)
SL-5P	a	552. ± 174. (15)	680. ± 126. (3)
SL-6P	a	494. ± 118. (13)	626. ± 118. (3)
	b	498. ± 106. (12)	584. ± 38. (3)
ML-21B		550. ± 34. (10)	1071. ± 283. (3)
SL-13		592. ± 128. (24)	804. ± 24. (3)
SL-25		648. ± 319. (5)	653. ± 117. (3)
SL-48		252. ± 17. (8)	462. ± 83. (1)
SL-49		274. ± 20. (8)	435. ± 71. (1)
SL-52		571. ± 240. (14)	740. ± 82. (3)
SL-54		670. ± 206. (11)	712. ± 181. (3)

[a]Sample region probed (see Figure V.9).

[b]Application of equation II.56 to all peak full width at half maxima, the number of peaks sampled is written in parentheses.

Table V.8a Commensurate calculations of HgTe-CdTe SLs

Sample	Period[a] expected (Å)	Period[a] calculated L (Å)	Avg. const. cell length[b] <c> (Å)	Const. cells per period[c]	weighted χ^2[d]	No. of peaks included in fit (central)	No. of peaks included in fit (satellite)
SL-13	157	157.1 ± 0.1	11.222 ± 0.002	14.00 ± 0.01	12.24	3	24
SL-25	93	89.7 ± 0.2	11.222 ± 0.003	8.00 ± 0.02	12.58	3	5
SL-48	94	93.5 ± 0.1	11.224 ± 0.008	8.33 ± 0.01	3.14	1	8
SL-49	97	95.5 ± 0.1	11.225 ± 0.007	8.50 ± 0.01	3.47	1	8
SL-52	97	97.3 ± 0.1	11.231 ± 0.003	8.66 ± 0.01	3.48	3	14
SL-54	69	67.3 ± 0.1	11.217 ± 0.004	6.00 ± 0.01	5.15	3	11

[a]Expected values provided from film growers, calculated values based on equation IV.18.

[b]Average constituent cell length along the growth direction based on central peak centroids.

[c]The SL period divided by the average constituent cell length.

[d]Defined by equation IV.24a.

Table V.8b Least-squares fit of HgTe-CdTe SL peak positions

Sample	Period[a] expected (Å)	Period[a] calculated L (Å)	Avg. const. cell length[b] <c> (Å)	Const. cells per period[c]	weighted χ^2[d]	No. of peaks included in fit (central)	No. of peaks included in fit (satellite)
SL-13	157	156.5 ± 0.4	11.218 ± 0.001	13.95 ± 0.04	12.03	3	24
SL-25	93	103. ± 2.	11.217 ± 0.002	9.2 ± 0.1	7.39	3	5
SL-48	94	93.8 ± 0.6	11.217 ± 0.003	8.34 ± 0.06	3.14	1	8
SL-49	97	96.4 ± 0.6	11.229 ± 0.004	8.55 ± 0.06	3.37	1	8
SL-52	97	97.9 ± 0.5	11.228 ± 0.002	8.72 ± 0.04	3.29	3	14
SL-54	69	68.3 ± 0.3	11.211 ± 0.002	6.09 ± 0.02	3.31	3	11

[a]Expected values provided from film growers, calculated values based on equations IV.25a-b.

[b]Average constituent cell length along the growth direction based on equations IV.25a-b.

[c]The SL period divided by the average constituent cell length.

[d]Defined by equation IV.24a.

CdTe sample (computing an average period based on all probed sample locations), larger deviations between the expected and calculated periods are observed. Comparing the incommensurate period calculations of these samples, the average deviation between the expected and calculated periods is 1 ± 12 Å. In general, the discrepancy between the expected and actual SL period is below one-half of the cubic zincblende unit cell. Better control of the SL period would require detailed knowledge of the lattice strain present in the constituent materials.

2. $Hg_{1-x}Mn_xTe$-CdTe

Six $Hg_{1-x}Mn_xTe$-CdTe SLs are characterized by performing ω-2θ scans along the growth direction. Both the SL period and average constituent cell size are calculated, and peak breadths are assessed. The available growth history of all six samples is listed in Table V.9. These samples were provided by Jean-Pierre Faurie at the University of Illinois at Chicago. The manganese concentration of these samples, relative to Hg within the $Hg_{1-x}Mn_xTe$ constituent layer, is between 8% and 11%. This particular range of Mn concentrations was selected for infrared detector applications (Faurie, Reno, Sivananthan, Sou, Chu, Boukerche & Wijewarnasuriya, 1986; Wall, Caprile, Franciosi, Reifenberger & Debska, 1986). All samples were grown by molecular beam epitaxy on GaAs substrates (Chu, Sivananthan & Faurie, 1987). Thick CdTe layers were deposited on the substrates to accommodate the large lattice mismatch between GaAs and the SL film.

Except for the collimator slit heights perpendicular to the scattering plane, which were set to the crystal height, identical scan

Table V.9 Available growth history of $Hg_{1-x}Mn_xTe$-CdTe SLs

Sample	Substrate		Buffer layer			Superlattice		
	growth normal	type	growth normal	type	thickness (μ)	growth normal	manganese concentration in HgMnTe layer	expected period (Å)
SL-62	[0,0,1]	GaAs	[1,1,1]	CdTe	3.8	[1,1,1]	11%	127
SL-63	[0,0,1]	GaAs	[1,1,1]	CdTe	3.1	[1,1,1]	11%	100
SL-64	[0,0,1]	GaAs	[1,1,1]	CdTe	5.0	[1,1,1]	9%	100
SL-65	[0,0,1]	GaAs	[1,1,1]	CdTe	3.0	[1,1,1]	8%	108
SL-66	[0,0,1]	GaAs	[1,1,1]	CdTe	2.3	[1,1,1]	9%	100
SL-67	[0,0,1]	GaAs	[1,1,1]	CdTe	2.9	[1,1,1]	10%	100

attributes were used during the diffraction characterization of each sample. Within the scattering plane, the collimating slit widths were set at 0.9 mm and 1.0 mm at the monochromator exit and detector entrance, respectively. The theta increment between scan points was 0.02° and the the count time per point was 20 seconds. The sample orientation was aligned with the x-ray beam by optimizing the (3,3,3) SL central peak. The monochromator was optimized on the W α_1 characteristic line, establishing a 1.47639 Å radiation wavelength. For reference, Figure V.13 shows the (1,1,1) constituent diffraction region of SL-65.

The broad SL peaks of SL-65 are indicative of all six SL samples. Table V.10 lists the Scherrer lengths associated with the broad diffraction maxima for each sample. Since the underlying CdTe substrate, having a lattice closely matched with the constituent lattice of the SL film, contributes to the central peak diffraction profile, a Scherrer length is independently calculated for the satellite and central peaks. The larger lengths associated with the central peaks confirm the presence of sharp unresolved substrate reflections. Information pertaining to the SL film should be extracted from satellite peak breadths only. Although specific knowledge of the SL film thickness is unknown, all thicknesses are larger than one micron (Monfroy, 1987). According to Table V.10, the calculated Scherrer lengths are approximately one order of magnitude less than expected. Relating the Scherrer lengths to the expected SL periods, only five to ten SL unit cells are coherently diffracting within these samples.

The precision of controlling the SL growth rate is determined by

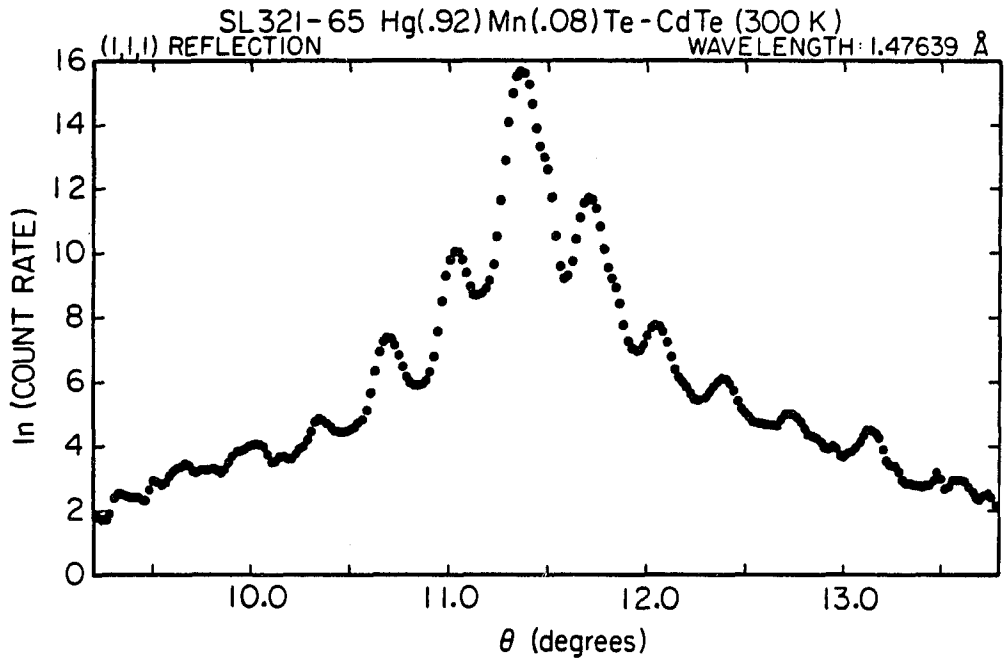

Figure V.13. ω-2θ scan over the (1,1,1) constituent diffraction region of SL-65 using a 1.47639 Å radiation wavelength. The natural logarithm of the diffracted intensity is plotted as a function of the Bragg angle θ

Table V.10 Calculated Scherrer lengths of $Hg_{1-x}Mn_xTe$-CdTe SLs

Sample	Scherrer length[a] satellite peaks (Å)		central peaks (Å)	
SL-62	545 ± 118	(20)	707 ± 136	(3)
SL-63	1023 ± 283	(15)	1452 ± 265	(3)
SL-64	743 ± 221	(12)	841 ± 239	(3)
SL-65	628 ± 171	(21)	869 ± 89	(3)
SL-66	482 ± 85	(15)	597 ± 48	(3)
SL-67	620 ± 176	(15)	863 ± 141	(3)

[a]Application of equation II.56 to all peak full width at half maxima, the number of peaks sampled is written in parentheses.

comparing the expected and measured SL periods. Tables V.11a and V.11b summarize the period calculations based on the commensurate and incommensurate SL assumptions, respectively. Differences between the two methods are less than two angstroms with the incommensurate calculations yielding consistently lower χ values (a better fit to the data). Comparing the expected periods with the incommensurate based calculations for these six SLs, the calculated periods average eleven angstroms longer than expected with a nine angstrom variance. This average difference corresponds to a growth rate resolution of approximately one hexagonal zincblende cell. However, on an individual basis, SL-65 exhibits the most dramatic difference, which is twenty angstroms or approximately two hexagonal unit cell lengths along the

Table V.11a Commensurate calculations of $Hg_{1-x}Mn_xTe$-CdTe SLs

Sample	Period[a] expected (Å)	Period[a] calculated L (Å)	Avg. const. cell length[b] <c> (Å)	Const. cells per period[c]	weighted χ^2[d]	No. of peaks included in fit (central)	No. of peaks included in fit (satellite)
SL-62	127	138.4 ± 0.1	11.225 ± 0.003	13.22 ± 0.01	7.04	(3)	(20)
SL-63	100	112.0 ± 0.1	11.197 ± 0.002	10.00 ± 0.01	14.10	(3)	(15)
SL-64	100	115.55 ± 0.06	11.185 ± 0.002	10.331 ± 0.006	3.87	(3)	(12)
SL-65	108	127.0 ± 0.2	11.202 ± 0.002	11.33 ± 0.01	11.05	(3)	(21)
SL-66	100	108.3 ± 0.1	11.207 ± 0.004	9.66 ± 0.01	3.24	(3)	(15)
SL-67	100	93.2 ± 0.1	11.193 ± 0.004	8.33 ± 0.01	3.94	(3)	(15)

[a]Expected values provided from film growers, calculated values based on equation IV.18.

[b]Average constituent cell length along the growth direction based on central peak centroids.

[c]The SL period divided by the average constituent cell length.

[d]Defined by equation IV.24a.

Table V.11b Least-squares fit of $Hg_{1-x}Mn_xTe$-CdTe SLs

Sample	Period[a] expected (Å)	Period[a] calculated L (Å)	Avg. const. cell length[b] <c> (Å)	Const. cells per period[c]	weighted χ^2[d]	No. of peaks included in fit (central)	No. of peaks included in fit (satellite)
SL-62	127	138.8 ± 0.4	11.219 ± 0.001	12.37 ± 0.04	6.99	(3)	(20)
SL-63	100	113.7 ± 0.3	11.200 ± 0.001	10.15 ± 0.03	13.09	(3)	(15)
SL-64	100	116.9 ± 0.5	11.182 ± 0.001	10.46 ± 0.05	2.85	(3)	(12)
SL-65	108	128.0 ± 0.4	11.202 ± 0.001	11.42 ± 0.03	10.71	(3)	(21)
SL-66	100	109.8 ± 0.7	11.204 ± 0.002	9.80 ± 0.06	2.41	(3)	(15)
SL-67	100	93.6 ± 0.5	11.189 ± 0.002	8.37 ± 0.05	3.87	(3)	(15)

[a]Expected values provided from film growers, calculated values based on equations IV.25a-b.

[b]Average constituent cell length along the growth direction based on equations IV.25a-b.

[c]The SL period divided by the average constituent cell length.

[d]Defined by equation IV.24a.

growth axis.

The average constituent cell lengths of all six SL samples are within the limits defined by the bulk lattice values. The hexagonal lattice parameter c_{hex} for $Hg_{1-x}Mn_xTe$ varies from 11.173 Å to 11.168 Å for x concentrations between 0.08 and 0.11, respectively, and c_{hex} for CdTe is 11.224 Å (Abrikosov, Bankina, Poretskaya, Shelimova & Skudnova, 1969).

Finally, all six SL samples have SL periods that are incommensurate with the average constituent cell length. Since the least-squares fit does not require the period to be commensurate with the constituent lattice, the number of average constituent cells per period must be derived from a least-squares fit to the peak centroid positions. This information is summarized in Table V.11b.

3. $Hg_{1-x}Zn_xTe$-CdTe

Three $Hg_{1-x}Zn_xTe$-CdTe SLs are characterized by performing ω-2θ scans along the growth direction. Both the SL period and average constituent cell size are calculated, and the SL peak breadths are assessed. The available growth history of all three samples is listed in Table V.12. These samples were provided by Jean-Pierre Faurie at the University of Illinois at Chicago. The zinc concentration of these samples are measured relative to mercury within the $Hg_{1-x}Zn_xTe$ constituent layer. Like the other alloyed SLs discussed in this chapter, $Hg_{1-x}Zn_xTe$ is important for infrared detector applications (Sivananthan, Chu, Boukerche & Faurie, 1985). All three samples were grown by molecular beam epitaxy on GaAs substrates (Faurie, Sivananthan, Chu, Reno &

Table V.12 Available growth history of $Hg_{1-x}Zn_xTe$-CdTe SLs

Sample	Substrate growth normal	Substrate type	Buffer layer growth normal	Buffer layer type	growth normal	Superlattice constituent layer ratio[a] (HgZnTe/CdTe Å)	zinc concentration in HgZnTe layer[b]
SL-85	GaAs	[0,0,1]	CdTe	[1,1,1]	[1,1,1]	56/29	1.1%
SL-88	GaAs	[0,0,1]	CdTe	[1,1,1]	[1,1,1]	85/30	10.3%
SL-92	GaAs	[0,0,1]	CdTe CdZnTe	[1,1,1] [1,1,1]	[1,1,1]	109/37	3.9%

[a]Estimated from growth rates of individual constituents.

[b]Zn percentage relative to Hg in $Hg_{1-x}Zn_xTe$ constituent layer.

Wijewarnasuriya, 1987). The composite SL system of both SL-85 and SL-88 consists of a thick CdTe layer between the GaAs and SL film. The composite sample SL-92 contains two buffer layers; a CdTe layer was deposited on the substrate first, followed by a $Cd_{1-x}Zn_xTe$ layer.

Except for the collimator slit heights perpendicular to the scattering plane, which were set to the sample height, and the theta increment between scan angles, identical scan attributes were used during the diffraction characterization of each sample. Within the scattering plane, the collimating slit widths were set at 1.0 mm and 1.2 mm at the monochromator exit and detector entrance, respectively. The theta increment between scan points was 0.025° for both SL-88 and SL-92, and 0.02° for SL-85. The count time per point was 60 seconds. Sample alignment was achieved by optimizing the (3,3,3) central peak. 1.47639 Å radiation was used to scan all three samples. Only two satellite peaks within the (3,3,3) constituent diffraction region of SL-88 were scanned because of problems encountered with the rotating anode generator.

The diffraction spectrum from all three samples exhibit well defined SL peaks that have breadths much larger than expected. Figure V.14 shows the (1,1,1) constituent diffraction region of scan of SL-92. The broad SL peaks of SL-92 are typical of all three samples. Table V.13 lists both the Scherrer lengths and the expected SL film thickness for each sample. Since the central peaks contain diffraction from both the SL film and buffer layer(s), Scherrer lengths are calculated separately for the central and satellite peaks. The coherence length of the SL film must be extracted from only the satellite Scherrer lengths.

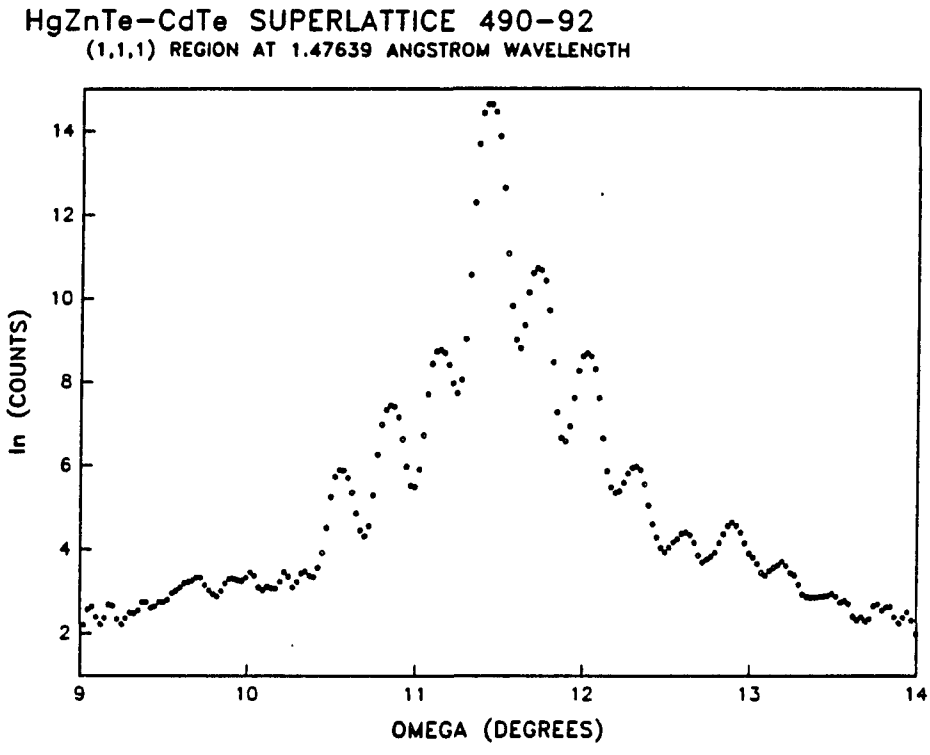

Figure V.14. ω-2Θ scan over the (1,1,1) constituent diffraction region of SL-92 using a 1.47639 Å radiation wavelength. The natural logarithm of the diffracted intensity is plotted as a function of the Bragg angle Θ

Comparing the Scherrer length with the SL film thickness (10000 Å = 1 μ), domains having thicknesses less than one tenth of the total SL film diffract coherently. Relating the Scherrer lengths to the expected SL periods, approximately 19, 27, and 40 SL unit cells coherently diffract within SL-85, SL-88, and SL-92, respectively.

Table V.13 Calculated Scherrer lengths of $Hg_{1-x}Zn_xTe$-CdTe SLs

Sample	Scherrer length[a] satellite peaks (Å)		central peaks (Å)		Superlattice film thickness[b] (μ)
SL-85	688 ± 140	(19)	854 ± 36	(3)	1.28
SL-88	642 ± 214	(18)	922 ± 54	(2)	1.73
SL-92	552 ± 116	(23)	626 ± 28	(3)	2.19

[a]Application of equation II.56 to all peak full width at half maxima, the number of peaks sampled is written in parentheses.

[b]Information provided by film growers.

The underlying buffer layer reflections and central peak reflections are unresolved for all three samples, indicating that the average constituent cell length of the SL film is nearly identical to the substrate unit cell length. This conclusion is further supported by the small variances associated with the central peak Scherrer calculations. Assuming that the buffer layer reflections significantly contribute to the total intensity observed at the central peak locations, small lattice parameter differences between the buffer layer and the average

constituent lattice of the SL would become more pronounced at larger scattering angles. Thus, the observed central speak breadths would appear wider for higher order reflections, resulting in successively smaller Scherrer lengths. This is not observed.

Additional diffraction structure, which is not attributed to either the substrate of SL film is observed for SL-88. Figure V.15 shows the (1,1,1) and (2,2,2) constituent diffraction regions of SL-88. In addition to the SL structure, two distinct peak are obvious: the (0,0,2) GaAs substrate reflection at 15.14° and an unexpected peak at 27.08°. This second peak corresponds to the CdTe (0,0,4) reflection. The corresponding (0,0,2) reflection is superimposed with the (1,1,1,5) satellite peak. Apparently, [0,0,1] growth formed during the [1,1,1] CdTe buffer layer deposition. Applying the Scherrer formula to the (0,0,4) CdTe peak breadth, a 390 ± 22 Å Scherrer length is calculated.

Differences between the calculated and expected SL periods are quite small for all three samples. A summary of the period calculations, based on the commensurate and incommensurate SL assumptions, is listed in Tables V.14a and V.14b, respectively. According to the χ values, periods based on the incommensurate method consistently fit the peak positions better than the commensurate method. According to Table V.14b, all three samples have SL periods that are incommensurate with the average constituent lattice. Comparing the incommensurate periods to the expected periods, differences of 0.1 Å, 0.6 Å, and -1.6 Å are observed for SL-85, SL-88, and SL-92, respectively. These small differences are well below one hexagonal unit cell length (~11.2 Å) of the constituent lattice. Better control of the SL growth would require

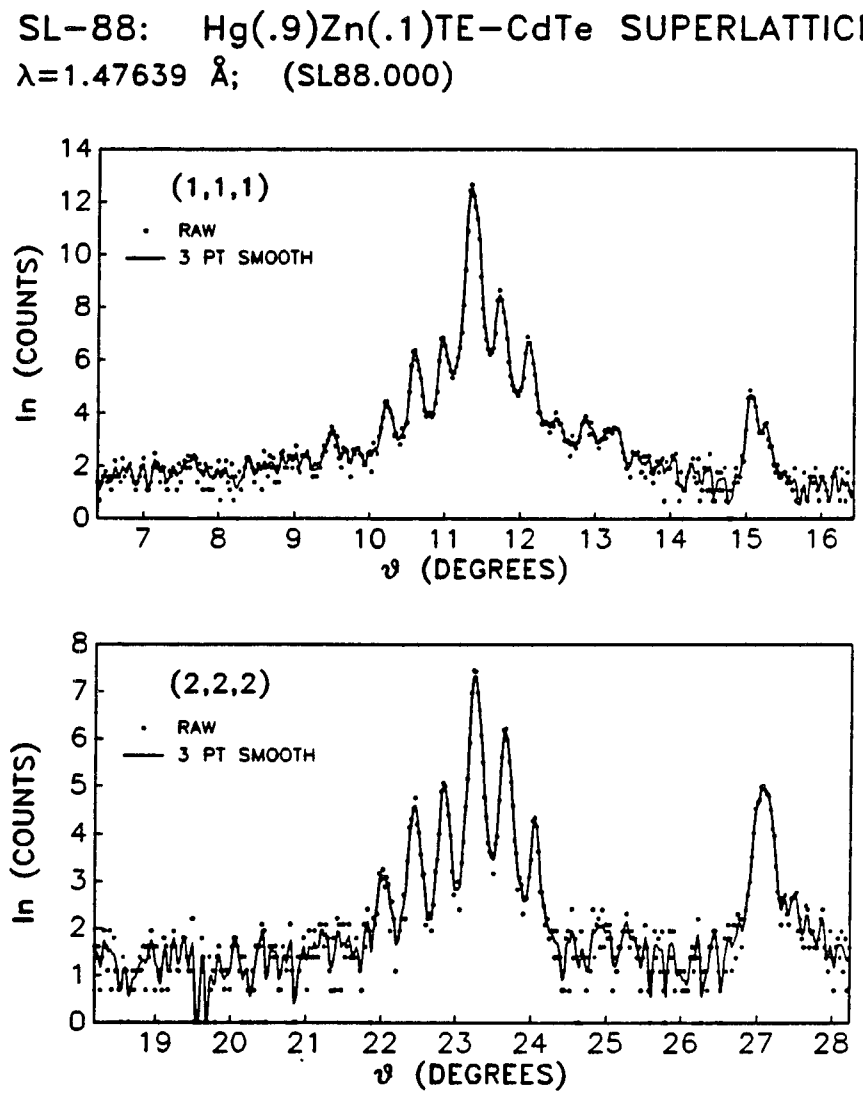

Figure V.15. ω-2θ scans over the (1,1,1) and (2,2,2) constituent diffraction regions of SL-88 using a 1.47639 Å radiation wavelength. The natural logarithm of the diffracted intensity is plotted as a function of the Bragg angle θ. The dots represent measured data, and the line represents a 3 point smooth over the measured data. The (0,0,2) GaAs reflection is observed at θ=15.068°, and a (0,0,4) CdTe buffer layer peak is observed at θ=27.078°

Table V.14a Commensurate calculations of $Hg_{1-x}Zn_xTe$-CdTe SLs

Sample	Period[a] expected (Å)	Period[a] calculated L (Å)	Avg. const. cell length[b] <c> (Å)	Const. cells per period[c]	weighted χ^2[d]	No. of peaks included in fit (central)	No. of peaks included in fit (satellite)
SL-85	85	85.9 ± 0.1	11.208 ± 0.002	7.67 ± 0.01	6.2	3	19
SL-88	115	115.7 ± 0.1	11.201 ± 0.003	10.33 ± 0.01	5.82	2	18
SL-92	146	149.2 ± 0.1	11.186 ± 0.003	13.33 ± 0.01	3.40	3	23

[a]Expected values provided from film growers, calculated values based on equation IV.18.

[b]Average constituent cell length along the growth direction based on central peak centroids.

[c]The SL period divided by the average constituent cell length.

[d]Defined by equation IV.24a.

Table V.14b Least-squares fit of $Hg_{1-x}Zn_xTe$-CdTe SLs

Sample	Period[a] expected (Å)	Period[a] calculated L (Å)	Avg. const. cell length[b] <c> (Å)	Const. cells per period[c]	weighted χ^2[d]	No. of peaks included in fit (central)	No. of peaks included in fit (satellite)
SL-85	85	84.9 ± 0.2	11.206 ± 0.001	7.58 ± 0.02	2.57	3	19
SL-88	115	114.4 ± 0.3	11.200 ± 0.001	10.21 ± 0.03	3.79	2	18
SL-92	146	147.6 ± 0.5	11.188 ± 0.001	13.19 ± 0.05	1.76	3	23

[a]Expected values provided from film growers, calculated values based on equations IV.25a-b.

[b]Average constituent cell length along the growth direction based on equations IV.25a-b.

[c]The SL period divided by the average constituent cell length.

[d]Defined by equation IV.24a.

detailed knowledge of the lattice strain within each constituent.

Finally, the average constituent cell lengths of all three SL samples are within the limits defined by the bulk lattice values. The hexagonal lattice parameter c_{hex} for $Hg_{1-x}Zn_xTe$ varies from 11.216 Å to 11.154 Å for x concentrations between 0.011 and 0.103, respectively, and c_{hex} for CdTe is 11.224 Å (Abrikosov, Bankina, Poretskaya, Shelimova & Skudnova, 1969).

4. $Hg_{1-x}Cd_xTe$-CdTe

Five $Hg_{1-x}Cd_xTe$-CdTe SLs are characterized by performing ω-2Θ scans along the growth direction. Both the SL period and average constituent cell size are calculated, peak breadths are assessed, and additional observed structure discussed. The available growth history of all six samples is listed in Table V.15. These samples were provided by Jean-Pierre Faurie at the University of Illinois at Chicago. Samples having cadmium concentrations of 2%, 8%, 16%, and 27%, relative to mercury in the $Hg_{1-x}Cd_xTe$ constituent layer, were grown by molecular beam epitaxy on GaAs substrates at approximately 185 C (Reno, Sou, Wijewarnasuriya & Faurie, 1986). Thick CdTe layers were deposited on the GaAs prior to SL deposition.

Except for the detector count time and angular increment, identical diffraction scan attributes were initially used to probe the five SL samples. A 1.4 mm diameter collimator was placed at the monochromator exit, and a 3.5 mm diameter collimator was placed at the detector entrance. The sample orientation was aligned with the x-ray beam by optimizing the (3,3,3) SL central peak. 1.47639 Å radiation was

Table V.15 Available growth history of $Hg_{1-x}Cd_xTe$-CdTe SLs

Sample	Substrate		Buffer layer				Superlattice constituent layer ratio[a] (HgZnTe/CdTe Å)	cadmium concentration in HgCdTe layer[b]
	growth normal	type	growth normal	type	thickness	growth normal		
SL-28	[0,0,1]	GaAs	[1,1,1]	CdTe	2.4	[1,1,1]	70/40	27%
SL-29	[0,0,1]	GaAs	[1,1,1]	CdTe	2.2	[1,1,1]	60/40	27%
SL-39	[0,0,1]	GaAs	[1,1,1]	CdTe	2.8	[1,1,1]	81/49	2%
SL-42	[0,0,1]	GaAs	[1,1,1]	CdTe	2.8	[1,1,1]	70/37	8%
SL-43	[0,0,1]	GaAs	[1,1,1]	CdTe	2.7	[1,1,1]	70/40	16%

[a]Estimated from growth rates of individual constituents.

[b]Cd percentage relative to Hg in $Hg_{1-x}Cd_xTe$ constituent layer.

used to scan all samples. A 60 second count time was used to scan samples SL-29 and SL-42, and an 80 second count time was used for samples SL-28, SL-39, and SL-43. A 0.02° angle increment in theta was used for sample SL-29, and a 0.05° increment was used to scan SL-28, SL-39, SL-42, and SL-43. These initial scans probed only the (2,2,2) constituent diffraction region.

Two samples, SL-42 and SL-43, were further characterized during the interdiffusion investigation. Room temperature scans over the (1,1,1), (2,2,2), and (3,3,3) constituent diffraction regions were performed prior to the diffusion experiments. These additional diffraction results are discussed in this subsection. A 0.02° angle increment was used for both scans. The count times were 2 seconds and 10 seconds for SL-42 and SL-43, respectively. One millimeter diameter collimators were placed at the monochromator exit and detector entrance during the scan of SL-42. A 1.5 mm by 3 mm slit incident collimator and a 1.6 mm by 8 mm slit detector collimator were used during the scan of SL-43.

The peak breadths of all five samples are much larger than expected. Table V.16 lists both the Scherrer lengths and expected SL film thickness for each sample. This information is extracted from the initial characterization scans over the (2,2,2) region. The peak breadths were corrected for instrumental broadening by subtracting the breadth of the nearest GaAs substrate reflection (Lorentzian approximation, see equation II.60b). Because of the large collimator diameters, this procedure was necessary to obtain meaningful information. All Scherrer lengths are at least one order of magnitude less than the total film thickness. Relating the Scherrer lengths to

Table V.16 Calculated Scherrer lengths of $Hg_{1-x}Cd_xTe$-CdTe SLs

Sample	Scherrer length[a] satellite peaks (Å)		central peaks (Å)		Superlattice film thickness[b] (μ)
SL-28	490 ± 173	(9)	631 ± 121	(1)	1.1
SL-29	1138 ± 492	(7)	1253 ± 189	(1)	0.9
SL-39	528 ± 321	(8)	961 ± 180	(1)	1.6
SL-42	1240 ± 736	(12)	1696 ± 313	(1)	1.1
SL-43	938 ± 661	(8)	2620 ± 694	(1)	1.1

[a]Application of equation II.56 to all corrected peak full width at half maxima. Instrumental resolution correction is based on equation II.60b using the observed GaAs reflections of the substrate. The number of peaks included in analysis is written in parentheses.

[b]Information provided by film growers.

the expected SL periods, approximately 4, 11, 4, 12, and 9 SL unit cells coherently diffract within SL-28, SL-29, SL-39, SL-42, and SL-43, respectively.

Differences between the calculated and expected SL periods are quite large compared to the other SL systems. A summary of the period calculations, based on the commensurate and incommensurate SL assumptions, is listed in Tables V.17a and V.17b, respectively. Calculations based on only one central peak are affected by sample misalignment errors, since the peak centroid positions could not be corrected for a θ_0 offset. The calculated periods based on the incommensurate assumption yield a consistently better fit of the

Table V.17a Commensurate calculations of $Hg_{1-x}Cd_xTe$-CdTe SLs

Sample	Period[a] expected (Å)	Period[a] calculated L (Å)	Avg. const. cell length[b] <c> (Å)	Const. cells per period[c]	weighted χ^2[d]	No. of peaks included in fit (central)	No. of peaks included in fit (satellite)
SL-28	110	89.7 ± 0.2	11.210 ± 0.009	7.99 ± 0.02	5.16	1	10
SL-29	100	69.24 ± 0.04	11.236 ± 0.005	6.16 ± 0.01	3.45	1	8
	(2nd period)	70.5 ± 0.1	11.151 ± 0.006	6.319 ± 0.01	8.31	1	7
SL-39	130	116.0 ± 0.2	11.226 ± 0.006	10.33 ± 0.02	3.72	1	9
SL-42	107	101.01 ± 0.03	11.228 ± 0.005	9.00 ± 0.01	3.08	1	12
		104.60 ± 0.06	11.209 ± 0.004	9.33 ± 0.01	2.08	3	11
SL-43	110	116.4 ± 0.7	11.232 ± 0.008	10.37 ± 0.06	18.47	1	13
		108.6 ± 0.2	11.229 ± 0.003	9.67 ± 0.02	11.66	3	12

[a]Expected values provided from film growers, calculated values based on equation IV.18.

[b]Average constituent cell length along the growth direction based on central peak centroids.

[c]The SL period divided by the average constituent cell length.

[d]Defined by equation IV.24a.

Table V.17b Least-squares fit of $Hg_{1-x}Cd_xTe$-CdTe SLs

Sample	Period[a] expected (Å)	Period[a] calculated L (Å)	Avg. const. cell length[b] <c> (Å)	Const. cells per period[c]	weighted χ^2[d]	No. of peaks included in fit (central)	No. of peaks included in fit (satellite)
SL-28	110	91.0 ± 0.5	11.200 ± 0.003	8.12 ± 0.04	4.26	1	10
SL-29	100	69.7 ± 0.2	11.227 ± 0.002	6.21 ± 0.02	2.18	1	8
	(2nd period)	70.4 ± 0.2	11.127 ± 0.002	6.33 ± 0.02	8.30	1	7
SL-39	130	116.6 ± 0.9	11.226 ± 0.003	10.39 ± 0.08	3.66	1	9
SL-42	107	100.9 ± 0.3	11.223 ± 0.002	8.99 ± 0.02	3.05	1	12
		103.4 ± 0.7	11.208 ± 0.002	9.23 ± 0.06	0.99	3	11
SL-43	110	119.6 ± 0.5	11.263 ± 0.003	10.62 ± 0.06	17.68	1	13
		108.4 ± 0.7	11.231 ± 0.002	9.65 ± 0.06	11.65	3	12

[a]Expected values provided from film growers, calculated values based on equations IV.25a-b.

[b]Average constituent cell length along the growth direction based on equations IV.25a-b.

[c]The SL period divided by the average constituent cell length.

[d]Defined by equation IV.24a.

diffraction data. Since the SL periods of all samples are incommensurate with the average constituent lattice (see Table V.17b), differences between the observed and calculated periods should be based on the incommensurate least-squares fit information. These differences are 19 Å, 30.3 Å, 13.4 Å, 6.1, and -9.6 Å for SL-29, SL-29, SL-39, SL-42, and SL-43, respectively. Except for SL-42 and SL-43, all differences are larger than one average constituent cell length (~11.206 Å).

Additional SL structure is observed for SL-29. The (2,2,2) constituent diffraction region of SL-29 is presented in Figure V.16. A second series of weak SL peaks is clearly visible in this figure. Apparently, two SL domains coexist in this sample. For comparison, the (2,2,2) region of SL-28 is presented in Figure V.17. According to the growth information, the only significant difference between these two samples is the ten angstrom larger $Hg_{.73}Cd_{.27}Te$ constituent layer of SL-28. The second observed period of SL-29 is listed Tables V.17a and V.17b. Unlike the multiple period SLs discussed in the HgTe-CdTe subsection, both SL domains of SL-29 have nearly identical periods. The average constituent cell lengths of these domains, however, are significantly different, indicating that the average chemical compositions of these domains are different. Since the presence of strain within each constituent layer affects the average constituent cell length along the growth direction, the average chemical composition can not be determined (Hornstra & Bartels, 1978).

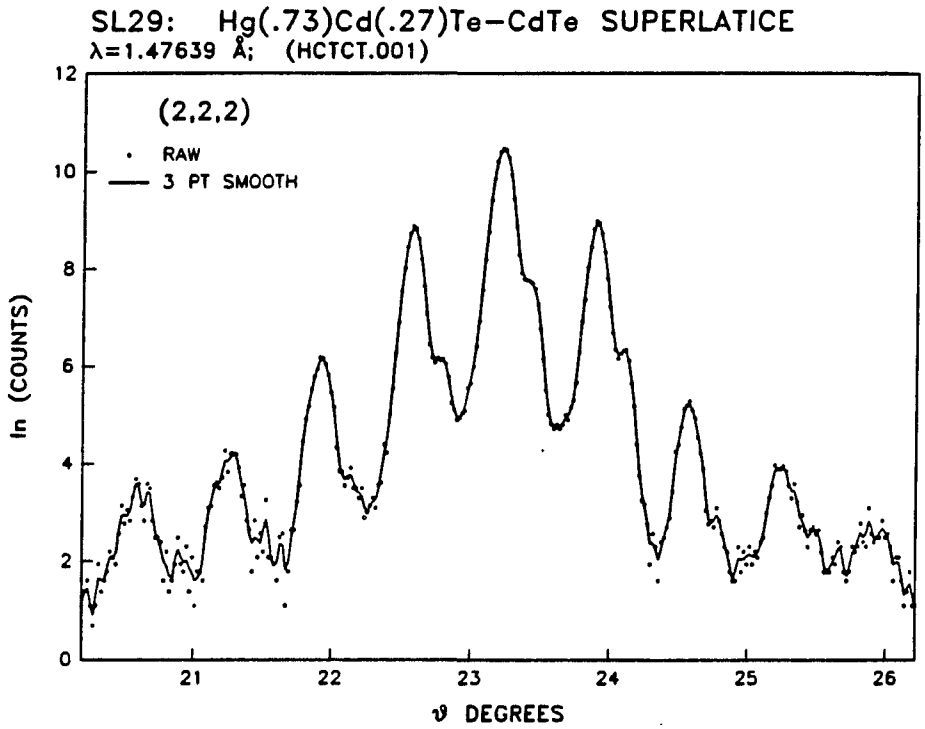

Figure V.16. ω-2Θ scans over the (2,2,2) constituent diffraction region of SL-29 using a 1.47639 Å radiation wavelength. The natural logarithm of the diffracted intensity is plotted as a function of the Bragg angle Θ. The dots represent measured data, and the line represents a 3 point smooth over the measured data. The "shoulders" to the high angle side of each peak represent unresolved diffraction from a second distinct SL domain

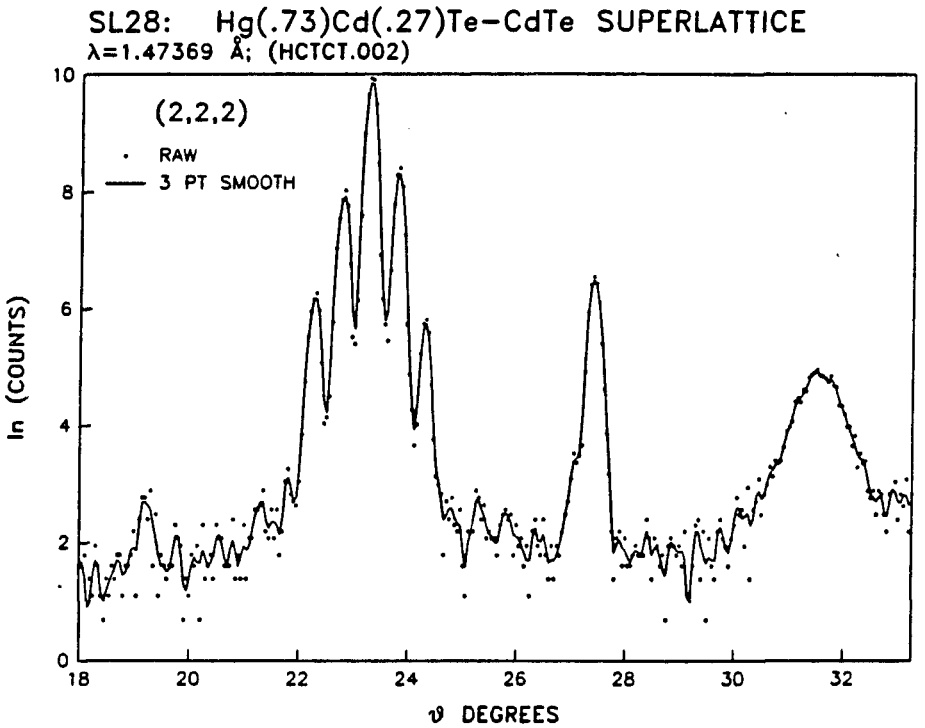

Figure V.17. ω-2Θ scans over the (2,2,2) constituent diffraction region of SL-28 using a 1.47639 Å radiation wavelength. The natural logarithm of the recorded intensity is plotted as a function of the Bragg angle Θ. The dots represent measured data, and the line represents a 3 point smooth over the measured data. Unlike SL-29 (see Figure V.16), only one well defined period is observed. A CdTe (0,0,4) reflection is observed at Θ=27.414°, and a very broad (0,0,4) GaAs reflection is observed at Θ=31.546°

D. Thermal Stability Investigation

1. Introduction

The success of $Hg_{1-x}X_xTe$-CdTe SLs as electronic devices crucially depends on both the crystalline perfection of the constituent materials and the integrity of the heterointerfaces. The growth of good quality HgTe, CdTe, $Hg_{1-x}Mn_xTe$, $Hg_{1-x}Zn_xTe$, and $Hg_{1-x}Cd_xTe$ epitaxial layers by molecular beam epitaxy is well established (Faurie & Million, 1981; Faurie & Million, 1982; Faurie, Reno, Sivananthan, Sou, Chu, Boukerche & Wijewarnasuriya, 1986). However, relatively little is known about the interdiffusion of these constituent materials when arranged in a SL structure. Sensitive to the chemical composition of the SL, x-ray diffraction provides information on the diffusion process, which occurs during and after the film deposition. This section concerns the diffusion of complete SL films at elevated temperatures and the following section addresses interdiffusion during growth.

Interdiffusion information is extracted from satellite intensities, which depend on the composition profile of the SL unit cell. Atomic migration across the interfaces will reduce the concentration gradient produced by the segregation of the constituents. Representing the chemical concentration function by a Fourier series expansion (see section III.C), diffusion across the interfaces will reduce the magnitude of all Fourier coefficients associated with nonzero harmonics. Related to these coefficients, the intensity of all satellite peaks will decay. Ultimately, the satellite peaks must vanish when the SL composition becomes uniform across the growth direction. The central peak intensities, however, are unaffected by interdiffusion, if the

average chemical composition does not change. The relationship between the satellite intensities and the Fourier expansion coefficients allows diffusion information to be extracted from the time evolution of the x-ray diffraction spectrum. DuMond & Youtz (1940) were the first to apply x-ray diffraction to the characterization of metal SL interdiffusion. Their work has provided the foundation for SL interdiffusion research.

This research investigation represents an extension of earlier HgTe-CdTe SL interdiffusion experiments (Arch, Faurie, Staudenmann, Hibbs-Brenner & Chow, 1986). The experimental procedure is improved and diffusion of alloyed SL samples are included in the investigation. The results of this interdiffusion investigation are presented in four published papers (Staudenmann, Horning, Knox, Reno, Sou, Faurie & Arch, 1986; Staudenmann, Knox, and Faurie, 1987a; Staudenmann, Knox & Faurie, 1987b; Staudenmann, Knox & Horning, 1988).

2. Mathematical background

The mathematical theory of diffusion is based on the hypothesis that the rate at which a substance diffuses through a area is proportional to the concentration gradient measured normal to the surface (Fick, 1855), that is,

$$F = -D\frac{\partial C}{\partial z} \quad , \tag{V.4}$$

where F is the transfer rate per unit area, D is the diffusion coefficient, C is the concentration of the diffusing substance, and z is the spatial coordinate normal to the area cross section. Equation V.4

is known as Fick's first law of diffusion. By invoking the conservation of mass, which asserts that diffusion across a bounded region must lead to a decrease in the chemical concentration within the boundary, a continuity equation is established. This equation, known as Fick's second law of diffusion, relates the time and spatial dependence of the concentration function,

$$\frac{\partial C}{\partial t} = \nabla\cdot(D\nabla C) \quad . \tag{V.5}$$

In general the diffusion coefficient depends on the diffusion environment, such as temperature, and on the concentration magnitude (Crank, 1985). Equation V.5 assumes that the concentration function is continuous, which is apparently inconsistent with atomic migration on an ordered crystal lattice. However, equation V.5 is applicable to SL diffusion in the long period limit, where the SL period is large compared to the interatomic spacing. This condition is satisfied for the SLs under investigation.

Since the chemical composition of the SL varies along the growth direction, equation V.5 is simplified to one dimension, which is arbitrarily chosen to be the z spatial coordinate. To further simplify the diffusion analysis, the diffusion coefficient is assumed to be concentration independent. This assumption is questionable for the large concentration gradients encountered across the heterointerfaces (Greer & Spaepen, 1985), and its consequences are discussed during the interpretation of the diffusion results. Since atomic diffusion is governed by an energy activation process, the diffusion coefficient does

depend on temperature. Thus, equation V.5 is written,

$$\frac{\partial C(z,t,T)}{\partial t} = D(T)\frac{\partial^2 C(z,t,T)}{\partial z^2} \quad , \tag{V.6}$$

where z is the spatial coordinate along the SL growth direction, t is the time variable, and T is the sample temperature during the diffusion experiment.

A solution to equation V.6 for a fixed temperature is obtained by separating the z and t variables. Expressing the concentration function as the product of two variables, $C(z,t,T)=A(z,T)B(t,T)$, the spatial and time dependencies are successfully isolated,

$$\frac{1}{T}\frac{\partial A}{\partial t} = -k^2 D = \frac{D}{z}\frac{\partial^2 B}{\partial z^2} \quad , \tag{V.7}$$

where $-k^2D$ represents the common constant. Solving these two differential equations,

$$A = e^{-k^2 Dt} \quad , \tag{V.8a}$$

$$B = e^{-ikz} \quad , \tag{V.8b}$$

the solution of equation V.6 is

$$C_k(z,t,T) = e^{-k^2 D(T)t} e^{ikz} \quad , \tag{V.9}$$

where k and D(T) are arbitrary real constants. Since equation V.6 is linear, any combination of solutions C_k is a solution. Knowing that the

concentration function is periodic with the SL period L, an equivalent solution to equation V.6 can be written as a Fourier series of period L,

$$C(z,t,T) = \frac{1}{2} \sum_{s=-\infty}^{+\infty} \phi_s(t,T) e^{ik_s z} \quad , \tag{V.10a}$$

$$k_s = \frac{2\pi s}{L} \quad , \tag{V.10b}$$

$$\phi_s(t,T) = \phi_s(0,T) e^{-k_s^2 D(T) t} \quad , \tag{V.10c}$$

where k_z is the harmonic wavenumber and $\phi_s(0,t)$, which satisfy the boundary conditions, are the Fourier expansion coefficients at the start of the diffusion process.

In section III.C, the concentration deviation function, $\Gamma(z) \equiv C - \langle C \rangle$, was represented by a Fourier series expansion identical to equation V.10a and the SL structure factor was related to the Fourier expansion coefficients. This established the relationship between the chemical composition and the diffracted intensity of the SL peaks (equation III.39). If the lattice mismatch between the constituent materials is small ($\gamma \simeq 0$), which is expected for the $Hg_{1-x}X_xTe$-CdTe SL system, equation III.39 is greatly simplified,

$$\frac{F(h,k,l,m)}{F(h,k,l,0)} \simeq \phi_m(t,T) \delta F'(h,k,l,m) \quad , \tag{V.11}$$

where the Fourier expansion coefficient ϕ_m is replaced by the time dependent coefficient $\phi_m(t,T)$, and $\delta F'(h,k,l,m)$ is a constant quantity that is related to the scattering amplitude difference between the pure

constituent materials at the scattering angle defined by the (h,k,l,m) reflection. However, the diffracted intensities are proportional to the structure factor squared. Thus, the experimentally relevant relationship concerns the ratio of peak intensities,

$$R(h,k,l,m) \equiv \frac{I(h,k,l,m)}{I(h,k,l,0)}$$

$$\simeq |\phi_m(0,T)\,\delta F'(h,k,l,m)|^2 e^{-2k_m^2 D(h,k,l,m,T)t} \quad , \qquad (V.12)$$

where I(h,k,l,m) and I(h,k,l,0) are the satellite and central peak intensities of the (h,k,l) constituent diffraction region, respectively, and D(h,k,l,m,T) is the diffusion coefficient associated with the time evolution of the (h,k,l,m) satellite peak. Since the exponential coefficient is time independent, the intensity ratio decays exponentially with time. A $\log_e$ plot of the intensity ratio R(h,k,l,m) as a function of time will yield a straight line having a slope that depends on the modulation wavenumber and the diffusion coefficient. By normalizing this slope to the wavenumber, a diffusion coefficient D(h,k,l,m,T) is extracted from the time evolution of R(h,k,l,m).

Two sample independent observations are predicted, if both the linear diffusion assumption (equation V.6) and the structure factor approximation (equation V.11) are valid. First, the diffusion coefficient should be independent of the constituent diffraction region, D(h,k,l,m,T)=D(m,T). This is reasonable, since differences among the regions are a manifestation of the added scattered phases from the same crystal structure. Second, the diffusion coefficient should be independent of the observed SL peak, D(h,k,l,m,T)=D(T). This is a

consequence of the linear diffusion approximation, where the diffusion coefficient is assumed to be concentration independent. The validity of these predictions are examined in the diffusion analyses.

The SL peak intensities are measured by performing one ω-2θ scan, having its scattering vector parallel to the SL growth direction. Once the diffusion temperature is attained, many ω-2θ scans are performed in succession. Diffusion information is extracted from the evolution of the intensity ratio R(h,k,l,m) among the recorded diffraction scans, where each scan represents one time of the diffusion experiment.

Additional information about the diffusion process is extracted from the temperature dependence of the diffusion coefficient. Over a wide range of temperatures, experimentally measured diffusion coefficients often fit the Arrhenius equation of diffusion (Manning, 1968),

$$D(T) = D_o e^{-(Q/kT)} \quad , \tag{V.13}$$

where D_o and Q are constants independent of temperature T, and k is the Boltzmann constant. The exponential temperature dependence of equation V.13 is a natural consequence of kinetic theory. Diffusion at the atomic scale consists of atoms moving between specific positions within the crystal lattice. The probability of an atom moving depends on its thermal energy and the confining potential energy barrier,

$$P_{a \to b} \sim e^{-(\Delta U/kT)} \quad , \tag{V.14}$$

where $P_{a \to b}$ is the probability of an atom moving from position a to b at any instant and ΔU is the potential energy barrier between positions a

and b. The constant Q of equation V.13 is known as the activation energy of the diffusion process. Comparing equations V.13 and V.14, the activation energy is obviously related to the confining potential energy barrier. However, the exact relationship depends on the type of atomic positions available for atomic diffusion (Girifalco, 1964; Sharma, 1970).

3. Experimental background

Previous to this research investigation, semiconductor SL interdiffusion has been characterized at room temperature after heating the samples at elevated temperatures for known time intervals (Fleming, McWhan, Gossard, Wiegmann & Logan, 1980). The heated sample are quickly cooled to room temperature in an effort to quench the diffusion process. Ideally, the subsequent characterization represents the interdiffusion during the heat treatment time interval. Although this quenched sample method is a relatively easy procedure to perform, the extracted diffusion results depend on two crucial assumptions. First, the quenched state of interdiffusion is assumed to be directly related to the time interval at the elevated temperature. If the interdiffusion is attributed to a single diffusion process, this assumption is expected to be valid. Second, diffusion during the quenching procedure, where the temperature is quickly raised and lowered, is assumed to be insignificant compared to the diffusion during the heat treatment. This is probably valid, if few heat treatments are performed. However, the cumulative effects of many heat treatments may significantly affect the diffusion characterization results.

This research investigation attempts to improve the quenched sample procedure by characterizing the diffusion process while the sample is maintained at a constant elevated temperature. By obtaining real-time information, the dynamics of the diffusion process are characterized. The success of this in-situ interdiffusion procedure depends on two requirements. First, the scan duration must be minimized so that the diffusion during the scan interval is insignificant. Second, the sample alignment with respect to the incident radiation must be properly maintained during the experiment. Both requirements are achieved and further discussed below.

Three methods were used to heat the SL samples: radiative, conductive-circulated, and conductive-encapsulated. The radiative method geometry consists of two heating elements that are placed in front of the sample, which is mounted on a small copper half-cylinder holder. A thin copper cross-bar, having a small screw at each end, holds the sample to the holder. The sample holder is thermally isolated from the goniometer head by a thin stainless steel tube. Both heating elements are long ceramic-coated heating coils in the form of 23 mm long rods, having a 3 mm diameter cross section. These two elements, spaced 5 mm apart, are placed a few millimeters in front of the sample. A Kaptan foil, which is similar to cellophane, surrounds the heating elements and the sample holder, isolating the immediate vicinity of the sample from the air atmosphere. If desired, a slight helium over-pressure can be established within the Kaptan shield, providing an oxidation-free environment at the sample surface. A small hole in the back of the sample holder allows a Chromel-Alumel thermocouple to be

directly attached at the back substrate of the sample. Heat sink grease is used to establish a good thermal contact between the thermocouple and sample. The thermocouple is used to monitor the sample temperature. Since the surface temperature (SL film) is not directly measured, a detailed experiment was performed to assess the temperature gradient through the sample. The surface temperature was measured and compared to the back thermocouple value for all relevant diffusion temperatures. Using this information, the temperature at the sample surface is deduced from the substrate mounted thermocouple.

The conductive-circulated method consists of mounting the sample onto a large heated copper holder. A thin copper cross-bar, having a small screw at each end, holds the sample to the holder. Heating coils located at both the top and bottom of the sample holder provide a fairly uniform temperature at the sample position. A Kaptan shield isolates the sample from the atmosphere. Like the radiative method, a slight helium over-pressure can be circulated past the sample surface, establishing an oxidation-free environment. A Chromel-Alumel thermocouple is mounted at the back side of the substrate. This provides a temperature reference that is used to maintain the holder at a constant temperature. At the conclusion of the diffusion experiment, the surface temperature is directly measured using a second thermocouple, which is attached directly to the sample surface.

The conductive-encapsulated heating method consists of mounting the sample inside an thin boron nitride tube, which is heated from one end. The sample is firmly pressed against the inside wall using a small bent piece of tantalum foil. The temperature is monitored using a Chromel-

Alumel thermocouple, which is attached on the outside wall near the sample position. Since the thermocouple is not directly mounted to the sample, the diffusion temperature is not known as well as the other two heating methods. The boron nitride material was selected for its absorption properties. This material is virtually transparent at the 0.7093 Å wavelength. The encapsulated method was specifically designed so that mercury vapor could be placed in equilibrium with the sample. At the diffusion temperatures relevant to this investigation, a mercury over-pressure is easily established by placing a small drop of mercury inside the container.

Once the SL sample is mounted on the heated sample holder, which is attached to the goniometer head of the diffractometer, the sample position is aligned with respect to the x-ray beam. Alignment is achieved by optimizing the (3,3,3,0) central peak reflection with respect to ω, χ, and ω-2θ. This procedure places the SL growth normal parallel to the scattering vector. Before the sample temperature is increased, several ω-2θ scans are performed using different slit widths, count times, and angle increments. From this information, scan attributes which minimize the scan time with little loss in diffraction resolution are selected for the diffusion experiment. Then the sample is quickly heated to the desired diffusion temperature. The (3,3,3,0) reflection is continually optimized during the temperature increase to compensate for sample movement. This is repeated once more after the proper sample temperature is achieved.

The diffusion temperature is monitored using a strip chart recorder, which plots the thermocouple voltage as a function of time. The sample

temperature remains stable within approximately 3 C of the desired value. Trends in the sample temperature are easily seen on the strip chart and are corrected by adjusting the heater supply current.

Once the correct diffusion temperature is attained, ω-2θ scans are repeated until no SL structure is observed. The sample alignment is continually checked by monitoring the maximum count value of the most intense central peak. Since the central peak intensity is not expected to decay with time, it provides a reference to gauge sample movement. Allowing for some change in the central peak intensity, abrupt changes indicate that the sample has moved from the optimized position. If sample movement is suspected, the diffraction scan series is briefly interrupted so that the (3,3,3,0) peak can be optimized.

4. Experimental results and discussion

The interdiffusion results are separated into two sections: nonalloyed and alloyed SL interdiffusion. First, nine HgTe-CdTe interdiffusion results are presented. This information is extracted from six samples: SL-13, SL-25, SL-48, SL-49, SL-52, and SL-54. These samples were provided by Jean-Pierre Faurie at the University of Illinois at Chicago. Two samples were large enough to separate into smaller pieces. SL-13 was reduced to three pieces and SL-49 was reduced to two pieces. Since the SL structure of the HgTe-CdTe samples quickly decayed with time, only the (2,2,2) constituent diffraction region was recorded to reduce the time per scan. The remainder of this subsection concerns diffusion results of four alloyed SL samples: SL-42, SL-43, SL-63, SL-67. The diffusion results of two cadmium alloyed and two

manganese alloyed samples are discussed. One of the manganese alloyed samples, SL-67, was large enough to split into two smaller pieces. Thus, five diffusion experiments were performed. Since the decay of satellite structure was much slower compared to the nonalloyed samples, longer scan times were possible. This permitted multiple constituent diffraction regions to be scanned during the diffusion process.

Table V.18 summarizes the experimental conditions for the HgTe-CdTe SL diffusions. Each diffusion experiment is characterized by the diffusion temperature, the gas environment surrounding the sample, the heating method employed, and the radiation wavelength used to monitor the interdiffusion process. Diffusion at temperatures between 110 C and 211 C were investigated for samples having air, helium, and mercury vapor environments using 1.47639 Å, 1.28181 Å, 1.20 Å (monochromatic synchrotron radiation), and 0.7093 Å radiation wavelengths. The available growth information and structural characterization results of each sample are found in section V.C.

Although all SL samples exhibited the general features of interdiffusion, two unexpected features were observed. First, the central peak intensity of all samples increased during the diffusion experiment. This is illustrated in Figure V.18 (Staudenmann, Horning, Knox, Reno, Sou, Faurie & Arch, 1986), which is a composite plot of five diffraction scans during the diffusion of SL-13 at 185 C. Although the satellite intensities decay with time, as expected, the central peak intensity increases by approximately 7%. Besides the fact that all intensities increase, no correlations between diffusion experiments are apparent. The fractional increase of the central peak intensity varied

Table V.18 Experimental conditions of HgTe-CdTe interdiffusion investigation

Sample	Experiment number	Radiation wavelength (Å)	Diffusion temperature (° K)	Surrounding environment	Heating method[a]
SL-13	1	1.47639	383	air	C-C
SL-13	2	1.28181	435	helium	R
SL-13	3	1.28181	458	helium	R
SL-25	4	1.20	484	helium	R
SL-48	5	0.7093	458	air	C-C
SL-49	6	0.7093	458	helium	R
SL-49	7	0.7093	483	helium	C-C
SL-52	8	0.7093	458	helium	R
SL-54	9	0.7093	458	mercury vapor	C-E

[a]R = radiative method, C-C = conductive-circulated, and C-E = conductive-encapsulated.

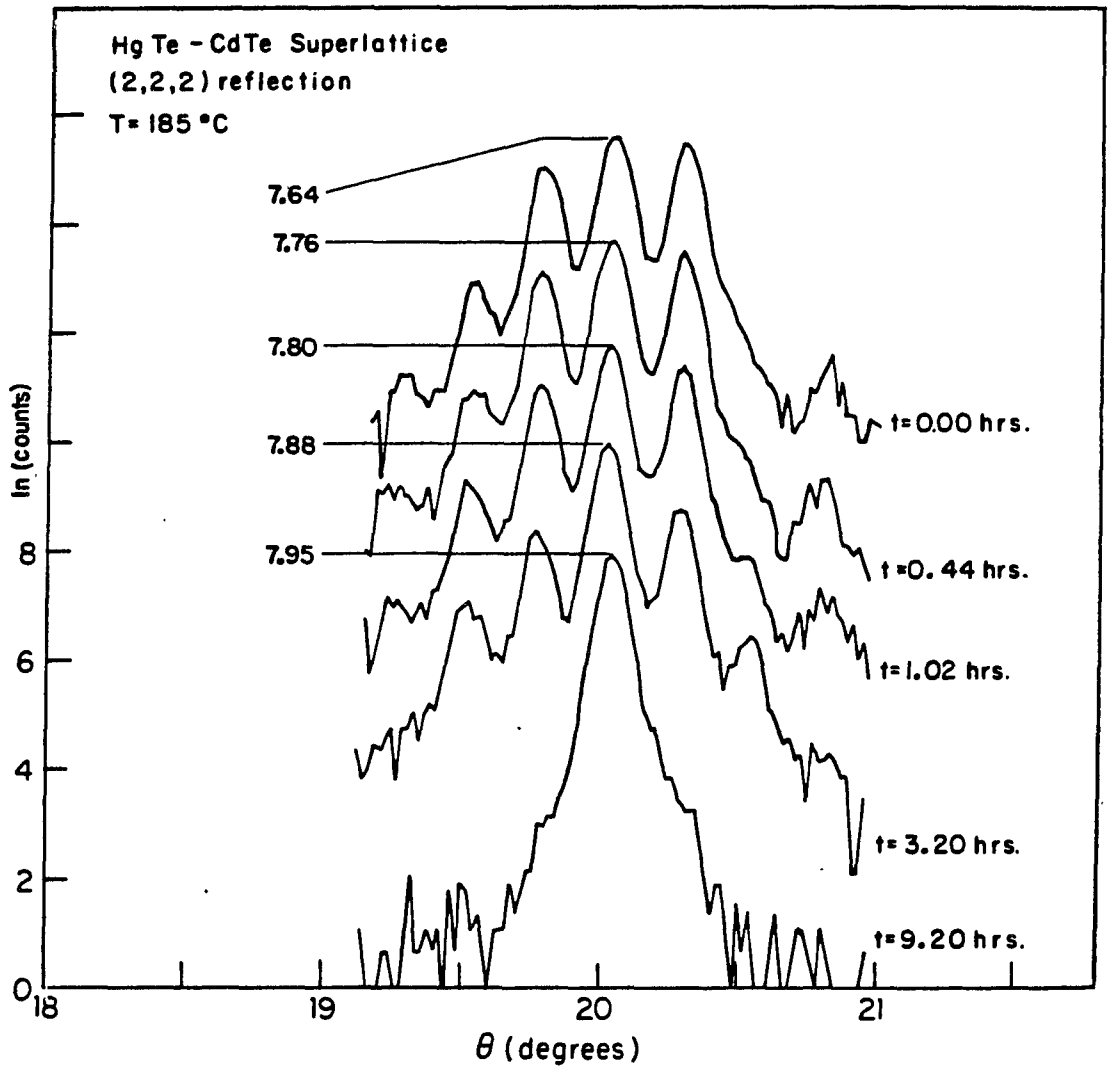

Figure V.18. Five ω-2θ scans over the (2,2,2) constituent diffraction region of SL-13 during diffusion experiment #3 (radiative method, see Table V.18). The first and fifth (2,2,2) spectra are the first and last recorded diffraction scans during the experiment. Each scan is offset by $\log_e 2$. Notice that the satellite intensities decay while the central peak intensity increases

not only from sample to sample, but also for the same sample diffused at different temperatures. In addition, the central peak widths do not change during the diffusion experiment. These observations could be explained by the a lateral annealing of the SL film (Henein & Hilliard, 1984). Since the scattering vector of the diffraction scans lies along the growth direction, an increasing depth of coherent diffraction along this direction would result in the narrowing of the SL reflections, which is not observed.

Second, at temperatures below 185 C, which is the growth temperature of the SL films, the satellite intensity ratio R(h,k,l,m) is constant early in the diffusion experiment before the onset of satellite decay. This is clearly seen in Figure V.19 (Staudenmann, Horning, Knox, Reno, Sou, Faurie & Arch, 1986), which shows the natural logarithm of the intensity ratios R(2,2,2,1), R(2,2,2,2), and R(2,2,2,3) as a function of time for SL-13 at 162 C. The constant intensity ratios are identified as "plateau" regions in Figure V.19. The time evolution of the negative order satellites are nearly identical. Figure V.20 shows the corresponding time evolution of the central peak intensity (Staudenmann, Horning, Knox, Reno, Sou, Faurie & Arch, 1986), where an 11% intensity increase is observed over a thirty hour time interval. Since the central peak intensity is increasing, a constant R(h,k,l,m) indicates that the satellite intensity increases with the central peak. For comparison, Figure V.21 shows the natural logarithm of the intensity ratios R(2,2,2,-1), R(2,2,2,-2), and R(2,2,2,-3) as a function of time for SL-13 at 185 C (Staudenmann, Horning, Knox, Reno, Sou, Faurie & Arch, 1986). No plateau regions are observed--the onset of

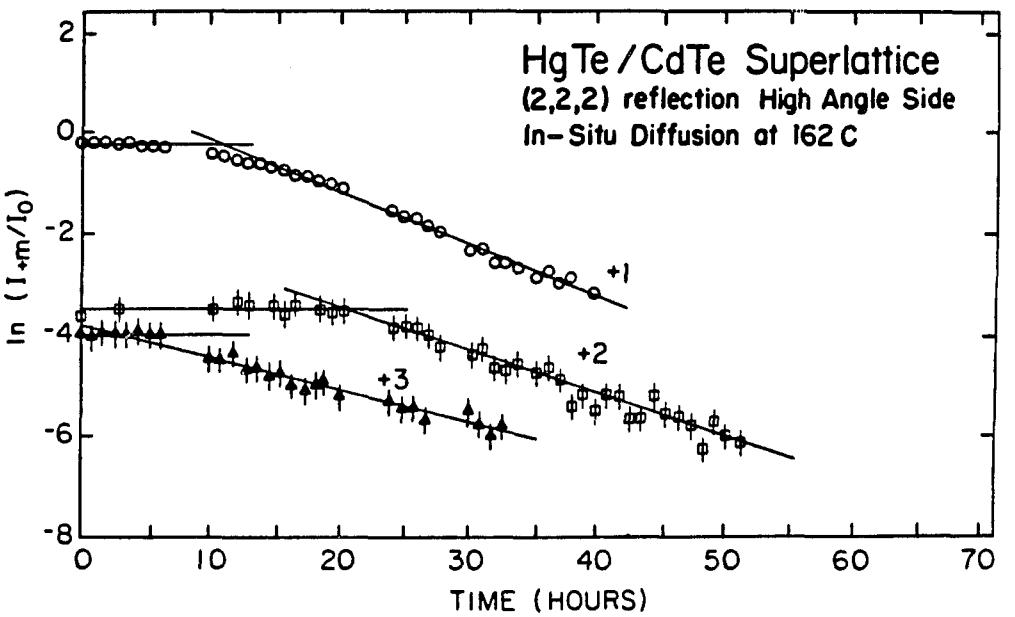

Figure V.19. The natural logarithm of the satellite intensity ratio is plotted as a function of diffusion time for the (2,2,2) constituent diffraction region of SL-13 at 435 K (diffusion experiment #2, see Table V.18). I_{+m} is the positive m order satellite intensity and I_0 is the central peak intensity. The lines distinguish the annealing ("plateau") and diffusion processes

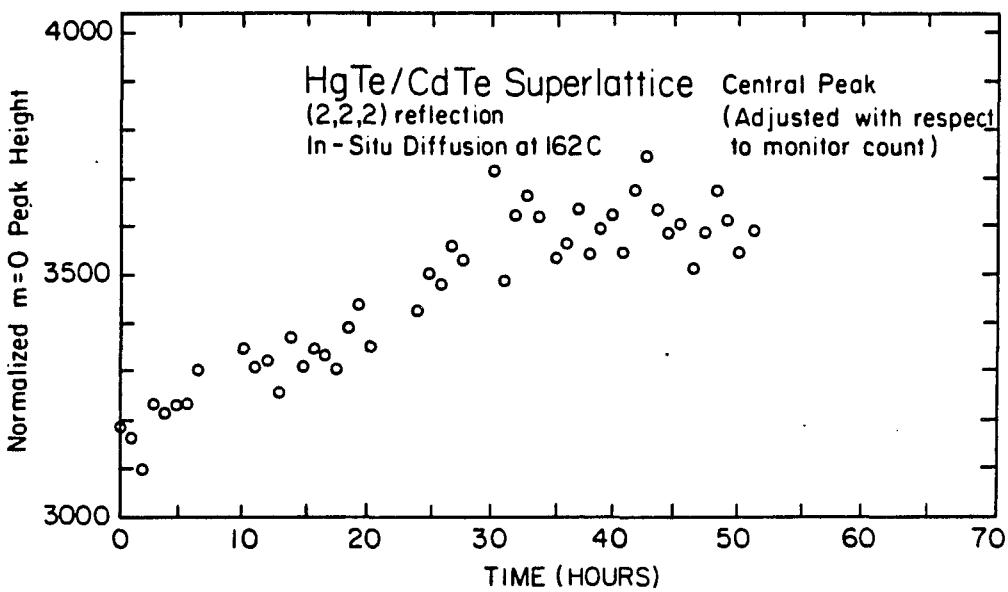

Figure V.20. The time evolution of the (2,2,2) central peak height intensity (normalized with respect to the incident intensity monitor, see section IV.A) during the diffusion of SL-13 (diffusion experiment #2, see Table V.18). An 11% increase of the central peak intensity is observed during the diffusion experiment

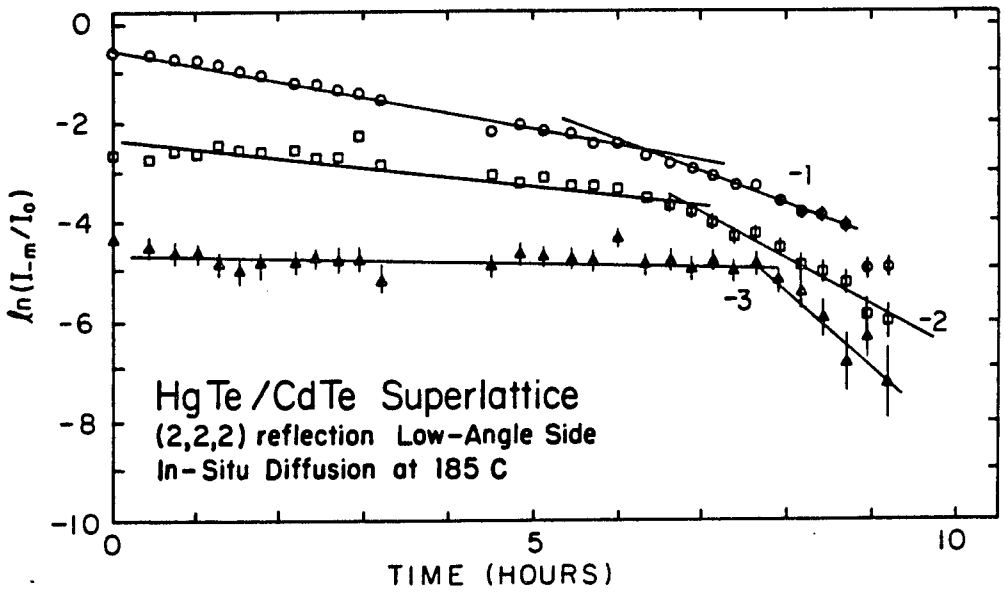

Figure V.21. The natural logarithm of the satellite intensity ratio is plotted as a function of diffusion time for the (2,2,2) constituent diffraction region of SL-13 at 458 K (diffusion experiment #3, see Table V.18). I_{-m} is the negative m order satellite intensity and I_0 is the central peak intensity

interdiffusion is immediate.

Apparently, the time evolution of R(h,k,l,m) represents two competing effects: annealing and interdiffusion. During the plateau region of the diffusion experiment, the constituent interfaces become more step-like, which requires larger contributions from higher order Fourier coefficients of the composition profile. Experimentally, this is observed as the increase of satellite intensities. Near the end of the plateau behavior, interdiffusion, which is identified by the decrease in satellite intensity with time, becomes the predominant process.

The individual diffusion coefficients D(h,k,l,m) are derived from the time evolution of $\log_e[R(h,k,l,m)]$ (see the discussion of equation V.12). A summary of this information is listed in Table V.19. All diffusion coefficients are normalized with respect to $k_m=2\pi m/L$, where m is the satellite index and L is the SL period. An experiment number, which is defined in Table V.18, identifies the experimental conditions. In addition to the tabulated diffusion coefficients, the duration of constant R(h,k,l,m) behavior is listed.

A comparison of the individual D(h,k,l,m) for any one sample suggests that the linear diffusion theory fails to describe the SL interdiffusion process. Ideally, one diffusion coefficient D(T) should describe the interdiffusion process for each sample. An inspection of Table V.19 clearly indicates that this is not observed. For example, the diffusion analysis of SL-13 at 162 C (435 K) indicates that $D(2,2,2,\pm4) \sim 0.01$ of $D(2,2,2,\pm1)$, $D(2,2,2,\pm3) \sim 0.05$ of $D(2,2,2,\pm1)$, and $D(2,2,2,\pm2) \sim 0.24$ of $D(2,2,2,\pm1)$. Similar nonlinear

Table V.19 Calculated diffusion coefficients of the HgTe-CdTe interdiffusion experiments

Experiment number[a]	Satellite index	Diffusion coefficient D(2,2,2,m) (10^{-24} m^2/second)	Initial plateau duration[b] (hours)	Initial plateau slope[c] (per hour)
1	-1	6.8 ± 0.8	83/214	-0.88 ± 0.08
	+1	6.4 ± 0.8	95/214	-0.5 ± 0.1
2	+3	6.2 ± 0.8	8/53	-3.98 ± 0.03
	-2	24. ± 1.	19.5/53	-2.81 ± 0.07
	+2	19. ± 1.	21/53	-3.51 ± 0.08
	-1	91. ± 2.	11/53	-0.73 ± 0.04
	+1	89. ± 1	11/53	-0.22 ± 0.04
3	-2	145. ± 13.	5.2/9.2	-2.9 ± 0.9
	+2	113. ± 10.	5.9/9.2	-3.53 ± 0.05
	-1	316. ± 4.	0/9.2	
	+1	307. ± 4.	0/9.2	
4	-3	20. ± 4.	0/1.4	
	+3	30. ± 6.	0/1.4	
	-2	135. ± 10.	0/1.4	
	+2	63. ± 10.	0/1.4	
	-1	1249. ± 89.	0/1.4	
	+1	1308. ± 93.	0/1.4	

[a]Defined in Table V.18.

[b](duration of plateau)/(elapse time at which no superlattice structure is observed).

[c]Slope of $\log_e[R(2,2,2,m)]$ vs. time (hours).

Table V.19 continued

Experiment number[a]	Satellite index	Diffusion coefficient D(2,2,2,m) (10^{-24} m^2/second)	Initial plateau duration[b] (hours)	Initial plateau slope[c] (per hour)
5	-1	6.7 ± 0.8	17/40	-2.20 ± 0.01
	+1	7.1 ± 0.8	17/40	-2.01 ± 0.01
6	-2	61. ± 8.	2.5/10.5	-4.3 ± 0.2
	+2	23. ± 6.	1.6/10.5	-5.1 ± 0.2
	-1	202. ± 16.	1/10.5	-2.4 ± 0.2
	+1	173. ± 14.	1/10.5	-2.1 ± 0.1
7	-2	18. ± 6.	0/1	
	-1	154. ± 14	0/1	
	+1	160. ± 12	0/1	
8	-1	29. ± 4.	0/23	
	+1	30. ± 3.	0/23	
9	-1	6.9 ± 0.6	0/47	
	+1	5.7 ± 0.5	0/47	

effects have been observed in HgTe-CdTe SLs (Arch, Faurie, Staudenmann, Hibbs-Brenner & Chow, 1986) and in GaAs-AlAs SLs (Fleming, McWhan, Gossard, Wiegmann & Logan, 1980) using the quenched sample procedure.

A general treatment of nonlinear SL diffusion is discussed by A. L. Greer and F. Spaepen (1985). This treatment, which concerns composition dependent diffusion, involves a less-simplified form of Fick's second law,

$$\frac{\partial C(z,t,T)}{\partial t} = D(C,T)\frac{\partial^2 C(z,t,T)}{\partial z^2} + \frac{\partial D(C,T)}{\partial C}\left[\frac{\partial C}{\partial z}\right]^2 , \qquad (V.15)$$

where the diffusion coefficient now depends on the composition function. Equation V.15 replaces the linear differential equation V.6. In general, the solution of equation V.15 requires numerical techniques and the extracted diffusion coefficient depends on the initial form of the composition function. Since all of the Fourier coefficients can not be extracted from x-ray diffraction information (only a limited number of satellite reflections are observed), the initial boundary values of the composition function are not known. Even if many satellite reflections were observed, the individual phases of the Fourier coefficients can not be determined by x-ray diffraction. Thus, diffusion information extracted from equation V.15 would depend on the assumptions of the initial composition profile.

A theoretical treatment of HgTe-CdTe SL interdiffusion is provided by Zanio (1986). This treatment depends on diffusion information of bulk HgTe-CdTe interfaces at temperatures between 400 C and 600 C (Zanio & Massopust, 1986). Within this temperature range, the diffusion

coefficient is observed to have the following form,

$$D_{Hg_{1-x}Cd_xTe}(\mu m^2/s) = (3.15)(10^{10-3.53x})(e^{-22400/T}) \quad , \qquad (V.16)$$

where x is the fractional cadmium concentration relative to mercury and T is the temperature (°K). By extrapolating the diffusion coefficient (equation V.16) to the SL growth temperature (185 C) and solving Fick's second diffusion equation iteratively, Zanio found that the HgTe constituent layers expand as the CdTe layers shrink. CdTe can penetrate more easily into HgTe constituent layer than HgTe diffusion into CdTe.

In an effort to confirm Zanio's predictions, an attempt to determine the constituent layer ratio of SL-13 using the step model structure factor was performed; the effects of interdiffusion are associated with changes of the constituent layer boundaries. By applying the step model to successive diffusion scans, the time evolution of the constituent layer boundaries could supply evidence of increasing HgTe layers. However, an unambiguous determination of the constituent layer thickness was not possible. This difficulty is probably related to the fitting of peak maxima instead of fitting peak profiles. Fitting the peak profiles was marginally successful. Figure V.22 shows one attempt to fit the peak profiles of SL-13 by representing each SL peak by a Pearson VII distribution. Two solid lines are drawn with the experimental data. One line represents the combined profile of all Pearson VII peaks, and the erratic line represents the difference plot between the calculated and experimental profiles. The large differences are indicative of all attempts to fit SL diffraction profiles.

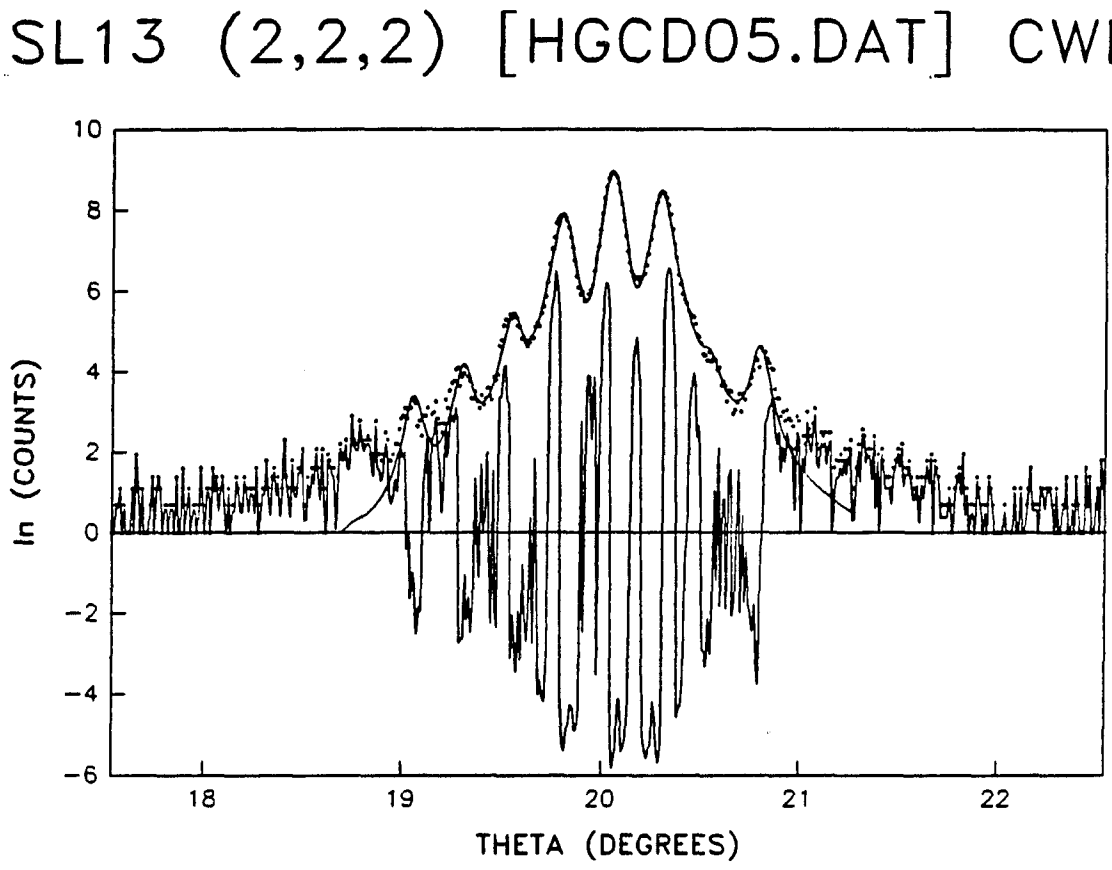

Figure V.22. A fit of the (2,2,2) constituent diffraction region of SL-13 recorded using a 1.47639 Å radiation wavelength. The diffraction data are represented by dots. An individual Pearson VII distribution (see section IV.B) is fit to each SL peak profile. Each peak is constrained to one common period and one common full width at half-maximum (FWHM). The smoothly varying line represents the total contribution of all individual Pearson VII distributions, and the erratic line represents the difference between the observed and fitted values

An inspection of Table V.19 reveals that the interdiffusion results at the same temperature vary dramatically from sample to sample. Although a concentration dependent diffusion coefficient is expected to depend on the relative concentrations of each constituent, a comparison between SL-49 and SL-52 suggest that the diffusion process depends on other growth attributes. According to Table V.18, both SLs have nearly identical HgTe and CdTe constituent layer widths, yet the diffusion coefficients extracted from the first order satellites are dramatically different. The diffusion coefficients of SL-49 are approximately 6 times larger than SL-52. This difference could be related to the different thicknesses of both the SL film and CdTe buffer layer (see Table V.4) or differences of the film quality during growth. Correlations of the diffusion coefficient among the different samples are not apparent, limiting the extraction of general SL interdiffusion conclusions.

An attempt to extract activation energy information from the diffusion investigation is illustrated in Figure V.23 (Staudenmann, Horning, Knox, Reno, Sou, Faurie & Arch, 1986), which shows the temperature dependence of the diffusion coefficients derived from samples having nearly identical attributes. Only samples having a [0,0,1] GaAs substrate, a thick CdTe buffer layer (greater than 2.2 μm), and similar constituent layer thicknesses are considered. The satellite order dependence on the activation energy emphasizes the composition dependent diffusion. The time evolution of the first, second, and third order satellites yield 0.90 eV, 0.72 eV, and 0.51 eV activation energies, respectively. Tang and Stevenson (1987a) have compared these

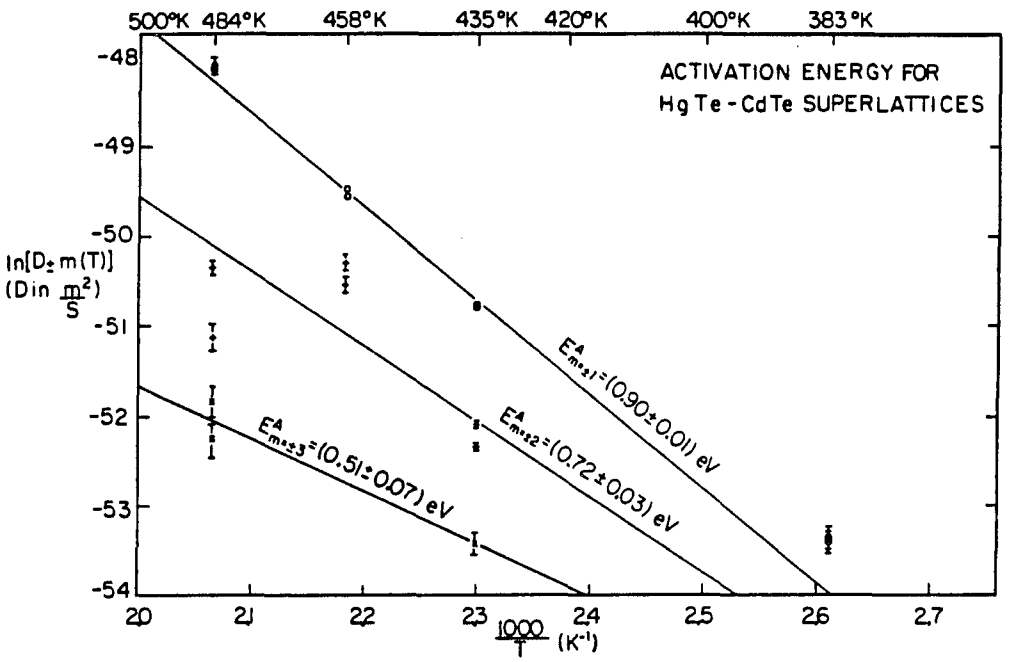

Figure V.23. The natural logarithm of the diffusion coefficients $D_m(T)$ as a function of 1000/T, where T is the absolute temperature (K). The slope of each line is related to the diffusion activation energies of each satellite order (see equation V.13). Only samples having [0,0,1] oriented GaAs substrates and thick (> 2μ) [1,1,1] oriented CdTe buffer layers are considered

results to their work on the diffusion of bulk HgTe-CdTe interfaces. Their investigation suggests that the diffusion coefficient becomes less dependent on concentration at temperatures below 300 C and that interstitial diffusion mechanism dominates the diffusion process. An extrapolation of their results to 185 C is consistent with the activation energies presented in Figure V.23 (Tang & Stevenson, 1987b).

Since $Hg_{1-x}Cd_xTe$ has a large mercury vapor pressure, the SL interdiffusion results might be explained by the loss of mercury during the diffusion experiment (Opyd, Dimiduk, Sigmon & Gibbons, 1985). This is unlikely since all HgTe-CdTe SLs are capped by a thin layer of CdTe. In addition, the large penetration depth of the x-ray radiation (several microns) probes a significant volume of the SL film, compared to the near surface region. Mercury movement within the irradiated volume must be associated with diffusion, not surface evaporation. If the mercury loss is significant, the central peak intensities would decrease with time and additional structure associate with the precipitation of tellurium would appear. These effects were not observed. However, a small loss of mercury, which would not alter the diffraction structure, could significantly affect the diffusion process. Since mercury evaporation depends on the partial pressure of mercury vapor surrounding the sample, the rate of mercury loss is expected to diminish when the sample is surrounded by mercury vapor. SL-54 was diffused in a mercury vapor environment to assess the extent of mercury evaporation. Comparing this experiment (see Table V.19) to other samples diffused at approximately the same temperature without the presence of mercury vapor, the diffusion coefficient of SL-54 is significantly lower than

the values associated with SL-13, SL-49, and SL-52, and is comparable to SL-48. Additional diffusions in a mercury environment failed because of excessive sample movement inside the boron nitride container. Thus, a low rate of mercury evaporation during the diffusion of samples in both air and helium environments remains a possibility.

In an effort to better understand the stability of HgTe-CdTe SLs, HgTe layers were alloyed with either cadmium or manganese (Faurie, Reno, Sivananthan, Sou, Chu, Boukerche & Wijewarnasuriya, 1986). On a theoretical basis, the HgTe bond strength is expected to weaken when cadmium is incorporated into the mercury sublattice (Sher, Chen, Spicer & Shih, 1985). This is related to the transfer of electrons from cadmium to mercury. These extra electrons must occupy antibonding states, since the bonding states of HgTe are occupied. The predicted destabilization of the HgTe bond in $Hg_{1-x}Cd_xTe$ alloys is consistent with experiment (Spicer, Silberman, Landau, Chen, Sher & Wilson, 1983). Like cadmium, manganese also weakens the HgTe bond strength (Sivananthan, Chu & Faurie, 1987). This has been experimentally established by monitoring the effects that manganese and cadmium have on the mercury sticking coefficient. Under identical growth rate and temperature conditions, changes in the mercury sticking coefficient are related to the bond strength of HgTe--the larger the sticking probability, the stronger the bond. The incorporation of manganese was found to destabilize the HgTe bond even more than cadmium. This experimental observation is consistent with the predicted hybridization of Mn 3d orbital electrons with the Te 5p electrons (Meheswaranathan, Sladek & Debska, 1985).

Since the diffusion process is related to the bonding energies of the constituent atoms, the interdiffusion of both $Hg_{1-x}Cd_xTe$-CdTe and $Hg_{1-x}Mn_xTe$-CdTe SL should reveal the effects of destabilized HgTe bonds, compared to HgTe-CdTe interdiffusion. Table V.20 lists the diffusion coefficients of the alloyed SL diffusion experiments. The available growth information of the manganese and cadmium alloyed SLs are listed in Tables V.9 and V.15, respectively. The alloyed SLs were grown at the same growth temperature as the HgTe-CdTe SLs. All diffusions were performed using the conductive-circulated heating method with helium gas flowing over the samples. All experiments were performed using a 1.47639 Å radiation wavelength.

Comparing Tables V.19 and V.20, the diffusion coefficients of the alloyed SLs are significantly less than the nonalloyed ones. This suggests that the alloyed samples are more stable during the interdiffusion process, which apparently contradicts the expected destabilized of the HgTe bonds. For example, at 436 K, the diffusion coefficients of SL-13 are approximately 16 and 25 times larger than SL-67 and SL-42, respectively. At 455 K, the diffusion coefficients are approximately 10 times larger than SL-63. Since manganese and cadmium content are essentially identical in SL-67 and SL-42, the diffusion at 436 K suggests that the cadmium alloyed SL is more stable than the manganese alloyed sample. Although both elements enhance the SL stability, this observation is consistent with relative differences of the manganese and cadmium destabilization observed by Sivananthan, Chu, and Faurie (1987).

Since the decay of satellite intensities were much slower during the

Table V.20 Diffusion coefficients of the $Hg_{1-x}Mn_xTe$-CdTe and $Hg_{1-x}Cd_xTe$-CdTe diffusion experiments

Sample	Composition	Diffusion temperature (° K)	Reflection (h,k,l,m)	Diffusion coefficient[a] ($X10^{-24}$ m^2/sec)	Linear correlation coefficient[b]
SL-67	$Hg_{.91}Mn_{.09}Te$-CdTe	436	(1,1,1,-2)	1.10 ± 0.06	-0.9714
			(1,1,1,+2)	1.38 ± 0.06	-0.9904
			(1,1,1,-1)	5.68 ± 0.08	-0.9975
			(1,1,1,+1)	6.07 ± 0.04	-0.9970
			(2,2,2,-2)	1.3 ± 0.1	-0.9471
			(2,2,2,+2)	0.9 ± 0.2	-0.8315
			(2,2,2,-1)	5.38 ± 0.08	-0.9931
			(2,2,2,+1)	5.57 ± 0.07	-0.9961
			(3,3,3,-2)	0.9 ± 0.2	-0.9572
			(3,3,3,-1)	5.3 ± 0.1	-0.9968
			(3,3,3,+1)	5.8 ± 0.1	-0.9963
		462	(2,2,2,-2)	10.3 ± 0.5	-0.9474
			(2,2,2,+2)	9.5 ± 1.0	-0.8517
			(2,2,2,-1)	50.2 ± 1.0	-0.9884
			(2,2,2,+1)	48.3 ± 0.7	-0.9943

[a]Based on linear diffusion theory (see equation V.12).

[b]Based on the linear fit of $\log_e[R(h,k,l,m)]$ vs time; -1.0 = complete correlation.

Table V.20 continued

Sample	Composition	Diffusion temperature (° K)	Reflection (h,k,l,m)	Diffusion coefficient[a] ($X10^{-24}$ m^2/sec)	Linear correlation coefficient[b]
SL-63	$Hg_{.9}Mn_{.1}Te$-CdTe	455	(2,2,2,-2)	8.7 ± 0.2	-0.9764
			(2,2,2,+2)	5.6 ± 0.2	-0.9072
			(2,2,2,-1)	42.8 ± 0.5	-0.9870
			(2,2,2,+1)	40.7 ± 0.3	-0.9938
SL-42	$Hg_{.92}Cd_{.08}Te$-CdTe	436	(1,1,1,-3)	0.17 ± 0.03	-0.9768
			(1,1,1,+3)	0.22 ± 0.03	-0.9866
			(1,1,1,-2)	0.65 ± 0.04	-0.9928
			(1,1,1,+2)	0.63 ± 0.03	-0.9964
			(1,1,1,-1)	2.66 ± 0.03	-0.9994
			(1,1,1,+1)	2.80 ± 0.02	-0.99995
			(2,2,2,-3)	0.29 ± 0.04	-0.9651
			(2,2,2,+3)	0.21 ± 0.06	-0.9062
			(2,2,2,-2)	0.56 ± 0.04	-0.9595
			(2,2,2,+2)	0.40 ± 0.05	-0.9255
			(2,2,2,-1)	2.71 ± 0.04	-0.9900
			(2,2,2,+1)	2.66 ± 0.04	-0.9964
			(3,3,3,-2)	0.44 ± 0.08	-0.9729
			(3,3,3,-1)	1.79 ± 0.09	-0.9881
			(3,3,3,+1)	2.52 ± 0.08	-0.9962
SL-43	$Hg_{.84}Cd_{.16}Te$-CdTe	471	(2,2,2,-2)	2. ± 2.	-0.2583
			(2,2,2,+2)	4. ± 2.	-0.8937
			(2,2,2,-1)	140. ± 10.	-0.9836
			(2,2,2,+1)	210. ± 20.	-0.9540

diffusion of the alloyed samples, compared to the nonalloyed diffusion experiments, time was available to scan multiple constituent diffraction regions. Figure V.24 illustrates the time evolution of the negative first order satellite in the (1,1,1), (2,2,2), and (3,3,3) constituent diffraction regions of SL-42 (Staudenmann, Knox & Faurie, 1987b). The slope of each line is directly related to the diffusion coefficient. The time evolution of both the R(1,1,1,-1) and R(2,2,2,-1) intensity ratios have nearly identical slopes, which are slightly greater than the slope associated with R(3,3,3,-1). All three m=-1 satellite peaks are proportional to the same Fourier coefficient (see equation V.12). The time evolution of these peaks should be identical, if the lattice parameters of both constituent materials are identical. The apparently slower decay of the (3,3,3,-1) satellite could be attributed to lattice relaxation, which is more noticeable at larger scattering angles.

The time evolution of the first three negative satellites in the (1,1,1) constituent diffraction region of SL-42 is illustrated in Figure V.25 (Staudenmann, Knox & Faurie, 1987b). Like the nonalloyed samples, the nearly identical slopes emphasize the nonlinear behavior of the interdiffusion process; under linear diffusion, the slope associated with the (1,1,1,-2) and (1,1,1,-3) satellites should be four and nine times greater than the evolution of the (1,1,1,-1) reflection. Unlike the nonalloyed diffusion experiments, no plateau behavior is observed for any satellite reflection at any diffusion temperature considered. For example, comparing Figures V.19 and V.25, the plateau behavior of the third, second and first order satellites of SL-13 lasted approximately 8, 20, and 11 hours, respectively. The onset of diffusion

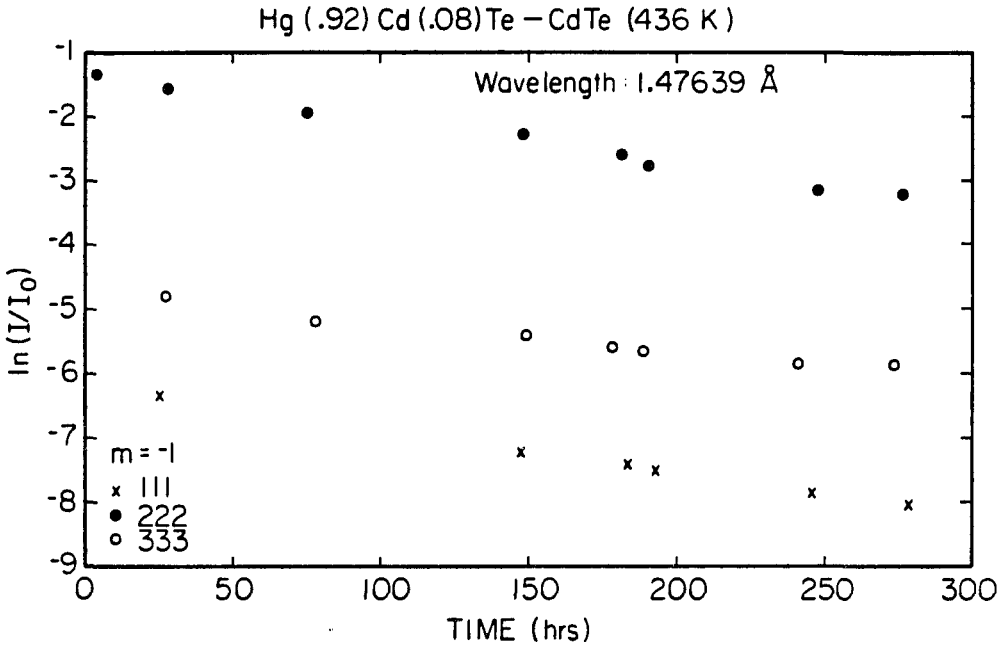

Figure V.24. The time evolution of the m=-1 satellite intensity ratios during the conductive-circulated diffusion of SL-42 at 436 K. The X, filled circle, and open circle markers represent data from the (1,1,1), (2,2,2), and (3,3,3) constituent diffraction regions, respectively. The intensity ratio is defined by the satellite intensity I and the corresponding central peak intensity I_0. A 1.47639 Å radiation wavelength was used during the diffusion experiment (see Table V.20)

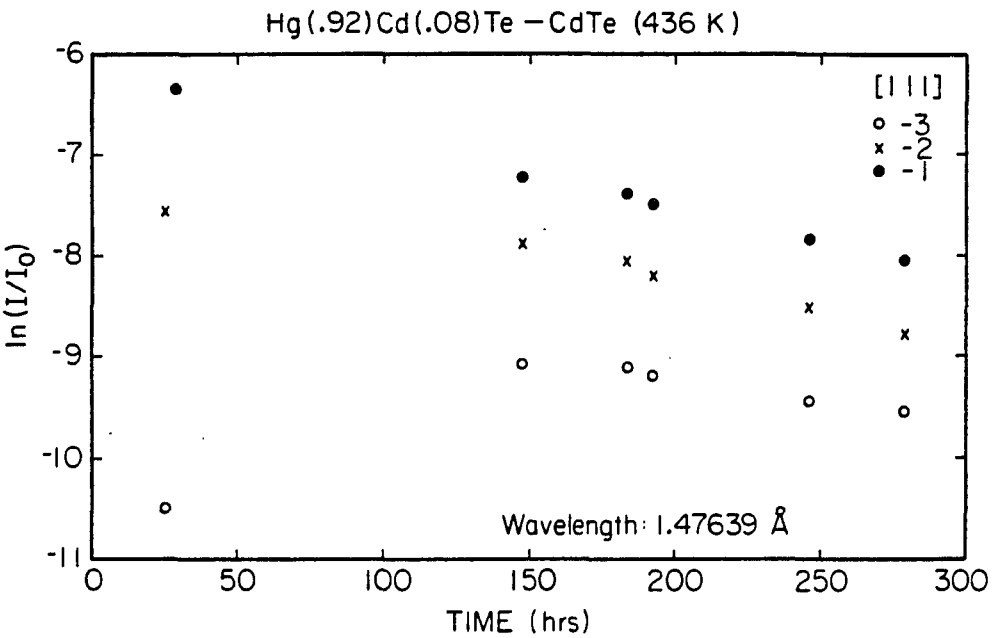

Figure V.25. The time evolution of the (1,1,1,-3), (1,1,1,-2), and (1,1,1,-1) peak intensity ratios of SL-42 during the conductive-circulated diffusion at 436 K (see Table V.20). The filled circle, X, and open circle markers represent the m=-1, m=-2, and m=-3 satellites. The intensity ratio is defined by the satellite intensity I and the (1,1,1) central peak intensity I_0. A 1.47639 Å radiation wavelength was used during the diffusion experiment (see Table V.20)

was immediate for all alloyed SL samples.

Although the composition function changes during the diffusion experiments, the SL period is stable. Figure V.26 shows the computed period of SL-42 during the diffusion experiment at 436 K (Staudenmann, Knox & Faurie, 1987b). Within the predicted uncertainties, the SL period is constant, suggesting that the boundaries of the SL unit cells are stable. If Zanio's interdiffusion theory (1986) is correct, the predicted HgTe layer expansion and CdTe layer contraction are constrained so that the combined length of both constituent layers is constant.

5. Summary

The use of x-ray diffraction to characterize SL interdiffusion has been quite successful. The sensitivity of this technique is derived from the ability to characterize the composition profile of many constituent layer interfaces at once. In addition, the in situ diffusion method is successful in monitoring the dynamics of the diffusion process. Compared to the quenched sample method, fewer uncertainties are subjected to the diffusion analysis.

Although the incorporation of either manganese or cadmium into HgTe is expected to weaken the atomic bonds, both $Hg_{1-x}Mn_xTe$-CdTe and $Hg_{1-x}Cd_xTe$-CdTe SL are found to be more stable than HgTe-CdTe. This is illustrated in Figure V.27 (Staudenmann, Knox & Faurie, 1987b), where the time evolution of the (2,2,2,1) satellite peak is shown for three different samples. At 436 K, the HgTe-CdTe SL structure is destroyed after 53 hours of diffusion. This is significantly lower than the 225

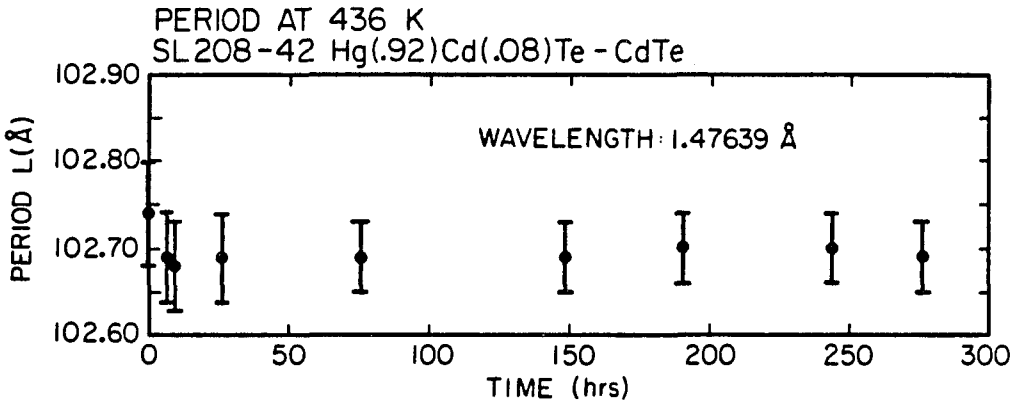

Figure V.26. A plot of the measured SL period as a function of time during the conductive-circulated diffusion of SL-42 at 436 K. The calculated periods were derived using the commensurate period approximation (see section IV.D.1). The horizontal lines represent the predicted period uncertainties

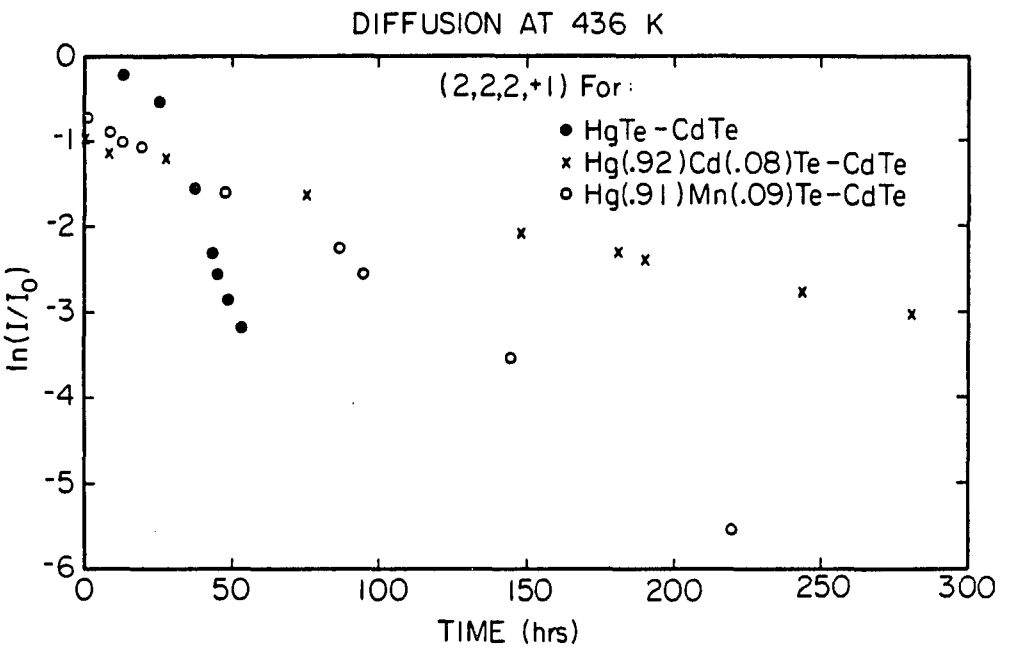

Figure V.27. A comparison of three diffusion experiments at 436 K. The time evolution of the (2,2,2,+1) satellite intensity ratio is plotted as a function of the diffusion time. The filled circle, X, and open circle markers represent diffusion data of SL-13, SL-42, and SL-67, respectively. The intensity ratio is defined by the (2,2,2,+1) satellite intensity I and the (2,2,2,0) central peak intensity I_0

and 280 hours required to destroy the $Hg_{1-x}Mn_xTe$-CdTe and $Hg_{1-x}Cd_xTe$-CdTe SLs, respectively.

The temperature dependence of the diffusion coefficients is characterized by the activation energy (see equation V.13). Although the diffusion coefficient appears to be heavily sample dependent, an approximate activation energy can be extracted from the diffusion results. This information is summarized in Table V.21. The activation energies are identified by satellite order only, regardless of the constituent diffraction region.

The amount of interdiffusion that occurs during growth can be approximated from diffusion experiments performed at the growth temperature. Relating the time required to completely destroy any visible satellite structure (experiment duration) to the SL period, a diffusion rate is defined: $R_d \equiv (L/2)/(\text{experiment duration})$, where L is the SL period. For the nonalloyed SLs, R_d varies from 2.8 Å/hour (SL-54) to 34 Å/hour (SL-13) for diffusion at the growth temperature. Only one alloyed SL, SL-63, was diffused at the growth temperature, yielding a 3.8 Å/hour diffusion rate.

An inspection of Tables V.19 and V.20 indicate that the diffusion coefficients depend on the satellite index. This dependence prevents comparisons to other diffusion analysis techniques, which associate one unique diffusion coefficient and activation energy to any specific diffusion process. The large differences between satellite orders indicates the failure of the linear diffusion theory to describe SL interdiffusion. A concentration dependent diffusion coefficient must be introduced into the diffusion analysis before attempting to identify the

diffusion mechanism responsible for SL interdiffusion.

Table V.21 Activation energies associated with the alloyed and nonalloyed SL diffusion experiments

Superlattice system	Satellite order	Activation[a] energy (eV)	Linear[b] correlation coefficient	Points/Temperatures[c]
HgTe-CdTe	1	0.90 ± 0.01	-0.996	8/4
	2	0.72 ± 0.03	-0.884	6/3
	3	0.51 ± 0.07	-0.983	3/2
$Hg_{1-x}Mn_xTe$-CdTe	1	1.65 ± 0.01	-0.991	10/3
	2	1.55 ± 0.05	-0.995	9/3
$Hg_{1-x}Cd_xTe$-CdTe	1	2.11 ± 0.05	-0.994	8/2
	2	0.85 ± 0.51	-0.456	5/2

[a]Nonalloyed results based on SL-13, SL-25, SL-52; alloyed results based on all four samples.

[b]Based on a fit to $\log_e[D(T,m)]$ vs T^{-1}; -1 is a perfect correlation.

[c](Number of data point in fit)/(Number of temperatures considered).

E. Structural Variations during Superlattice Growth

According to the interdiffusion investigation of HgTe-CdTe SLs at the growth temperature (185 C), interdiffusion during the SL deposition may significantly affect the composition profile of early-deposited atomic layers. Unlike the interdiffusion investigation presented in section V.D, growth interdiffusion is a nonuniform effect, where the early-deposited layers have more time to diffuse than the near surface layers. In an effort to investigate growth interdiffusion, two thick SLs were fabricated: SL-93 and SL-95. These samples were provided by

Jean-Pierre Faurie at the University of Illinois at Chicago. Both SLs were grown at 185 C by molecular beam epitaxy on [0,0,1] oriented GaAs substrates (Faurie, Million & Piaguet, 1982) The available growth information is listed in Table V.22. The growth time of both SLs, 7 hours for SL-93 and 8.3 hours for SL-95, are comparable to the time required to completely destroy SL-13 at the growth temperature. Thus, the early-deposited layers of each SL are expected to be almost totally diffused, provided that the onset of diffusion is immediate after deposition.

In an ideal experiment, growth interdiffusion would be explored by successively removing one period, and investigating the chemical composition of the freshly exposed layer before removing another period. This procedure would provide an unambiguous characterization of the interdiffusion process. The degradation of each interface could be examined as a function film depth. However, there are no known methods that reliably etch HgTe and CdTe in a controlled manner.

By exploiting the penetration properties of x-ray radiation, some growth interdiffusion information can be extracted from thick film SL samples. Depending on the penetration length of the incident radiation, the effective volume of diffraction can be varied from the near surface region to the entire sample (see section II.D). By comparing diffraction spectra that were recorded using different wavelengths, qualitative information about the growth interdiffusion process can be extracted in a nondestructive manner.

Both SL-93 and SL-95 were characterized using four radiation wavelengths: 1.47639 Å, 1.28181 Å, 1.09855 Å, and 0.7093 Å. The

Table V.22 Available growth history of SL-93 and SL-95

Sample	Substrate		Buffer layer			Superlattice		
	growth normal	type	growth normal	type	thickness (μ)	growth normal	constituent layer ratio[a] (HgTe/CdTe Å)	thickness / time[b] (μ / hours)
SL-93	[0,0,1]	GaAs	[1,1,1]	CdTe	2.6	[1,1,1]	144/58	6.33 / 7.0
SL-95	[0,0,1]	GaAs	[1,1,1]	CdTe	2.5	[1,1,1]	85/72	6.60 / 8.3

[a]Constituent layer thickness predicted during growth.

[b]Total SL thickness and the time required to grow the SL film.

penetration lengths $\mu(\lambda)$ (see equation II.28) associated with these wavelengths are listed in Table V.23. The effective penetration depth d_p, which is defined along the growth direction, depends on both the penetration length $\mu(\lambda)$ and the Bragg angle Θ,

$$d_p = \mu(\lambda)\sin\Theta \quad . \tag{V.17}$$

According to the Bragg relation, $\sin\Theta$ depends only on the radiation wavelength, for any given crystallographic reflection. Thus, when comparing reflections at different wavelengths, the associated penetration depth d_p will vary as the product of $\mu(\lambda)\lambda$, which is listed in Table V.23. If d_p is much smaller than the SL film thickness, only the near-surface structure (last atomic layers to be deposited) diffracts. If d_p is much larger than the SL film thickness, however, the entire SL volume is characterized. Unfortunately, diffraction from regions deep within the sample (early-deposited layers) can not be isolated from the near-surface diffraction, complicating the interpretation of the diffraction spectra.

Without reference to a particular model, only qualitative information can be extracted from the wavelength dependence of the diffraction spectra. Growth interdiffusion affects the structure factor of each SL unit cell without affecting the position of the unit cell. This latter point is based on the observed stability of the SL period during the interdiffusion investigation. Since growth interdiffusion affects each SL unit cell differently, all individual structure factors are not identical, and the intensity function can no longer be expressed

Table V.23 Penetration length as a function of wavelength for SL-93 and SL-95

Sample	Penetration length			
	1.47639 Å (μ)	1.28181 Å (μ)	1.09855 Å (μ)	0.7093 Å (μ)
SL-93	6.47 (9.55)	9.41 (12.06)	14.2 (15.6)	21.3 (15.1)
SL-95	6.79 (10.02)	9.89 (12.68)	15.0 (16.5)	26.3 (18.7)

[a]Penetration depth, using the mass absorption coefficients calculated by Cromer (1983), assuming no refractive deflection at the HgTe/CdTe interfaces. The penetration length multiplied by the wavelength is listed in parentheses. This value is related to the effective penetration depth.

in terms of a geometrical progression (see section III.B). Both the intensity and breadth of the SL reflections will depend on the correlations between individual SL unit cells; the intensity will decrease and the breadth will increase as the correlations between individual cells diminishes (Guinier, 1963; James, 1982). The severity of growth interdiffusion within any SL unit cell depends on its location along the growth direction. This suggests that structure factor correlations among individual unit cells will depend on their separation along the growth direction, with the degree of correlation diminishing as this separation increases. Along the growth direction, the number of unit cells that significantly contribute to the total diffracted intensity depends on the penetration depth d_p. Thus, the breadth (in reciprocal space) of every SL peak is expected to increase with the penetration depth.

Both SL-93 and SL-95 clearly exhibit a broadening of the SL peak breadths as the penetration depth increases. This is illustrated in Figures V.28-33, which show the ω-2θ diffraction spectra of both samples. The diffracted intensity is plotted as a function of the reciprocal scattering magnitude ($q=4\pi\sin\theta/\lambda$). Peak broadening is more pronounced in SL-93. This is most noticeable in the diffraction scans at 0.7093 Å, where the SL structure is almost completely masked by the very broad peaks. Since SL-93 contains a significantly larger HgTe constituent layer, HgTe appears to be less stable than CdTe, which is in agreement with Zanio (1986). The scan resolution within the diffraction plane was identical for all scans. Within the scattering plane, a 1 mm incident slit width and a 1.2 mm detector slit defined the scan

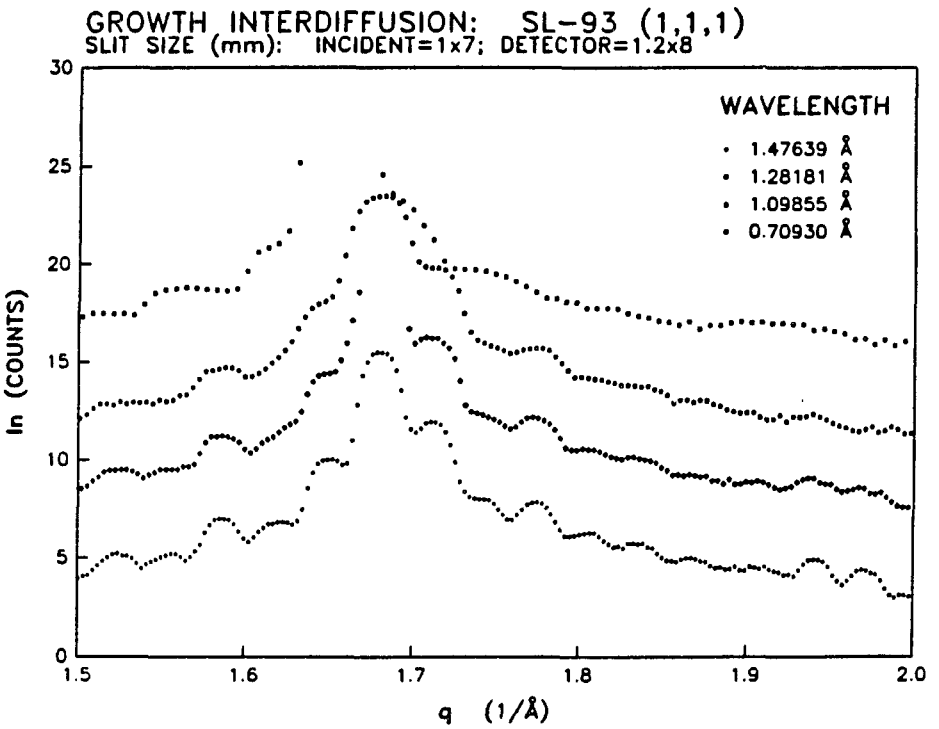

Figure V.28. ω-2θ diffraction scans over the (1,1,1) constituent diffraction region of SL-93 using 1.47639 Å, 1.28181 Å, 1.09855 Å, and 0.7093 Å radiation wavelengths, from bottom to top, respectively. A 1 mm by 7 mm (sample height) incident and a 1.2 mm by 8 mm detector collimator were used. The natural logarithm of the diffracted intensity is plotted as a function of $q=4\pi\sin\theta/\lambda$, where θ is the Bragg angle, and λ is the radiation wavelength (Å). The central peak intensity blanked the detector during the 1.28181 Å and 0.7093 Å radiation scans

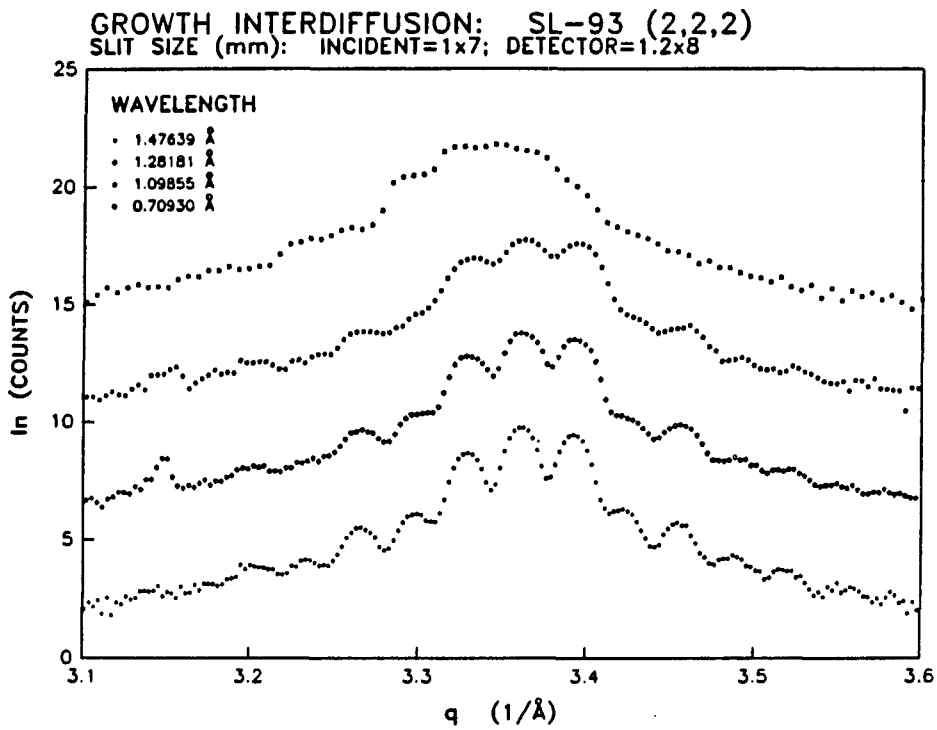

Figure V.29. ω-2θ diffraction scans over the (2,2,2) constituent diffraction region of SL-93 using 1.47639 Å, 1.28181 Å, 1.09855 Å, and 0.7093 Å radiation wavelengths, from bottom to top, respectively. A 1 mm by 7 mm (sample height) incident and a 1.2 mm by 8 mm detector collimator were used. The natural logarithm of the diffracted intensity is plotted as a function of $q=4\pi\sin\theta/\lambda$, where θ is the Bragg angle, and λ is the radiation wavelength (Å)

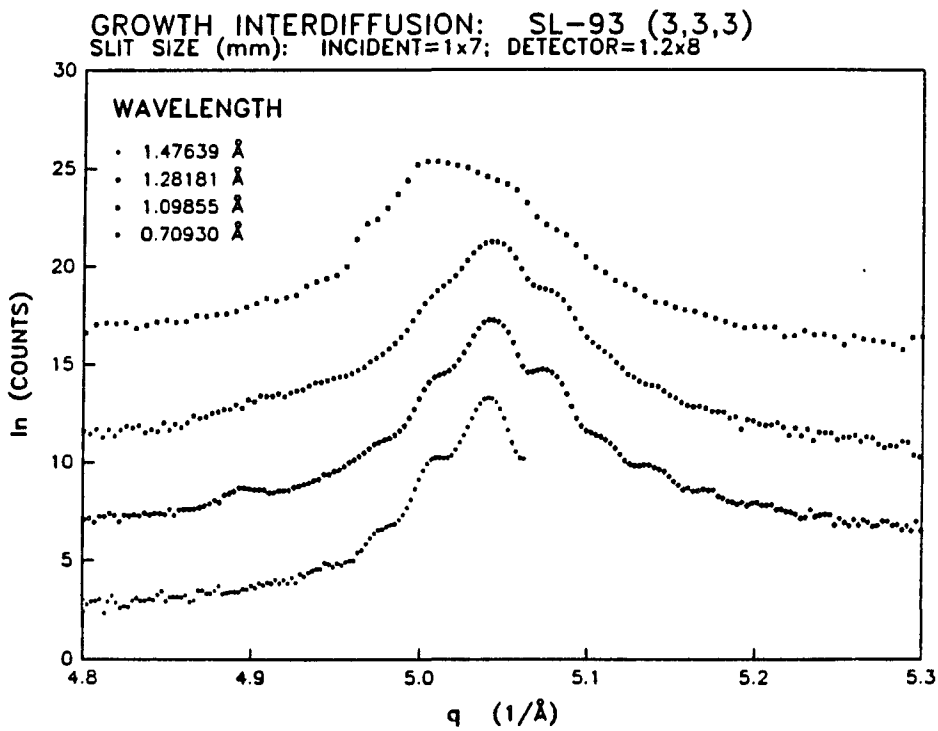

Figure V.30. ω-2Θ diffraction scans over the (3,3,3) constituent diffraction region of SL-93 using 1.47639 Å, 1.28181 Å, 1.09855 Å, and 0.7093 Å radiation wavelengths, from bottom to top, respectively. A 1 mm by 7 mm (sample height) incident and a 1.2 mm by 8 mm detector collimator were used. The natural logarithm of the diffracted intensity is plotted as a function of $q=4\pi\sin\Theta/\lambda$, where Θ is the Bragg angle, and λ is the radiation wavelength (Å). The x-ray generator malfunctioned during the 1.47639 Å radiation scan

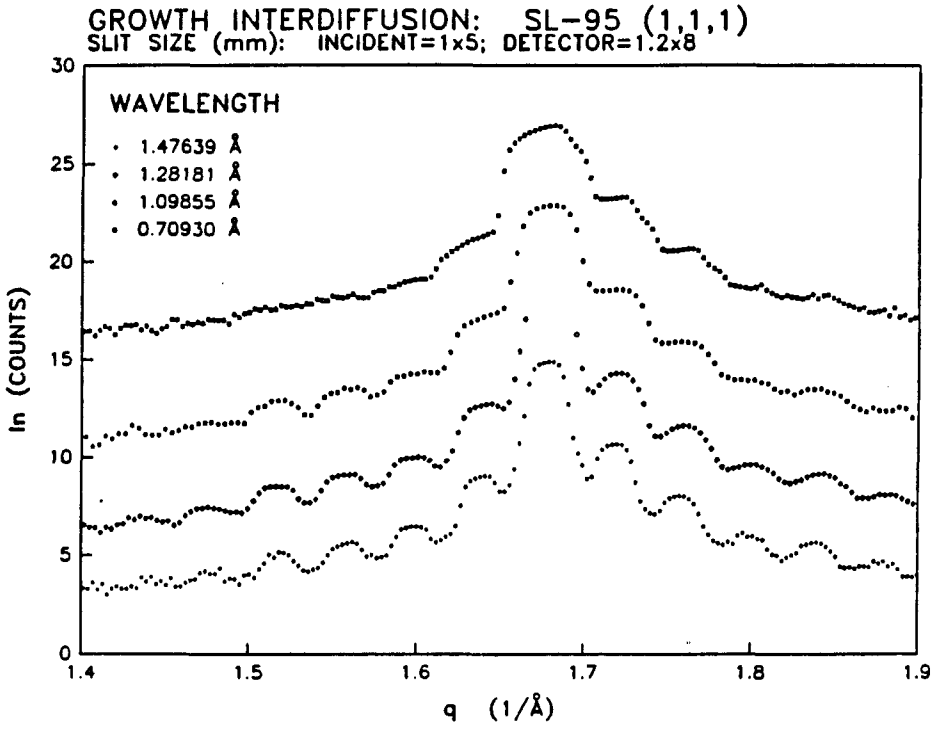

Figure V.31. ω-2Θ diffraction scans over the (1,1,1) constituent diffraction region of SL-95 using 1.47639 Å, 1.28181 Å, 1.09855 Å, and 0.7093 Å radiation wavelengths, from bottom to top, respectively. A 1 mm by 5 mm (sample height) incident and a 1.2 mm by 8 mm detector collimator were used. The natural logarithm of the diffracted intensity is plotted as a function of $q=4\pi\sin\Theta/\lambda$, where Θ is the Bragg angle, and λ is the radiation wavelength (Å). The central peak intensity blanked the detector during the 1.28181 Å radiation scan

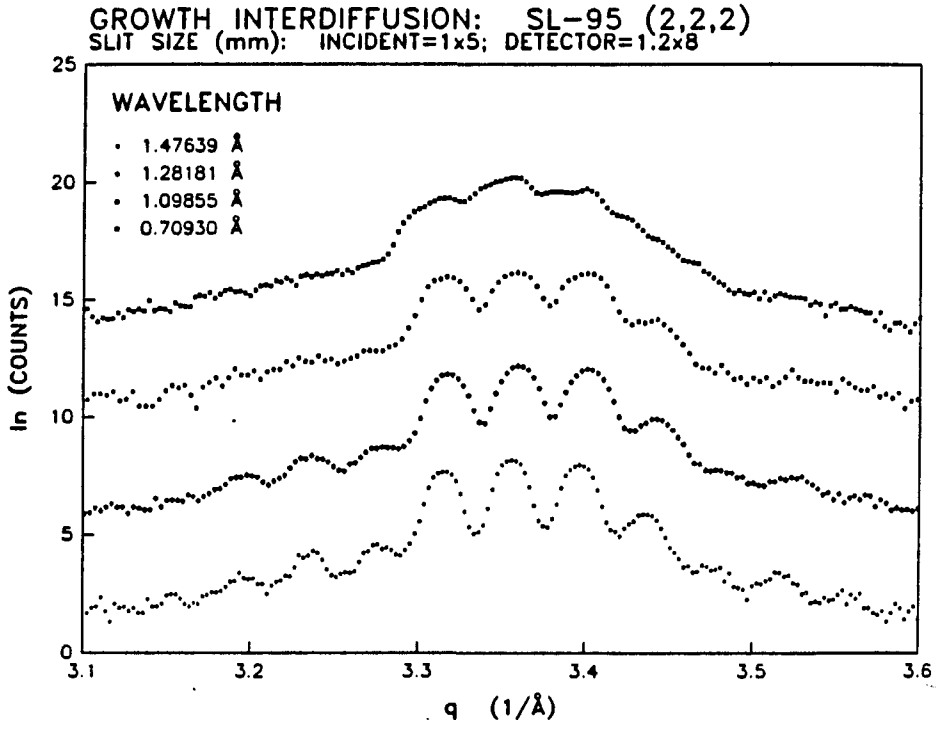

Figure V.32. ω-2θ diffraction scans over the (2,2,2) constituent diffraction region of SL-95 using 1.47639 Å, 1.28181 Å, 1.09855 Å, and 0.7093 Å radiation wavelengths, from bottom to top, respectively. A 1 mm by 5 mm (sample height) incident and a 1.2 mm by 8 mm detector collimator were used. The natural logarithm of the diffracted intensity is plotted as a function of $q=4\pi\sin\theta/\lambda$, where θ is the Bragg angle, and λ is the radiation wavelength (Å)

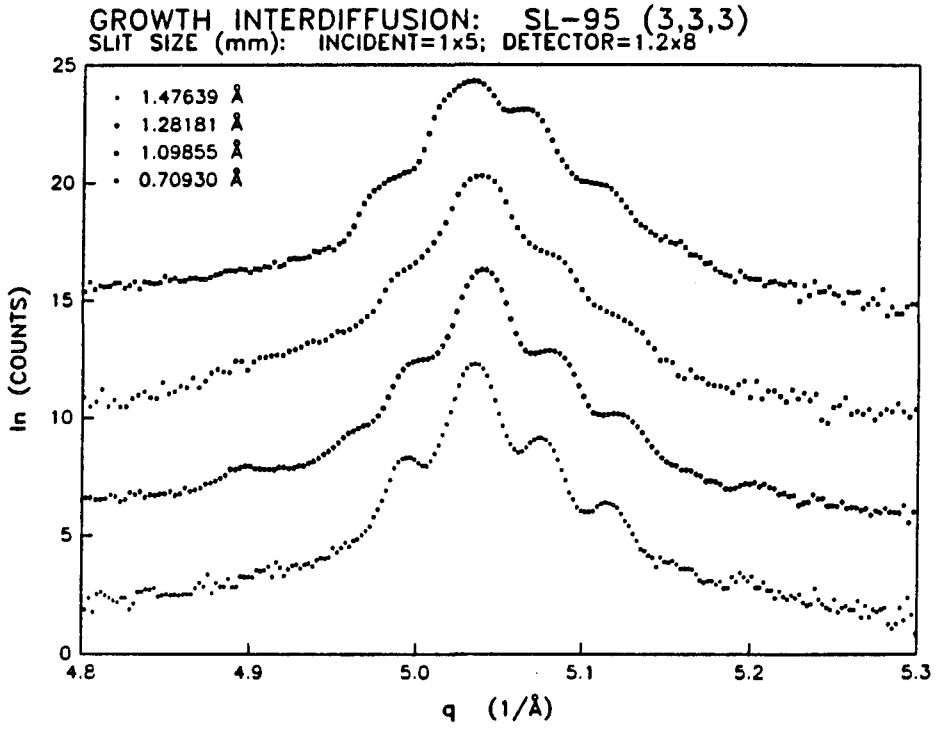

Figure V.33. ω-2θ diffraction scans over the (3,3,3) constituent diffraction region of SL-95 using 1.47639 Å, 1.28181 Å, 1.09855 Å, and 0.7093 Å radiation wavelengths, from bottom to top, respectively. A 1 mm by 5 mm (sample height) incident and a 1.2 mm by 8 mm detector collimator were used. The natural logarithm of the diffracted intensity is plotted as a function of $q=4\pi\sin\theta/\lambda$, where θ is the Bragg angle, and λ is the radiation wavelength (Å)

resolution. The collimator width perpendicular to the scattering plane was set to the sample height, which is 7 mm for SL-93 and 5 mm for SL-95. Sample alignment with respect to the incident radiation was achieved by optimizing the (3,3,3,0) satellite peak.

Both the SL period and average constituent cell length were calculated as a function of wavelength. This information is summarized in Table V.24. Because of the poor SL structure, period information could not be extracted from the 0.7093 Å wavelength data. Yielding consistently lower χ values, only the incommensurate least-squares fit results are listed. The period of SL-93 varies from 197.6 ± 0.9 Å using 1.28181 Å radiation to 202. ± 0.1. Å using 1.09855 Å radiation. The period of SL-95 varies from 154.0 ± 0.5 Å using 1.09855 Å radiation to 165.9 ± 0.4 Å using 1.47639 Å radiation. If period fluctuations were present in these samples, peak broadening that varies linearly with the satellite order would be observed (McWhan, 1985). This distinctive type of peak broadening is known as strain broadening. A slight broadening trend that increases with satellite order is observed in the diffraction data of both SL-93 and SL-95. Fitting a line to these broadening trends a period range is extracted (Gyorgy, McWhan, Dillon, Walker & Waszczak, 1982). A 13 ± 5 Å and 18 ± 12 Å period range is obtained for SL-93 and SL-95, respectively. These values are unaffected by the radiation wavelength used to probe the sample. The relatively large uncertainties of these quantities are related to the poor linear relationship of the peak broadening trend.

Table V.24 Incommensurate least-squares fit of both SL-93 and SL-95 as a function of wavelength

Sample	Wavelength (Å)	Period[a] L (Å)	Avg. const. cell length[b] <c> (Å)	Const. cells per period[c]	weighted χ^2[d]	No. of peaks included in fit (central)	(satellite)
SL-93	1.47639	198.6 ± 0.6	11.218 ± 0.001	17.70 ± 0.05	6.56	3	25
	1.28181	197.6 ± 0.9	11.215 ± 0.002	17.62 ± 0.08	8.26	3	24
	1.09855	202. ± 1.	11.207 ± 0.003	18.00 ± 0.11	4.97	3	16
SL-95	1.47639	156.9 ± 0.4	11.232 ± 0.001	13.97 ± 0.03	8.15	3	32
	1.28181	154.8 ± 0.5	11.223 ± 0.001	13.80 ± 0.04	8.37	2	27
	1.09855	154.0 ± 0.5	11.226 ± 0.002	13.72 ± 0.05	5.86	3	21

[a]Based on equations IV.25a-b.

[b]Average hexagonal constituent cell length along the growth direction based on equations IV.25a and IV.25b.

[c]The SL period divided by the average constituent cell length.

[d]Defined by equation IV.24a.

VI. EXPERIMENTAL RESULTS: CdTe-ZnTe

A. Experiment Overview

This chapter contains a summary of all experimental investigations related to two CdTe-ZnTe SLs, SL-17 and SL-18. The experimental results are divided into three sections: precession photography, diffractometer data, and step model results. Precession photography results are presented in section VI.B. Since the background information is discussed in section V.B, only specific precession photographs are illustrated and interpreted.

Section VI.C concerns diffractometer results. The SL period, the average constituent cell length along the growth direction, the in-plane constituent lattice parameter, and the Scherrer lengths are extracted from the diffraction spectra and discussed for both SL-17 and SL-18.

Information derived from SL peak intensities are discussed in section VI.D. By fitting SL peak intensities to the step model structure factor, the individual constituent lattice parameters are determined. After introducing the essential definitions, the step model fitting procedure is outlined and applied to both SL-17 and SL-18. Finally, the constituent lattice strain along the growth direction is derived from the step model results and compared to theory.

B. Precession Photography

Unlike the $Hg_{1-x}X_xTe$-CdTe system, precession photographs of the CdTe-ZnTe SLs do reveal satellite structure. Most of the CdTe-ZnTe SL samples have periods between 40 Å and 60 Å. The satellite separation at

these modulation wavelengths is slightly larger than the resolution limit of the precession camera. In addition, the strain that is present in most of the CdTe-ZnTe SLs causes the second and third order satellites to be the most intense. The separations between these satellites and the central peak are easily within the camera resolution. However, the satellite intensities are low compared to the average constituent lattice and underlying buffer layer reflections, making quantitative measurements extremely difficult.

Precession results of two SLs (SL-17 and SL-18) are discussed in this section. A summary of sample attributes is presented in Table VI.1. Both SLs were provided by Jean-Pierre Faurie at the University of Illinois at Chicago, and were grown by molecular beam epitaxy (Monfroy, Sivananthan, Chu, Faurie, Knox & Staudenmann, 1986). A thick $Cd_{.5}Zn_{.5}Te$ buffer layer is deposited on the GaAs substrate in an effort to confine misfit dislocations to this region. Both the buffer layer and SL film are oriented identically with the substrate. The deposition normal is coincident with the [0,0,1] crystallographic direction.

A precession photograph of SL-17 is shown in Figure VI.1. The precession film vertical represents the [0,0,1] growth direction and the film horizontal represents the [1,1,0] direction. Satellite reflections are clearly visible; they are directed vertically and are centered on all reflections of the average constituent lattice. The spacing between adjacent satellites is approximately 1.1 mm on the precession film. GaAs reflections are also present and appear as isolated spots. For reference, Figure VI.2 illustrates the constituent reciprocal lattice level associated with Figure VI.1.

Figure VI.1. Precession photograph of a CdTe-ZnTe SL (SL-17) deposited on a GaAs substrate. Reciprocal lattice points along both the [0,0,1] SL growth direction and the [0,0,1] GaAs surface normal are observed along the film vertical. The circled dot represents the approximate film center. Molybdenum K_α radiation, which passes through a zirconium filter, is incident on the sample (see section IV.E for precession geometry details). The attenuated molybdenum continuum radiation causes the observed radial streaking of the diffraction maxima. Unlike the HgTe-CdTe SLs, satellite structure is visible as diffuse patches about the central peaks

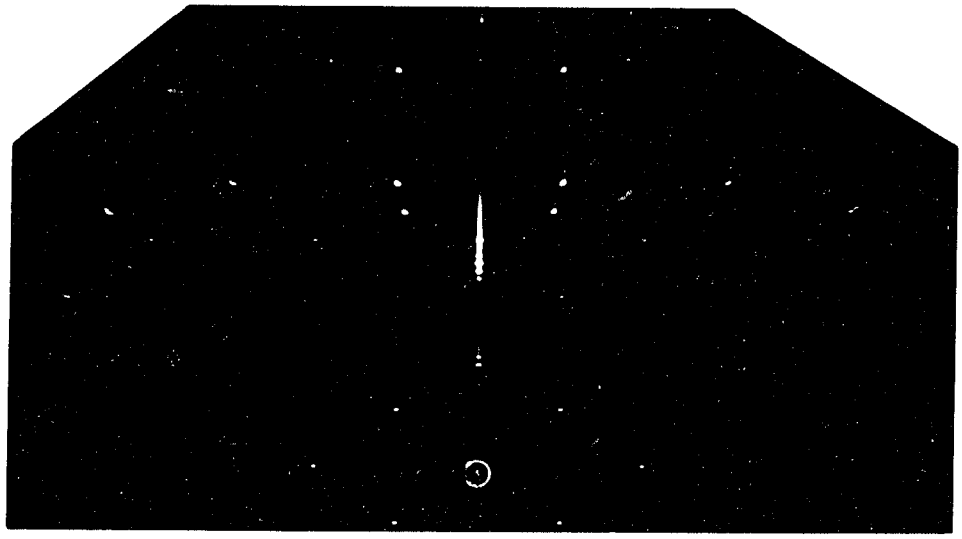

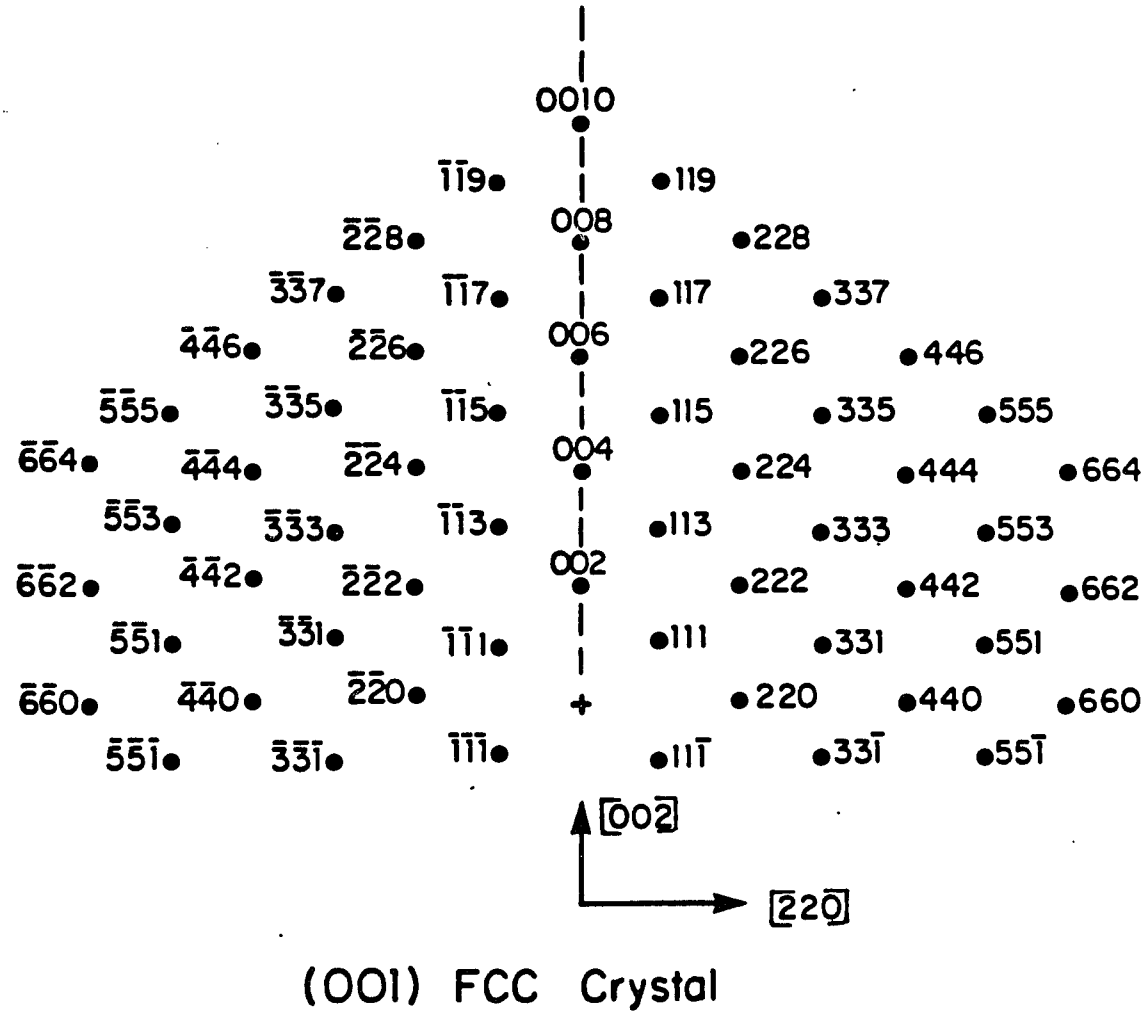

(001) FCC Crystal

Figure VI.2. An illustration of an indexed precession film that corresponds to a face-centered cubic lattice having a [0,0,1] surface normal. This plane represents the GaAs reflections of the precession film shown in Figure VI.1

Figure VI.1 confirms that both the SL film and buffer layer are deposited epitaxially onto the substrate and that the crystalline quality is quite good. The enormous cell size mismatch, 5.653 Å for GaAs and approximately 6.3 Å for the average composition of the SL film, has not disrupted the macroscopic coherence of the SL film. The crystalline quality is related to the size and distribution of the diffraction spots--the more localized the spots, the better the film quality. All reflections are quite localized, although the GaAs reflections appear to be more localized than the buffer and SL. Since the $Cd_{.5}Zn_{.5}Te$ buffer layer peaks and average constituent SL peaks are not resolved on the precession film, the origin of the slight broadening can not be isolated.

Table VI.1 Growth history of superlattice CdTe-ZnTe superlattices used as examples for precession photography

Sample	Substrate type	Buffer layer type	Buffer layer depth (μ)	Film type[a]	Film depth (μ)	Film period[b] (Å)
SL-17	GaAs	$Cd_{.5}Zn_{.5}Te$	1.8	CdTe-ZnTe (55%-45%)	1.64	40
SL-18	GaAs	$Cd_{.5}Zn_{.5}Te$	1.6	CdTe-ZnTe (45%-55%)	1.56	80

[a]Constituent ratio measured by energy dispersive spectroscopy (EDS).

[b]Expected period based on measured growth rate of constituents.

For comparison, a precession photograph of SL-18 is shown in Figure VI.3. Like Figure VI.1, the film vertical represents the [0,0,1] growth

Figure VI.3. Precession photograph of a CdTe-ZnTe SL (SL-18) deposited on a GaAs substrate. Reciprocal lattice points along both the [0,0,1] SL growth direction and the [0,0,1] GaAs surface normal are observed along the film vertical. The circled dot represents the approximate film center. Molybdenum K_α radiation, which passes through a zirconium filter, is incident on the sample (see section IV.E for precession geometry details). The attenuated molybdenum continuum radiation causes the observed radial streaking of the diffraction maxima. Unlike the HgTe-CdTe SLs, satellite structure is visible as diffuse patches about the central peaks

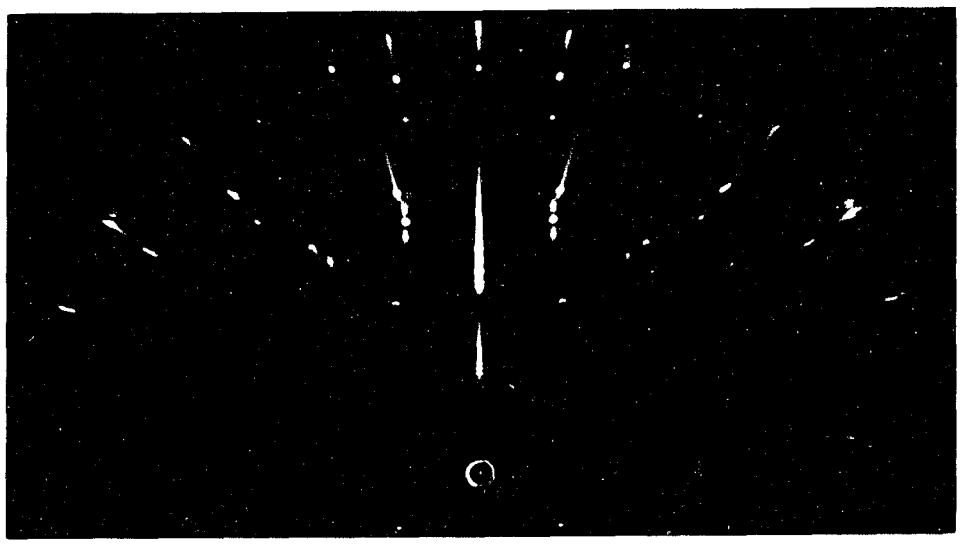

direction and the film horizontal represents the [1,1,0] direction. Since the precession photographs of both SL-17 and SL-18 were recorded using the same sample to film distance (F), layer screen radius, and layer screen to film distance, a direct comparison of the two is relevant. The smaller satellite spacing seen in Figure VI.3 is consistent with the larger period of SL-18. A closer inspection of Figure VI.3 reveals that the second and third order satellites are the most intense. The first order satellites are most intense in Figure VI.1. This qualitatively suggests that SL-18 contains more strain between the constituent layers.

The good epitaxial quality suggested by Figures VI.1 and VI.3 are indicative of most CdTe-ZnTe SL studied in this research investigation. The anticipated [0,0,1] growth is confirmed for all CdTe-ZnTe SLs. The coexistence of other crystallographic phases, such as [1,1,1] growth, was not detected within the precession camera resolution. However, because of the 2-fold symmetry present with the reciprocal lattice level illustrated in Figure VI.2, the coexistence of twinned regions can not be distinguished. Unlike the [1,1,1] growth discussed in section V.B, the two fold symmetry about the [0,0,1] axis requires that peaks from each twin domain diffract onto the same film positions.

C. Diffractometer Results

This sections contains a summary of diffractometer information. Only two SL samples are discussed: SL-17 and SL-18. Except for the SL period and total SL thickness, the composite SL samples are nearly identical. Both samples were provided by Jean-Pierre Faurie at the

University of Illinois at Chicago, and were grown by molecular beam epitaxy at 300 C on [0,0,1] oriented GaAs substrates (Monfroy, Sivananthan, Chu, Faurie, Knox & Staudenmann, 1986). The available growth information is listed in Table VI.1. The growth rate, determined by in-situ reflecting high energy electron diffraction, for both SLs was approximately 2.9 Å/second and 3 Å/second for the ZnTe and CdTe constituent layers, respectively (Monfroy, 1987). Although these two SLs are nearly identical in many respects, the diffraction characterization reveals interesting differences.

1. SL-18

SL-18 was characterized by performing ω-2Θ and ω scans along both the [0,0,1] and [1,1,1] crystallographic directions, using 1.47639 Å radiation. The (0,0,2), (0,0,4), and (0,0,6) constituent diffraction regions are shown in Figure VI.4. Two features are immediately apparent. First, the sharp GaAs substrate peaks are clearly visible in all three regions. The (0,0,2), (0,0,4), and (0,0,6) GaAs reflections are located at 15.136° ± 0.002°, 31.486° ± 0.002°, and 51.577° ± 0.006°, respectively. The widths of these reflections are much smaller than the SL peaks, revealing the better crystalline quality of the GaAs substrate. Second, the distribution of satellite intensities is very different between constituent diffraction regions. This indicates a variation of the constituent cell length along the SL growth direction, which is expected, since CdTe (a_c=6.48 Å) and ZnTe (a_c=6.09 Å) have significantly different lattice constants. The diffraction spectra shown in Figure VI.4 is typical of strained-layer SLs. It is

Figure VI.4. ω-2θ scans over the (0,0,2), (0,0,4), and (0,0,6) constituent diffraction regions of SL-18. The natural logarithm of the diffracted intensity is plotted as a function of the Bragg angle θ. The dots represent measured data, and the line represents a 3 point smooth over the measured data. The sharp GaAs reflections are visible in all three regions. Notice that each region resembles no other. This is attributed to variations of the constituent lattice cell length along the growth direction

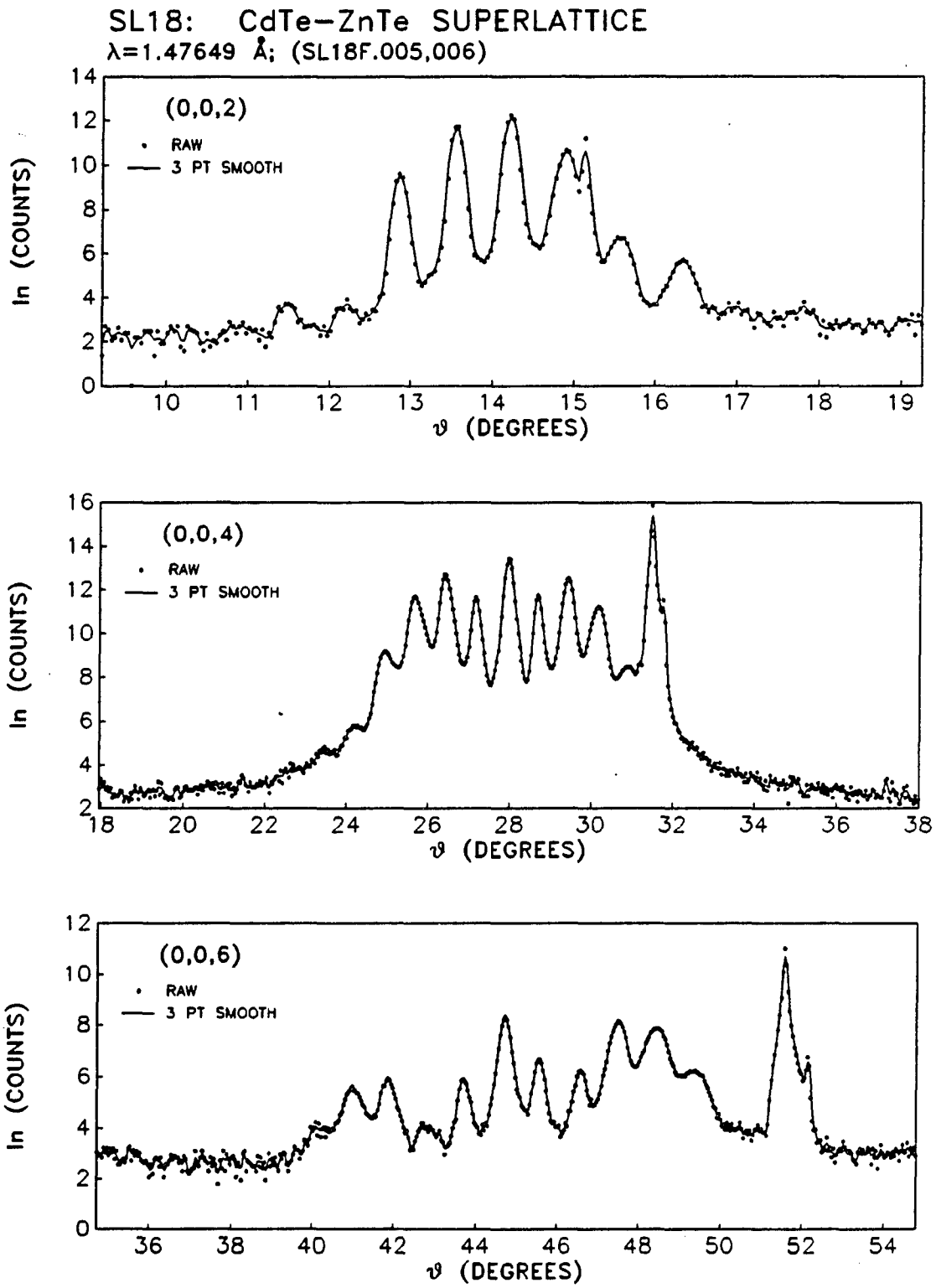
SL18: CdTe–ZnTe SUPERLATTICE
λ=1.47649 Å; (SL18F.005,006)
(0,0,2)
RAW
3 PT SMOOTH
ln (COUNTS)
ϑ (DEGREES)
(0,0,4)
RAW
3 PT SMOOTH
ln (COUNTS)
ϑ (DEGREES)
(0,0,6)
RAW
3 PT SMOOTH
ln (COUNTS)
ϑ (DEGREES)

instructive to compare Figure VI.4 to any of the diffraction spectra presented in Chapter V, which concerns SLs that have nearly lattice matched constituents.

Table VI.2 SL-18 period information

Parameter	Commensurate calculation	Incommensurate least-squares fit
Period: L	63.0 ± 0.2 Å	63.8 ± 0.1 Å
Average constituent cell length: $\langle c \rangle^a$	6.292 ± 0.002 Å	6.301 ± 0.001 Å
Number of constituent cells per period: N^b	10.13 ± 0.02	10.02 ± 0.03
Weighted chi: χ^c	12.41	10.43

[a]Cubic unit cell length along growth direction.

[b]$N=L/\langle c \rangle$.

[c]Defined by equation IV.24a.

Period information is extracted from the centroid peak positions of an ω-2θ scan, which has its scattering vector parallel to the [0,0,1] growth direction. A 0.8 mm by 5.0 mm incident collimator and a 1.0 mm by 8.0 mm detector collimator were used during this scan. A 0.04° angle increment defined the scan resolution, and the detector count time was 110 seconds. The sample was aligned with respect to the incident radiation by optimizing ω, χ, and ω-2θ on the (0,0,4,0) central peak. The period information extracted from this scan is listed in Table VI.2.

The incommensurate least-squares calculation yields a slightly better fit (smaller χ value) to the peak centroid values. According to the incommensurate fit, there are ten average constituent cells per period. The calculated period is approximately 16 Å shorter than the 80 Å period expected during the growth. This discrepancy is slightly less than 3 average constituent cell lengths along the growth direction.

The distortion of the constituent lattice was investigated by performing two ω-2Θ scans, having scattering vectors along the [0,0,1] and [1,1,1] crystallographic directions. If the lattice mismatch between CdTe and ZnTe is is not entirely relieved by misfit dislocations, a tetragonal distortion of the constituent lattices is expected (Miles, McGill, Sivananthan, Chu & Faurie, 1987). If no dislocations are present, the in-plane lattice parameters of each constituent are equal. The average constituent cell length along the growth direction <c> is 6.301 ± 0.001 Å. This is larger than the strain-free 6.266 Å value, which corresponds to the average bulk cell lengths of 45% CdTe and 55% ZnTe (see the growth information in Table VI.1). Assuming a tetragonal distortion, the in plane unit cell length is 6.274 ± 0.005 Å. This value is slightly smaller than the predicted 6.286 Å value of $Cd_{.5}Zn_{.5}Te$ buffer layer.

The observed peak breadths of both the ω and ω-2Θ diffraction scans provide information about the structural coherence of the SL film. Table VI.3 lists the peak breaths of the SL reflections. Three observations are immediately apparent. First, the peak breaths are much larger than expected. Since the film thickness of SL-18 is 1.56 μ, only the experimental broadening should be observed. Based on the GaAs

Table VI.3 SL-18 peak breadth information

Reflection (h,k,l,m)	Peak full width at half maximum[a] (°) ω-2θ	ω
(0,0,2,-4)	0.391 ± 0.034	
(0,0,2,-3)	0.266 ± 0.022	
(0,0,2,-2)	0.298 ± 0.022	
(0,0,2,-1)	0.132 ± 0.011	0.578 ± 0.037
(0,0,2, 0)	0.120 ± 0.011	0.494 ± 0.025
(0,0,2,+1)	0.130 ± 0.011	0.566 ± 0.028
(0,0,2,+2)	0.178 ± 0.016	0.879 ± 0.043
(0,0,2,+3)	0.272 ± 0.021	0.802 ± 0.044
(0,0,2,+4)	0.269 ± 0.022	
(0,0,2,+5)	0.435 ± 0.034	
(0,0,2,+6)	0.389 ± 0.028	
(0,0,4,-5)	0.632 ± 0.032	
(0,0,4,-4)	0.436 ± 0.026	1.063 ± 0.051
(0,0,4,-3)	0.272 ± 0.019	0.821 ± 0.039
(0,0,4,-2)	0.206 ± 0.017	0.611 ± 0.030
(0,0,4,-1)	0.165 ± 0.014	0.486 ± 0.023
(0,0,4, 0)	0.166 ± 0.013	0.594 ± 0.028
(0,0,4,+1)	0.158 ± 0.158	0.491 ± 0.024
(0,0,4,+2)	0.214 ± 0.017	0.562 ± 0.028
(0,0,4,+3)	0.306 ± 0.022	0.723 ± 0.035
(0,0,4,+4)		0.896 ± 0.047
(0,0,6,-4)	0.529 ± 0.029	0.856 ± 0.044
(0,0,6,-3)	0.353 ± 0.024	0.624 ± 0.033
(0,0,6,-2)	0.843 ± 0.035	
(0,0,6,-1)	0.281 ± 0.021	0.459 ± 0.026
(0,0,6, 0)	0.226 ± 0.017	0.544 ± 0.030
(0,0,6,+1)	0.249 ± 0.018	0.456 ± 0.024
(0,0,6,+2)	0.293 ± 0.023	0.506 ± 0.025
(0,0,6,+3)	0.380 ± 0.025	0.588 ± 0.028
(0,0,6,+4)	0.548 ± 0.029	0.602 ± 0.031
(0,0,6,+5)		0.836 ± 0.037

[a]Not corrected for instrumental broadening.

reflections, an upper limit to the experimental broadening is 0.049°, 0.055°, and 0.075° for the (0,0,2), (0,0,4), and (0,0,6) constituent diffraction regions, respectively. Second, the ω peak breadths are significantly larger than the corresponding ω-2θ breadths. Since the scattering vector is aligned parallel to the growth direction before performing the scan, an ω rocking curve is sensitive to the lateral (in-plane) coherence of the SL film. Thus, the larger ω peak breadths suggest that the lateral structural quality of the SL film is worse than along the growth direction. The poorer lateral coherence could be attributed to inhomogeneous film growth. Third, a trend of increasing peak breadth with the satellite order is present in all constituent diffraction regions. This indicates a strain-like broadening of the film (Gyorgy, McWhan, Dillon, Walker & Waszczak, 1982).

After correcting the peak breadths for instrumental broadening, quantitative information of the SL film can be extracted from the ω-2θ diffraction scan along the [0,0,1] growth direction. If the film is composed of a distribution of incoherent domains, the SL peak breadths will have a constant longitudinal width in reciprocal space (McWhan, 1985), which is simply the domain size broadening discussed in section II.G. In addition to this constant reciprocal width effect (Δq=constant), there is strain broadening, which has a constant ($\Delta q/q$) peak width dependence. A complete separation of these two effects is difficult (Warren, 1969).

The increasing peak breadth with satellite order is a characteristic of strain broadening. Relating the increasing reciprocal width Δq linearly with the scattering magnitude q, the extracted slope represents

the fractional spread of SL periods ($\Delta L/L$) throughout the SL film,

$$\Delta q(m) = \left[\frac{\Delta L}{L}\right] q(m) + \Delta q(0) \quad , \tag{VI.1a}$$

$$q(m) = \frac{2\pi m}{L} \quad , \tag{VI.1b}$$

$$\Delta q(m) = \frac{4\pi(\Delta\theta)\cos\theta}{\lambda} \quad , \tag{VI.1c}$$

where L is the SL period, m is the satellite index, $\Delta\theta$ is the peak breadth in radians, and λ is the radiation wavelength (Gyorgy, McWhan, Dillon, Walker & Waszczak, 1982). Table VI.4 lists the application of equation VI.1a to the corrected peak breadths of SL-18. Ideally, the calculated period range ΔL should be the same for each constituent diffraction region. Averaging over all three constituent diffraction regions, a 5.9 ± 1.2 Å period spread is observed for SL-18.

Table VI.4 The range of superlattice periods associated with the satellite peak breadths of SL-18

Constituent diffraction region	Period range (Å)	Linear correlation coefficient[a]
(0,0,2)	4.9 ± 0.7	0.9642 (4)
(0,0,4)	7.3 ± 0.6	0.9643 (8)
(0,0,6)	5.5 ± 0.5	0.9502 (7)

[a]Based on the slope ($\Delta L/L$) of equation VI.1a. The number of peaks considered in the fit is given in parentheses.

The observed central peak breadths are larger than the values obtained by extrapolating the satellite peak breadth trend to the zero order. This suggests that the observed central peak breadth is influenced by nearly coincident buffer layer peaks. From the observed trend of the central peaks, a 0.015 ± 0.005 Å lattice parameter range is calculated. This range is consistent with the lattice parameter difference of the predicted buffer layer (6.286 Å) and the observed average constituent cell length derived from the central peak centroid positions (6.292 ± 0.002 Å). The extrapolated values show no increasing trend with q. Applying the Scherrer formula to these extrapolated values, a 2640 ± 1370 Å domain depth is calculated for the SL film. This value corresponds to approximately 41 SL unit cells, or approximately one-sixth of the total SL film thickness.

2. SL-17

SL-17 was characterized by performing ω-2θ and ω scans along both the [0,0,1] and [1,1,1] crystallographic directions, using 1.47639 Å, 1.28181 Å, and 0.7093 Å radiation wavelengths. The (0,0,2), (0,0,4), and (0,0,6) constituent diffraction regions are shown in Figures VI.5, VI.6, and VI.7, respectively. Each figure shows the diffraction spectrum from each of the three wavelengths used in this investigation. The additional structure to the high angle side of each peak in the 0.7093 Å data represents diffraction from contaminating molybdenum $K\alpha_2$ radiation. Before discussing the quantitative aspects, three qualitative characteristics of SL-17 are apparent in Figures VI.5-7. First, like SL-18, the sharp GaAs substrate peaks are clearly visible in

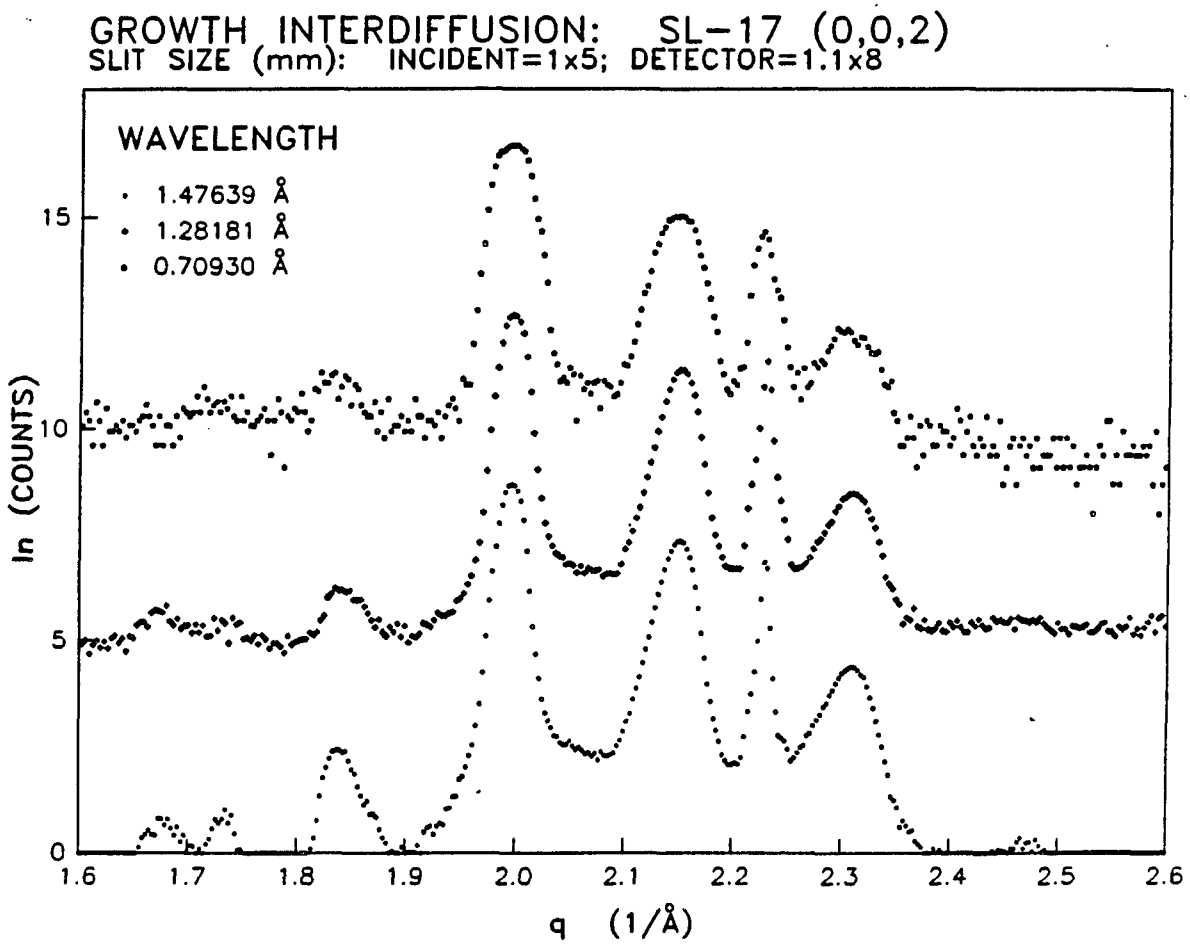

Figure VI.5. ω-2θ diffraction scans over the (0,0,2) constituent diffraction region of SL-17 using 1.47639 Å, 1.28181 Å, and 0.7093 Å radiation wavelengths, from top to bottom, respectively. A 1 mm by 5 mm (sample height) incident and a 1.1 mm by 8 mm detector collimators were used. The natural logarithm of the diffracted intensity is plotted as a function of $q=4\pi\sin\theta/\lambda$, where θ is the Bragg angle, and λ is the radiation wavelength (Å). The central peak is located at $q\sim2$ Å^{-1}, and the (0.0.2) GaAs reflection is located at $q\sim2.2$ Å^{-1}

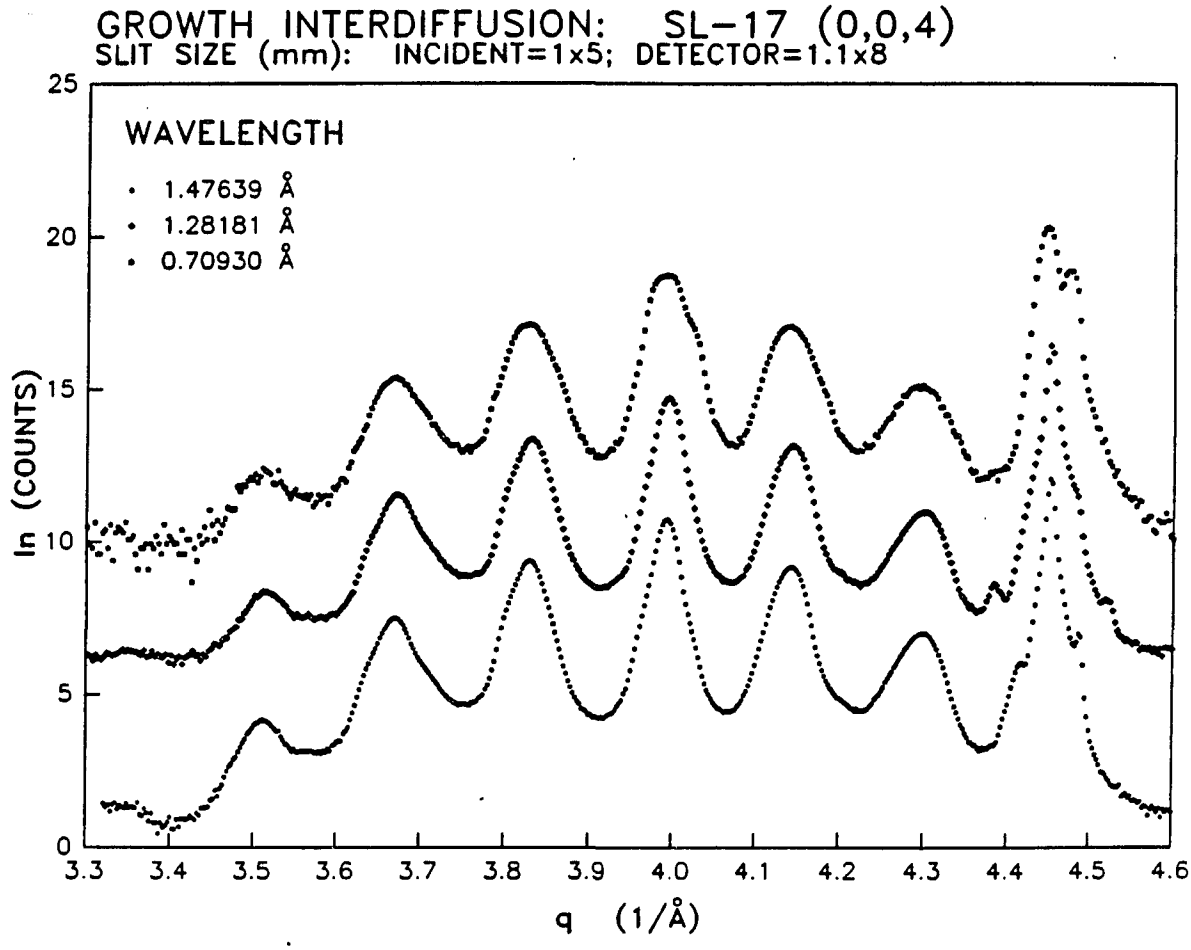

Figure VI.6. ω-2Θ diffraction scans over the (0,0,4) constituent diffraction region of SL-17 using 1.47639 Å, 1.28181 Å, and 0.7093 Å radiation wavelengths, from top to bottom, respectively. A 1 mm by 5 mm (sample height) incident and a 1.1 mm by 8 mm detector collimators were used. The natural logarithm of the diffracted intensity is plotted as a function of $q=4\pi\sin\Theta/\lambda$, where Θ is the Bragg angle, and λ is the radiation wavelength (Å). The central peak is located at $q\sim4$ Å^{-1}, and the (0,0,4) GaAs reflection is located at $q\sim4.45$ Å^{-1}

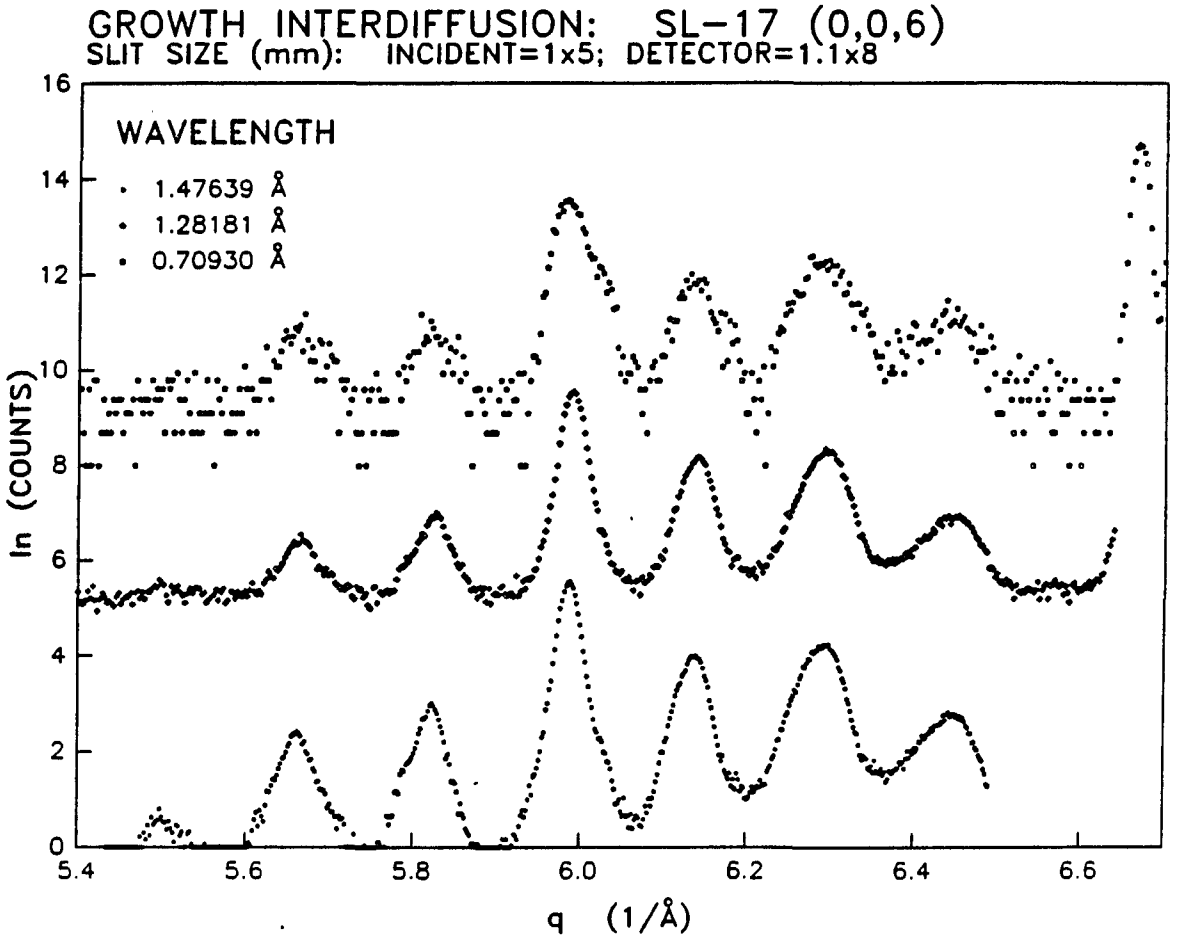

Figure VI.7. ω-2θ diffraction scans over the (0,0,6) constituent diffraction region of SL-17 using 1.47639 Å, 1.28181 Å, and 0.7093 Å radiation wavelengths, from top to bottom, respectively. A 1 mm by 5 mm (sample height) incident and a 1.1 mm by 8 mm detector collimators were used. The natural logarithm of the diffracted intensity is plotted as a function of $q=4\pi\sin\theta/\lambda$, where θ is the Bragg angle, and λ is the radiation wavelength (Å). The central peak is located at $q\sim5.98$ Å^{-1}, and the (0,0,6) GaAs reflection is located at $q\sim6.68$ Å^{-1}

all three constituent regions. The width of these reflections are much smaller than the SL peaks, revealing the better crystalline quality of the GaAs substrate. Since the quality of commercially available GaAs substrates are nearly perfect (Blakemore, 1982), the GaAs peak widths represent an upper limit of the instrumental broadening.

Table VI.5 Penetration depth of CdTe and ZnTe at x-ray wavelengths used in this research investigation

Wavelength (Å)	Absorption coefficient[a] CdTe (μm)	ZnTe (μm)
1.47639	7.97	10.31
1.28181	11.66	9.09
1.09855	17.73	13.81
0.7093	59.17	45.27

[a]Based on the mass absorption coefficients computed by Cromer (1983).

Second, the breadth of the diffraction peaks increase as the wavelength decreases. Since Figures VI.5-7 are plotted as a function of reciprocal angstroms, the widths should remain constant, if the SL structure is uniform. As the wavelength decreases, both CdTe and ZnTe become less absorbing. This is summarized in Table VI.5, which lists the penetration depth of CdTe and ZnTe at the four wavelengths relevant to this research investigation. An increasing penetration depth increases the weight given to SL structure near the substrate. Thus,

the increasing breadth observed in Figures VI.5-7 suggests that the unit cell size varies slightly along the growth direction (Clemens & Gay, 1987). The poorer satellite contrast of the (0,0,6) constituent diffraction region as the wavelength decreases further supports this conclusion (Kervarec, Baudet, Caulet, Auvray, Emery & Regreny, 1984).

Third, unlike SL-18, the distribution of satellite intensities among the constituent diffraction regions changes moderately from region to region. This is obvious by comparing Figures VI.5-7 to Figure VI.4. Apparently, the variation of the constituent cell length along the growth direction is not as severe for SL-17, compared to SL-18. A smaller variation of the constituent lattice parameter implies a smaller tetragonal distortion of the constituent lattice. This is understood by considering two cubic unit cells that have different lattice constants. If both cells are constrained to share a common face (epitaxy), each cell will distort. Although a complete description of this distortion depends on the elastic parameters of each material and on the crystallographic orientation of the common lattice interface, the cell length perpendicular to the interface will vary inversely with the common length parallel to the interface (Hornstra & Bartels, 1978). Perpendicular to the common interface, the larger unit cell must expand and the smaller cell must contract, enhancing the lattice parameter difference of these distorted cells.

Period information is extracted from the centroid peak positions of the [0,0,1] directed ω-2θ diffraction scans. A 1.0 mm by 5 mm incident collimator and a 1.1 mm by 8 mm detector collimator were used during these scans. The sample was aligned with respect to the incident x-ray

beam by optimizing the (0,0,4) central peak reflection. The extracted period information based on the commensurate and incommensurate period assumptions is listed in Tables VI.6a and VI.6b, respectively. The calculated SL attributes are found to be relatively unaffected by the radiation wavelength used during the investigation. According to the χ value, the incommensurate least-squares calculations yield significantly better fits to the peak centroid positions. Since the SL period is unaffected by the radiation wavelength, a SL period which best represents SL-17 is obtained by averaging the three wavelength results. This average yields a 40.05 ± 0.05 Å period, which is in exact agreement with the period predicted during growth.

The distortion of the constituent lattice was investigated by performing two ω-2θ scans, having scattering vectors along the [0,0,1] and [1,1,1] crystallographic directions. Since the [0,0,1] direction is coincident with the SL growth direction, the ω-2θ scan along this direction uniquely determines the average constituent lattice parameter <c>. An average of <c> over the three wavelengths yield a 6.304 ± 0.003 Å average constituent cell length along the growth direction. Based on this value, the SL period is incommensurate with the average constituent lattice. The calculated <c> is identified as the strain-free value, which corresponds to the average bulk length associated with 55% CdTe and 45% ZnTe (see the growth information listed in Table VI.1).

Assuming that the constituent lattice is tetragonally distorted along the growth direction (Miles, McGill, Sivananthan, Chu & Faurie, 1987), the in-plane lattice parameter is extracted from the ω-2θ scan along the [1,1,1] direction with knowledge of <c>. Two [1,1,1] ω-2θ

Table VI.6a Commensurate period calculations of SL-17

Wavelength (Å)	Period[a] L (Å)	Avg. const. cell length[b] <c> (Å)	Const. cells per period[c]	weighted χ^2[d]	No. of peaks included in fit (central)	(satellite)
1.47649	40.97 ± 0.09	6.296 ± 0.002	6.51 ± 0.02	10.33	3	14
1.28181	40.95 ± 0.10	6.293 ± 0.002	6.51 ± 0.02	10.76	3	14
0.7093	40.99 ± 0.07	6.300 ± 0.001	6.51 ± 0.01	12.94	5	20

[a]Based on equation IV.18.

[b]Average constituent cell length along the growth direction based on central peak centroids.

[c]The SL period divided by the average constituent cell length.

[d]Defined by equation IV.24a.

Table VI.6b Incommensurate least-squares fit of SL-17

Wavelength (Å)	Period[a] L (Å)	Avg. const. cell length[b] <c> (Å)	Const. cells per period[c]	weighted χ^2[d]	No. of peaks included in fit (central)	(satellite)
1.47649	40.0 ± 0.1	6.304 ± 0.001	6.34 ± 0.02	4.82	3	14
1.28181	40.1 ± 0.10	6.301 ± 0.001	6.36 ± 0.02	6.909	3	14
0.7093	40.04 ± 0.09	6.306 ± 0.001	6.35 ± 0.01	7.40	5	20

[a]Based on equations IV.25a-b.

[b]Average constituent cell length along the growth direction based on equations IV.25a-b.

[c]The SL period divided by the average constituent cell length.

[d]Defined by equation IV.24a.

scans were performed using 1.47639 Å and 0.7093 Å radiation wavelengths. The in-plane lattice parameters extracted from these scans, using the appropriate <c>, do not agree within the predicted uncertainty. The extracted in-plane lattice parameters are 6.280 ± 0.003 Å and 6.294 ± 0.005 Å using 1.47639 Å and 0.7093 Å radiation, respectively. The 0.014 Å discrepancy between these values implies a variation of the in-plane lattice parameter along the growth normal. However, the observed discrepancy could be related to the different refractive indices of the two wavelengths (Miceli, Neumann & Zabel, 1986). The refractive index can be represented by $n=1-\delta$, where δ is typically 10^{-6} (James, 1982) and is proportional to the square of the radiation wavelength. Compared to <c>, the 0.7093 Å wavelength result implies virtually no tetragonal distortion of the constituent lattice. Assuming that the lattice parameter of the $Cd_{.5}Zn_{.5}Te$ buffer layer is 6.286 Å (based on Vegard's law), a contraction of the in-plane lattice parameter is observed using 1.47649 Å wavelength radiation, and an expansion is observed using 0.7903 Å radiation.

The observed peak breadths of the [0,0,1] oriented ω-2θ scans provide information about the structural coherence of the SL film along the growth direction. Using the procedure outlined in the discussion of SL-18, the SL period variation ($\Delta L/L$), the average constituent cell length variation ($\Delta\langle c\rangle/c$), and the domain depth predicted by the Scherrer equation, are estimated. This information is listed in Table VI.7. The peak breadths are corrected for instrumental broadening by subtracting the nearest GaAs peak width (Lorentzian approximation, see equation II.60b). A slight broadening of the satellite peak breadths

Table VI.7 Lattice parameter variations and Scherrer lengths extracted from ω-2θ peak breadth information of SL-17

Wavelength (Å)	$\Delta\langle c\rangle$[a] (Å)	ΔL[b] (Å)	Scherrer length[c] (Å)
1.47639	0.001 ± 0.003	3.2 ± 0.5	1681 ± 53
1.28181	0.001 ± 0.003	3.3 ± 0.3	946 ± 186
0.7093	0.003 ± 0.003	2.7 ± 0.7	1391 ± 863

[a]Based on the trend of extrapolated central peak breadths (derived from the satellites) as a function of $q=4\pi\sin\theta/\lambda$ using equation VI.1a.

[b]Based on the trend of corrected satellite peak breadths (see equations VI.1a-c).

[c]Computing an average Scherrer length of the extrapolated central peak breadths (derived from the satellites) using equation II.56.

with satellite order indicates a SL period variation of 3.1 ± 0.3 Å. By extrapolating the peak breadth to zero order, a central peak breadth that is not influenced by buffer layer reflections is obtained. Using these extrapolated central peak breadths, no variation of the average constituent lattice is observed. In fact, no broadening trend is observed for the experimentally measured central peaks. This suggests that either the buffer layer peaks are precisely coincident with the central peaks, or the buffer layer peaks are too weak to influence the measured central peak reflections. The latter possibility agrees with earlier characterization studies of $Cd_{1-x}Zn_xTe$ epitaxial layers on GaAs substrates (Qadri & Dinan, 1985; Feldman, Austin, Dayem & Westerwick, 1986). The Scherrer lengths based on the extrapolated central peak breadths are listed in Table VI.7. The average of these values is 1339 ± 370 Å, which corresponds to approximately 33 SL unit cells, or one-twelfth of the total SL thickness.

In addition to the ω-2θ scans, extended ω scans were performed about the SL peak centroid positions. These scans reveal very unusual double peak structures. Figure VI.8a shows the ω profiles of the (0,0,4) constituent diffraction region. Similar double peak structures are observed in the (0,0,2) and (0,0,6) regions. Although it is difficult to see on the logarithmic scale, two very broad overlapping peaks are observed in all satellite scans. The peak separation increases with satellite order, with only one peak observed in the central peak scans. The inset Figure VI.8b illustrates the centroid positions of the double peak structure in reciprocal space. If only one peak were observed in each ω scan, the resulting off-normal trend ($\Delta q_w \neq 0$) of the satellite

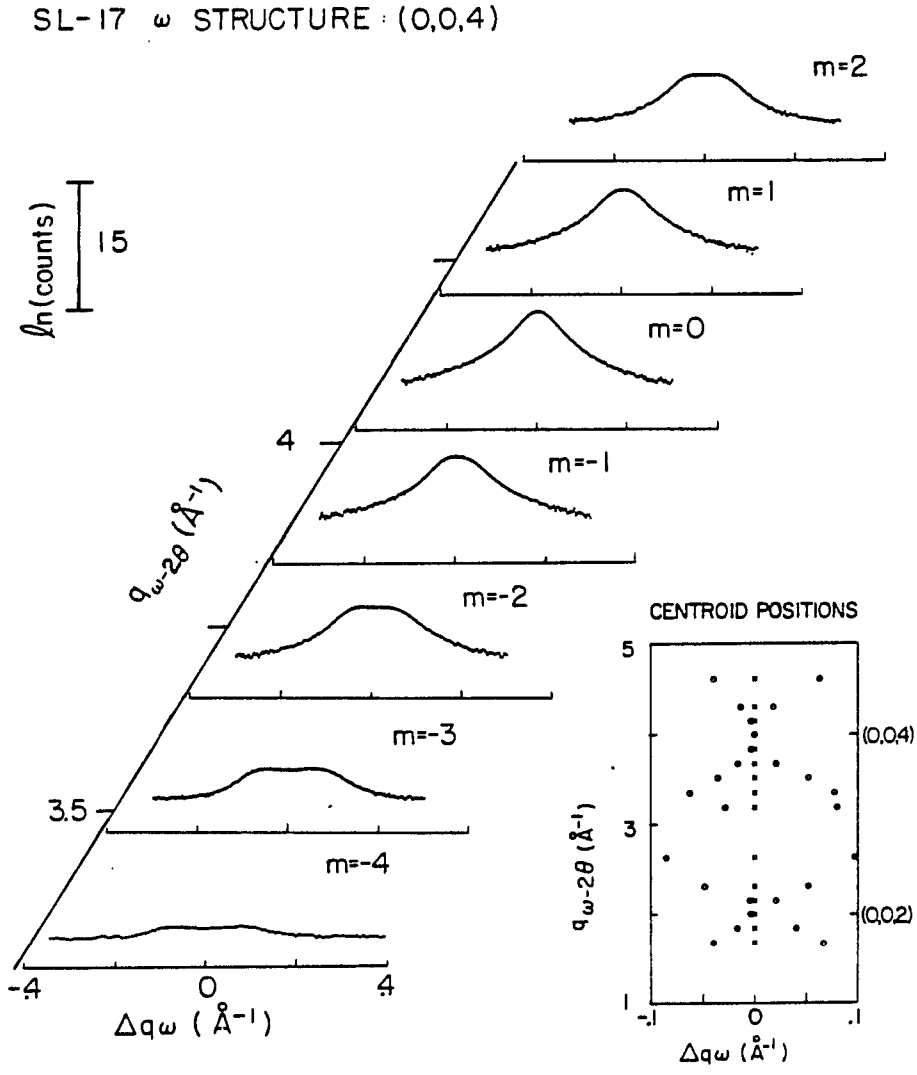

Figure VI.8. Figure (a) (left illustration) shows the ω scan profiles (along the horizontal axis) of SL-17 when the detector is positioned at $q_{\omega-2\theta}=4\pi\sin\theta/\lambda$ (sloping axis). Unresolved double peak structures are observed in every $m\neq 0$ ω scan. The peak separation increases with the satellite order m. The inset Figure (b) illustrates the centroid positions in reciprocal space within the (0,0,2) and (0,0,4) constituent diffraction regions, where $\Delta q=(q_{\omega-2\theta})-(q_{\omega})$

positions would resemble SL terracing (see section III.D). The double peak structure could be a manifestation of multiply diffracting domains, which have the same average chemical composition.

Three different regions of SL-17 were probed in an effort to identify the presence of distinct SL domains. Using 1.47639 Å wavelength radiation and 1 mm diameter collimators, three sample locations separated by 2 mm were probed by performing an ω-2Θ scan over the (0,0,4) constituent diffraction region. Figure VI.9 shows a composite plot of all three scans. Although the central peak profile appears to be unaffected, subtle changes of the satellite peak profiles are visible. The most notable variations are present on the (0,0,4,±3) peaks. Among the three scans, a period variation of approximately one angstrom is observed with essentially no variation of the average constituent lattice parameter. Multiple SL domains could explain the observed asymmetric peak profiles and double peak structures of Figure VI.9. An unambiguous determination of multiple domain structure will require higher resolution information.

D. Step Model Results

1. Introduction

Strained layer SLs offer a unique opportunity to investigate the lattice parameter variations throughout the SL unit cell. As demonstrated above, both the period and average constituent cell parameters are accurately determined from the centroid peak positions. However, the individual lattice parameters can not be directly extracted from this information alone. The SL peak intensities provide the

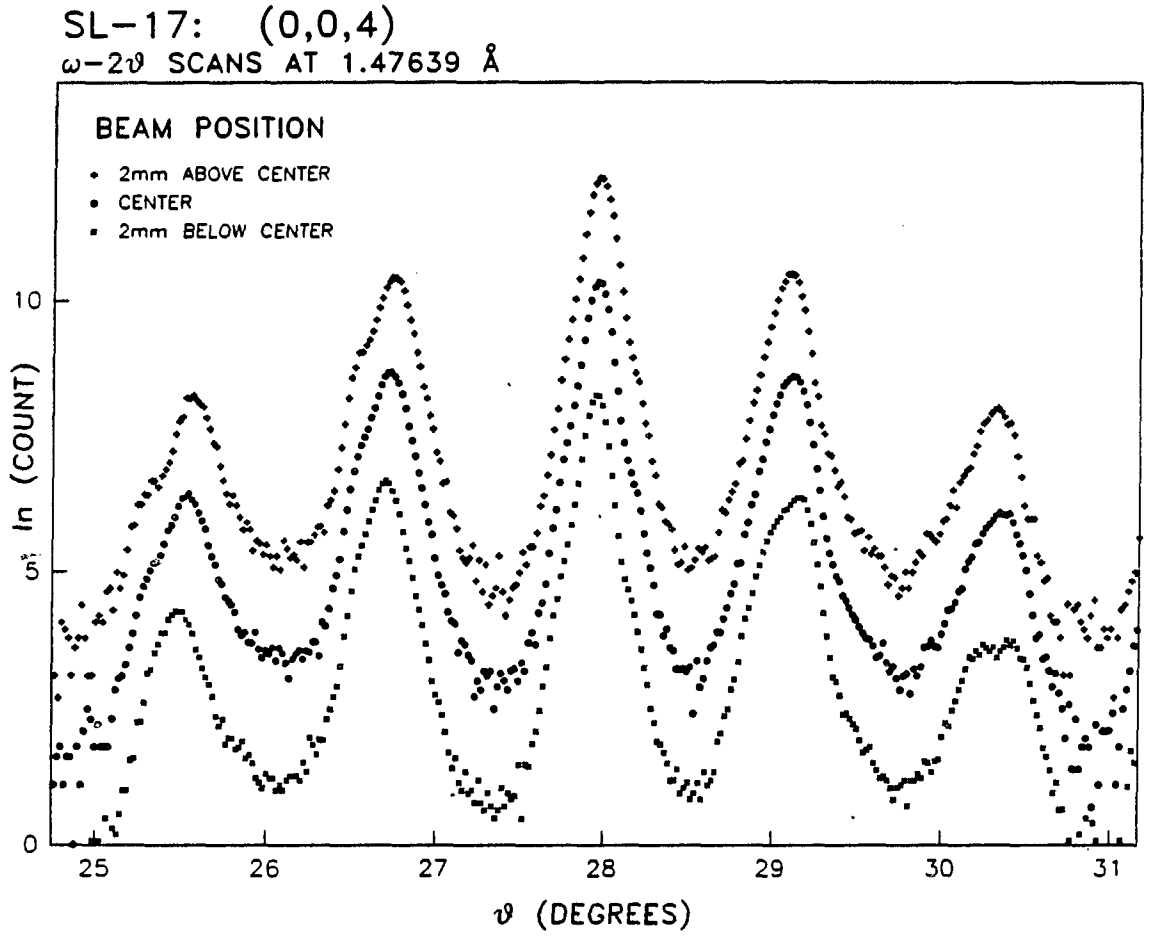

Figure VI.9. Three ω-2θ diffraction scans over the (0,0,4) constituent diffraction region of SL-17 using a 1.47639 Å radiation wavelength. The top, middle, and bottom scans represent diffraction from three sample positions along the length of the sample. Each probed area is separated by 2 mm. The natural logarithm of the diffracted intensity is plotted as a function of the Bragg angle θ.

information necessary to calculate individual lattice parameters.

Unless many SL reflections are observed along a variety of distinct crystallographic directions, a structure factor model is required to extract constituent lattice information. Introducing the parameters of interest into a suitable model, information is extracted by fitting the parameters to the observed peak intensities. The structure factor provides the necessary link between experiment and theory.

The step model structure factor discussed in section III.B provides a logical first approach to extract lattice parameter information (Segmuller & Blakeslee, 1973). This model depends on two assumptions. First, the constituent interfaces are abrupt. This implies that no interdiffusion occurs during growth. To a first order approximation, this assumption is reasonable. Second, all constituent SL unit cells diffract coherently. Initially, this assumption appears to be invalid, since all peaks are observed to be much broader than the theoretical peak breadths associated with the known film thickness. If the broad peaks are attributed to multiple SL domains, the extracted lattice parameter information would represent average values, where diffraction within each domain is assumed to be coherent. This would be consistent with the coherent diffraction assumption. In fact, the constituent cell parameters are found to be relatively insensitive to the coherency requirement. This is further discussed below.

The various step model parameters are identified by four general categories: the number of two atom (a-b) basis cells within each constituent (N_1, N_2), the corresponding basis lengths (d_1, d_2), the fractional occupation of the a_1, b_1, a_2, and b_2 atom sites (f_{a1}, f_{b1},

f_{a2}, f_{b2}), and the Debye-Waller parameters associated with the atoms (M_{a1}, M_{b1}, M_{a2}, M_{b2}). The a-b basis cells are illustrated in Figure III.11 for both SL growth directions. Along the cubic [0,0,1] direction, the a-b atom pairs form alternating a-b atomic plains, which are parallel to the growth surface (see section II.B). Here, the letters a and b are associated with groups II_B and VI_A of the periodic chart. The a-b atom spacing is one-fourth the zincblende unit cell length, with two sets of a-b planes for each zincblende unit cell (see Figure III.11). In the absence of a tetragonal distortion, the a-b basis lengths are one-half of the cubic unit cell length.

The fractional occupation parameters f_{a1}, f_{b1}, f_{a2}, and f_{b2}, define the occupation probability of the individual constituent atoms a_1, b_1, a_2, and b_2. These fractional parameters represent an average over the entire constituent material. For example, $f_{a2}=0.45$ would indicate that there is a 45% chance of finding a group II_B atom in the second constituent material. A Debye-Waller factor, which describes random atomic displacements about the true atom position (see section II.F), is associated with each constituent atom type. Two approximations are routinely employed when assigning values to these parameters. The first approximation assigns all four Debye-Waller parameters to one common value: $M_{a1}=M_{b1}=M_{a2}=M_{b2}\equiv M$. This is typically performed during the initial stages of the step model fitting procedure. The second approximation assigns a common value to the a and b atoms within each constituent: $M_{a1}=M_{b1}\equiv M_1$, $M_{a2}=M_{b2}\equiv M_2$. Before discussing the specific fitting procedure, a qualitative discussion will clarify the influence of both the second step model assumption and the fitting parameters.

The effects of coherent and incoherent diffraction from the SL unit cells are illustrated in Figures VI.10a and VI.10b. The relevant parameter information associated with these illustrated distributions is summarized in Table VI.8. Figures VI.10a and VI.10b represent incoherent and coherent diffraction, respectively, from three SL unit cells. Incoherent diffraction is defined by adding the diffracted intensity of each unit cell, where the intensity is proportional to the square of the scattered amplitude. Coherent diffraction is defined by the square of the total added amplitude from all diffracting unit cells. The predominant feature of Figures VI.10a and VI.10b are nearly identical. Comparing these figures, all principal maxima occur at the same reciprocal magnitude ($q=4\pi\sin\theta/\lambda$) and the relative distribution of satellite intensities is approximately equivalent. The coherently scattered intensity, however, is consistently larger, which is expected.

The diffracted peak breadths are expected to decrease as the number of participating unit cells increases. This is qualitatively demonstrated in Figures VI.11a and VI.11b, which represent incoherent and coherent diffraction, respectively, from nine SL unit cells (see Table VI.8 for a summary of relevant parameter information). Comparing these distributions to Figures VI.10a and VI.10b, the decrease in peak breadth is obvious. As the peaks widths decrease, the satellite structure becomes more apparent.

The satellite peak symmetry observed in the above examples is indicative of a uniform lattice parameter throughout the SL unit cell. The symmetry is destroyed when the constituent materials have different

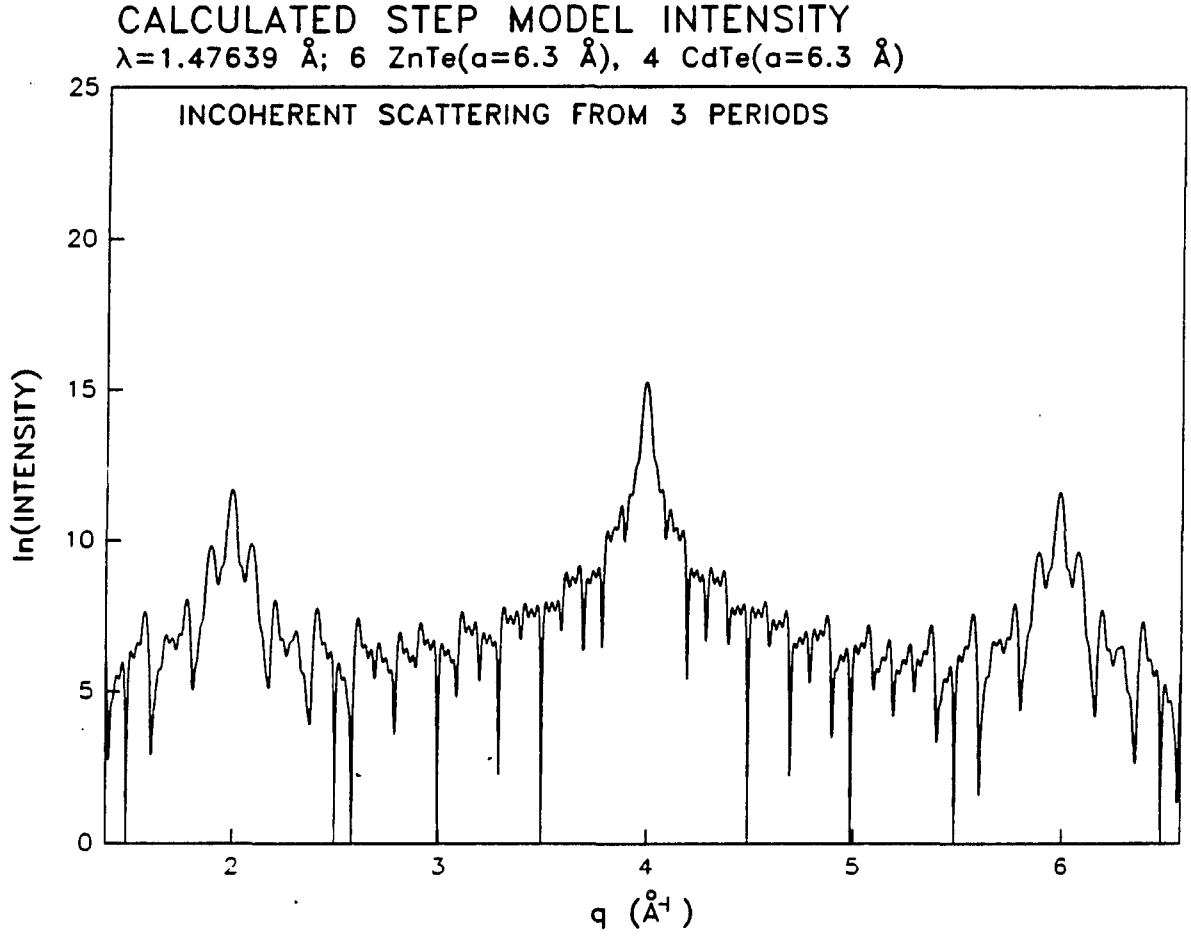

Figure VI.10a. Step model intensity distribution from three incoherently diffracting SL unit cells. Table VI.8 lists the step model parameters of this distribution. The intensity represents the square of the structure factor. $q \equiv 4\pi \sin\theta/\lambda$, where θ is the Bragg angle and λ is the 1.47639 Å radiation wavelength. This example represents a lattice matched SL

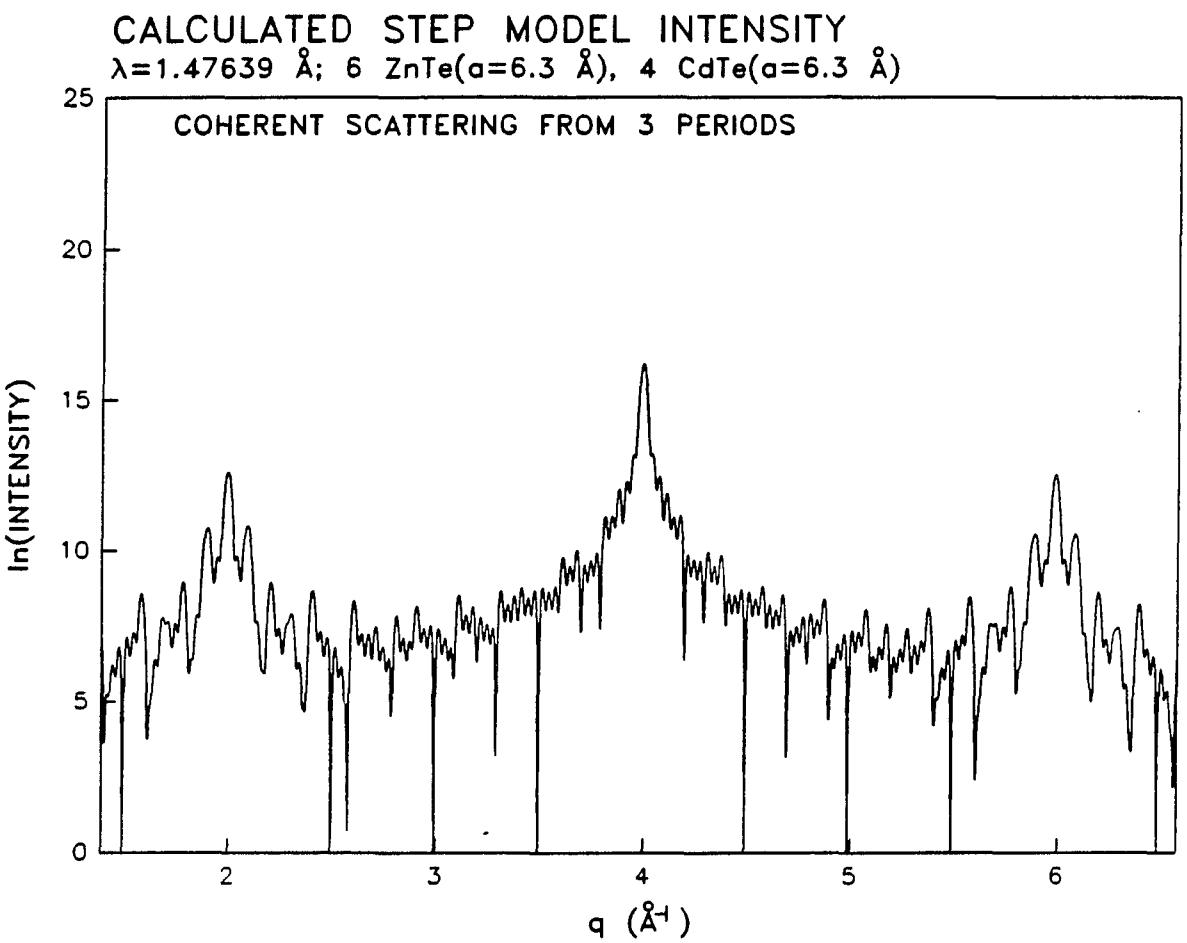

Figure VI.10b. Step model intensity distribution from three coherently diffracting SL unit cells. Table VI.8 lists the step model parameters of this distribution. The intensity represents the square of the structure factor. $q \equiv 4\pi \sin\theta/\lambda$, where θ is the Bragg angle and λ is the 1.47639 Å radiation wavelength. This example represents a lattice matched SL

Table VI.8 Parameters used to generate the step model examples discussed in step model introduction

Figure	Constituent material #1 a_1b_1	#2 a_2b_2	N_1	N_2	d_1 (Å)	d_2 (Å)	Number of superlattice unit cells	Diffraction mode
VI.10a	ZnTe	CdTe	6	4	3.15	3.15	3	incoherent
VI.10b	ZnTe	CdTe	6	4	3.15	3.15	3	coherent
VI.11a	ZnTe	CdTe	6	4	3.15	3.15	9	incoherent
VI.11b	ZnTe	CdTe	6	4	3.15	3.15	9	coherent
VI.12a	ZnTe	CdTe	6	4	2.98	3.41	9	incoherent
VI.12b	ZnTe	CdTe	6	4	2.98	3.41	9	coherent

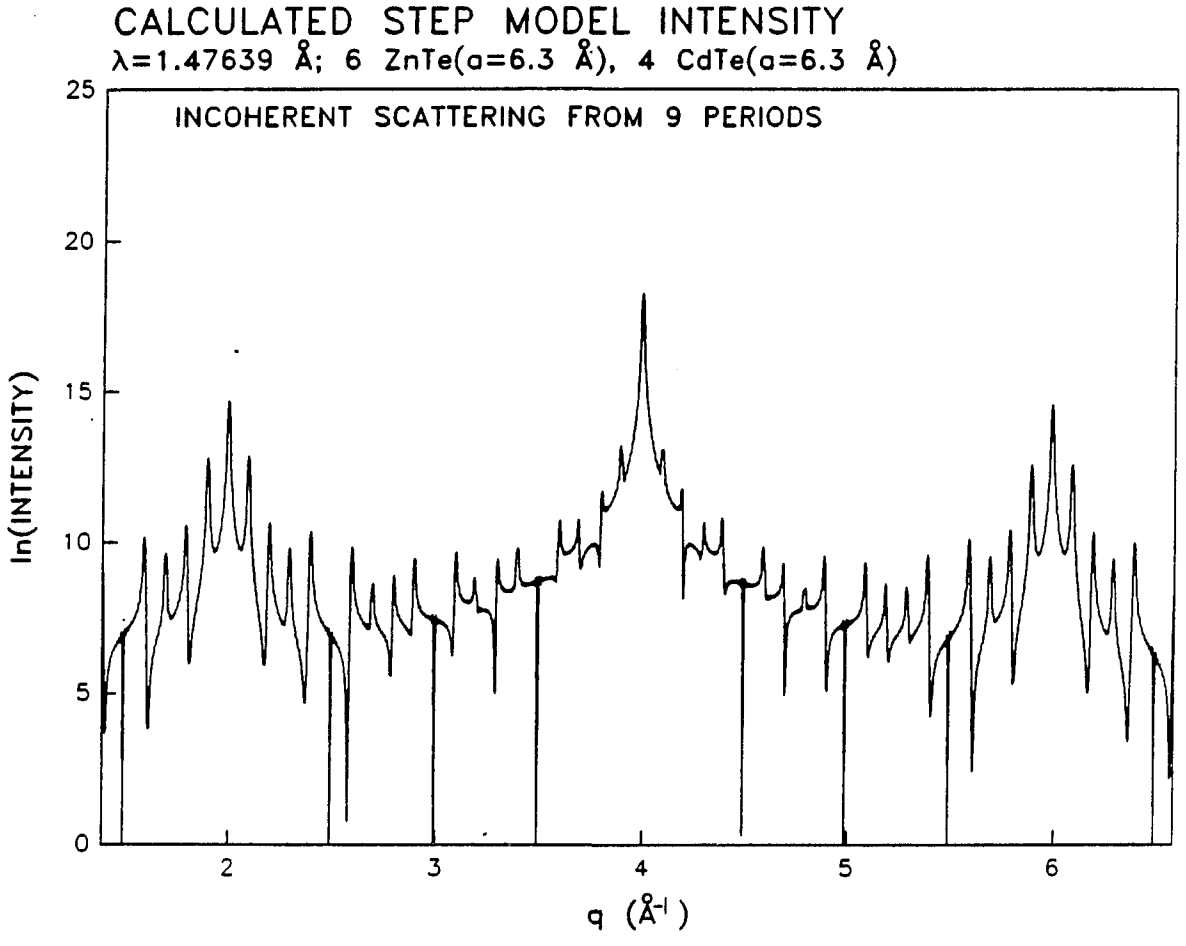

Figure VI.11a. Step model intensity distribution from nine incoherently diffracting SL unit cells. Table VI.8 lists the step model parameters of this distribution. The intensity represents the square of the structure factor. $q \equiv 4\pi \sin\theta/\lambda$, where θ is the Bragg angle and λ is the 1.47639 Å radiation wavelength. This example represents a lattice matched SL. Notice that these peaks are more narrow than the peaks in Figure VI.10a

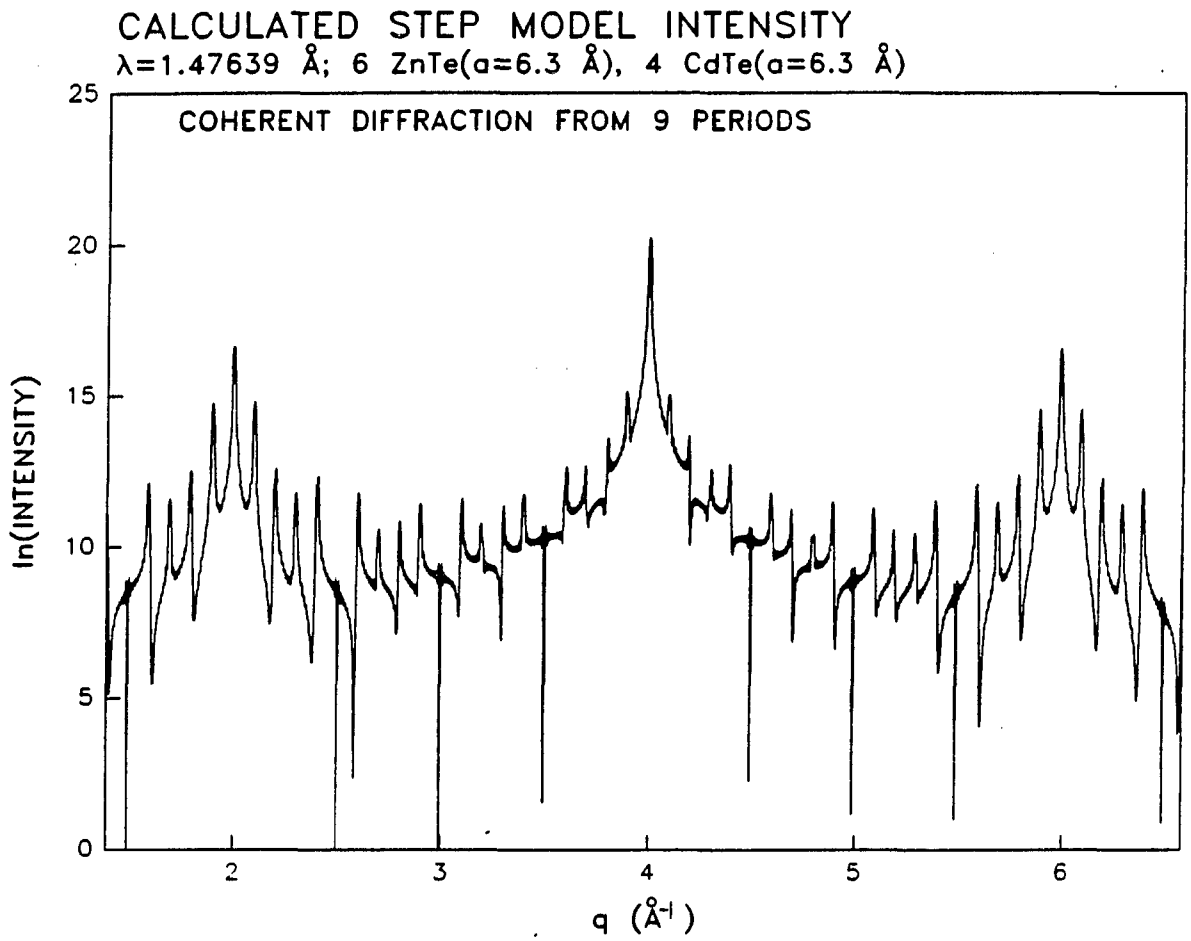

Figure VI.11b. Step model intensity distribution from nine coherently diffracting SL unit cells. Table VI.8 lists the step model parameters of this distribution. The intensity represents the square of the structure factor. $q \equiv 4\pi \sin\theta/\lambda$, where θ is the Bragg angle and λ is the 1.47639 Å radiation wavelength. This example represents a lattice matched SL. Notice that these peaks are more narrow than the peaks in Figure VI.10b

unit cell dimensions. This is illustrated in Figures VI.12a and VI.12b, which represent incoherent and coherent diffraction, respectively, from nine SL unit cells having different constituent cell lattice parameters (see Table VI.8 for a summary of relevant parameter information). The ZnTe constituent material has a 5.9 Å unit cell length along the growth direction, and the CdTe constituent has a corresponding 6.81 Å length. Not only is the symmetry of the satellite intensities within each constituent diffraction region destroyed, but the relative form of the constituent diffraction regions are no longer similar. These characteristics are indicative of strained layer SL samples, where the constituent lattice parameters are different. If the constituent lattice parameters are significantly different, the (0,0,4) constituent diffraction region is modulated by broad envelopes. This is observed in Figures VI.12a and VI.12b. The (0,0,4) constituent diffraction region ($q \simeq 4$ Å^{-1}) is modulated by two envelopes, which are attributed to the individual constituent unit cell lengths. The width of these envelopes are related to the lengths of the constituent materials along the growth direction (Quillec, Goldstein, Le Roux, Burgeat & Primot, 1984).

A comparison of the incoherent and coherent diffraction examples discussed above suggest that the step model parameters are relatively insensitive to the degree of coherent diffraction. Differences in the absolute intensity become more pronounced as the number of participating SL unit cells increases. However, the relative features of the diffraction spectra remain similar.

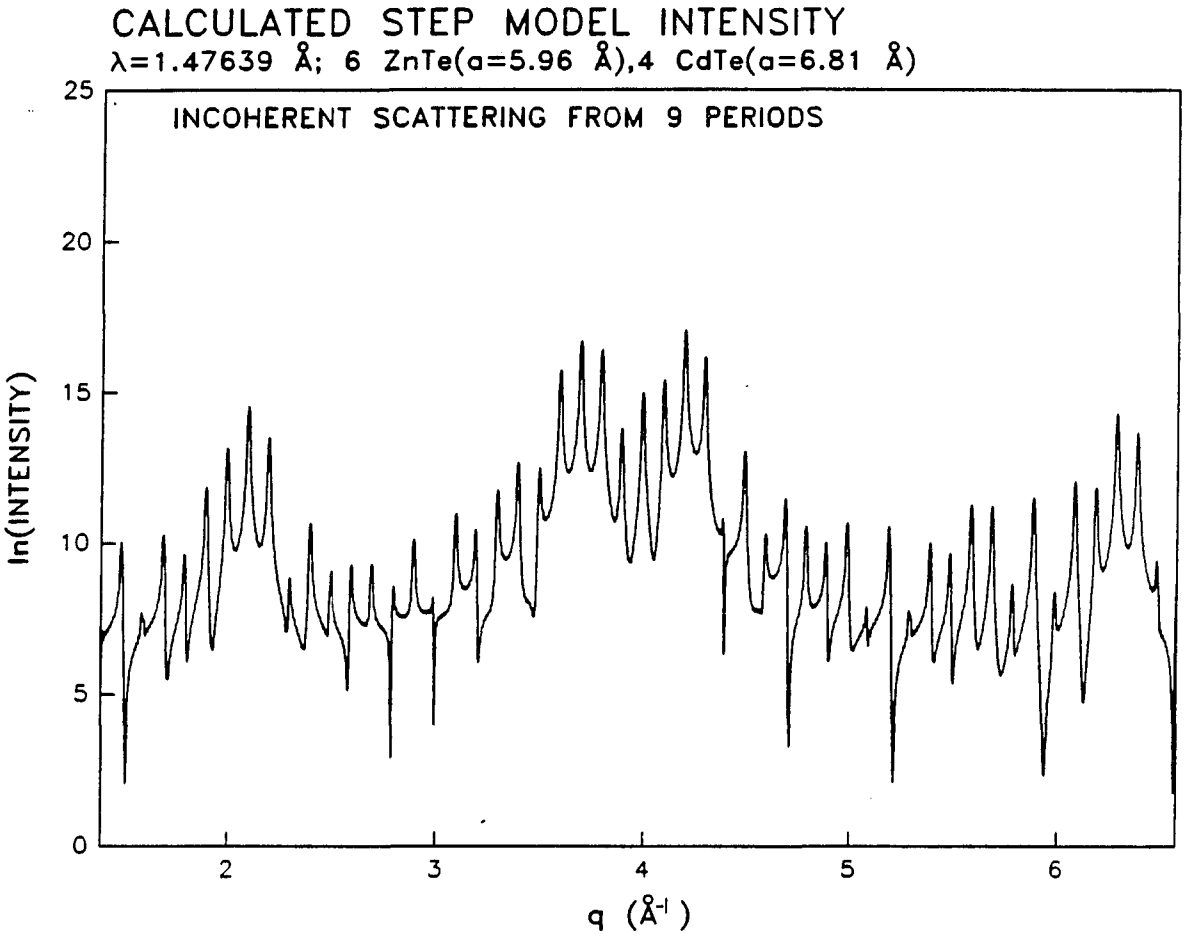

Figure VI.12a. Step model intensity distribution from nine incoherently diffracting SL unit cells. Table VI.8 lists the step model parameters of this distribution. The intensity represents the square of the structure factor. $q \equiv 4\pi \sin\theta/\lambda$, where θ is the Bragg angle and λ is the 1.47639 Å radiation wavelength. This example represents a strained layer SL that is similar to SL-18

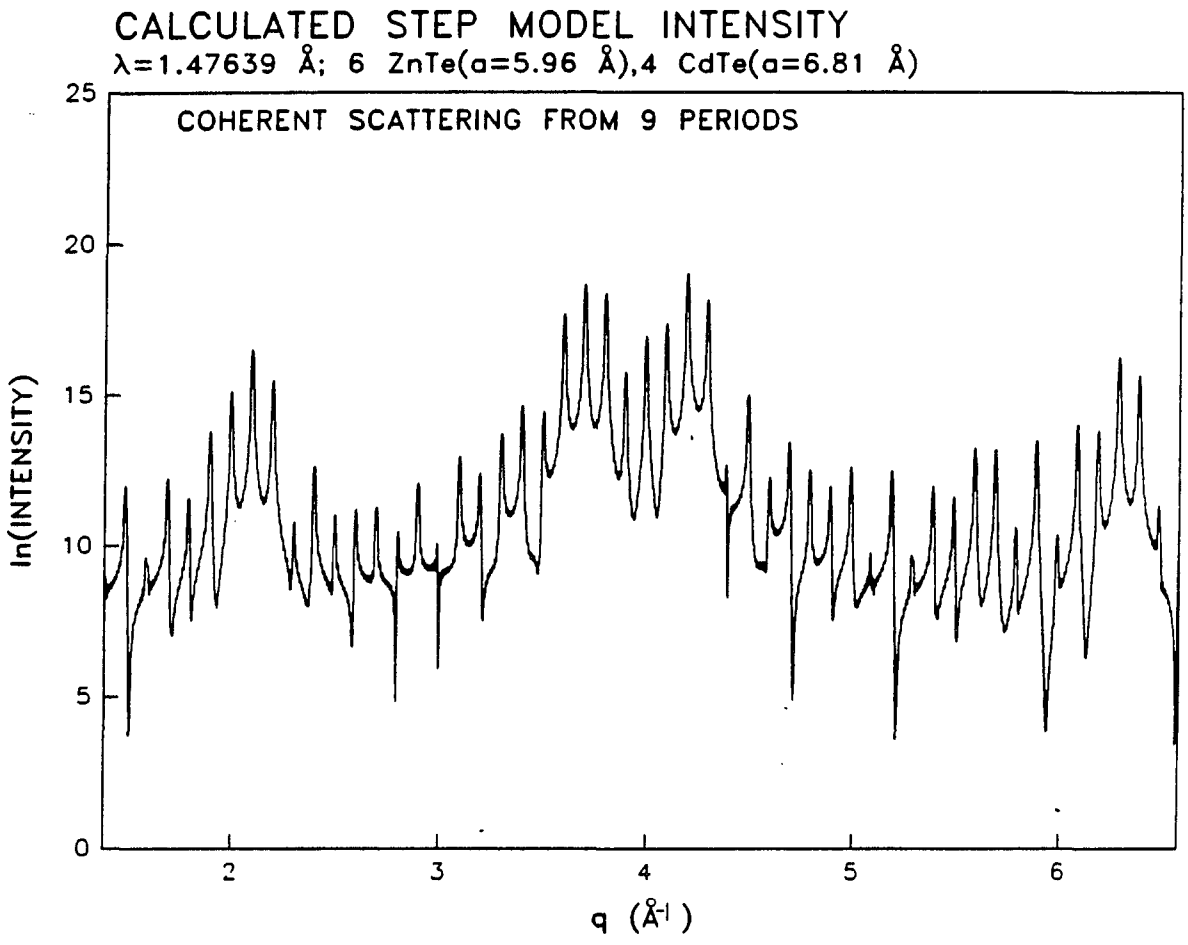

Figure VI.12b. Step model intensity distribution from nine coherently diffracting SL unit cells. Table VI.8 lists the step model parameters of this distribution. The intensity represents the square of the structure factor. $q \equiv 4\pi \sin\theta/\lambda$, where θ is the Bragg angle and λ is the 1.47639 Å radiation wavelength. This example represents a strained layer SL that is similar to SL-18

2. Procedure

The step model structure factor is defined by equation III.12, where $c_1=2d_1$ and $c_2=2d_2$. This function was transformed into FORTRAN code so that a nonlinear least-squares fitting routine (Bevington, 1969) can fit the square of the structure factor to the peak intensities of the any SL diffraction spectrum. A proportionality constant is included into the fit to compensate for all fixed attributes of the diffraction apparatus. Since the measured SL peak profiles do not fit the interference function distribution (equation III.13a) only the maximum peak heights are fit to the step model function. This greatly reduces the number of data points that are fit and increases the uncertainty of the extracted information. In addition, the central peaks are not included in the fit, since the influence of the diffracting buffer layer on the measured central peak intensities is unknown. The constituent lattice parameters are extracted by performing a weighted fit, where the weight assigned to each peak intensity is set to the square of the uncertainty (instrumental weighting). Parameters can be selectively included in the iterative fitting process. Parameters that are not included remain constant. The iterative procedure terminates when the improvement in the calculated R-factor (see equation IV.7b) is less than 0.1%.

Before instigating the fitting procedure, a set of initial constituent lattice parameters must be assigned. Knowing the constituent layer ratio predicted during growth, the measured SL period, and the average constituent cell length along the growth direction, the number of two atom basis cells is determined for each constituent material. The total number of average constituent cells is determined

by dividing the period by the average constituent cell length along the growth direction. Multiplying this value by the appropriate constituent layer fraction (growth information), a trial N_1 and N_2 are determined. In an effort to define a standard initial parameter assignment procedure, the initial constituent lattice parameters are set to the average constituent cell length. The fractional occupation values are all set to one, and the Debye-Waller factors are constrained so that one parameter M is common to all four constituent atoms. Initially, M is set to zero.

Once the initial parameters have been defined, the fitting procedure is instigated by fitting the proportionality constant with all constituent lattice parameters excluded from the fit. Then, in succession, the constituent lattice parameters, Debye-Waller factors, and fractional occupation values are included in the fit and refined. The number of two atom basis cells are excluded from the fit, since these must be integer values.

When the fitting procedure is finished, a different pair of N_1 and N_2 parameters are introduced and the fitting procedure is repeated. This compensates for the uncertainty of knowing the actual values--only the predicted values are known. However, since the period and average constituent cell length are directly measured, each pair of trail N_1 and N_2 values must be consistent with the sum N_1+N_2 derived from the peak positions. The pair of N_1 and N_2 that yield the lowest χ value (see equation IV.7a) are assumed to be the correct values.

After acquiring some experience with the fitting process, the step model structure factor was modified to include an intermediate region at

the CdTe→ZnTe and ZnTe→CdTe constituent layer interfaces. Six additional fitting parameters were introduced: N_{I11}, N_{I12}, N_{I21}, N_{I22}, d_{I1}, and d_{I2}. These parameters define the number and length of the a-b atom pairs that describe the interface regions, allowing for a graded lattice parameter transition between the constituent materials (Vandenberg, Hamm, Panish & Temkin, 1987). N_{Iij} is defined to be the number of a-b atom pairs of constituent j within the i^{th} interface. The application of the above fitting procedure to SL-17 and SL-18 is presented below.

3. Results

Based on the diffractometer data, the sum N_1+N_2 for SL-17 and SL-18 are 13 and 20, respectively. In the following discussion, constituents one and two represent ZnTe and CdTe, respectively. By fitting several N_1 and N_2 trail pairs, a set that yields the lowest R-factor was established. For SL-17, these values are $N_1=6$ and $N_2=7$, and for SL-18, $N_1=13$ and $N_2=7$. Table VI.9 summarizes the step model fitting parameters of both SL-17 and SL-18. There are two entries for SL-17. The first entry represents an intermediate result, which describes the best fit obtained before introducing fractional atom occupation. The second entry represents the final situation that yields the lowest χ value.

The quality of the step model fit is determined by both the χ value and R-factor. Ideally, χ should be one and the R-factor should be zero. The values listed in Table VI.9 provide conflicting information. The χ values are quite large, and the R-factors indicate a reasonable fit. This discrepancy suggests that either the weighting scheme or the

Table VI.9 Step model parameter summary for both SL-17 and SL-18, where (a_1=Zn, b_1=Te) represents constituent #1 and (a_2=Cd, b_2=Te) represents constituent #2

Sample	N_1	d_1	N_2	d_2	N_{I1}[a]	d_{I1}	N_{I2}[b]	d_{I2}	M_1[c]	M_2[c]	f_{a1}	f_{b1}	f_{a2}	f_{b2}	χ	R (%)
SL-17	4	6.022	5	6.586	1/1	6.362	1/1	6.098	2.91	3.87	1.00	1.00	1.00	1.00	83	22.5
	4	6.088	5	6.552	1/1	6.360	1/1	6.056	6.68	8.17	0.99	1.00	0.80	1.00	16	6.6
SL-18	10	5.966	6	6.707	2/0	6.568	1/1	6.491	5.14	7.76	1.0	1.0	0.97	1.0	25	11.9

[a] N_{I11} / N_{I12} (see text).

[b] N_{I22} / N_{I21} (see text).

[c] Debye-Waller constant: $M=8\pi^2\langle\Delta r^2\rangle^2$ (see equation II.48).

estimated intensity uncertainties must be modified. Neither the χ values nor the R-factors are listed in published step model fits of other SL systems, suggesting that other research institutions experience similar difficulties. According to Vandenberg (1987), the most reliable assessment of a step model fit is determined by inspection (observing the differences in a plot of the observed and calculated values as a function of reciprocal scattering magnitude). The results of the step model fit are illustrated in Figures VI.13-VI.15, which show the natural logarithm of both the observed and calculated peak intensities as a function of the SL index l'. Figures VI.13 and VI.14 illustrate the fit of SL-17 before and after refining the atomic fractional occupation parameters, respectively. Figure VI.15 illustrates the final fit of SL-18.

The illustrated step model results approximate the actual diffracted peak intensities. Figure VI.14 appears to be the best fit. Refining the fractional occupation parameters improved the agreement of the (0,0,2) constituent diffraction region. However, the refined Cd occupancy of 80.0% is highly unrealistic (Monfroy, 1987). Agreement between the observed and calculated intensities within the (0,0,4) constituent diffraction region is quite good for both samples. This is probably related to the generally more intense reflections found within this region compared to the (0,0,2) and (0,0,6) regions.

The constituent cell lengths that are extracted from the step model fit provide constituent lattice strain information along the growth direction. The in-plane lattice parameters were extracted from peak position information (see section VI.C). Assuming that these values

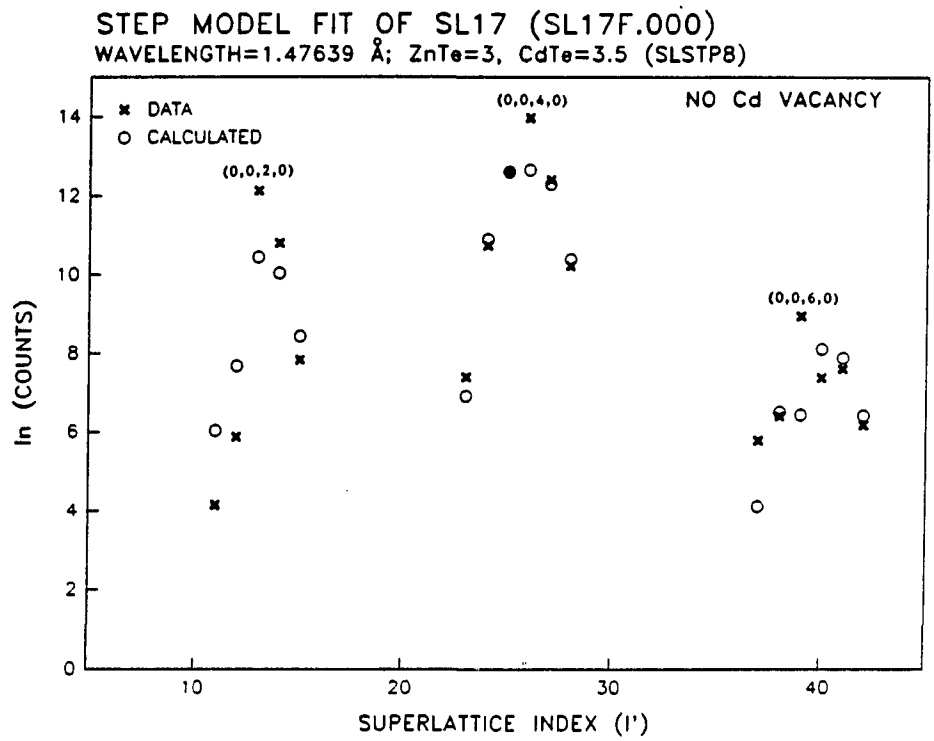

Figure VI.13. Measured (X) and calculated (O) SL peak intensities of SL-17 as a function of the SL index $l'=2L\sin\theta/\lambda$, where L is the SL period, θ is the Bragg angle, and λ is the 1.47639 Å radiation wavelength. The calculated values are derived from the step model using the parameters listed in Table VI.9. This is not the final fit, but rather an intermediate fit before allowing the atomic vacancy parameters to vary

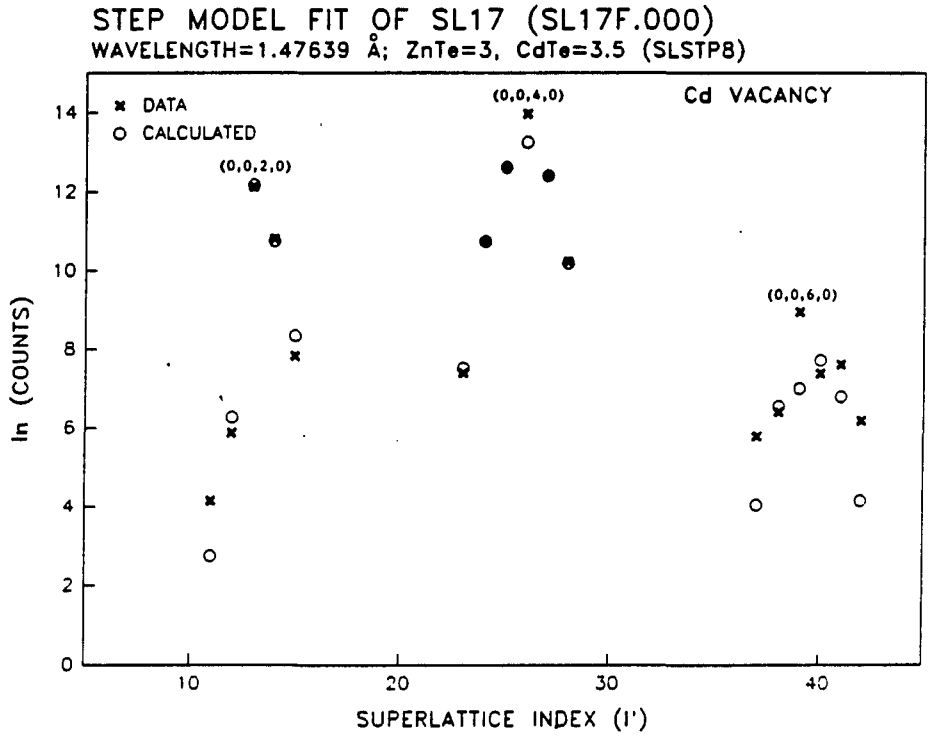

Figure VI.14. Measured (X) and calculated (O) SL peak intensities of SL-17 as a function of the SL index $l'=2L\sin\theta/\lambda$, where L is the SL period, θ is the Bragg angle, and λ is the 1.47639 Å radiation wavelength. The calculated values are derived from the step model using the parameters listed in Table VI.9. This is the final fit, which yields a 6.6% R-factor and indicates a 20% Cd vacancy

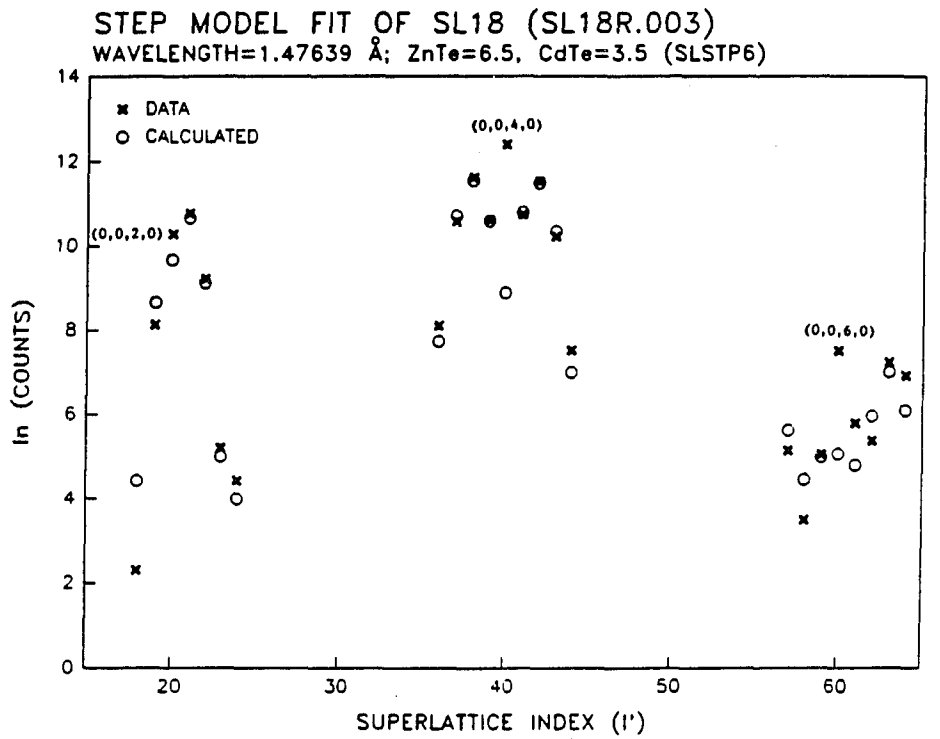

Figure VI.15. Measured (X) and calculated (0) SL peak intensities of SL-18 as a function of the SL index $l'=2L\sin\Theta/\lambda$, where L is the SL period, Θ is the Bragg angle, and λ is the 1.47639 Å radiation wavelength. The calculated values are derived from the step model using the parameters listed in Table VI.9. This is the final fit, which yields an 11.9% R-factor

represent an in-plane parameter common to both constituents, as opposed to an average of different constituent parameters, the constituent lattice strain parallel to the growth direction ε_p can be calculated,

$$\varepsilon_p = \frac{c-a_p}{a_p} \quad , \tag{VI.2}$$

where c is the lattice cell length along the growth direction and a_p is the in-plane lattice cell length. The calculated strain information based on the step model results (Table VI.9) is listed in Table VI.10. Two in-plane lattice parameters are listed for SL-17. These values are extracted from diffraction spectra recorded using different wavelengths (see section IV.C). Using 1.47639 Å and 0.7093 Å radiation, a 6.280 ± 0.003 Å and 6.294 ± 0.005 Å in-plane lattice parameter are observed. The in-plane lattice parameter listed for SL-18 is derived from 1.47639 Å radiation.

The calculated strains ε_p are nearly one-fourth of the value predicted under the ideal epitaxy condition. The strain perpendicular to an ideally commensurate interface can be estimated from the elastic constants and crystallographic orientation of the constituent materials (Hornstra & Bartels, 1978). Along the [0,0,1] crystallographic direction (SL growth direction), the perpendicular strain ε_p is calculated from the bulk cubic lattice parameters,

$$\varepsilon_{p1} = \left[\frac{a_1-a_2}{a_2}\right]\left[\frac{c_{11}+2c_{12}}{c_{11}}\right] \quad , \tag{VI.3}$$

Table VI.10 Calculated constituent lattice strain perpendicular to the growth direction for both SL-17 and SL-18 using in-plane lattice constants derived from peak positions (assuming a tetragonal distortion) and using perpendicular lattice constants extracted from the step model

Constituent material	Unit cell length[a] along growth direction c (Å)	Strain[b] SL-17 (a_p=6.280 Å) ε_p (%)	SL-17 (a_p=6.294 Å) ε_p (%)	SL-18 (a_p=6.274 Å) ε_p (%)
ZnTe	6.022	-4.11	-4.32	
	6.088	-3.06	-3.27	
	5.966			-4.91
CdTe	6.586	+4.87	+4.64	
	6.552	+4.33	+4.10	
	6.707			+6.90

[a]From step model, see Table VI.9.

[b]Defined by equation VI.2, a_p is the in-plane lattice cell length extracted from peak positions.

where ε_{p1} is the perpendicular strain of constituent one, a_1 and a_2 are the bulk cubic lattice cell lengths of each constituent, and c_{11} and c_{12} are the elastic constants of constituent one. The elastic constants of both CdTe and ZnTe are listed in Table VI.11. Applying equation VI.3 to the tabulated elastic constants, the perpendicular strain of CdTe and ZnTe are -12.9% and +15.2%, respectively. These values are significantly larger than the stain extracted using the step model. If the step model parameters accurately represent the SL films, the lower observed strains suggest that the interfaces are partially relieved by misfit dislocations.

Table VI.11 Room temperature elastic constants of CdTe and ZnTe

Parameter	Elastic constant ($X10^{-11}$ dyne/cm^2) CdTe[a]	ZnTe[b]
c_{11}	5.350	7.13
c_{12}	3.681	4.07
c_{44}	1.994	3.12

[a]McSkimin & Thomas (1962).

[b]Martin (1970).

VII. CONCLUSIONS

A. Achievements

The application of x-ray diffraction, using both a precession camera and a diffractometer, is successfully applied to II-VI semiconductor SLs. This research investigation describes the first published attempt and successful application of the in-situ method, which is both fundamentally different and superior to the quenched sample approach. The thermal stability of the mercury-based SLs is investigated by performing in-situ interdiffusion measurements at temperature between 383 K and 484 K (the SL growth temperature is 458 K for all samples). A linear diffusion model is used to extracted diffusion coefficients from the time evolution of the decreasing satellite intensities.

The step model is applied to diffracted peak maxima in an effort to assess the constituent lattice strain along the growth direction. This "perfect" SL model is modified to include vacancies, atomic thermal motion, and strained layer transition regions at the constituent interfaces. The angular dependence of the atomic scattering factors, which is commonly approximated by a constant scattering value in the literature, is included in the structure factor calculation.

B. $Hg_{1-x}X_xTe$-CdTe Experiments

Precession films verify that all SL components are epitaxially related, despite the 14% lattice mismatch between the GaAs substrate and CdTe buffer layer. The crystallographic orientation of each component is easily identified. Twinning is observed in all [1,1,1] oriented

HgTe-CdTe, $Hg_{1-x}Mn_xTe$-CdTe, $Hg_{1-x}Zn_xTe$-CdTe, and $Hg_{1-x}Cd_xTe$-CdTe SL samples.

From ω-2θ peak position information, several structural attributes of the macroscopic SL volume are extracted. First, inhomogeneous SL growth is identified. This requires sample dimensions that are several times larger than the collimated beam cross section. All samples that met this requirement exhibit inhomogeneous SL growth, with period variations as large as 16% over a 9 mm lateral distance observed. Second, essentially all SL samples have periods that are incommensurate with the average constituent lattice, suggesting that the constituent interfaces are not chemically abrupt. The incorporation of manganese, cadmium, or zinc into the HgTe layers does not influence the commensurability of the HgTe-CdTe SL period. Third, the measured SL periods are compared to the predicted periods. On average, the measured periods are found to be under one average constituent cell length along the growth direction. However, differences as large as three constituent cell lengths are observed. Finally, several samples exhibit multiple domains that have distinct periods. In general, no correlation among the multiple periods is apparent, however, for one HgTe-CdTe sample (ML-21B), the presence of two distinct periods is attributed to the the multiple domain structure of the CdTe substrate.

Based on peak breadth information, the macroscopic coherence of the SL films is found to exist over a much smaller volume, compared to the total SL volume. Applying the Scherrer formula to the observed ω-2θ peak breadths, only three to ten SL unit cells coherently diffract along the growth direction in the HgTe-CdTe samples, five to ten cells in the

$Hg_{1-x}Mn_xTe$-CdTe samples, nineteen to forty cells in the $Hg_{1-x}Zn_xTe$-CdTe samples, and four to twelve cells in the $Hg_{1-x}Cd_xTe$-CdTe samples. All SL films are at least 250 SL cells thick.

The thermal stability of $Hg_{1-x}X_xTe$-CdTe SLs is investigated using the in-situ method. Although the interdiffusion process appears to be heavily sample dependent, several general conclusions are derived from this investigation. The linear diffusion theory clearly fails to describe the interdiffusion process. The large concentration gradient across each interface is most likely responsible for this failure.

The thermal stability of HgTe-CdTe SLs that are alloyed with either cadmium or manganese is significantly enhanced, contradicting the predicted destabilizing properties that both cadmium and manganese are expected to have on the HgTe bonds. At 436 K, the HgTe-CdTe SL structure is destroyed after 53 hours, which is significantly shorter than the 225 and 280 hours required to destroy $Hg_{1-x}Mn_xTe$-CdTe and $Hg_{1-x}Cd_xTe$-CdTe SL samples, respectively. This suggests that both alloying elements enhance the structural stability of the SL by reducing lattice defects. Both cadmium and manganese could be filling lattice vacancies or preventing interstitial occupation. This is further supported by observed lattice annealing characteristics. At temperatures below 458 K, the satellite intensities of HgTe-CdTe SLs increase at the start of the interdiffusion experiment. Later in the experiment, this annealing process is dominated by layer interdiffusion until the satellite structure is completely destroyed. However, both cadmium and manganese alloyed SLs exhibit the immediate onset of interdiffusion, independent of the diffusion temperature.

Finally, the in-situ diffusion experiments performed at the SL growth temperature suggest that interdiffusion during film deposition could significantly affect the early deposited layers. This is in agreement with the growth interdiffusion experiment, which exploits the penetration depth dependence on x-ray wavelength to extract growth interdiffusion information. The diffraction spectra of two thick HgTe-CdTe samples (6.2 μ for SL-93 and 6.6 μ for SL-95) significantly broaden as the penetration depth of the x-ray radiation increases from 6 μ to 26 μ. This broadening is attributed to changes in the structure factor of earlier deposited SL unit cells.

Since the interdiffusion process is heavily sample dependent, the diffusion mechanism can not be unambiguously identified. Even if this dependence was not observed, a nonlinear diffusion theory, which assumes a concentration dependent diffusion coefficient, is required to extract information that can be compared to other investigational techniques. The activation energies extracted from the HgTe-CdTe interdiffusion experiments (0.9-0.51 eV) are approximately consistent with either an interstitial or vacancy diffusion mechanism. The significantly larger activation energies of both the $Hg_{1-x}Mn_xTe$-CdTe (1.7 eV) and the $Hg_{1-x}Cd_xTe$-CdTe (2.1 eV) samples suggest that a different diffusion mechanism is responsible for layer interdiffusion in the alloyed SLs.

C. CdTe-ZnTe Experiments

Zero level precession films verify that the GaAs substrate, $Cd_{.5}Zn_{.5}Te$ buffer layer, and CdTe-ZnTe SL film are epitaxially related. Extended satellite reflections are distinguished from the intense

central peak reflections on the films.

From both ω and ω-2θ diffraction scans, several general attributes of the SL samples are extracted. All SL periods are incommensurate with the average constituent lattice. No correlation between the growth environment and the fractional number of average constituent cells is apparent. Differences as large as 17 Å between the measured and predicted periods are observed. ω-2θ scans having scattering vectors along both the [0,0,1] growth normal and the [1,1,1] average constituent lattice direction indicate that the constituent unit cells are tetragonally distorted along the growth direction. Distortions as large as 5% are observed. Applying the Scherrer formula to the observed ω-2θ peak breadths, approximately 33 to 44 of the 280 to 400 SL unit cells coherently diffract along the growth direction. Variations of the peak breadth with satellite order imply a maximum period variation of 10% along the growth direction. Complicated ω scan structures are observed in one sample (SL-17). This SL, which is the least strained, exhibits double ω maxima. The separation of these maxima increase with satellite order. In contrast, single ω maxima are observed in SL-18, which is more strained along the growth direction than SL-17.

Applied to the strained layer samples, the step model is found to be most sensitive to the constituent cell length parameters. The square of the step model structure factor is fit to two CdTe-ZnTe strained layer SLs, SL-17, and SL-18, yielding 6.6% and 11.9% final R-factors, respectively. The ZnTe constituent unit cells contract approximately 3.2% and 4.9%, compared to their bulk values, and the CdTe layers expand approximately 4.2% and 6.9%, for SL-17 and SL-18, respectively. These

values are approximately one-fourth the theoretical values, which are based on ideally commensurate CdTe-ZnTe interfaces. This suggests that the misfit strain is partially relieved by misfit dislocations.

D. Conclusions and Suggestions

In conclusion, the quality of all investigated II-VI semiconductor SLs is not comparable to device quality. Clearly, the demanding tolerance required to produce II-VI SL devices has not been achieved. Both the discrepancy between the predicted and measured SL attributes and the degree of lateral film inhomogeneity must be significantly reduced. The predicted electronic properties of SLs require step model-like interfaces and structural coherence that extends throughout the total film volume. These properties are not observed. In addition, the thermal stability experiments suggest that HgTe-CdTe SL devices are unstable at temperatures slightly above 300 K. Alloying HgTe-CdTe SL with either manganese or cadmium could extend this threshold temperature.

An extension of this research investigation should include a systematic study of large single wafer SL samples. By reducing the large wafer to smaller samples, many inhomogeneous growth measurements and interdiffusion experiments can be performed. This would reduces the sample dependent factors that influence both the diffusion coefficients and activation energies.

VIII. BIBLIOGRAPHY

Abrikosov, N. K., Bankina, V. F., Poretskaya, L. V., Shelimova, L. E. & Skudnova, E. V. (1969). Semiconducting II-VI, IV-VI, and V-VI Compounds. New York: Plenum Press.

Anderson, J. C., Leaver, K. D., Rawlings, R. D. & Alexander, J. M. (1985). Materials Science. 3rd edition. London: Van Nostrand Reinhold (UK) Co. Ltd.

Arch, D. K., Faurie, J.-P., Staudenmann, J.-L., Hibbs-Brenner, M. & Chow, P. (1986). J. Vac. Sci. Technol. A, 4, 2101.

Arch, D. K., Shur, M., Abrokwah, J. K. & Daniels, R. R. (1987). J. Appl. Phys., 61, 1503.

Bearden, J. A. (1967). Rev. Mod. Phys., 39, 78.

Bettini, M. & Brandt, G. (1979). J. Appl. Phys., 50, 6938.

Bevington, P. R. (1969). Data Reduction and Error Analysis for the Physical Sciences. New York: McGraw-Hill.

Blakemore, J. S. (1982). J. Appl. Phys., 53, R123.

Borrmann, G. (1941). Phys. Z., 42, 157.

Borrmann, G. (1950). Phys. Z., 127, 297.

Brinkman, W. F. (1985). Report on Artificially Structured Materials. Washington, D.C.: National Research Council, National Academy Press.

Buerger, M. J. (1944). The Photography of the Reciprocal Lattice, ASXRED Monogr. No. 1. The American Society for X-ray and Electron Diffraction. New York: ACA.

Buerger, M. J. (1964). The Precession Method in X-ray Crystallography. New York: John Wiley.

Burns, G. (1985). Solid State Physics. New York: Academic Press, Inc.

Capasso, F. (1987). Science, 235, 172.

Chang, L. L. & Ludeke, R. (1975). Epitaxial Growth, edited by J. W. Matthews, pp 37-72. New York: Academic Press, Inc.

Chrzan, D. & Dutta, P. (1985). J. Appl. Phys., 59, 1504.

Chu, X., Sivananthan, S. & Faurie, J.-P. (1987). Appl. Phys. Lett., 50, 597.

Clemens, B. M. & Gay, J. G. (1986). Phys. Rev. B, 35, 9337.

Cohen, P. I., Pukite, P. R., Van Hove, J. M. & Lent, C. S. (1986). J. Vac. Sci. Technol. A, 4, 1251.

Crank, J. (1985). The Mathematics of Diffusion. Oxford, England: Clarendon Press.

Cromer, D. T. (1983). J. Appl. Crystallogr., 16, 437.

Cromer, D. T. & Waber, J. T (1974). International Tables for X-Ray Crystallography, vol. 4, edited by James A. Ibers & Walter C. Hamilton, pp 71-147. Burmingham, England: Kynoch Press.

Cullity, B. D. (1978). Elements of X-ray Diffraction. Cambridge, Mass.: Addison-Wesley Publishing Company, Inc.

Darwin, C. G. (1914). Phil. Mag., 27, 315.

Davis, P. J. (1972). Handbook of Mathematical Functions, edited by M. Abramowitz & I. A. Stegun, pp 253-293. New York: Dover Publications, Inc.

Debye, P. (1913). Verh. der Deutsch. Phys. Ges., 15, 678.

de Fontaine, D. (1966). Local Atomic Arrangements Studied by X-Ray Diffraction, Vol. 36, edited by J. B. Cohen & J. E. Hilliard, pp 51-94. New York: Gordon and Breach Science Publishers.

de Wolf, P. M. (1984). Modulated Structure Materials, edited by T. Tsakalakos, pp 247-264. The Hague, Netherlands: Martinus Nijhoff Publishers.

DuMond, J. & Youtz, J. P. (1940). J. Appl. Phys., 11, 357.

Elad, E. (1970). Symposium on Energy Dispersion X-Ray Analysis: X-Ray and Electron Probe Analysis, p 57. Toronto, ASTM STP-485.

Elderton, W. D. & Johnson, N. L, (1969). Systems of Frequency Curves. Cambridge, England: Cambridge Press.

Elliott, R. P. (1965). Constitution of Binary Alloys, first supplement. New York: McGraw-Hill.

Esaki, L. (1985). Synthetic Modulated Structures, edited by L. L. Chang & B. C. Giessen, pp 3-41. New York: Academic Press, Inc.

Esaki, L. & Tsu, R. (1970). IBM J. Res. Develop. 14, 61.

Faurie, J.-P. & Million, A. (1981). J. Cryst. Growth, 54, 577.

Faurie, J.-P. & Million, A. (1982). J. Cryst. Growth, 54, 582.

Faurie, J.-P., Million, A. & Piaguet J. (1982). Appl. Phys. Lett. 41, 713.

Faurie, J.-P., Reno, J., Sivananthan, S., Sou, I. K., Chu, X., Boukerche, M. & Wijewarnasuriya, P. S. (1986). J. Vac. Sci. Technol. A, 4, 2067.

Faurie, J.-P., Sivananthan, S., Chu, X., Reno, J. & Wijewarnasuriya, P. S. (1987). J. Vac. Sci. Technol. B, 5, 700.

Feldman, R. D., Austin, R. F., Dayem, A. H. & Westerwick, E. H. (1986). Appl. Phys. Lett., 49, 797.

Fick, A. (1855). Annln. Phys., 170, 59.

Fleming, R. M., McWhan, D. B., Gossard, A. C., Wiegmann, W. & Logan, R. A. (1980). J. Appl. Phys., 51, 357.

Girifalco, L. A. (1964). Atomic Migration in Crystals. Waltham, Mass.: Blaisdell Publishing Company.

Glass, A. (1987). Science, 235, 1003.

Greer, A. L. & Spaepen, F. (1985). Synthetic Modulated Structures, edited by L. L. Chang & B. C. Giessen, pp 419-486. New York: Academic Press, Inc.

Guinier, A. (1963). X-Ray Diffraction in Crystals, Imperfect Crystals, and Amorphous Bodies. San Francisco: W. H. Freeman and Company.

Guinier, A. & Dexter, D. L. (1963). X-Ray Studies of Materials. New York: Interscience Publishers.

Gyorgy, E. M., McWhan, D. B., Dillon, J. F., Walker, L. R. & Waszczak, J. V. (1982). Phys. Rev. B, 25, 6739.

Hall, M. M., Jr. (1977). J. Appl. Crystallogr., 10, 66.

Halliwell, M. A. G. & Lyons, M. H. (1984). J. Cryst. Growth, 68, 523.

Hamilton, P. H. (1964). International Tables for X-Ray Crystallography, vol. 4, edited by James A. Ibers & Walter C. Hamilton, pp 287-292. Birmingham, England: Kynoch Press.

Hamilton, P. H. (1964). Prod. and Solid State Technology, 7, 15.

Henein, G. E. & Hilliard, J. E. (1984). J. Appl. Phys., 55, 2895.

Henry, N. F. M. & Lonsdale, K. (1952). International Tables for X-Ray Crystallography, vol. 1, edited by N. F. M. Henry & K. Lonsdale, pp 15-21. Burmingham, England: Kynoch Press.

Horning, R. D. & Staudenmann, J.-L. (1986). Appl. Phys. Lett., 49, 1590.

Horning, R. D. & Staudenmann, J.-L. (1987). J. Cryst. Growth, 80, 125.

Hornstra, J. & Bartels, W. J., (1978). J. Cryst. Growth, 44, 513.

James, R. W. (1982). The Optical Principles of the Diffraction of X-Rays. Woodbridge, Connecticut: Ox Bow Press.

Jones, F. W. (1939). Proc. Roy. Soc. London, A, 166, 16.

Kelly, A. & Groves, G. W. (1970). Crystallography and Crystal Defects. Cambridge, Mass.: Addison-Wesley.

Kervarec, J., Baudet, M., Caulet, J., Auvray, P., Emery, J. Y. & Regreny, A. (1984). J. Appl. Crystallogr., 17, 196.

Ketter, R. L. & Prawel, S. P. (1969). Modern Methods of Engineering Computation. New York: McGraw-Hill.

Kittel, C. (1986). Introduction to Solid State Physics, Sixth edition. New York: John Wiley and Sons, Inc.

Knox, R. D., Staudenmann, J.-L., Monfroy, G., Faurie, J.-P. & Wu, O. K. T. (1988). Superlattices and Microstructures, 4, 165.

Kobayashi, M., Konagai, M. & Takahashi, K. (1986). J. Appl. Phys., 61, 1015.

Kruse, P. W., McGlauchlin, L. D. & McQuistan, R. B. (1962). Elements of Infrared Technology: Generation, Transmission, and Detection, Chap. 9. New-York: John Wiley and Sons, Inc.

Ladd, M. F. C. & Palmer, R. A. (1978). Structure Determination by X-Ray Crystallography. New York: Plenum Press.

Landau, L. D. & Lifshitz, E. M. (1975). The Classical Theory of Fields. Oxford, England: Pergamon Press.

Laue, M. V. (1918). Ann. d. Physik, 56, 497.

Lawson, W. P., Nielsen, S., Putley, E. H. & Young, A. S. (1959). J. Phys. Chem. Solids, 9, 325.

Long, D. & Schmit, J. L. (1970). Semiconductors and Semimetals, Vol. 5, edited by R. K. Willardson & A. C. Beer, pp 175-255. New York: Academic Press, Inc.

Manning, J. R. (1968). Diffusion Kinetics for Atoms in Crystals. London: D. Van Nostrand Company, Inc.

Martin, R. M. (1970). Phys. Rev. B, 1, 4005.

Matthews, J. W., Mader, S. & Light, T. B. (1970). J. Appl. Phys., 41, 3800.

McGill, T. C., Wu, G. Y. & Hetzler, S. R. (1986). J. Vac. Sci. Technol. A, 4, 2091.

McWhan, D. B. (1985). Synthetic Modulated Structures, edited by L. L. Chang & B. C. Giessen, pp 43-73. New York: Academic Press, Inc.

McWhan, D. B., Gurvitch, M., Rowell, J. M. & Walker, L. R. (1983). J. Appl. Phys., 54 3886.

McSkimin, D. G. & Thomas, D. G. (1962). J. Appl. Phys., 33, 56.

Meheswaranathan, P, Sladek, R. J. & Debska, U. (1985). Phys. Rev. B, 31, 5212.

Miceli, P. F., Neumann, D. A. & Zabel, H. (1986). Appl. Phys. Lett., 48, 24.

Miles, R. H., McGill, T. C., Sivananthan, S., Chu, X. & Faurie, J.-P. (1987). J. Vac. Sci. Technol. B, 5, 1263.

Monfroy, G. (1987). Private communication. University of Illinois at Chicago.

Monfroy, G., Sivananthan, S., Chu, X., Faurie, J.-P., Knox, R. D. & Staudenmann, J.-L. (1986). Appl. Phys. Lett., 49, 152.

Murphy, W. J., Chapman, L. D., Staudenmann, J.-L. & Liedl, G. L. (1985). J. Appl. Crystallogr., 18, 724.

Nelson, J. B. & Riley, D. P. (1945). Proc. Phys. Soc. (London), 57, 160.

Neumann, D. A., Zabel, H. & Morkoc, H. (1983). Appl. Phys. Lett., 43, 59.

Opyd, W. G., Dimiduk, K. C., Sigmon, T. W. & Gibbons, J. F. (1985). J. Vac. Sci. Technol. A, 3, 276.

Parthe, E. (1964). Crystal Chemistry of Tetrahedral Structures. New York: Gordon and Breach Science Publishers.

Patten, E. (1986). Private communication. Hughes Santa Barbara Research Center.

Picraux, S. T., Dawson, L. R., Osbourn, G. C. & Chu, W. K. (1983). Appl. Phys. Lett., 43, 59.

Qadri, S. B. & Dinan, J. H. (1985). Appl. Phys. Lett., 47, 1066.

Quillec, M., Goldstein, L., Le Roux, G., Burgeat, J. & Primot, J. (1984). J. Appl. Phys., 55, 2904.

Reno, J., Sou, I. K., Wijewarnasuriya, P. S. & Faurie, J.-P. (1986). Appl. Phys. Lett., 48, 1069.

Reno, J., Sporken, R., Kim, Y. J., Hsu, C. & Faurie, J.-P. (1987). Appl. Phys. Lett., 51, 1545.

Schulman, J. N. & Chang, Y.-C. (1985). Appl. Phys. Lett., 46, 571.

Scherrer, P. (1918). Nachr. Gottinger Gesell., 98, 394.

Schulman, J. N. & McGill, T. C. (1979). Appl. Phys. Lett. 34, 663.

Segmuller, A. & Blakeslee, A. E. (1973). J. Appl. Crystallogr., 6, 19.

Segmuller, A. & Murakami, M. (1985). Thin Films from Atoms and Particles, edited by K. J. Klabunde, pp 325-351. New York: Academic Press, Inc.

Sevenhans, W., Gijs, M. & Bruynseraede, Y. (1986). Phys. Rev. B, 34, 5955.

Sharma, B. L. (1970). Diffusion in Semiconductors. Clausthal-Zellerfield, Ger.: Trans Tech Publications.

Sher, A., Chen, A.-B., Spicer, W. E. & Shih, C.-K. (1985). J. Vac. Sci. Technol. A, 3, 105.

Sivananthan, S., Chu, X., Boukerche, M. & Faurie, J.-P. (1985). Appl. Phys. Lett., 47, 1291.

Sivananthan, S., Chu, X. & Faurie, J.-P. (1987). J. Vac. Sci. Technol. B, 5, 694.

Sivananthan, S., Chu, X., Reno, J. & Faurie, J.-P. (1986). J. Appl. Phys., 60, 1359.

Smith, D. L., McGill, T. C. & Schulman, J. N. (1983). Appl. Phys. Lett., 43, 180.

Spicer, W. E., Silberman, J. A., Landau, I., Chen, A.-B., Sher, A. & Wilson, J. A. (1983). J. Vac. Sci. Technol. A, 1, 1735.

Staudenmann, J.-L., Chapman, L. D., Murphy, W. J., Horning, R. D. & Liedl, G. L. (1985). J. Appl. Crystallogr., 18, 519.

Staudenmann, J.-L., Horning, R. D. & Knox, R. D. (1987). J. Appl. Crystallogr., 20, 210.

Staudenmann, J.-L., Horning, R. D., Knox, R. D., Reno, J., Sou, I. K., Faurie, J.-P. & Arch, D. K., (1986). Semiconductor-Based Heterostructures: Interface Structure and Stability, edited by M. L. Green, Baglin, J. E. E., Chin, G. Y., Deckman, H. W., Mayo, W. & Narasinham, D., pp 41-57. Warrendale, Penn.: Conference Proceedings of the Metallurgical Society of AIME.

Staudenmann, J.-L., Knox, R. D. & Faurie, J.-P. (1987a). Materials Modification and Growth Using Ion Beams, edited by U. Gibson, A. E. White, & P. P. Pronko, pp 193-199. Pittsburgh, Penn.: Materials Research Society, Volume 93.

Staudenmann, J.-L., Knox, R. D. & Faurie, J.-P. (1987b). J. Vac. Sci. Technol. A, 5, 3161.

Staudenmann, J.-L., Knox, R. D. & Horning, R. D. (1988). J. Cryst. Growth, 86, 436.

Staudenmann, J.-L., Sandholm, M., Chapman, L. D. & Liedl, G. L. (1984). Nuc. Instr. Meth. in Phys. Res., 222, 177.

Stowell, M. J. (1975). Epitaxial Growth, edited by J. W. Matthews, pp 437-492. New York: Academic Press, Inc.

Tang, M.-F. S. & Stevenson, D. A. (1987a). Appl. Phys. Lett., 50, 1272.

Tang, M.-F. S. & Stevenson, D. A. (1987b). J. Vac. Sci. Technol. A, 5, 3124.

Thomson, J. J. (1893). Recent Researches in Electricity and Magnetism. Oxford, England: Clarendon Press.

Vandenberg, J. M. (1987). Private communication. AT&T Bell Laboratories, Murray Hill, New Jersey.

Vandenberg, J. M., Bean, J. C., Hamm, R. A. & Hull, R. (1988). Appl. Phys. Lett., 52, 1152.

Vandenberg, J. M., Hamm, R. A., Macrander, A. T., Panish, M. B. & Temkin, H. (1986). Appl. Phys. Lett., 48, 1153.

Vandenberg, J. M., Hamm, R. A., Panish, M. B. & Temkin, H. (1987). J. Appl. Phys., 62, 1278.

Vook, R. W. (1975). Epitaxial Growth, edited by J. W. Matthews, pp 339-364. New York: Academic Press, Inc.

Wall, A., Caprile, C., Franciosi, A., Reifenberger, R. & Debska, U. (1986). J. Vac. Sci. Technol. A, 4, 818.

Walter, F. J. (1970). Symposium on Energy Dispersion X-Ray Analysis: X-Ray and Electron Probe Analysis, p 82. Toronto, ASTM STP-485.

Warren, B. E. (1941). J. Appl. Phys., 12, 375.

Warren, B. E. (1969). X-Ray Diffraction. Cambridge, Mass.: Addison-Wesley publishing company.

Watanabe, D. & Terasaki, O. (1984). Modulated Structure Materials, edited by T. Tsakalakos, pp 247-264. The Hague, Netherlands: Martinus Nijhoff Publishers.

Welker, H. & Kellner, W. (1983). Concise Encyclopedia of Sold State Physics, edited by R. G. Lerner & G. L. Trigg, pp 247-248. Cambridge, Mass.: Addison-Wesley Publishing Company.

Woltersdorf, J. (1981). Thin Solid Films, 85, 241.

Wood, E. A. (1963). Crystal Orientation Manual. New York: Columbia University Press.

Wroge, M. L., Leopold, D. J., Ballingall, J. M., Peterman, D. J., Morris, B. J., Broerman, J. G., Ponce, F. A. & Anderson, G. B. (1986). J. Vac. Sci. Technol. B, 4, 1303.

Wu, O. K. T. (1987). Private communication. Hughes Research Laboratory, Santa Barbara.

Zachariasen, W. H. (1945). Theory of X-Ray Diffraction in Crystals. New York: John Wiley and Sons, Inc.

Zanio, K. (1986). J. Vac. Sci. Technol. A, 4, 2106.

Zanio, K. & Massopust, T. (1986). J. Electron. Mater., 15, 103.

Zur, A. & McGill, T. C. (1983). J. Appl. Phys., 55, 378.

IX. ACKNOWLEDGMENTS

I thank Gerard Monfroy for the additional sample information that he provided, Robert Horning for his helpful comments and suggestions, Jean-Pierre Faurie for the samples that he provided, and Mike Sandholm for his maintenance of the rotating anode x-ray generator. I gratefully acknowledge the samples provided by E. Patten and W. L. Ahlgren from the Hughes Santa Barbara Research Center, and O. K. T. Wu from the Hughes Research Laboratory. I especially thank Jean-Louis Staudenmann for his guidance and sincere support throughout this research investigation. Finally, I thank my father, Ralph B. Knox, for his technical writing advise.